The Dissertation Committee for Won Kyoung Choi Certifies that this is the approved version of the following dissertation:

Dynamic Properties of Ash-Flow Tuffs

Committee:

Kenneth H. Stokoe II, Supervisor

Ellen M. Rathje

Fulvio Tonon

Clark R. Wilson

Loukas F. Kallivokas

Dynamic Properties of Ash-Flow Tuffs

by

Won Kyoung Choi, B.S.; M.S.

Dissertation

Presented to the Faculty of the Graduate School of
The University of Texas at Austin
in Partial Fulfillment
of the Requirements
for the Degree of

DOCTOR OF PHILOSOPHY

The University of Texas at Austin
May, 2008

Dedication

To

My Wife, My Parents and My Son

Acknowledgements

I would like to thank my supervising professor Dr. Kenneth H. Stokoe, II for his great guidance and encouragement during entire period of this study. His passion and enthusiasm in his work and life have always inspired me.

I would also like to thank to my dissertation committee members, Dr. Ellen M Rathje, Dr. Fulvio Tonon, Dr. Clark R. Wilson and Dr. Loukas F. Kallivokas for reviewing this dissertation and for valuable suggestions and advice. Thanks are also extended to the rest of the faculty members in geotechnical engineering faculty, Dr. Roy E. Olson, and Dr. Stephen G. Wright, Dr. Robert B. Gilbert for their lectures that broadened my knowledge.

The support from the Sandia National Laboratory, Las Vegas, Nevada, and the Kleinfelder are gratefully acknowledged.

I would like to thank Farn-Yuh Menq for his precious help and encouragement. Thanks are also extended to Celestino Valle, Seong yul Jeon, Jung Jea Lee, Bohyoung Lee, and Ian Johnson who have helped through all research. I would also like to thank Brady R. Cox and Yin-Cheng Lin for data collection and analysis of in-situ seismic measurement. Thanks are extended to many other graduate students that I unfortunately omitted.

I would like to thank Mr. Michael Schuhen, Zane Walton, and Joe Laird for their help and guidance for project management and quality assurance. Thanks are also extended to Teresa Tice-Boggs, Chris Trevino, and Norma J Gonzales for their administrative support, and Johnie Williams, Max Trevino, Frank Wise and Wayne

Fontenot for their technical assistance. The assistance from Mr. Johnie Williams, Frank Wise and Max Trevino in constructing the new device is especially appreciated.

Finally, I would like to thank my parents and my wife Kyung Ah for their love, support and patience.

Dynamic Properties of Ash-Flow Tuffs

Publication No._____________

Won Kyoung Choi, Ph.D.
The University of Texas at Austin, 2008

Supervisor: Kenneth H. Stokoe, II

Ash-flow tuff (ignimbrite) is a general term indicating consolidated deposits of volcanic ash flow; a flow of a mixture of gas and pyroclastic materials as products of explosive volcano eruptions (Smith, 1960). Two different ash-flow tuffs are studied in this research: 1. Topopah Spring Tuff at Yucca Mountain, Nevada and 2. the Bandelier Tuff at Pajarito Plateau, New Mexico. Various dynamic test parameters (e.g. confining pressure, shearing strain, etc) were studied with two existing devices: (1) the combined resonant column and torsional shear (RCTS) device, and (2) the free-free, unconfined, resonant column (URC) device. The effects of these parameters are evaluated for two different types of ash-flow tuffs. In addition, a Large Resonant Column (LgRC) device was developed and used to test the some tuffs from Yucca Mountain at larger strain amplitudes than possible with the RCTS and URC devices. Relationships between the linear and nonlinear dynamic properties and lithostratigraphic features were further investigated. Finally, potential problems related to sample disturbance and specimen size are considered based on comparisons of small-strain shear wave velocity (V_S) values measured in the laboratory and in the field.

Table of Contents

List of Tables xii
List of Figures xiv
Chapter 1
Introduction 1
    1.1 Background 1
    1.2 Objective of Research 2
    1.3 Organization of Dissertation 3
Chapter 2
Geological Overview and Test Materials 5
    2.1 Introduction 5
    2.2 Topopah Spring Tuff 6
        2.2.1 Stratigraphy of the Topopah Spring Tuff 11
        2.2.2 Tested Topopah Spring Tuff Specimens 18
    2.3 Bandelier Tuff 25
        2.3.1 Stratigraphy of the Bandelier Tuff 27
        2.3.2 Tested Bandelier Tuff Specimens 33
    2.3 Summary 38
Chapter 3
Literature Review 40
    3.1 Introduction 40
    3.2 Degree of Welding of Pyroclastic Deposits 42
    3.3 Effect of Porosity on Young's Modulus and Poisson's Ratio 49
    3.4 Factors Affecting Young's Modulus and Poisson's Ratio 54
        3.4.1 Confining Pressure 54
        3.4.2 Strain Rate (or Loading Frequency) 61
        3.4.3 Saturation 65
        3.4.4 Specimen Size 68
        3.4.5 Strain Amplitude 70

3.5 Summary 76
Chapter 4
Laboratory Test Equipment and Test Program 77
4.1 Introduction 77
4.2 Testing with the RCTS Device 80
4.2.1 Brief Background on RCTS Measurements 80
4.2.2 Stage Testing with the RCTS Device 83
4.3 Testing with the URC Device 90
4.3.1 URC Test Set-Up 92
4.3.2 Typical URC Measurements 94
4.3.3 Evaluating the URC Device with Metal Specimens 99
4.4 Summary 102
Chapter 5
Development of a Large Resonant Column (LgRC) Device 104
5.1 Introduction 104
5.2 Background Theory and Calibration of the LgRC Test 110
5.2.1 Mass Polar Moment of Inertia of the Flexure Bearing Unit of the LgRC Device 114
5.2.1.1 Mass Polar Moment of Inertia of Drive Plate for Fixed-Free Specimen Configuration for the RCTS Device 115
5.2.1.2 Mass Polar Moment of Inertia of Drive Table for Free-Free Specimen Configuration of the LgRC Device 118
5.2.2 Equivalent Shear Strain in the LgRC Test Specimen 123
5.2.3 Equipment-Generated Damping in the LgRC Device 125
5.3 Validation of the LgRC Device 133
5.3.1 Validation with a Metal Specimen 133
5.3.2 Validation with a Rock Specimen 140
5.4 Summary 145

Chapter 6

Small-Strain Dynamic Properties of Ash-Flow Tuff 146

6.1 Introduction 146

6.2 Small-Strain Shear Moduli of Ash-Flow Tuffs at $\sigma_o = 0$ 147

6.2.1 Topopah Spring Tuff 147

6.2.2 Bandelier Tuff 153

6.3 Log V_S – Log σ_o and Log G_{max} – Log σ_o Relationships of Ash-Flow Tuffs 155

6.3.1 Topopah Spring Tuff 155

6.3.2 Bandelier Tuff 158

6.4 Small-Strain Material Damping Ratio in Shear of Ash-Flow Tuffs at $\sigma_o = 0$ 167

6.5 Log D_{min} – Log σ_o Relationship of Ash-Flow Tuffs 171

6.6 Other Potential Factors That Might Influence Small-Strain Dynamic Properties of Ash-Flow Tuffs 177

6.5.1 Effect of Frequency 178

6.5.2 Change in Water Content due to Specimen Preparation 183

6.4.3 Effect of Lithophysal Cavities 188

6.5 Summary 195

Chapter 7

Comparisons of Laboratory Tuff Measurements with Field V_S Measurements and Laboratory Granular Soils Measurements 197

7.1 Introduction 197

7.2 Comparison of Field and Laboratory V_S Measurements 198

7.2.1 Topopah Spring Tuff 198

7.2.2 Bandelier Tuff 201

7.3 Comparison Between Tuffs and Granular Soils 205

7.3.1 G_{max} Relationships 205

7.3.2 D_{min} Relationships 211

7.4 Summary 217

Chapter 8

Nonlinear Dynamic Properties of Ash-Flow Tuffs

Nonlinear Dynamic Properties of Ash-Flow Tuffs..218

8.1 Introduction..218

8.2 G – Log γ and G/G_{max} – Log γ Relationships of Ash-Flow Tuffs 219

8.2.1 Topopah Spring Tuff...219

8.2.2 Bandelier Tuff..227

8.3 D – Log γ Relationships of Ash-Flow Tuffs...239

8.3.1 Topopah Spring Tuff...239

8.3.1 Bandelier Tuff..250

8.4 G – Log γ, G/G_{max} – Log γ and D– Log γ Relationships of Ash-Flow Tuffs Determined from the Large Resonant Column (LgRC) Device..263

8.5 Effect of Lithophysal Cavities in Nonlinear Range..274

8.6 Summary...278

Chapter 9

Summary, Conclusions, and Recommendations..279

9.1 Summary...279

9.2 Conclusions...281

9.2.1 Small-Strain Dynamic Properties of Ash-Flow Tuffs 281

9.2.2 Nonlinear Dynamic Properties of Ash-Flow Tuffs...............................287

9.3 Recommendations...295

Appendix A...296

Small-Strain Moduli and Small-Strain Material Damping Ratios and Poisson’s Ratios of Ash-Flow Tuffs..296

A.1 Introduction..296

A.1 Small-Strain Dynamic Properties from Unconfined, Free-Free RC Tests..297

References...302

Vita 308

List of Tables

Table 2.1 Criteria for Degree of Welding of Tuffs from the Topopah Spring Tuff....13

Table 2.2 Thirty Eight Topopah Spring Tuff (Tpt) Specimens Dynamically Tested for This Research....19

Table 2.3 Parent Boreholes and Surface Tunnel Locations and Number of Tpt Original Cores; Free-Free Resonant Column Testing at the University of Texas at Austin....22

Table 2.4 Stratigraphic Units, Locations, and Associated Information of the Sixteen Tpt Tuff Specimens from the Yucca Mountain Site; Combined Resonant Column and Torsional Shear (RCTS) Testing at the University of Texas at Austin....23

Table 2.5 Eighteen Bandelier Tuff Specimens Dynamically Tested in This Research....35

Table 3.1 Field Descriptive Terms for Welding Textures in the Bishop Tuff (after Wilson and Hildreth, 2003)....46

Table 3.2 Four Welding Zones and Associated Strengths and Strength Rating (after Quane and Russell, 2003)....47

Table 3.3 Range of Physical Properties for Six Ranks (after Quane and Russell, 2005)....48

Table 3.4 Petrographic Characteristics Used for Ranking Welding Intensity (after Quane and Russell, 2005)....48

Table 3.5 Frequency Ranges for Four Test Methods and Dimensions of Welded Specimens from the Topopah Spring Formation (after Haupt et al., 1991)....62

Table 4.1 Summary of Test Performed on the Specimens from the Topopah Spring Tuff....85

Table 4.2 Summary of Test Performed on the Specimens from the Bandelier Tuff....87

Table 4.3 Initial Characteristics of the Core Specimens from the Bandelier Tuff Dynamically Tested Using an Unconfined, Free-Free, Resonant Column Set-Up at the University of Texas at Austin....91

Table 5.1 Four Added Masses and Mass Polar Moment Inertia of Bottom Mass Assembly from Changes in the Resonant Frequency in Free-Free LgRC Tests....122

Table 5.2 Six Metal Specimens Used in Calibration of the LgRC Device 128

Table 5.3 Information on Metal Specimen No. 2 135

Table 5.4 Mass Polar Moment of Inertia Values of Metal Specimen No.2 and Top and Bottom Added Masses 135

Table 5.5 Comparison of Test Results from the LgRC Device with Test Results from the RCTS Device 140

Table 5.6 Mass Polar Moment of Inertia Values of Calico Hills Specimen and Added Masses 142

Table 6.1 Initial Characteristics of Six Specimens Used for Effect of Change in Water Content Due to Specimen Preparation 184

Table 6.2 Initial Characteristics of Specimens 8C-2 and 13C-2 189

Table A.1 Small-Strain Wave Velocities of Four Specimens from the Bandelier Tuff 301

Table A.2 Small-Strain Moduli and Material Damping Ratios and Poisson’s Ratios of Four Specimens from the Bandelier Tuff 301

List of Figures

Figure 2.1 Yucca Mountain Geologic Map (after Buesch et. al, 1996) 7

Figure 2.2 General Stratigraphy Description for Yucca Mountain (after Rigby, 2004) 9

Figure 2.3 Plan View of Repository Layout (after Rigby, 2004) 10

Figure 2.4 Members, Zones, Subzones, and Intervals of the Topopah Spring Tuff at Yucca Mountain, Nevada (after Buesch et al., 2006) 12

Figure 2.5 Components of: (a) Lithophysae, Veinlets, and Streaks and (b) Spots in Welded Tuffs at Yucca Mountain Site (after Buesch, 1994) 16

Figure 2.6 Fractures and Lithophysae of the Topopah Spring Tuff (after Rigby, 2004) 17

Figure 2.7 Surface Boreholes in the Vicinity of Yucca Mountain and Near the ESF Tunnel from which 27 Tuff Cores were Recovered 20

Figure 2.9 Map of Major Tectonic Features in the Vicinity of Jemez Mountains in Northern New Mexico (after Gardner and Goff, 1984) 26

Figure 2.10 Location of LANL and Geology of the Surrounding Area (after Broxton and Reneau, 1995) 28

Figure 2.11 Generalized Geologic Profile of Bandelier Tuff (after Broxton and Reneau, 1995) 29

Figure 2.12 Sample Container and Chock Detectors: (a) Wooden Core Boxes and (b) Sampling Steel Tubes for the Bandelier Tuff Samples 37

Figure 3.1 Schematic Illustration of the Welding Process: (a) An Initial Undeformed Pyroclastic Deposit, (b) the Deposit Deformed after about 30 % Compaction, (c) Profiles of Porosity and Density when about 30 % Compaction has Occurred and (d) Shapes of Pumice Lapilli when about 30 % Compaction has Occurred (after Quane and Russell, 2003) 43

Figure 3.2 Zone of Welding and Zone of Crystallization on the Cross Section of the Upper Member of the Bandelier Tuff in San Diego Canyon, Jemez Plateau, NM (after Smith and Bailey, 1966) 44

Figure 3.3 Apparent Flatness and Determination of Flattening Ratios of Pumice Fragment (after Peterson, 1979) 45

Figure 3.4 Variation of (a) Young's Modulus (E) and (b) Poisson's Ratio (ν) with Functional Porosity (n) of Saturated Samples from the Calico Hills, Bullfrog and Tram Tuffs at the Yucca Mountain (after Price, 1983)....................50

Figure 3.5 Variation of Young's Modulus (E) with Functional Porosity (n) of Saturated Nonlithophysal Specimens from the Calico Hills, Bullfrog, Tram, and the Topopah Spring Tuff at the Yucca Mountain Site (after Price and Bauer, 1985)....................51

Figure 3.6 Variation of (a) Young's Modulus (E) and (b) Poisson's Ratio (ν) with Porosity (ϕ) of Saturated Nonlithophysal Specimens from the Nonlithophysal Specimens from Drill Holes along the Explaratory Study Facilities (ESF) North Ramp (after Price et al., 1994)....................53

Figure 3.7 Variation of Elastic Wave Velocities in Compression (V_P) and Shear (V_S) of a Dry Welded Specimen from the Topopah Spring Tuff Collected from the Busted Butte Outcrop (after Martin et al., 1992)....................56

Figure 3.8 Variation of Elastic Wave Velocities of (a) Tiva Canyon Welded Tuff and (b) Paintbrush Nonwelded Tuff with Effective Confining Pressure (after Price et al., 1994)....................57

Figure 3.9 Variation of Attenuation of (a) Tiva Canyon Welded Tuff and (b) Paintbrush Nonwelded Tuff with Effective Confining Pressure (after Price et al., 1994)....................59

Figure 3.10 Variation of (a) Small-Strain Shear Modulus (G_{max}) and (b) Small-Strain Material Damping Ratio (D_{min}) of the Welded and Nonwelded Bandelier Tuff Specimens with Effective Confining Pressure (after Stokoe et al., 1993)....................60

Figure 3.11 Variation of (a) Young's Modulus (E) and (b) Extensional Attenuation (Q_E^{-1}) of the Welded Topopah Spring Tuff as Determined Four Different Methods (after Haupt et al., 1991)....................63

Figure 3.12 Variation of (a) Small-Strain Shear Modulus (G_{max}) and (b) Small-Strain Material Damping Ratio (D_{min}) of the Bandelier Tuff Specimens (Normalized with Measurements at 1 Hz) (after Stokoe et al., 1993)....................64

Figure 3.13 Variation of (a) Elastic Wave Velocities (V_S and V_P) and (b) Poisson's Ratio (ν) of Five Welded Topopah Spring Tuff Specimens (after Martin et al., 1993)....................66

Figure 3.14 Variations of Young's Modulus (E) and Poisson's Ratio (ν) of Seventy-One Lithophysal Specimens from the Topopah Spring Tuff (Tptpll) with Different Degrees of Saturation (after Price, 2004) 68

Figure 3.15 Variations of (a) Young's Modulus (E) and (b) Poisson's Ratio (ν) of Thirty-Four Nonlithophysal Specimens from the Topopah Spring Tuff, Tptpmn (after Price, 1986) 69

Figure 3.16 Variations of (a) Young's Modulus (E) and (b) Poisson's Ratio (ν) of Seventy-One Lithophysal Specimens from the Topopah Spring Tuff, Tptpll (after Price, 2004) 71

Figure 3.17 Variations of (a) Young's Modulus (E) and (b) Extensional Attenuation (Q_e^{-1}) of Welded Topopah Spring Tuff Specimen (after Haupt et al., 1991) 72

Figure 3.18 Variations of (a) Normalized Shear Modulus (G/G_{max}) and (b) Material Damping Ratio (D) of Specimens from the Bandelier Tuff (after Stokoe et al., 1993) 74

Figure 3.19 Variations of Axial Strain at Failure ($(\varepsilon_{ax})_u$) with Sample Diameter for the Specimens of the Topopah Spring Tuff (after Price, 1986; Price 2004) 76

Figure 4.1 Photograph of Combined Resonant Column (RC) and Torsional Shear (TS) Device (Confining Chamber not Shown) 78

Figure 4.2 Photograph of Unconfined, Free-Free, Resonant Column (URC) Set-Up 79

Figure 4.3 Simplified Diagram of a Combined Resonant Column (RC) and Torstional Shear (TS) Device (after Stokoe et al., 1999) 80

Figure 4.4 Frequency Response Curve Determined in the Resonant Column (RC) Test (after Stokoe et al., 1999) 81

Figure 4.5 Material Damping Ratio as Determined from Half-Power Bandwidth Method in the Resonant Column (RC) Test (after Stokoe et al., 1999) 82

Figure 4.6 (a) Free-Vibration Decay Curve and (b) Logarithmic Decrements of Normalized Peak-to-Peak Amplitude Determined in the Resonant Column (RC) Test (after Stokoe et al., 1999) 82

Figure 4.7 Hysteresis Loop Determined from the Torsional Shear (TS) Test (after Stokoe et al., 1999) 83

Figure 4.9 Configuration of URC Equipment for Compressional (Longitudinal) Resonance Testing and Direct-Travel-Time Measurements 95

Figure 4.10 Configuration of URC Equipment for Torsional Resonance Testing....96

Figure 4.12 Frequency Spectrum for Longitudinal Waves in Resonance in a Cylindrical Rod as a Function of Dimensionless Wave Number (after Lewis, 1990)....98

Figure 4.13 Measurements of Direct P-Wave Arrival; Aluminum Specimen....100

Figure 4.14 Influence of Wavelength on Calculated Wave Velocities for Three Aluminum Reference Specimens (after Stokoe et al. 1994) 101

Figure 4.15 Influence of Frequency Bandwidth on Measured Values of Material Damping for Three Aluminum Reference Specimens (after Stokoe et al. 1994) 102

Figure 5.1 Six Inch Sand Specimen in the Large-Scale, Multi-Mode, Free-Free, Resonant Column (MMD) Device with the Confining Chamber (After Menq, 2003) 105

Figure 5.2 Cutaway of Cantilever-Type Flexure Bearing....106

Figure 5.3 Torsional Shaker and Its Rotational Mass Assembly 107

Figure 5.4 General Overview of the Large Scale Resonant Column (LgRC) Device....108

Figure 5.5 Configuration of Equipment for the Large Resonant Column (LgRC) Tests....109

Figure 5.6 Torque and Rotation in a Cross-Sectional Element of a Rod in Torsional Vibration....110

Figure 5.7 Rotation of a Rod in Torsional Vibration 112

Figure 5.8 Metal Specimens Used in Calibration of the Fixed-Free Resonant Column and Torsional Shear (RCTS) Device....116

Figure 5.9 Idealized Two-Degree-of-Freedom System for the LgRC Test Set-Up with Metal Specimen No. 2 119

Figure 5.10 Change in Natural Frequency with Added Mass 121

Figure 5.11 Shear Strain on the Perimeter of the Specimen in the LgRC Test....124

Figure 5.12 Change in Equipment-Generated Damping with Loading Frequency Using Half-Power Bandwidth Method 128

Figure 5.13 Change in Equipment Generated Damping in Free Vibration Decay with Loading Frequency 130

Figure 5.14 Variation of Resonant Frequency and Equipment-Generated Damping Ratio in Free-Vibration Decay with Shearing Strain Amplitude 131

Figure 5.15 Variation of Frequency Response Curve with Driving Input Voltage 132

Figure 5.16 Metal Specimen No. 2 Used in Validation Tests 134

Figure 5.17 Response Curves from Outputs of Accelerometers Located at the Top and Bottom of Metal Specimen No. 2 136

Figure 5.18 Phase Shift between Outputs of the Top and Bottom Accelerometers 137

Figure 5.19 Displacement on the Perimeter of Metal Specimen No. 2 at Resonance 138

Figure 5.20 Free-Vibration Decay Curves Measured on Metal Specimen No. 2 by: (a) top accelerometer and (2) bottom accelerometer 139

Figure 5.21 Specimen UTA-42-AH (34C) Set-Up in the Large Resonant Column (LgRC) Device 142

Figure 5.22 Variation of Shear Modulus with Shearing Strain Determined from Fixed-Free RC Tests and Free-Free LgRC Tests; Calico Hills Specimen 143

Figure 5.23 Variation of Normalized Shear Modulus with Shearing Strain Determined from Fixed-Free RC Tests and Free-Free LgRC Tests; Calico Hills Specimen 143

Figure 5.24 Variation of Material Damping Ratio with Shearing Strain Determined from Fixed-Free RC Tests and Free-Free LgRC Tests; Calico Hills Specimen 144

Figure 6.1 Variation of Small-Strain Shear Wave Velocity with Total Unit Weight from Unconfined, Free-Free Resonant Column (URC) Tests for Thirty-Eight Specimens from the Topopah Spring Tuff 148

Figure 6.2 Four Flawed Samples from (a) the Tptrl (γ_t = 131.6 pcf and V_S = 3686 fps), (b Tptpll (γ_t = 125.3 pcf and V_S = 6862 fps), (c) Tptll (γ_t = 127.4 pcf and V_S = 7110 fps), and (d) Tptpln (γ_t = 145.9 pcf and V_S = 7373 fps) Units from the Topopah Spring Tuff....151

Figure 6.3 Variation of Small-Strain Shear Modulus with Total Unit Weight from Unconfined, Free-Free Resonant Column (URC) Tests for Thirty-Eight Sepcimens from the Topopah Spring Tuff....152

Figure 6.4 Variation of Small-Strain Shear Wave Velocity with Total Unit Weight from Unconfined, Free-Free Resonant Column (URC) Tests for Thirty-Eight Specimens from the Topopah Spring Tuff and Four Specimens from the Bandelier Tuff....154

Figure 6.5 Variation in Low-Amplitude Shear Wave Velocity with Isotropic Confining Pressure of Sixteen Specimens from the Topopah Spring Tuff as Determined from Resonant Column (RC) Tests....156

Figure 6.6 Variation in Low-Amplitude Shear Modulus with Isotropic Confining Pressure of Sixteen Specimens from the Topopah Spring Tuff as Determined from Resonant Column (RC) Tests....157

Figure 6.7 Summary Plot of the Variation in Low-Amplitude Shear Wave Velocity with Isotropic Confining Pressure of Eighteen Specimens from the Bandelier Tuff as Determined from Resonant Column (RC) Tests....159

Figure 6.8 Summary Plot of the Variation in Low-Amplitude Shear Modulus with Isotropic Confining Pressure of Eighteen Specimens from the Bandelier Tuff as Determined from Resonant Column (RC) Tests....160

Figure 6.9 Variation of n_V with V_S at σ_o of 0.3 atm for the Bandelier Tuff Specimens....162

Figure 6.10 Variation of n_V with V_S at σ_o of 0.3 atm for all Ash-Flow Tuffs with $V_{S,\ 0.3\ atm}$ > 3000 ft/sec....164

Figure 6.11 Variation of V_S at σ_o of 0.3 atm with γ_t for all Ash-Flow Tuff....164

Figure 6.12 Variation of n_G with G_{max} at σ_o of 0.3 atm for the Bandelier Tuff....166

Figure 6.13 Variation of n_G with G_{max} at σ_o of 0.3 atm for all Ash-Flow Tuffs....167

Figure 6.14 Variation of Small-Strain Material Damping Ratio with Total Unit Weight from Unconfined, Free-Free Resonant Column (URC) Tests for Thirty-Eight Specimens from the Topopah Spring Tuff 168

Figure 6.15 Variation of Small-Strain Material Damping Ratio with Total Unit Weight from Unconfined, Free-Free Resonant Column (URC) Tests for Thirty-Eight Specimens from the Topopah Spring Tuff and Four Specimens from the Bandelier Tuff 170

Figure 6.16 Variation of Small-Strain Material Damping Ratio with Small-Strain Shear Wave Velocity from Unconfined, Free-Free Resonant Column (URC) Tests for Thirty-Eight Specimens from the Topopah Spring Tuff and Four Specimens from the Bandelier Tuff 171

Figure 6.17 Variation in Low-Amplitude Material Damping Ratio with Isotropic Confining Pressure of Sixteen Specimens from the Topopah Spring Tuff as Determined from Resonant Column (RC) Tests 172

Figure 6.18 Summary Plot of the Variation in Low-Amplitude Material Damping Ratio with Isotropic Confining Pressure of Eighteen Specimens from the Bandelier Tuff as Determined from Resonant Column (RC) Tests 174

Figure 6.19 Variation of n_D with D_{min} at 0.3 atm for All Ash-Flow Tuffs 175

Figure 6.20 Variation of n_D with V_S at 0.3 atm for All Ash-Flow Tuffs 175

Figure 6.21 Variation of n_D with Small-Strain Shear Wave Velocity (V_S) at 0.3 atm for All Ash-Flow Tuffs 177

Figure 6.22 Variations of (a) Normalized G_{max} and (b) Normalized D_{min} with Loading Frequency of the Specimens from the Topopah Spring Tuff 180

Figure 6.23 Variation of Normalized Low-Amplitude Shear Modulus of the Specimens in (a) Groups 1 and 2, (b) Group 3 and (c) Group 4 from the Bandelier Tuff 181

Figure 6.24 Variation of Normalized Low-Amplitude Material Damping Ratio of the Specimens in (a) Groups 1 and 2, (b) Group 3 and (c) Group 4 from the Bandelier Tuff 182

Figure 6.25 Changes in (a) Total Unit Weight and (b) Estimated Average Water Content of Six Specimens from the Topopah Spring Tuff 185

Figure 6.26 Changes in (a) Low-Amplitude Shear Modulus (G_{max}) and (b) Loa-Amplitude Material Damping Ratio (D_{min}) of Five Specimens from the Topopah Spring Tuff....187

Figure 6.27 (a) Drilling Pattern and (b) Four Different Size of Artificial Void Segment (AVS) Used for Specimen 8C-2....190

Figure 6.28 Specimens with Seven Artificial Void Segments (AVS): (a) Specimen 8C-2 with 1/2-in. Diameter AVS and (b) Specimen 13C-2 with 5/8-in. Diameter AVS....191

Figure 6.29 Changes in: (a) Volume and (b) Total Unit Weight of Specimens 8C-2 and 13C-2 with Seven Artificial Void Segments (AVS) with Different Diameter Sizes....192

Figure 6.30 Changes in: (a) Small-Strain Shear Modulus (G_{max}) and (b) Small-Strain Material Damping Ratio (D_{min}) of Specimens 8C-2 and 13C-2 with Total Unit Weight....193

Figure 6.31 Comparison between Trends with AVS and Trends in Natural Specimens with Real Variations in Total Unit Weight....195

Figure 7.1 Comparison of Vs Values Measured in the Laboratory and In-Situ for the Topopah Spring Tuff....199

Figure 7.2 General Locations of the SASW Tests Performed in ESF and ECRB Tunnels (from Lin, 2007)....200

Figure 7.3 Comparison of Vs Values Measured in the Laboratory and In-Situ for Bandelier Tuff (Stokoe et al., 2006)....202

Figure 7.4 Complete Profile for Borehole DSC-1B Constructed with Average Trend Lines of Shear Wave Velocity with Confining Pressure Determined in the Laboratory....204

Figure 7.5 Comparison of the Variation in Low-Amplitude Shear Modulus with Isotropic Confining Pressure of Poorly Welded Specimens from the Bandelier Tuff (Groups 3 and 4) and Two Shear Moduli of Very Dense Sand and Very Loose Sand Predicted by Seed et al. (1986)....207

Figure 7.6 Summary of the Variation of e_{max} and e_{min} with Uniformity Coefficient, C_u of Granular Materials Tested in the US and Japan (from Menq, 2003)....208

Figure 7.7 Comparison of the Variation in Low-Amplitude Shear Modulus with Isotropic Confining Pressure of Poorly Welded Specimens from the Bandelier Tuff (Groups 3 and 4) and Similar Relationships for Granular Soils....210

Figure 7.8 Comparison of the Variation in Low-Amplitude Shear Modulus with Isotropic Confining Pressure of Specimens from the Bandelier Tuff (Groups 1 and 4) and Three Shear Moduli of Very Dense Sand, Very Loose Sand, and Dense Gravel Predicted by Seed et al. (1986) 212

Figure 7.9 Comparison of the Variation in Low-Amplitude Material Damping Ratio with Isotropic Confining Pressure of Poorly Welded Specimens from the Bandelier Tuff (Group 3) and Similar Relationships for Granular Soils 214

Figure 7.10 Comparison of the Variation in Low-Amplitude Material Damping Ratio with Isotropic Confining Pressure of Poorly Welded Specimens from the Bandelier Tuff (Group 4) and Similar Relationships for Granular Soils 215

Figure 8.1 Variation of Shear Modulus with Shearing Strain from Fixed-Free Resonant Column Tests of Sixteen Specimens from the Topopah Spring Tuff....................220

Figure 8.2 Variation of Normalized Shear Modulus with Shearing Strain from Fixed-Free Resonant Column Tests of Sixteen Specimens from the Topopah Spring Tuff....................221

Figure 8.3 Variation of Shearing Strain when G/G_{max} is 0.98 with: (a) Total Unit Weight and (b) V_S at σ_o of 0.3 atm of Sixteen Specimens from the Topopah Spring Tuff....................223

Figure 8.4 Variation of Shearing Strain when G/G_{max} is 0.94 with: (a) Total Unit Weight and (b) V_S at σ_o of 0.3 atm of Sixteen Specimens from the Topopah Spring Tuff....................226

Figure 8.5 Variation of Shearing Strain: (a) when G/G_{max} is 0.98 and (b) when G/G_{max} is 0.94 as Determined at Two Different Pressures of Thirteen Specimens from the Topopah Spring Tuff 228

Figure 8.6 Variation of Normalized Shear Modulus with Shearing Strain of Eighteen Specimens from the Topopah Spring Tuff 229

Figure 8.7 Variation of Shearing Strain when G/G_{max} is 0.98 with: (a) Total Unit Weight and (b) V_S at σ_o of 0.3 atm of Eighteen Specimens from the Bandelier Tuff 231

Figure 8.8 Variation of: (a) Shearing Strain when G/G_{max} is 0.98 and (b) Shearing Strain when G/G_{max} is 0.94 with: Isotropic Confining Pressure (σ_o) of Eighteen Specimens from the Bandelier Tuff....................232

Figure 8.9 Variation of: (a) Shearing Strain when G/G_{max} is 0.80 and (b) Shearing Strain when G/G_{max} is 0.50 with Isotropic Confining Pressure (σ_o) of Eighteen Specimens from the Bandelier Tuff 234

Figure 8.10 Variations of: (a) Shearing Strain when G/G_{max} is 0.98 and (b) Shearing Strain when G/G_{max} is 0.80 with Isotropic Confining Pressure (σ_o) of Sixteen Specimens from the Bandelier Tuff 235

Figure 8.11 Variations of Increments in: (a) Shearing Strain when G/G_{max} is 0.98 and (b) Shearing Strain when G/G_{max} is 0.80 with Increment in Isotropic Confining Pressure (σ_o) of Sixteen Specimens from the Bandelier Tuff 236

Figure 8.12 Variations of Reference Strain (γ_r) with Isotropic Confining Pressure (σ_o) of Sixteen Specimens from the Bandelier Tuff Determined from the Fixed-Free Resonant Column (RC) Tests at Two Difference Isotropic Confining Pressures (σ_o) 237

Figure 8.13 Variations of Curvature Coefficient (“a” value) with Reference Strain (γ_r) of Sixteen Specimens from the Bandelier Tuff Determined from the Fixed-Free Resonant Column (RC) Tests at Two Difference Isotropic Confining Pressures (σ_o) 238

Figure 8.14 Variation of Material Damping Ratio with Shearing Strain from Fixed-Free Resonant Column Tests of Sixteen Specimens from the Topopah Spring Tuff 240

Figure 8.15 Variation of “Nonlinear Damping” ($D\text{-}D_{min}$) with Shearing Strain from Fixed-Free Resonant Column Tests of Sixteen Specimens from the Topopah Spring Tuff 241

Figure 8.16 Variation of $D\text{-}D_{min}$ at $\gamma_{0.98}$ from Fixed-Free Resonant Column Tests of Sixteen Specimens from the Topopah Spring Tuff 242

Figure 8.17 Variation of Shearing Strain when $D\text{-}D_{min}$ is 0.2 with: (a) Total Unit Weight and (b) V_S at σ_o of 0.3 atm of Sixteen Specimens from the Topopah Spring Tuff 244

Figure 8.18 Variation of Shearing Strain when $D\text{-}D_{min}$ is 0.5 % with: (a) Total Unit Weight and (b) V_S at σ_o of 0.3 atm of Sixteen Specimens from the Topopah Spring Tuff 245

Figure 8.19 Variation of Shearing Strain: (a) when D-D_{min} is 0.2 % and (b) when D-D_{min} is 0.5 % as Determined at Two Different Pressures of Thirteen Specimens from the Topopah Spring Tuff 246

Figure 8.20 Example of Least-Squares Fitting with the Proposed "Nonlinear Damping" Model for D – log γ Relationship at Its Estimated In-Situ Effective Stress Determined from Fixed-Free Resonant Column Tests of Specimen 15C from the Qbt3L Unit of the Bandelier Tuff 248

Figure 8.21 Example of Fitting the D - log γ Relationship with: (a) Different γ_D Values and (b) Different a_D Values 249

Figure 8.22 Variation of Material Damping Ratio with Shearing Strain of Eighteen Specimens from the Bandelier Tuff at Their Estimated In-Situ Mean Effective Stress (σ_m') from Resonant Column (RC) Tests 251

Figure 8.23 Variation of "Nonlinear Damping" with Shearing Strain of Eighteen Specimens from the Bandelier Tuff at Their Estimated In-Situ Mean Effective Stress (σ_m') from Resonant Column (RC) Tests 252

Figure 8.24 Variation of Shearing Strain when D-D_{min} is 0.2 % with: (a) Total Unit Weight and (b) V_S at σ_o of 0.3 atm of Eighteen Specimens from the Bandelier Tuff 254

Figure 8.25 Variation of: (a) Shearing Strain when D-D_{min} is 0.2 % and (b) Shearing Strain when D-D_{min} is 0.5 % with Isotropic Confining Pressure (σ_o) of Eighteen Specimens from the Bandelier Tuff 255

Figure 8.26 Variation of: (a) Shearing Strain when D-D_{min} is 2.0 % and (b) Shearing Strain when D-D_{min} is 5.0 % with Isotropic Confining Pressure (σ_o) of Eighteen Specimens from the Bandelier Tuff 256

Figure 8.27 Variations of: (a) Shearing Strain when D-D_{min} is 0.2 % and (b) Shearing Strain when D-D_{min} is 2.0 % with Isotropic Confining Pressure (σ_o) of Sixteen Specimens from the Bandelier Tuff 258

Figure 8.28 Variations of Increments in: (a) Shearing Strain when D-D_{min} is 0.2 % and (b) Shearing Strain when D-D_{min} is 2.0 % with Increment in Isotropic Confining Pressure (σ_o) of Sixteen Specimens from the Bandelier Tuff 259

Figure 8.29 Variations in: (a) Curvature Coefficient for G/G_{max} – log γ relationship ("a" value) and (b) Curvature Coefficient for D – log γ relationship ("a_D" value) with Isotropic Confining Pressure (σ_o) of Sixteen Specimens from the Bandelier Tuff....................260

Figure 8.30 Variations of Reference Strain for D – log γ relationship (γ_D) with Isotropic Confining Pressure (σ_o) of Sixteen Specimens from the Bandelier Tuff 261

Figure 8.31 Variations of Curvature Coefficient for D – log γ relationship ("a_D" value) with Reference Strain for D – log γ relationship (γ_D) of Sixteen Specimens from the Bandelier Tuff 262

Figure 8.32 G – log γ Relationships from Fixed-Free Resonant Column Tests and Large Resonant Column Tests on Four Specimens from the Topopah Spring Tuff..264

Figure 8.33 D – log γ Relationships from Fixed-Free Resonant Column Tests and Large Resonant Column Tests on Four Specimens from the Topopah Spring Tuff (Only D values Lower than 5 % are Shown for Comparison Purposes.) 265

Figure 8.34 G/G_{max} – log γ Relationships from Fixed-Free Resonant Column Tests and Large Resonant Column Tests on Four Specimens from the Topopah Spring Tuff...266

Figure 8.35 Specimens with Cracks that were Created during the Large Resonant Column Tests 267

Figure 8.36 D – log γ Relationships from Fixed-Free Resonant Column Tests and Large Resonant Column Tests on Four Specimens from the Topopah Spring Tuff..268

Figure 8.37 Normalized Displacement Response Curves from Large Resonant Column Tests on Specimens Lg41C at Various Strains 268

Figure 8.38 Comparison of G – log γ Relationships from Fixed-Free Resonant Column Tests on Eighteen Specimens and from Large Resonant Column Tests on Four Specimens from the Topopah Spring Tuff...270

Figure 8.39 Comparisons in: (a) G/G_{max} – log γ relationships and (b) ($D - D_{min}$) – log γ relationships from Fixed-Free Resonant Column Tests and Large Resonant Column Tests on Specimens from the Nonlithophysal Units 272

Figure 8.40 Comparisons in: (a) G/G_{max} – log γ relationships and (b) (D – D_{min}) – log γ relationships from Fixed-Free Resonant Column Tests and Large Resonant Column Tests on Specimens from the Lithophysal Units 273

Figure 8.41 Comparisons in: (a) G/G_{max} – log γ relationships and (b) (D – D_{min}) – log γ relationships from Fixed-Free Resonant Column Tests on Specimen 8C-2 with Seven Artificial Void Segments (AVS) with Different Sizes 275

Figure 8.42 Comparisons in: (a) G/G_{max} – log γ relationships and (b) (D – D_{min}) – log γ relationships from Fixed-Free Resonant Column Tests on Specimen 13C-2 with Seven Artificial Void Segments (AVS) with Different Sizes 276

Figure 8.43 Comparisons of (a) G/G_{max} – log γ and (b) (D – D_{min}) – log γ relationships from Fixed-Free Resonant Column Tests on Natural Specimens and Specimens with AVS with Different Sizes 277

Figure 9.1 Variation of n_V with V_S at σ_o of 0.3 atm for the Specimens from the Topopah Spring and Bandelier Tuffs 283

Figure 9.2 Variation of V_S at σ_o of 0.3 atm with Total Unit Weight for Specimens from the Topopah Spring and Bandelier Tuffs 284

Figure 9.3 Variation of: (a) Low-Amplitude Shear Modulus and (b) Low-Ampliutde Material Damping Ratio with Total Unit Weight 286

Figure 9.4 Variation of: (a) $\gamma_{0.98}$ and (b) $\gamma_{Dmin+0.2\%}$ with Total Unit Weight of Specimens from the Topopah Spring and Bandelier Tuffs 288

Figure 9.5 Comparison between $\gamma_{0.98}$ with $\gamma_{Dmin+0.2\%}$ of Specimens from the Topopah Spring and Bandelier Tuffs 289

Figure 9.6 Comparisons of: (a) $\gamma_{0.94}$ and (b) $\gamma_{0.80}$ with $\gamma_{0.98}$ of Specimens from the Topopah Spring and Bandelier Tuffs 290

Figure 9.7 Comparison between: (a) $\gamma_{0.94}$ and $\gamma_{Dmin+0.5\%}$ and (b) $\gamma_{0.80}$ and $\gamma_{Dmin+2.0\%}$ of Specimens from the Topopah Spring and Bandelier Tuffs 291

Figure 9.8 Variations of: (a) $\gamma_{0.94}$ and $\gamma_{Dmin+0.5\%}$ (b) $\gamma_{0.80}$ and $\gamma_{Dmin+2.0\%}$ with Isotropic Confining Pressure of Specimens from the Bandelier Tuffs 293

Figure A.1 Variation of Small-Strain Young's Modulus (E_{max}) with Total Unit Weight of Thirty Eight Specimens from the Topopah Spring Tuff 298

Figure A.2 Variation of Small-Strain Constrained Compression Modulus (M_{max}) with Total Unit Weight of Thirty Eight Specimens from the Topopah Spring Tuff 298

Figure A.3 Variation of Poisson's Ratio (ν_{MG}) from the Relationship between M_{max} and G_{max} with Small-Strain Shear Wave Velocity of Thirty Eight Specimens from the Topopah Spring Tuff 299

Figure A.4 Variation of Poisson's Ratio (ν_{ME}) from the Relationship between M_{max} and E_{max} with Small-Strain Shear Wave Velocity of Thirty Eight Specimens from the Topopah Spring Tuff 299

Figure A.5 Variation of Poisson's Ratio (ν_{EG}) from the Relationship between E_{max} and G_{max} with Small-Strain Shear Wave Velocity of Thirty Eight Specimens from the Topopah Spring Tuff 300

Chapter 1

Introduction

1.1 BACKGROUND

Ash-flow tuff (ignimbrite) is a general term indicating consolidated deposits of volcanic ash flow; a flow of a mixture of gas and pyroclastic materials as products of explosive volcano eruptions (Smith, 1960). The deposit is emplaced at high temperature, and the lower portion of the deposit typically becomes welded by internal heat and weight of the overlying materials. A large proportion of welded ash flows are crystallized. Lithophysal zones can also be created where vapor concentrates in the densely welded ignimbrite to form lithophysal cavities (Buesch et al., 1996). An ash flow deposit could be either a single or compound cooling unit depending upon the duration and patterns of deposition, welding and crystallization (Broxton, 1995). Because of the complex characteristics in origin, the subsurface material profile of a local site composed of ash-flow tuffs can be very complicated; large differences in material properties (such as stiffness and density) may exist between two adjacent layers having sufficient thickness; a thick soft layer can also possibly exist as a single cooling unit.

Two different ash-flow tuffs are studied in this research: 1. Topopah Spring Tuff at Yucca Mountain, Nevada and 2. the Bandelier Tuff at Pajarito Plateau, New Mexico. Ash-flow tuffs in these areas have received much attention because they exist at U.S. Department of Energy (DOE) facilities and their future behavior during earthquakes is an issue in the seismic hazard evaluation of the facilities. For instance, intact samples were recovered from the various cooling units of the Bandelier Tuff. These samples show that the welding condition varies significantly from nonwelded (poorly welded) to densely welded. Recent site response sensitivity studies (Houston et al., 2003) noted that linear and nonlinear dynamic characteristics of a very poorly welded (nonwelded) zone (about 15 m (50 ft) thick) have a significant impact on the ground response of the site. While physical properties of these specimens are mainly affected by welding alone (Quane and Russell, 2005), intact cores from the Topopah Spring Tuff have various lithostratigraphic features. Lithophysal cavities exist in the specimens as noninterconnected macropscopic porosity. The size, amount, and distribution of these features are strongly related to the engineering properties of the tuffs from lithophysal zones (Avar et al., 2003) and the engineering properties of the tuffs need to be investigated.

1.2 OBJECTIVE OF RESEARCH

The objectives of this research are: (1) determination of the linear and nonlinear dynamic properties (shear modulus (G) and material damping ratio (D)) of intact ash-flow tuff specimens, (2) investigation of the factors having the greatest impact on these properties, and (3) development of the Large Resonant Column (LgRC) device to test large-scale specimens dynamically and to test smaller specimens at larger strain amplitudes than previously possible. Various dynamic test parameters (e.g. confining pressure, shearing strain, etc) were studied with two major existing devices: (1) the combined resonant column and torsional shear (RCTS) device, and (2) the free-free, unconfined, resonant column (URC) device. The effects of these parameters are evaluated for two different types of ash-flow tuffs from: (1) the Topopah Spring Tuff formation and (2) the Bandelier Tuff formation. Relationships between their dynamic properties and lithostratigraphic features are further investigated. Finally, potential problems related to sample disturbance and specimen size are considered based on comparisons of small-strain shear wave velocity (V_S) values measured in the laboratory and in the field.

1.3 ORGANIZATION OF DISSERTATION

Geologic information of the two tuff formations is described in Chapter two. The general descriptions of the project sites and the lithostratigraphic features (e.g. degree of welding, crystallization, lithophysae) related to the stratification of the formations are summarized. Information about the test specimens, including specimen dimensions, parent boreholes and their locations, transportation, and sample preparation is presented.

Published literature discussing the geologic characteristics of pyroclastic deposits and mechanical properties of ash-flow tuffs forming the deposits are presented in Chapter Three. Various schemes to map welding facies are summarized. Existing studies about factors affecting the mechanical properties of these ash-flow tuffs are also summarized.

Basic operational principles of the two major devices used in this research, the RCTS and URC devices, are described in Chapter Four. Brief backgrounds of the tests are presented. A summary of the testing sequence in terms of confining pressure and strain amplitude used in the RCTS testing is also presented.

A detailed description of the LgRC device is presented in Chapter Five. The proposed theoretical approach to evaluate the characteristics of the device itself and test materials are discussed. Validation of the system with results from two different known materials is also discussed.

Small-strain dynamic properties of the tuffs with the two major devices (RCTS and URC) are presented in Chapter Six. Empirical correlations of the small-strain shear modulus, G_{max}, and small-strain material damping ratio, D_{min}, with the total unit weight,

γ_t, of air-dry specimens are discussed in terms of their lithostratigraphic characteristics. The effects of excitation frequency, change in water content due to specimen preparation, and large lithophysae on the dynamic properties of the tuffs are discussed.

The small-strain shear wave velocity, V_S, values measured in the laboratory are compared with in-situ measurements in Chapter Seven. The test results of the poorly welded tuffs are also compared with the dynamic properties of granular soils.

Nonlinear dynamic properties of ash-flow tuffs measured with the RCTS device and the LgRC device are discussed in Chapter Eight. The effect of shearing strain on the dynamic properties is discussed in terms of the lithostratigraphic characteristics of the specimens.

A summary of the study and conclusions are presented in Chapter Nine.

The small-strain unconstrained compression modulus (E_{max}), constrained compression modulus (M_{max}), and material damping ratio in unconstrained compression ($D_{C,\ min}$) of the tuff specimens determined using the URC device were presented in Appendix A. These data and correlations of these moduli and material damping ratio with γ_t are also discussed.

Chapter 2

Geological Overview and Test Materials

2.1 INTRODUCTION

In this research, the dynamic properties of two different volcanic tuff formations from different parts of the United States were evaluated and studied. The first tuff formation is the Topopah Spring formation at Yucca Mountain, Nevada. A total of 38 tuff specimens were dynamically tested and studied. The Topopah Spring tuffs are densely welded and crystallized rocks. The lithostratigraphic features of these tuffs include lithophysal cavities which are associated with the depositional, welding and cooling processes that the tuff unit experienced. Physical properties of these rocks are highly affected by these features (Buesch et al., 2006). The second tuff formation studied is the Bandelier formation at Pajarito Plateau, New Mexico. A total of 18 Bandelier tuff specimens were dynamically tested. The degree of welding of the Bandelier specimens varies from nonwelded (poorly welded) to densely welded, representing complex variations in the deposition and crystallization processes at the site.

The studies on the dynamic properties of the two tuff formations were associated with two research projects: (1) Yucca Mountain Site Characterization Project (YMP) at the future Yucca Mountain High-Level Nuclear Waste Repository Site and (2) the Chemistry and Metallurgical Research Replacement (CMRR) project at Los Alamos National Laboratory (LANL). Both sites are related to the U.S. Department of Energy (DOE) facilities and evaluation of the seismic hazard of the facilities has been under study.

Information regarding test specimens and geologic information of the sites where the samples were collected are presented in this chapter. The chapter is divided into two sections according to the tuff formation and geologic location as follows: Section 2.2 for the Topopah Spring Tuff at the Nevada Test Site in southern Nevada and Section 2.3 for the Bandelier Tuff at the Jemez volcanic field in northern New Mexico. In each section, the following information related to the tuffs and project sites is provided: (1) general geologic and geographic features at the sites, (2) stratigraphic units of the tuffs and (3) specimens dynamically tested in the laboratory.

2.2 TOPOPAH SPRING TUFF

The Topopah Spring Tuff is one of the formations of the Paintbrush Group exposed at Yucca Mountain, Nevada. Yucca Mountain is in the Southwestern Nevada Volcanic Field (SNVF), south of the Timber Mountain and Claim Canyon calderas as shown in Figure 2.1. These calderas were the sources for the volcanic rocks exposed in this area (Byers and others, 1976a and b; Christiansen and others, 1977). The SNVF was active from 15.1 to 7.5 million years ago. The Paintbrush Group, comprising most of Yucca Mountain, erupted between 12.8 and 12.7 Ma (Sawyer and others, 1994). The primary deposit of this group was created by pyroclastic flow and fallout from the volcanic activities. The Paintbrush Group is composed of four formations (Sawyer and others 1994): the regionally extensive ignimbrites of the Tiva Canyon and Topopah Spring Tuffs and the comparatively less extensive ignimbrites of the Yucca Mountain and Pah Canyon Tuffs. These four formations are pyroclastic flow deposits (ash-flow tuffs called historically) that are typically poorly to moderately sorted deposits composed of pumice, crystals, lithic clasts in a matrix of glass shards and dust (Limpman et al., 1966).

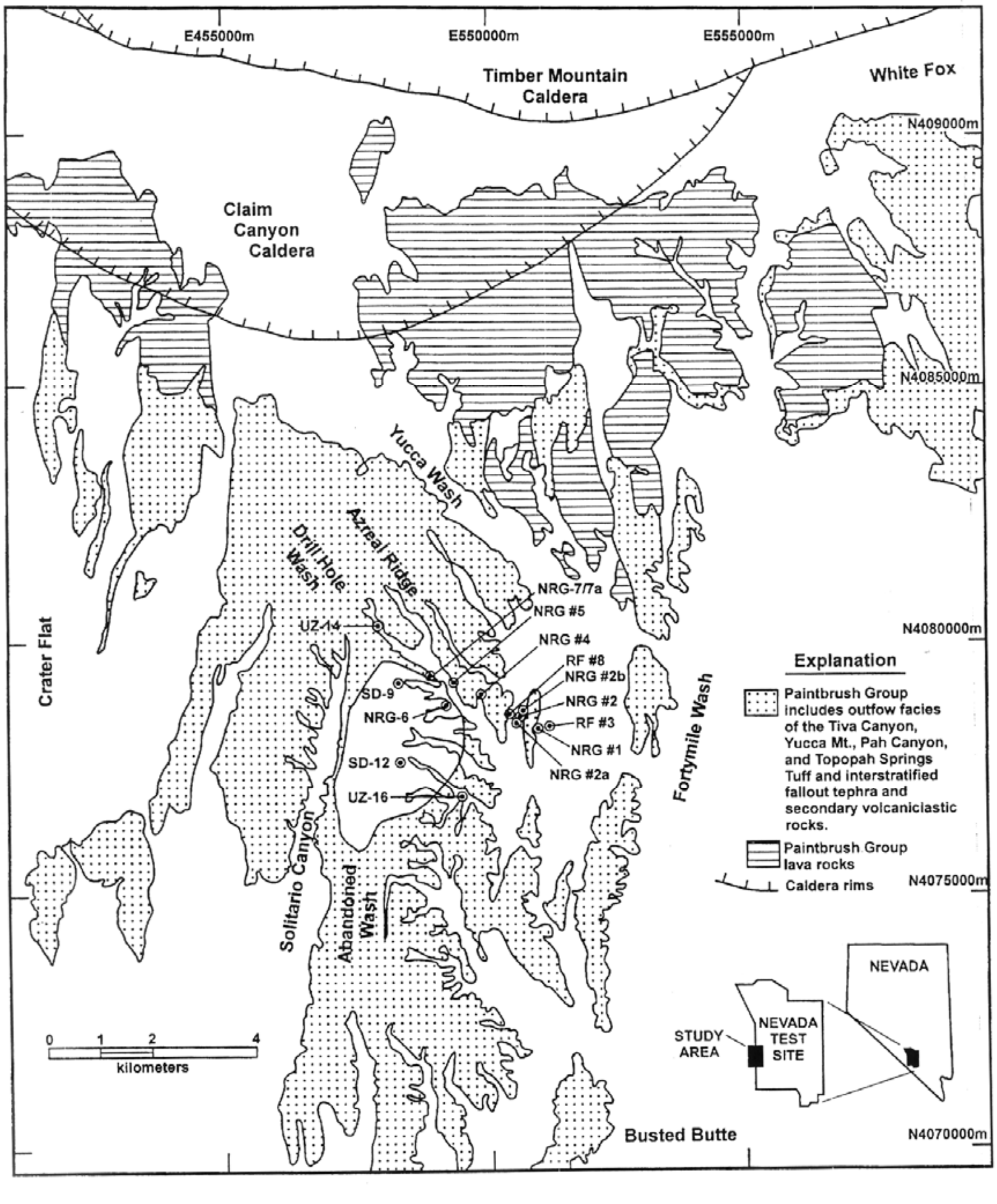

Figure 2.1 Yucca Mountain Geologic Map (after Buesch et. al, 1996)

The lowest formation is the Topopah Spring Tuff, which forms the host rock for the radioactive waste repository, and therefore is one of the most intensely studied formations at Yucca Mountain. Figure 2.2 illustrates the sequence of the four formations comprising the Paintbrush Group. The lithostratigraphic details in the Topopah Spring Tuff formation are also shown in the figure. In short, the Topopah Spring Tuff consists of two members (crystal rich and crystal poor). Each member has three zones (vitric zone, nonlithophysal zone, and lithophysal zone). Four units (zones) in the crystal-poor member of the Topopah Spring Tuff are planned to host the waste. The criteria and descriptions of each unit are summarized in the following section.

The Repository Host Horizon (RHH) lies from the Topopah Spring, Crystal Poor, Lower Nonlithophysal (Tptpln) unit through the Topopah Spring, Crystal Poor, Upper Lithophysal (Tptpul) unit as shown in Figures 2.2 and 2.3. Note that the abbreviation for each unit consists of the letters related to lithostratigraphic information of the unit. For example, the Tptpln consists of: (1) formation (the first three letters, Tpt), (2) amount of crystal fragments (crystal poor, p), (3) relative depth in the formation (lower unit, l), and (4) presence of lihtophysae (nonlithophysal unit, n). Details about this lithostratigraphic nomenclature for the Topopah Spring formation are described in Section 2.2.1. The RHH is the body of rock in which the future repository is planned to be excavated. The total length of all excavated openings is about 110 km (68 miles). Lithophysal units comprise about 85 % of the emplacement area (about 81 % in the Topopah Spring, Crystal Poor, Lower Lithophysal (Tptpll) unit and about 4 % in the the Topopah Spring, Crystal Poor, Upper Lithophysal (Tptpul) unit). The Tptpmn unit comprises about 12 % of the area whereas the Tptpln comprises only 3 % of the area (after Rigby, 2004).

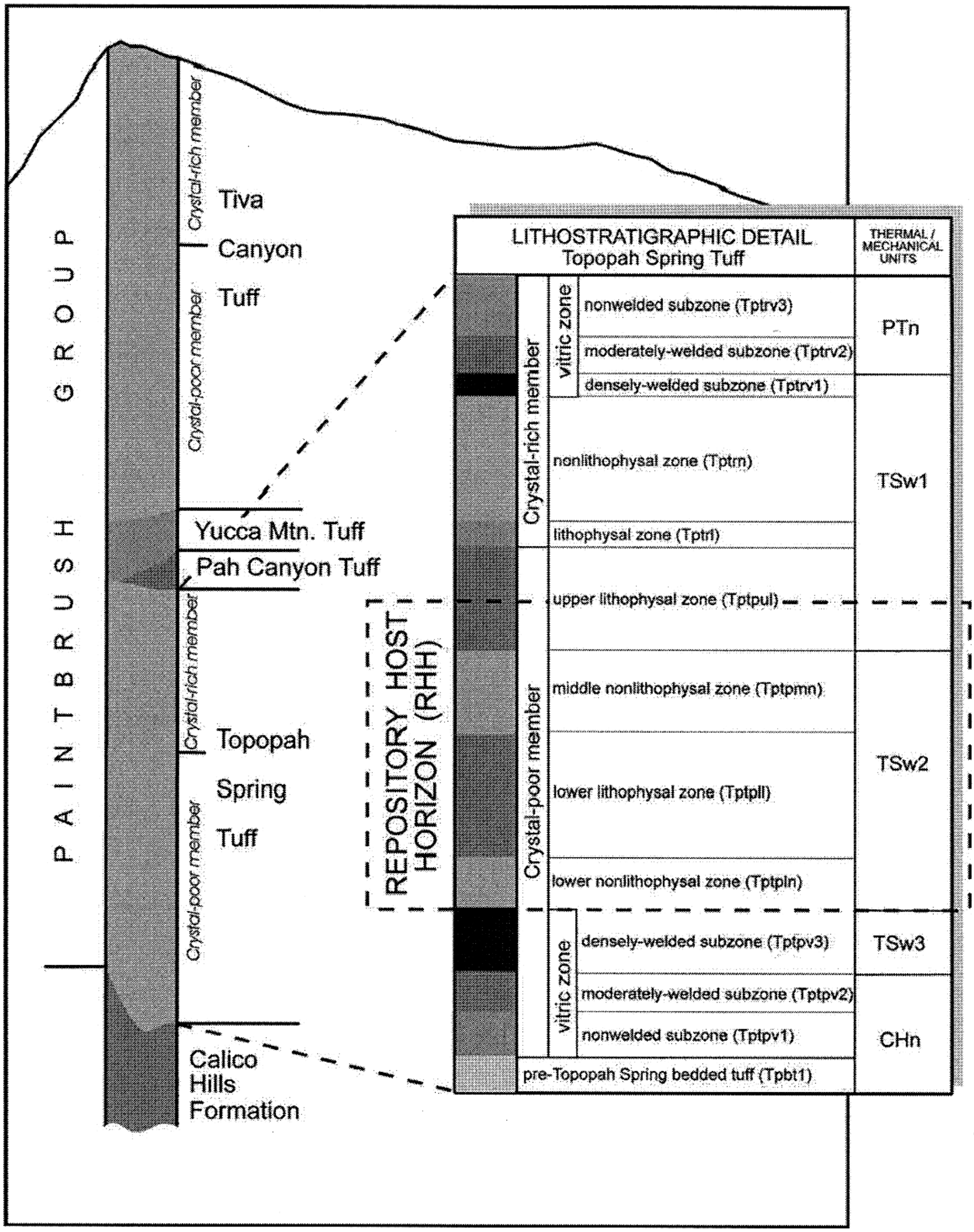

Figure 2.2 General Stratigraphy Description for Yucca Mountain (after Rigby, 2004)

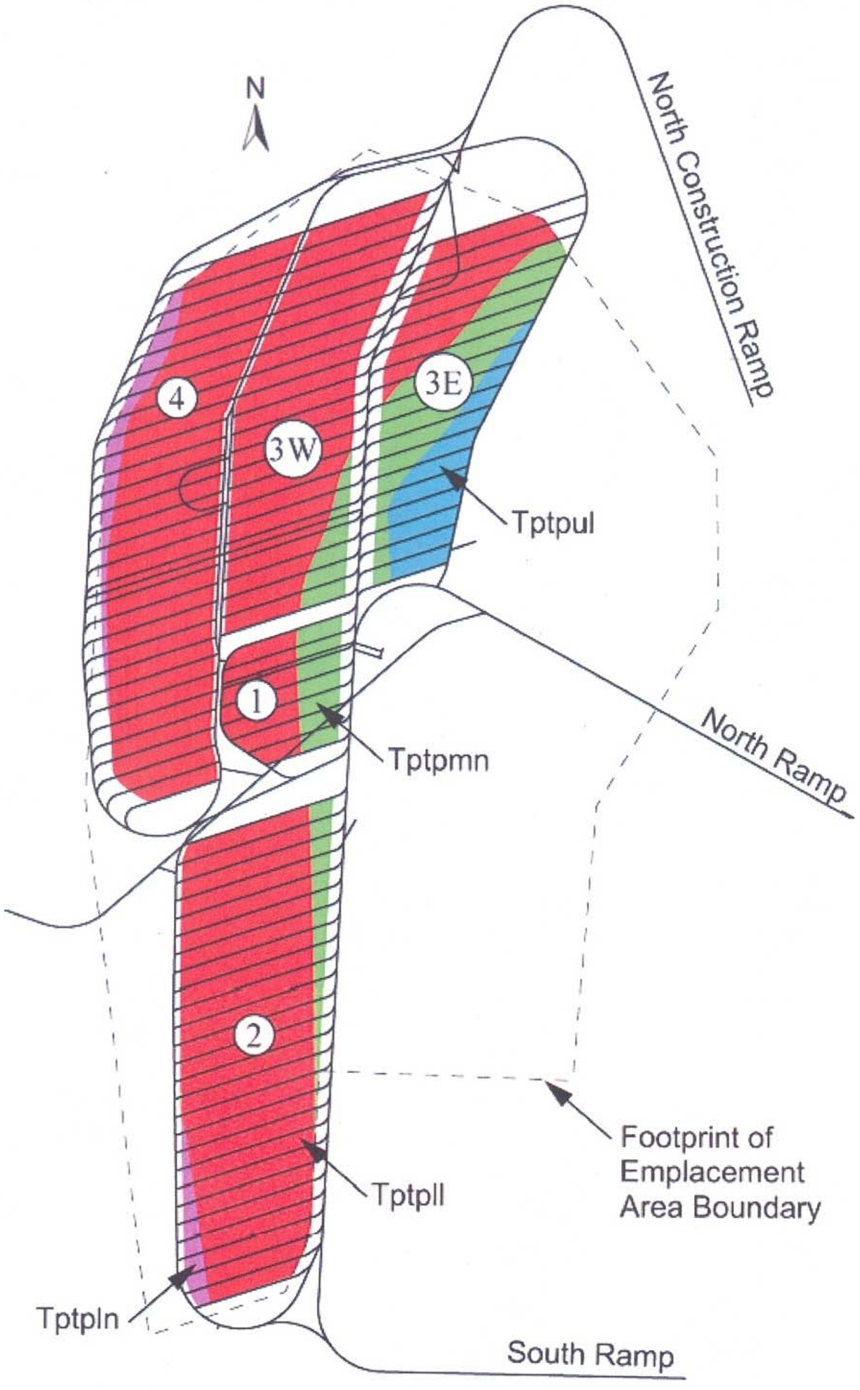

Note: circled numbers indicate Construction Panel Numbers.

Figure 2.3 Plan View of Repository Layout (after Rigby, 2004)

Underlying the Topopah Spring Tuff is the Calico Hills formation. This formation consists of a complex series of rhyolitic tuffs and lavas that resulted from an episode of volcanism approximately 12.9 Ma. The Calico Hills formation overlies older Tertiary volcanic rocks of similar composition that comprise the Crater Flat Group. In turn, the Crater Flat Group overlies pre-Tertiary basement rocks, which consists mostly of Paleozoic sedimentary rocks that were created about 225 to 570 Ma.

2.2.1 Stratigraphy of the Topopah Spring Tuff

The Topopah Spring Tuff at Yucca Mountain appears to be a single depositional and cooling unit (Buesch and Spengler, 1998). Therefore, the lithostratigraphic features (such as the amount of crystal fragments (phenocrysts), welding intensity, the amount of lithophysae, and whether the material is glass (vitric) or crystallized represent the processes of deposition, welding, crystallization, and cooling (Buesch et al, 1996). The tuff in this context is divided into lithostratigraphic units (members, zones, subzones, and intervals) on the basis of the distribution of the lithostratigraphic features. Members are defined according to the amount and assemblage of phenocrysts. They represent changes in magma chemistry or eruptive mechanism. Most of the formations in the SNVF have an upper crystal-rich member and a lower crystal-poor member. Zones, subzones and intervals are defined by textures and structures related to the depositional and post-depositional processes and the mechanical properties. Zones of the Topopah Spring Tuff are mainly defined by: (1) crystallization and (2) development of lithophysae and spots. Subzones and intervals add more details about the zones related to the abundance of pumice clasts, amount of welding, crystallization and type of alteration of pumice clasts, etc.

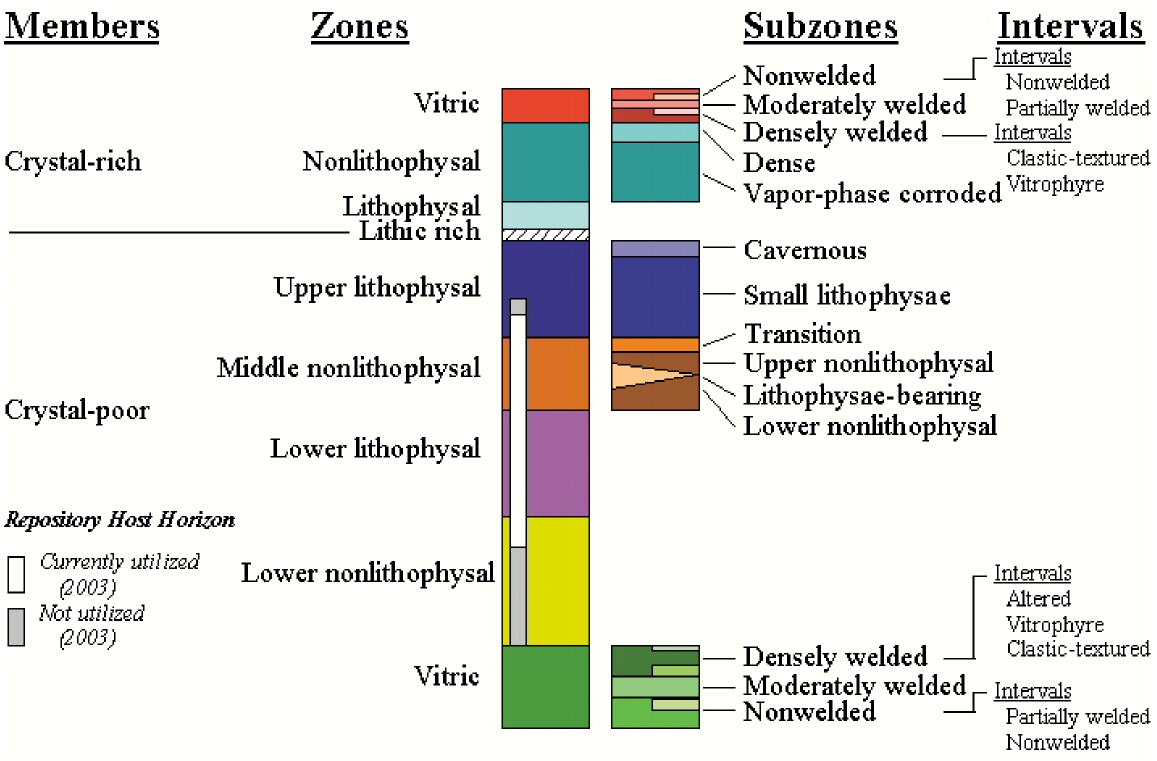

Figure 2.4 Members, Zones, Subzones, and Intervals of the Topopah Spring Tuff at Yucca Mountain, Nevada (after Buesch et al., 2006)

Figure 2.4 illustrates the lithostratigraphic units of the Topopah Spring Tuff proposed by Buesch et al. (2006). The authors defined the units by the macroscopic features observed in surface exposures and borehole samples. The descriptions and criteria for the major zones in the classifications are summarized below:

(1) Phenocryst Assemblage

The Topopah Spring Tuff in general has fewer crystals than many rocks in the SNVF; therefore, the tuffs in the crystal-rich member have at most 8 to 12 percent phenocrysts in its upper part and only 3 to 5 percent phenocrysts in its crystal-transition subzone. The crystal-rich member is composed of a vitric zone (Tptrv) underlain by devitrified tuffs that locally contain lithphysae (Tptrn and Tptrl).

(2) Welding Zones

Criteria to define the degree of welding include the deformation of shards and pumice, breakage across or around the shards and pumice clasts, compaction of intershard dust and development of foliation. The criteria are based on the terminology of Smith (1960) for vitric rocks, but many of these textures are preserved in devitrified rocks. The degree of welding is classified into four textures: nonwelded, partially welded, moderately welded, and densely welded as summarized in Table 2.1.

Table 2.1 Criteria for Degree of Welding of Tuffs from the Topopah Spring Tuff

Degree of Welding	Shards and Pumice Clasts	Macroscopic Porosity and Matrix Constituents (Intershard Ash and Dust)	Vitroclastic Texture of Pumice, Shards, and Ash	Elongated Pumice and Lithic Clasts
Nonwelded	Not Deformed	Visible with a Hand Lens	Discernible	Randomly Oriented and Not Aligned
Partially Welded	Slightly Deformed	Visible with a Hand Lens but Reduced	Discernible	Slightly Aligned
Moderately Welded	Significantly Deformed	Small Amount	Discernible	Defined Moderately Developed Foliation
Densely Welded	Fused Together with Matrix.	Absent	Discernible or Not Discernable (Vitrophyres)	Defined Moderately Developed Foliation

(3) Crystallization Zones

The development of crystallization zones in ignimbrite (ash-flow tuff) is strongly related to the emplacement temperature, composition of glass, surface areas of the grains, and vapor species and abundance (Smith, 1960; Ross and Smith, 1961). Four crystallization zones are identified in the Topopah Spring Tuff as follows:

Vitric Zones – vitric zones are characterized by the absence of crystallization textures, so they are not included in the original description of the crystallization zone (Smith, 1960). The degree of welding varies in the vitric zones at the top and bottom of the Topopah Spring Tuff and tends to increase close to the crystallization zones. Vapor-phase minerals are found in zones in the vitric zones.

Zones of High-Temperature Devitrification – the zones of high-temperature devitrification contains fine-grain aggregates of alkali feldspar and cristobalite in the groundmass. Spherulites and fine-grained granophyric intergrowths are well-developed locally and discernable macroscopically. The majority of the Topopah Spring Tuff is devitrified.

Zones of Vapor-Phase Crystallization – the zones of vapor-phase crystallization are characterized by fine-grained aggregates of tridymite and other minerals such as biotite, amphibole, etc). The vapor-phase crystals grow: (1) in pore spaces in nonwelded to partially welded tuffs, (2) in pore spaces by lithophysae or by corrosion of glass due to vapor-phase alteration, or (3) along fractures (Smith, 1960; Ross and Smith, 1961).

Lithophysal Zones - these zones occur where vapor concentrates in the densely welded ignimbrites resulting in lithophysal cavities (Ross and Smith,

> 1961). The vapor can be originated from trapped air and gas between pyroclastic materials when deposited, exsoluted from pumice and shards, or released during devitrification. Figure 2.5 illustrates two types of cavities in the welded tuffs at the Yucca Mountain site: (a) lithophysae and (b) spot, respectively. A lithophysa consists of a cavity surrounded by rim and a thin border. The inner wall of the cavity is commonly coated by vapor-phase minerals. The porosity of this coating is about 0.3 to 0.8. The porosity of the outer material decreases as their grain size decreases. The grain sizes of these materials decrease with distance away from the cavity. Spots are commonly found in lithophysal zones. They are about 1 to 5 cm in diameter. Some spots simply represent portions of rims with a small isolated area of groundmass on the lithophysae. Others have a crystal or lithic clast in the middle (Buesch, 1994).

Fractures at Yucca Mountain are generally of three types: cooling joints, later tectonic fractures and late joints created by erosional unloading. The cooling joints are the majority of fractures and associated features mapped underground, although there are also localized tectonic fracture zones related the faults. Some cooling joint fractures and incipient fractures are characterized by four major features: veinlets, stringers, streaks, and vapor-phase partings. The first three fractures may have formed while the rock was still glassy, and some cooling fractures served as pathways that transferred vapor during cooling and welding of the ignimbrite. These pathways led to either porous rim material along the open fractures or, later in time, surface deposits of vapor phase minerals. Vapor-phase partings are relatively continuous and rough cooling fractures. These fractures are subparallel to the dip of the rock unit, and are filled with concentrations of vapor-phase mineralization (primary tridymite and cristobalite). Figure 2.6 illustrates

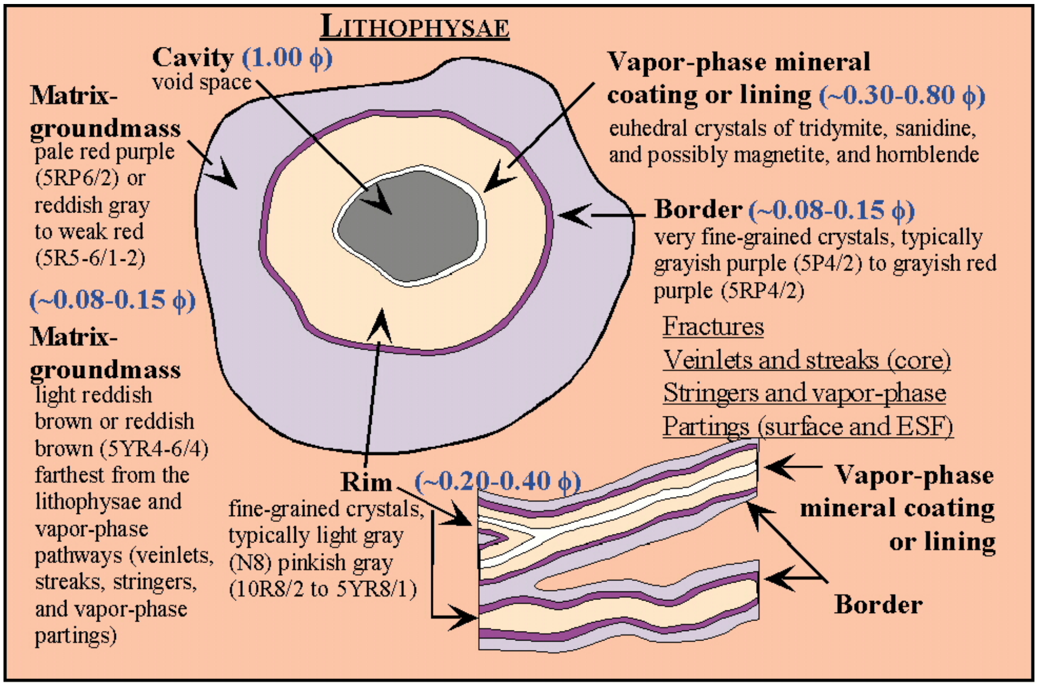

(a) Lithophysae, Veinlets and Streaks

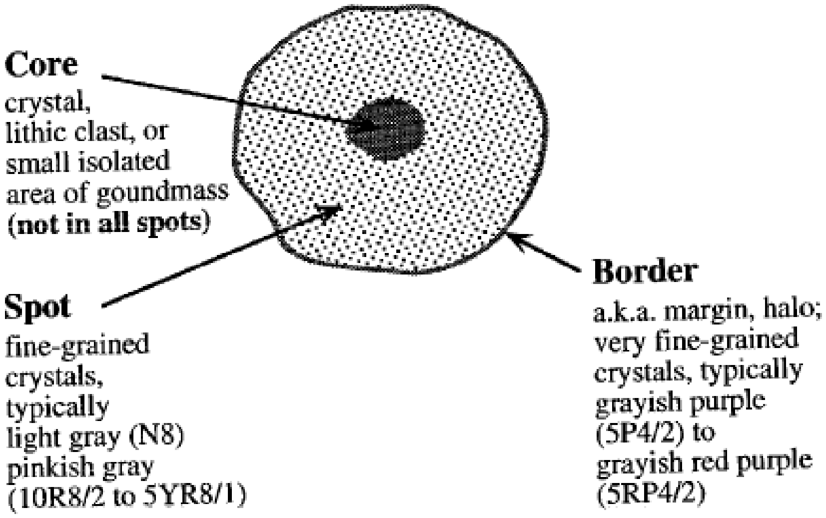

(b) Spots

Figure 2.5 Components of: (a) Lithophysae, Veinlets, and Streaks and (b) Spots in Welded Tuffs at Yucca Mountain Site (after Buesch, 1994) schematically the structure of the Topopah Spring Tuff. The general occurrence of fracturing and lithophysae in the units for the Proposed Repository Horizon (PRH) are presented in the figure. The nonlithophysal units contain numerous fractures with small porosities. On the contrary, the lithophysal units have significantly fewer fractures but have large porosity related to the lithophysal features.

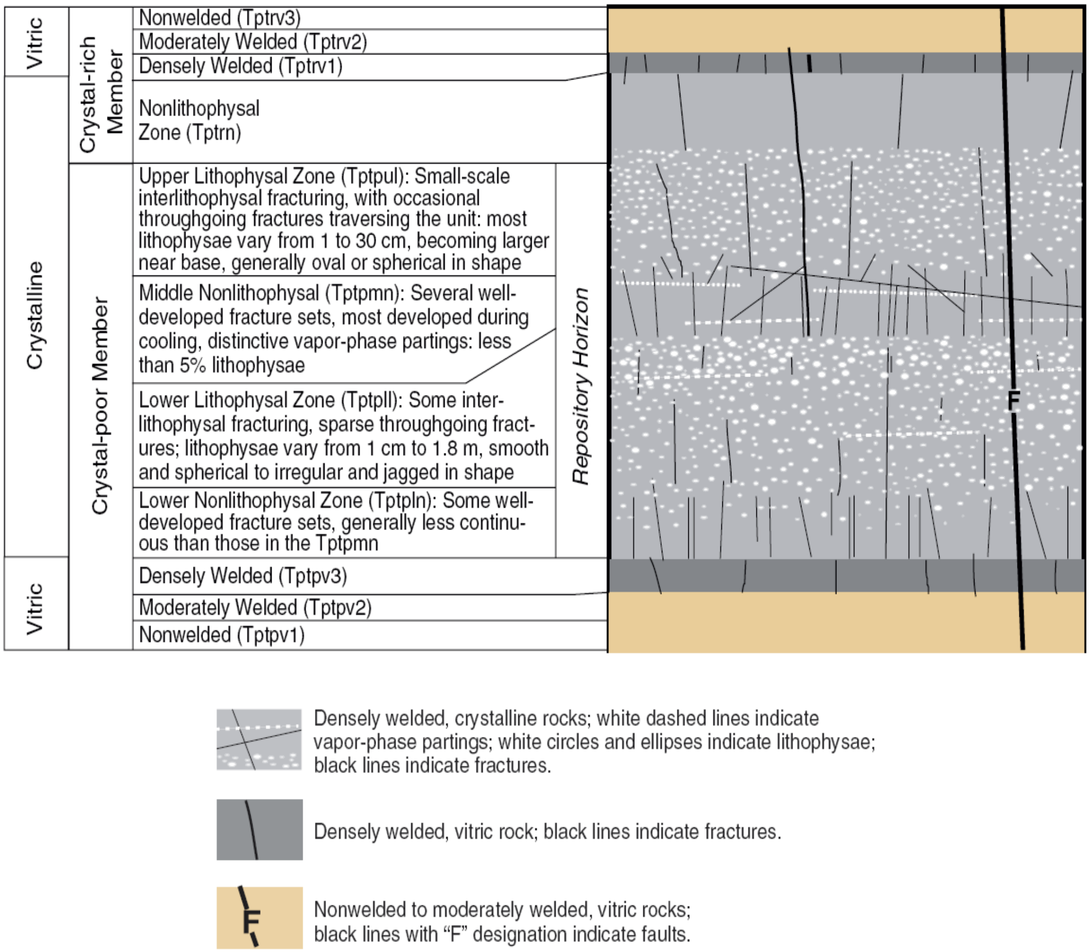

Figure 2.6 Fractures and Lithophysae of the Topopah Spring Tuff (after Rigby, 2004)

2.2.2 Tested Topopah Spring Tuff Specimens

The unconfined, free-free, resonant column (URC) tests were performed on a total of 38 welded specimens from the Topopah Spring Tuff as listed in Table 2.2. (Device and test program for URC tests are described in Chapter 4.) Sample cores for these tests vary in diameter and length, but typically they had a diameter of 1.8 in (46 mm) to 3.8 in. (96 mm) and a height of 6.2 to 10.5 in. (157 to 267 mm). Their total unit weights are between 108.6 to 145.9 lb/ft^3 (1.74 to 2.34 gr/cm^3). All samples were also visually inspected not only for overall size and distribution of lithophysae or spots but also for features (which can be referred to as "inhomogeneities" or "flaws") such as relatively large lithophysae, fairly continuous fractures, or missing pieces of the core.

The tuff specimens that were tested were collected from both existing and new boreholes from various locations around Yucca Mountain, near the North Portal Facility and surrounding area, in the Exploratory Studies Facility (ESF) tunnel, and in the Enhanced Characterization of Repository Block (ECRB) tunnel. The surface boreholes and boreholes in the ESF and ECRB tunnels are shown in Figures 2.7 and 2.8, respectively. The boreholes circled in Figure 2.7 and those designated by arrows in Figure 2.8 are the boreholes where the original whole cores were recovered. All parent boreholes and locations are tabulated in Table 2.3, with the number of cores from each borehole noted. A total of 27 Tpt cores were recovered from seven surface boreholes and a total of 11 Tpt cores were recovered from seven tunnel boreholes.

After completion of the free-free tests on all 38 specimens, 14 specimens were selected to perform the fixed-free resonant column and torsional shear (RCTS) tests. These specimens are listed in Table 2.4. Twelve specimens were cored from the original cores to a smaller diameter and cut to the final length. Two specimens (Specimens 9A-2 and 10A-2) were only cut to the final length because their original diameter was small

Table 2.2 Thirty Eight Topopah Spring Tuff (Tpt) Specimens Dynamically Tested for This Research

Litho. Unit	SMF Sample No.	Borehole	Depth, ft		Length, in.	Diameter, in.	Total Unit Weight, lb/ft^3
			Top	Bottom			
Tptrn	01025863	USW UZ-14	363.7	364.4	8.34	2.40	128.6
Tptrn	01025897	USW SD-7	402.1	402.9	9.97	3.26	131.5
Tptrn	01025887	USW SD-12	405.3	406.1	9.47	2.41	136.1
Tptrn	01025895	USW NRG-6	414.5	415.4	10.57	3.28	137.5
Tptrn	01025886	USW SD-12	375.7	376.3	7.31	2.40	131.5
Tptrn	01025862	USW UZ-14	341	341.7	8.44	2.41	131.6
Tptrl	01025902	USW NRG-7/7A	482.5	483.1	7.15	3.22	131.6
Tptrl	01025901	UE-25 NRG#4	666.1	666.8	8.55	3.25	122.1
Tptpul	01025889	USW SD-12	504.9	505.6	8.14	2.39	108.6
Tptpul	01025888	USW SD-12	499.7	500.3	7.15	2.41	112.7
Tptpul	01025866	USW UZ-14	496.2	496.8	7.23	2.40	117.7
Tptpul	01025865	USW UZ-14	495.2	495.9	8.16	2.40	118.4
Tptpul	01025905	ESF-HD-TEMP-5	38.5	39.2	8.35	1.76	136.6
Tptpul	01025868	USW UZ-14	577	577.7	8.48	2.39	133.9
Tptpul	01025867	USW UZ-14	564.1	564.9	9.12	2.38	133.2
Tptpmn	01025871	USW UZ-14	823	823.8	9.99	2.41	143.0
Tptpmn	01025906	ESF-HD-TEMP-5	12.2	13	9.39	1.76	140.6
Tptpmn	01025907	ESF-HD-WH-49	21.9	22.6	8.31	2.41	139.8
Tptpmn	01025910	ESF-HD-TEMP-2	144.7	145.4	8.76	2.40	144.0
Tptpmn	01025908	ESF-HD-TEMP-2	8.8	9.5	8.20	2.41	141.8
Tptpmn	01025869	USW UZ-14	812.5	813.2	7.93	2.41	142.4
Tptpmn	01025909	ESF-HD-TEMP-2	85.2	85.9	8.41	2.41	142.6
Tptpmn	01025938	ESF-NAD-F/M#3	16.2	16.9	8.67	2.41	142.8
Tptpll	01025912	ECRB-SYBT-LA#9	4.2	4.7	6.32	1.78	138.8
Tptpll	01025872	USW UZ-14	1016.2	1016.9	8.33	2.39	142.8
Tptpll	01025914	UE-25-UZ#16	866.7	867.3	7.19	2.40	131.5
Tptpll	01025913	ECRB-SYBT-LA#2	19.2	19.7	6.17	1.78	133.4
Tptpll	01025926	ECRB-GTEC-CS2150-01	6.3	7.1	10.06	3.77	125.3
Tptpll	01025925	ECRB-GTEC-CS2150-01	0.2	0.8	7.10	2.50	127.4
Tptpll	01025873	USW UZ-14	1059	1059.7	8.27	2.41	139.5
Tptpln	01025876	USW UZ-14	1242.7	1243.4	7.95	2.41	145.9
Tptpln	01025874	USW UZ-14	1246	1246.7	7.82	2.40	143.9
Tptpln	01025919	UE-25-UZ#16	1073.3	1073.9	7.24	2.40	145.9
Tptpln	01025875	USW UZ-14	1248.9	1249.7	9.19	2.40	145.4
Tptpln	01025918	UE-25-UZ#16	1045.1	1045.8	7.96	2.40	144.8
Tptpln	01025917	UE-25-UZ#16	993.2	993.7	8.34	2.38	143.5
Tptpln	01025915	UE-25-UZ#16	950.6	951.3	8.18	2.39	145.0
Tptpln	01025916	UE-25-UZ#16	991.6	992.3	8.32	2.39	144.0

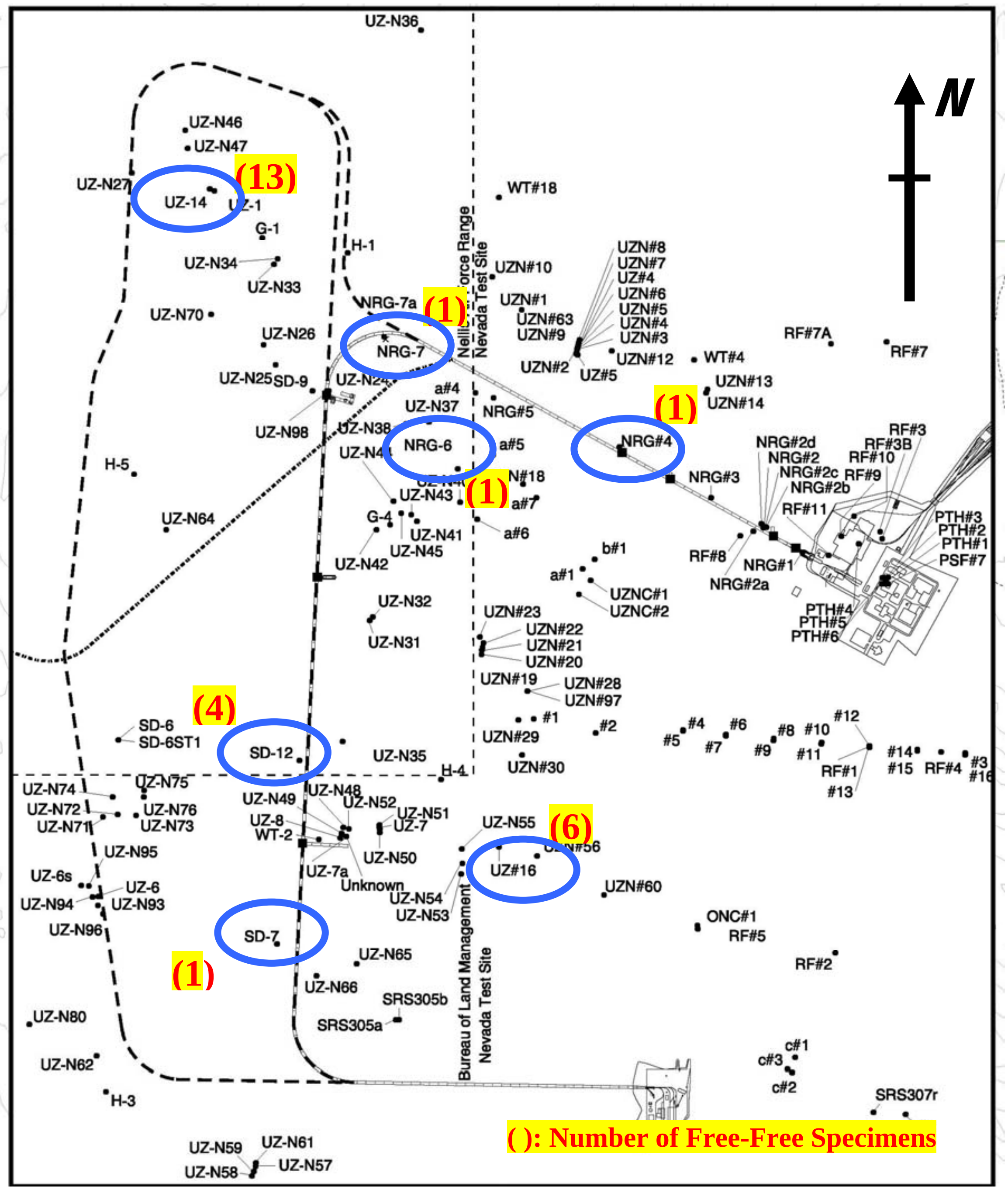

Figure 2.7 Surface Boreholes in the Vicinity of Yucca Mountain and Near the ESF Tunnel from which 27 Tuff Cores were Recovered

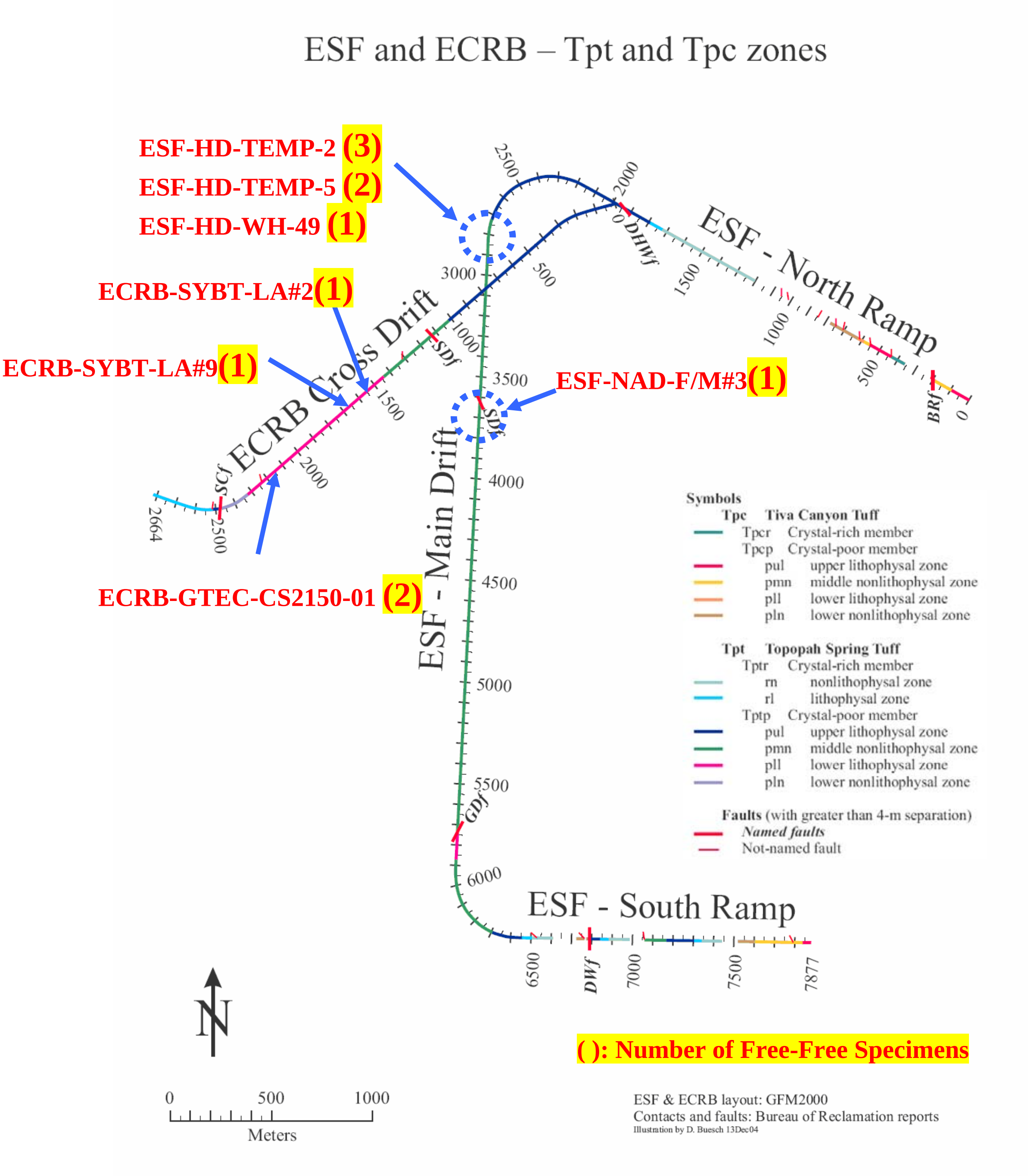

Figure 2.8 Boreholes in the ESF and ECRB Tunnels from which 11 Tuff Cores were Recovered

Table 2.3 Parent Boreholes and Surface Tunnel Locations and Number of Tpt Original Cores; Free-Free Resonant Column Testing at the University of Texas at Austin

Parent Borehole	**Num. of Specimens**	**Locations**
ECRB-GTEC-CS2150-01	2	ECRB 21+50
ECRB-SYBT-LA#2	1	ECRB 15+50
ECRB-SYBT-LA#9	1	ECRB 16+50
ESF-HD-TEMP-2	3	ESF Alcove 5
ESF-HD-TEMP-5	2	ESF Alcove 5
ESF-HD-WH-49	1	ESF Alcove 5
ESF-NAD-F/M#3	1	ESF Alcove 6
UE-25 NRG#4	1	Surface
UE-25-UZ#16	6	Surface
USW NRG-6	1	Surface
USW NRG-7/7A	1	Surface
USW SD-12	4	Surface
USW SD-7	1	Surface
USW UZ-14	13	Surface

A total of 38 Tpt cores

Table 2.4 Stratigraphic Units, Locations, and Associated Information of the Sixteen Tpt Tuff Specimens from the Yucca Mountain Site; Combined Resonant Column and Torsional Shear (RCTS) Testing at the University of Texas at Austin

Spec. No.	UT Specimen ID	Stratigraphic Unit	Unit Abbreviation	Parent Borehole	Specimen ID	Depth (ft)	
						Top	Bottom
Tuff1	UTA-42-A (1G-1)	TOPOPAH SPRING TUFF Crystal-Rich, Lithophysal	Tptrl	USW NRG-7/7A	01025902	482.5	483.1
Tuff2a	UTA-42-B (2B-3)	TOPOPAH SPRING TUFF Crystal-Poor, Upper Lithophysal	Tptpul	ESF-HD-TEMP-5	01025905	38.5	39.2
Tuff2b	UTA-42-B (2C-2)*						
Tuff3a	UTA-42-C (3C-2)	TOPOPAH SPRING TUFF Crystal-Poor, Middle Nonlithophysal	Tptpmn	ESF-HD-TEMP-2	01025910	144.7	145.4
Tuff3b	UTA-42-C (3K-2)**						
Tuff4	UTA-42-D (4C-2)	TOPOPAH SPRING TUFF Crystal-Rich, Nonlithophysal	Tptrn	USW SD-12	01025886	375.7	376.3
Tuff5	UTA-42-E (5C-2)	TOPOPAH SPRING TUFF Crystal-Poor, Lower Lithphysal	Tptpll	UE-25-UZ#16	01025914	866.7	867.3
Tuff6	UTA-42-F (6C-2)	TOPOPAH SPRING TUFF Crystal-Poor, Lower Nonlithophysal	Tptpln	UE-25-UZ#16	01025915	950.6	951.3
Tuff7	UTA-42-I (9A-2)	TOPOPAH SPRING TUFF Crystal-Poor, Lower Lithphysal	Tptpll	ECRB-SYBT-LA#2	01025913	19.2	19.7

Notes: *UTA-42-B (2C-2) was cored from Specimen UTA-42-B (2B-3)
**UTA-42-C (3K-2) was cored from Specimen UTA-42-C (3D)

Table 2.4 Continued - Stratigraphic Units, Locations, and Associated Information of the Sixteen Tpt Tuff Specimens from the Yucca Mountain Site; Combined Resonant Column and Torsional Shear (RCTS) Testing at the University of Texas at Austin

Spec. No.	UT Specimen ID	Stratigraphic Unit	Unit Abbreviation	Parent Borehole	Specimen ID	Depth (ft)	
						Top	Bottom
Tuff8	UTA-42-J (10A-2)	TOPOPAH SPRING TUFF Crystal-Poor, Lower Lithphysal	Tptpll	ECRB-SYBT-LA#9	01025912	4.2	4.7
Tuff9	UTA-42-K (11C-1)	TOPOPAH SPRING TUFF Crystal-Poor, Upper Lithophysal	Tptpul	USW UZ-14	01025867	564.1	564.9
Tuff10	UTA-42-L (12C-1)	TOPOPAH SPRING TUFF Crystal-Poor, Upper Lithophysal	Tptpul	USW UZ-14	01025868	577	577.7
Tuff11	UTA-42-M (13C-2)	TOPOPAH SPRING TUFF Crystal-Poor, Middle Nonlithophysal	Tptpmn	ESF-HD-TEMP-2	01025908	8.8	9.5
Tuff12	UTA-42-O (14C-2)	TOPOPAH SPRING TUFF Crystal-Poor, Middle Nonlithophysal	Tptpmn	USW UZ-14	01025871	823	823.8
Tuff13	UTA-42-P (15C-3)	TOPOPAH SPRING TUFF Crystal-Poor, Lower Lithphysal	Tptpll	USW UZ-14	01025873	1059	1059.7
Tuff14	UTA-42-Q (16C-2)	TOPOPAH SPRING TUFF Crystal-Poor, Lower Lithphysal	Tptpll	ECRB-GTEC-CS2150-01	01025925	0.2	0.8

enough for testing. Beside the 14 specimens, 2 other specimens (Specimens 2C-2 and 3K-2) were cored from larger test specimens as noted in Table 2.4. The stratigraphic units, boreholes and associated information of the 16 tuff specimens are listed in the table.

Following the preparation, the specimens were affixed in the RCTS device. All specimens, except Specimen 1G-1, were tested with a thin epoxy membrane. The thickness of the epoxy membrane was about 0.025 cm which is thinner than a normal rubber membrane thickness (approximately from 0.03 to 0.04 cm). The epoxy membrane resulted in filling the small lithophysae exposed on the specimen surface. Note that the testing program with the RCTS device is discussed in Chapter 4.

2.3 BANDELIER TUFF

The second tuff formation that was tested in this research is the Bandelier Tuff. The Bandelier Tuff is a volcanic rock formation present in the Jemez volcanic field, New Mexico. The Jemez mountains form the volcanic field in north central New Mexico as shown in Figure 2.9. The volcanic field is bounded on the west by the Colorado Plateau and spreads to the east and is bounded by the Española basin (Smith, 1970). The volcanic field has dimensions of about 40 miles (64 km) east-west and about 60 miles (97 km) north-south. It consists of two stratigraphic members (Otowi member and Tshirege member) that resulted from a pair of caldera-forming eruptions in the plateau (Bailey et al. (1969) and Smith et al. (1970)). The first eruption from the Toledo caldera occurred 1.61 million years ago (1.61 Ma) and created the Otowi member. The Tshirege member was produced by the second eruption from the Valles caldera 1.22 Ma (Izett and Obradovich, 1994). The Valles Caldera (VC) complex is in the central part of the Jemez Mountains as shown in Figure 2.9.

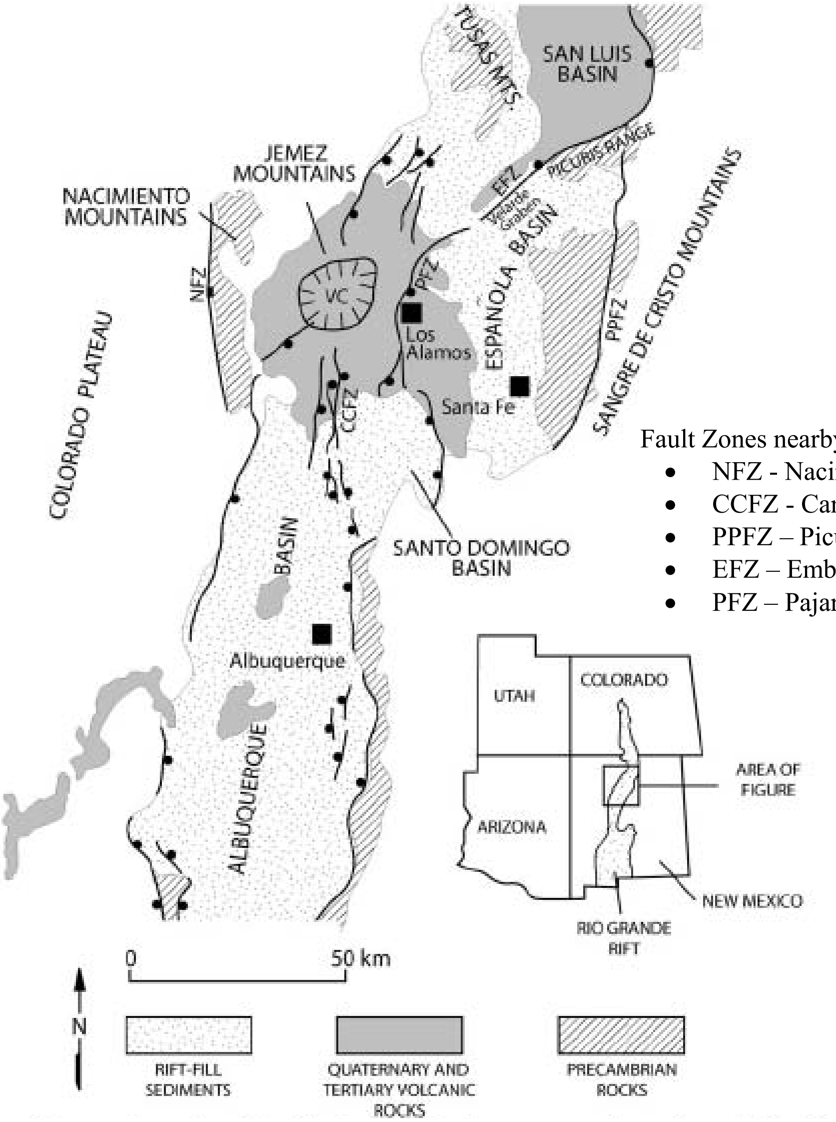

Fault Zones nearby Jemez Mountains
- NFZ - Nacimiento Fault Zone
- CCFZ - Canada del Cochiti Fault Zone
- PPFZ – Picuris-Pecos Fault Zone
- EFZ – Embudo Fault Zone
- PFZ – Pajarito Fault Zone

Figure 2.9 Map of Major Tectonic Features in the Vicinity of Jemez Mountains in Northern New Mexico (after Gardner and Goff, 1984)

The major tectonic features in northern New Mexico are shown in Figure 2.9. Major fault systems are schematically shown with a solid dot on the downthrown side of each system. Five major fault systems exist nearby the VC; from west to east, NFZ, CCFZ, PFZ, EFZ, and PPPFZ. Los Alamos National Laboratory (LANL) is located astride the Pajarito Fault Zone (PFZ) as shown in Figure 2.9. This zone is an active fault system containing 25 faults that have been identified as potential seismic sources for the significant ground shaking at the LANL (Macon and Mello, 1997). Figure 2.10 shows the location of LANL and the geography of the surrounding area. The future Chemistry and Materials Research Replacement (CMRR) building is located at LANL's Technical Area 55 (TA-55) on the Pajarito Plateau. The Tshirege member in the vicinity of the CMRR site is generally subdivided into four principal units (from bottom to top, Cooling Unit 1 (Qbt1) to Cooling Unit 4 (Qbt4)). The geologic characteristics of the units are sufficiently distinct enough to be recognized and correlated both in outcrops and in borehole samples (Broxton and Reneau, 1995). The stratigraphy of Bandelier Tuff is summarized in the following section based on the system of nomenclature proposed by Broxton and Reneau (1995).

2.3.1 Stratigraphy of the Bandelier Tuff

A generalized geologic profile of the Bandeier Tuff at the Pajarito Plateau is illustrated in Figure 2.11 as detailed in Broxton and Reneau (1995). The Bandelier Tuff is predominantly composed of a complex sequence of nonwelded to welded ignimbrites that were created from the two major eruptions as described in the previous section. A unit of volcanicalstic rocks and tuffs of the Cerro Toledo interval separates the members formed from the eruptions, the Otowi member and Tshirege member (Smith et al., 1970).

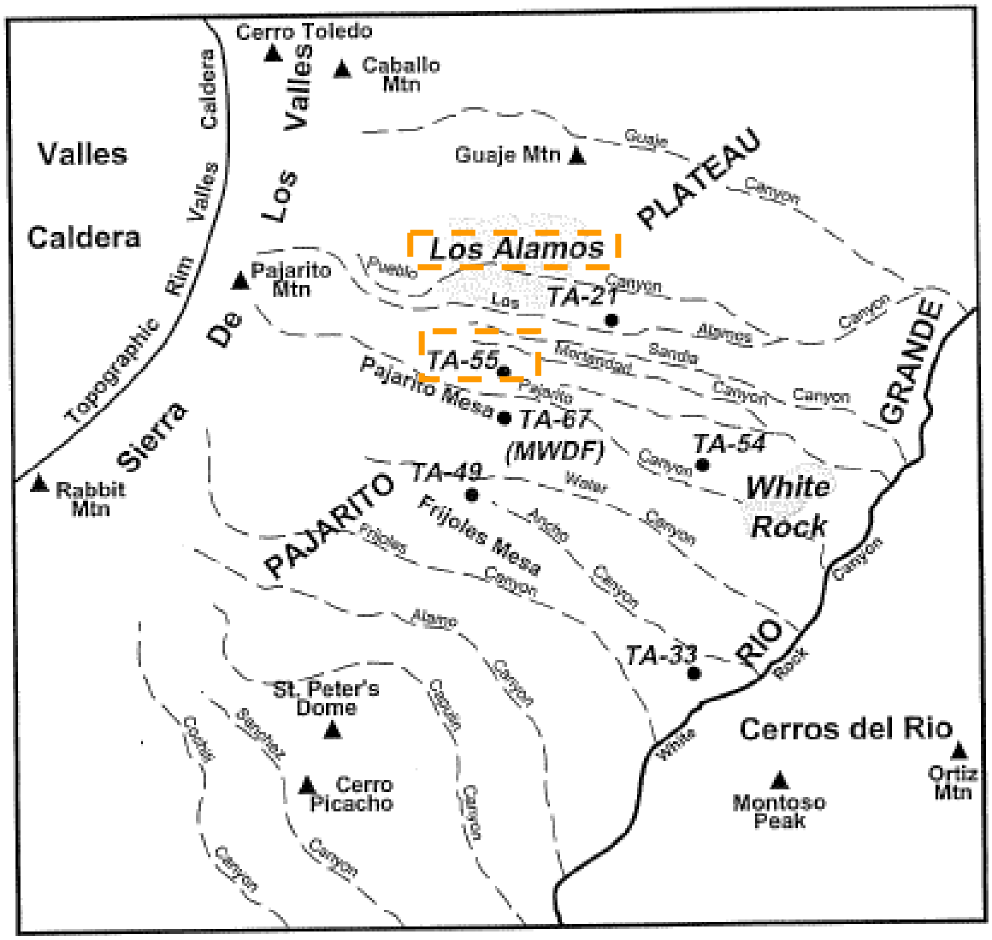

Figure 2.10 Location of LANL and Geology of the Surrounding Area (after Broxton and Reneau, 1995)

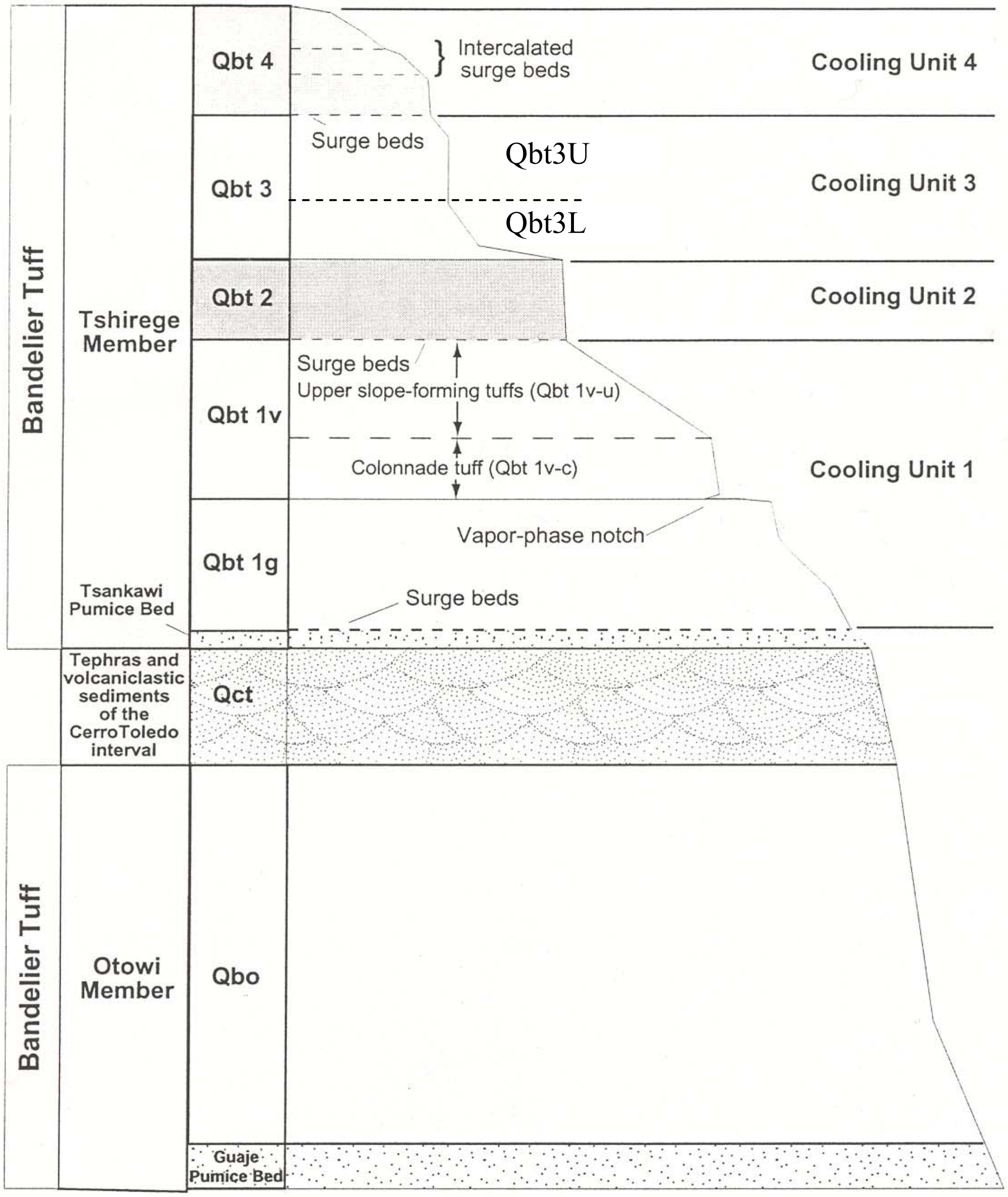

Figure 2.11 Generalized Geologic Profile of Bandelier Tuff (after Broxton and Reneau, 1995)

The Tshirege member consists of at least four mappable units (Cooling Units 1 through 4). Figure 2.11 shows the nomenclature for the Bandelier Tuff recommended by Broxton and Reneau (1995). The system was developed based on the lithological characteristics in cooling units observed in both outcrops and boreholes. The details in the geologic features for each unit are described in the report of Broxton and Reneau (1995) and briefly summarized below.

The Otowi (Qbo) member of the Bandelier Tuff is a relatively homogenous unit consisting of successive deposit of ash-flow tuffs. These tuffs are nonwelded to partially welded forming a single cooling unit. The thickness of the Otowi member is variable cross the site because it was deposited over various levels of old deposit and was subjected to about 400,000 years of erosion until the Tshirege member was deposited over the member. The Otowi member contains light gray to pinkish orange pumice lapilli (rock fragments between 2 and 64 mm in diameter) supported by a white-to-tan ashy matrix. The pumice lapilli are circular to semi-circular (aspect ratios (= ratio of length to height) = 1:1 to 2:1) and typically make up about 10 to 30 % of the tuff. The size of the pumice lapilli ranges from 0.5 to 6 cm in diameter. The matrix is made up of glassy and clear shards, phenocryst (7 to 9 %) and pumice clasts. The base of the Otowi member is the Guaje Pumice Bed. The Guaje Pumice Bed is a pumice fall deposit that is about 10 to 20 m thick.

Tephras and Volcaniclastic Sediments from the Cerro Toledo Interval is an intercalated unit between the Tshirege and Otowi members. This unit consists of mainly rhyolitic lava flows and phyroclastic rocks that were erupted from the Cerro Toledo and Rabbit Mountain rhyolite domes located in the Sierra de los Valles (see Figure 2.10). This unit is not considered part of the Bandelier Tuff because of its different eruption style, source, and petrologic features. The thickness of the unit widely varies from 3 to

42 m in the area of LANL (Broxton et al., 1995; Stimac et al., 1995; Gardner et al., 1993).

The Tshirege member (Qbt) of the Bandelier Tuff is about 1.22 Ma and is composed of compound cooling units on the Pajarito Plateau. This member is divided into four distinct cooling units that represent four sequences of rapid ash-flow eruptions and depositions. The partial cooling resulted from the inactivity between each event that separates the units. These units are labeled Cooling Units 1 through 4 in ascending order as shown in Figure 2.11. The maximum thickness of this member is about 170 m and was reported in a borehole at TA-49 (see Figure 2.10) (Stimac et al., 1995). The base of this member is a pumice fall deposit named the Tsankawi Pumice Bed. The thickness of this deposit is typically 20 to 100 cm in the site. This deposit consists of angular to subangular pumice lapilli up to 6 cm in diameter. The pumices in this deposit are mostly rhyolitic, but there are some hornblende-bearing pumices. These pumices are a diagnostic feature of the Tsankawi Pumice Bed (Bailey et al., 1969). The descriptions of the four cooling units above this deposit are as follows:

(1) Unit 1 (Qbt1)

Qbt1 is a thick ash-flow tuff deposit spread over a wide area of the Pajarito Plateau. The unit is in general non-welded where exposed, despite its large thickness in some areas. This unit is further divided into two layers: (1) a lower glassy tuff layer (Qbt1g) and an upper devitrified and vapor-phase crystallized tuff layer (Qbt1v). The main body of Qbt1g exhibits abundant volcanic glass, lack of welding, and a distinct Swiss-cheese appearance on cliff faces. The tuffs in Qbt1g consist of light-gray, vitreous, pumice lapilli supported by a matrix of coarse ash, shards, pumice fragments, and abundant (12 to 16 %) phenocrysts (Broxton et al., 1995). The basal part of Qbt1v has a "colonnade" appearance because of the abundant vertical fractures resulting in smooth dihedral surfaces on cliff faces (Qbt1v-c in Figure 2.11). This colonnade tuff is overlain by mainly slope forming tuffs that make up the greater part of Qbt1v (Qbt1v-u in Figure 2.11). Volcanic glass initially emplaced in Qbt1v crystallized to cristobalite, alkali feldspar, and minor tridymite during devitrification and vapor-phase crystallization. Pumice clasts typically make up 30 to 50 % of the tuffs in Qbt1v and are commonly up to 6 cm in diameter.

(2) Unit 2 (Qbt2)

Qbt2 is the most strongly welded unit of the Tshirege member in the eastern and central part of the LANL. The tuff in Qbt2 is in general, moderately to densely welded, with a pumice aspect ratio ranging from about 3:1 to 10:1 at TA-67 (see Figure 2.10) (Broxton et al., 1995). Pumices are generally smaller (< 2 cm) and less abundant (2 to 15 %) than in Qbt1. Most of the primary vitroclastic textures in the tuffs have been destroyed by devitrification and vapor-phase crystallization The phenocrysts are more abundant (17 to 32 %) compared with Qbt1. Devitrification and vapor-phase crystallization is also abundant in the tuff. Numerous well-developed fractures are found in Qbt2. Most fractures are nearly vertical and extend to the upper part of Unit1v.

(3) Unit 3 (Qbt3)

Qbt3 can be subdivided into two components: (1) lower slope-forming tuffs (Qbt3L) and (2) upper cliff-forming tuffs (Qbt3U). The change from Qbt2 to Qbt3 is again abrupt due to the abrupt change in welding intensity. The lower part of Qbt3 (Qbt3L) consists of nonwelded tuffs made of white to light-gray ashy material made up of shards, pumice fragment, and abundant phenocrysts

(18 to 33 %). Pumice clasts are sparse (less than 5 %) and have a sugary texture resulted from extensive vapor-phase crystallization. The upper part of Qbt3 (Qbt3U) consists of similar contents as Qbt3L but Qbt3U has a larger portion of pumice clasts (10 to 30 %) and higher welding intensity. Fractures are also more common in the cliff-forming tuffs at the upper part of Unit 3 compared with the nonwelded tuffs at the base of the unit.

(4) Unit 4 (Qbt4)

Qbt4 consists of a pyroclastic surge deposit and overlying pumice-poor ash-flow tuffs. The surge deposit contains abundant phenocrysts as much as 50 % of the tuffs in the deposit. The ash-flow tuffs of Qbt4 are nonwelded to partially welded at Pajarito Mesa. They have less abundant relict pumice (less than 5 %) and phenocrysts (less than 8 %).

In addition to the units described above, dacite and dacite sediments underlie the Guaje Pumice Bed. As defined in the nomenclature above, the Unit 3 of the Tshirege Member (Qbt) is subdivided, for this study, into Unit 3 Upper (Qbt3U) and Unit 3 Lower (Qbt3L) because of their significant geomechanical differences (Kleinfelder, 2005). Qbt3L is a nonwelded to partially welded unit consisting of slope-forming tuffs that overlie a broad bench developed on top of Unit 2. Qbt3U consists of moderately welded cliff-forming tuffs.

2.3.2 Tested Bandelier Tuff Specimens

A total of 18 Bandelier tuff samples from the Los Alamos site were tested. As listed in Table 2.5, the specimens consist of:

1. two (2) moderately welded tuff (Qbt3U) specimens,
2. eight (8) poorly welded tuff (Qbt3L) specimens,
3. two (2) moderately to strongly welded tuff (Qbt2) specimens,
4. two (2) poorly welded tuff (Qbt1v) specimens,
5. two (2) poorly welded tuff (Qbt1g) specimens, and
6. two (2) poorly welded tuff (Qbo) specimens.

The initial characteristics of the specimens are presented in Table 2.5. It is worth noting the criteria to define the degree of welding of the test specimens are listed in the right-hand column in Table 2.5. The following description and criteria is part of the Rock Classification System of the LANL Engineering Manual (Kleinfelder, 2007):

(1) Poorly welded tuffs

Poorly to nonindurated and easily crumbles into flour-like. Some zones display some strength and may produce intact core with short lengths. Some core produces thin wafers that are friable and easily broken by hand. The core is lightweight and very low density. The pumices have significantly void space within the pumice structure. Pumices that survive the drilling (and sampling procedures) are open, not elongated. Pumice aspect ratios are roughly equant (1:1) to 2:1.

(2) Moderately welded tuffs

Appear to be moderately indurated and break readily with light hammer blows. Pumices are elongated with some appearance of structure. Approximate pumice aspect ratios are 2:1 to 6:1. Generally, the core remains intact for lengths of several inches to feet.

Table 2.5 Eighteen Bandelier Tuff Specimens Dynamically Tested in This Research

Spec. No.	UT Spec. ID	Boring No.*	Sample No.*	Geologic Unit*	Sample Type*	Depth (ft)		Lateral Stress Ratio, K_o*$^{+}$	In-Situ Mean Effec.Stress, σ'_m (psi)*$^{++}$	In-Situ Mean Effec.Stress, σ'_m (ksf)*$^{++}$	Total Unit Weight, γ_t, lb/ft^3	Water Content, w, %	Description/ Sample Condition*
						Top	Bottom						
Tuff3	3C	DSC-2	R6	Qbt3U	HQ core	29.4	29.7	0.5	13.3	1.9	94.1	0.30	Moderately welded tuff
Tuff5	5E	DSC-1A	R14	Qbt3U	HQ core	68.9	69.2	0.5	30.7	4.4	97.1	0.33	Moderately welded tuff
Tuff11	15C	DSC-2A	R26	Qbt3L	3" Pitcher	100.3	100.9	1.0	49.8	7.2	95.1	6.51	Poorly welded tuff
Tuff12	16C	DSC-2A	R31	Qbt3L	3" Pitcher	113.7	114.2	1.0	57.7	8.3	94.7	5.60	Poorly welded tuff
Tuff14	18C	SSC-2A	R26	Qbt3L	6" Pitcher	91.3	91.9	1.0	43.2	6.2	94.1	9.74	Poorly welded tuff
Tuff15	19C	SSC-2A	R32	Qbt3L	6" Pitcher	102.5	103.1	1.0	50.2	7.2	92.6	7.16	Poorly welded tuff
Tuff18	22C	SSC-2A	R41	Qbt3L	6" Pitcher	121.3	121.8	1.0	60.8	8.8	94.5	8.48	Poorly welded tuff
Tuff13	17C	DSC-1	R19	Qbt3L	6" Pitcher	83.2	83.6	1.0	38.7	5.6	91.0	9.01	Poorly welded tuff
Tuff16	20C	DSC-1	R31	Qbt3L	6" Pitcher	105.2	105.6	1.0	51.7	7.4	90.0	5.25	Poorly welded tuff
Tuff17	21C	DSC-1	R37	Qbt3L	6" Pitcher	117.3	117.9	1.0	58.7	8.5	91.5	6.37	Poorly welded tuff
Tuff2	2G	DSC-1A	R40	Qbt2	HQ core	155.2	155.6	0.5	81.5	11.7	118.2	0.13	Strongly welded tuff
Tuff1	1G	DSC-2	R29	Qbt2	HQ core	136.2	136.7	0.5	71.3	10.3	118.9	0.12	Moderately welded tuff
Tuff4	4H	DSC-1A	R55	Qbt1v	HQ core	234.6	235.0	1.0	122.7	17.7	82.1	0.09	Poorly welded tuff
Tuff9	10C	DSC-1B	R75	Qbt1v	3" Pitcher	248.9	249.5	1.0	131.6	19.0	83.1	7.30	Poorly welded tuff
Tuff6	7C	DSC-1B	R83	Qbt1g	3" Pitcher	281.8	282.3	1.0	151.3	21.8	79.7	7.49	Poorly welded tuff
Tuff7	8C	DSC-2A	R76	Qbt1g	3" Pitcher	284.8	285.4	1.0	154.5	22.2	80.2	5.10	Poorly welded tuff
Tuff8	9C	DSC-2A	R109	Qbo	3" Pitcher	420.1	420.5	1.0	240.8	34.7	78.4	4.68	Poorly welded tuff
Tuff10	11C	DSC-1B	R170	Qbo	3" Pitcher	530.5	531.0	1.0	304.2	43.8	87.8	10.14	Poorly welded tuff

Notes: *information provided by Kleinfelder

$^{+}$lateral rock stress ratio is the lateral earth pressure ratio at rest

$^{++}$estimated in-situ mean effective stress (σ_m') estimated with the lateral stress ratio provided by Kleinfelder as: $\sigma_m' = 1/3(\sigma_v'+2K_o\sigma_v')$

(3) Strongly welded tuffs

Strongly indurated and have pumice aspect ratios of roughly > 6:1. Generally, the core remains intact, solid, and dense with flattening of pumices such that little evidence of the pumices may remain. Strongly welded tuffs are not often encountered and require hammers to break apart core and also require air-rotary drilling to obtain sample.

Five samples from Units Qbt2, Qbt3U and Qbt1v were recovered as HQ size Geo-Barrel cores (outside diameter of 96 mm and inside diameter of 63 mm). The remaining samples (Qbt1v, Qbt1g, Qbo, and Qbt3L) were recovered with either 3-in. or 6-in. (76-mm or 152-mm) diameter Pitcher samplers. It is worth noting that the 6-in. Pitcher sampler was used to recover five samples from the Qbt3L unit which exhibits the lowest welding intensity (discussed in Chapter 4) and has the largest possibility of being disturbed. Moreover, based on a "Site Response and Sensitivity Study for the CMRR Facility" (2003), Tom Houston, DOE-LANL, and Dr. Carl Costantino, LANL Consultant, noted that low-strain, shear wave velocity, and nonlinear dynamic strain characteristics of the Qbt3L unit have a significant impact on the ground response of the site. Sampling with the large diameter (6-in.) sampling tube was successful based on an excellent match between the values of the small-strain shear wave velocity (V_S) measured in-situ and in the laboratory (discussed in Chapter 6).

All field samples were critical care samples as specified for Groups C and D in ASTM D4220-95, Standard Practices for Preserving and Transporting Soil Samples. Packaging of these levels of samples is required to be sufficient to minimize vibrations during transportation. The packaging containers also have to be instrumented with approved acceleration limiting tell-tale devices. All HQ cores were placed in a wooden core box in which each row was lined with foam padding at least 0.5-in. thick. Wooden spacers or packing materials were placed to fill empty spaces in the core box and to pack the core securely in place. Each core box has a twist-lock latch that minimizes the risk of accidental opening and exerts downward pressure on the box lid at closure. Approved 10g Drop-n-tells^{TM} acceleration limiting tell-tale devices (shock detectors) were applied to the outside surfaces of core boxes (and also to the outside surfaces of sample tubes) as shown in Figure 2.12. A detector in each of three orthogonal directions was placed at approximately the middle of the box. The conditions of the detectors were checked prior to and after shipments/movements and logged. All core boxes were transported by automobile to the UT laboratory.

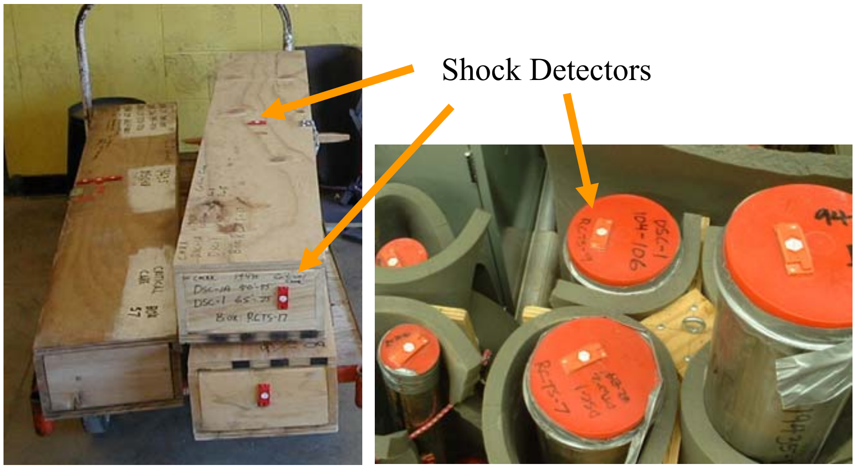

(a) Wooden core boxed (b) Sampling steel tubes

Figure 2.12 Sample Container and Chock Detectors: (a) Wooden Core Boxes and (b) Sampling Steel Tubes for the Bandelier Tuff Samples

All specimens were trimmed by hand to the final dimensions. In some cases, only the ends were trimmed and in other cases the sides and ends were trimmed. Each specimen was glued to the base pedestal of the RCTS equipment. The top cap was also glued to the specimen before testing. In all cases, the specimen was allowed to drain during testing; hence, an open drainage port communicated with the specimen.

2.3 SUMMARY

Dynamic properties of two different volcanic tuff formations from two different parts of the United States were studied in this research. The two tuff formations are the Topopah Spring formation at Yucca Mountain, Nevada and the Bandelier formation at Pajarito Plateau, New Mexico. Future U.S. Department of Energy (DOE) facilities will be placed above or within these two tuff formations. This research has been performed as part of the static and dynamic site characterization of these materials.

A total of 38 tuff specimens from the Topopah Spring Tuff, Nevada, were dynamically tested in this research. The Topopah Spring Tuff at Yucca Mountain is a single depositional and cooling unit. Therefore, the lithostratigraphic features present in the tuff represent the processes of deposition, welding, crystallization, and cooling. Zones of the Topopah Spring Tuff are mainly defined by crystallization and development of lithophysae and spots. The samples tested in this research were recovered from 27 surface boreholes and 11 tunnel boreholes and represent six crystallized lithophysal and nonlithophysal zones.

Tests on 18 tuff specimens from the Bandelier Tuff at Pajarito Plateau, New Mexico, were also included in this research. The Bandelier Tuff consists of two sequential ignimbrite deposits that were created from two major eruptions. The later deposit is further subdivided by four distinct cooling units. Various welding and crystallization conditions of the deposit represent complex variations in the depositional process at the site. Samples recovered from six surface boreholes were transported and handled as critical care samples until dynamic testing was performed.

Chapter 3

Literature Review

3.1 INTRODUCTION

The mechanical properties of intact tuffs have been studied in conjunction with both static and seismic site characterizations to evaluate the stability of existing facilities or to design new surface and/or underground structures at various sites. Specifically, over the past two decades a great amount of data has been collected on the mechanical properties of intact tuff specimens at Yucca Mountain, Nevada. Because of the large amount of data and the high standards of the quality assurance program for this site, the Yucca Mountain project has been producing the most voluminous database of high quality tests of tuffs in the world. The data and findings summarized in this chapter are mostly from literature related to this site. The studies on dynamic properties of the Bandelier tuffs at Los Alamos National Laboratory (LANL) in New Mexico are also included in this chapter. The wide range of welding intensity within the Bandelier tuffs provides helpful information on the variations of the linear and nonlinear mechanical properties of ignimbrite (ash-flow tuff).

The stratigraphic profiling of the pyroclastic deposits requires a systematic classification scheme to define degree of welding. Since three major welding zones in a pyroclastic deposit were characterized based on a thorough study of petrographic characteristics of lapilli and ash shards by Smith (1960), various ways to define the characteristics of each welding zone semi-quantitatively have been developed and adopted to researches for various pyroclastic deposits. The previous schemes are reviewed in this chapter: (1) to explore their effectiveness and limitations in engineering applications and (2) to see the necessity and efficiency of the dynamic properties measured in this study for describing the mechanical characteristics of the welding zones as other effective quantitative indices.

The Young's modulus (E) and Poisson's ratio (ν) have been the two major elastic constants routinely determined while various strength properties have generally been the major concerns as design parameters of structures. The values of E and ν of intact ignimbrites are discussed in terms of their correlations with physical properties of the tuffs. Researchers have found a strong relationship between E and porosity (e.g., Price 1983; Price and Bauer, 1985; Price et al, 1994). The variation of porosity is directly related to the welding intensity for the pyroclastic tuffs that preserve their vitroclastic texture. Furthermore, the densely welded and crystallized rocks of the Topopah Spring Tuff contain lithophysal cavities and the physical properties of these rocks are highly affected by these features (Buesch et al., 2006). The values of E and ν are influenced by various conditions inherent in the specimens relative to the specimen size and conditions related to the test methods and procedures (e.g., effective confining pressure (σ_o'), strain rate (or loading frequency), saturation, and strain amplitude).

In this chapter, the classification of welding zones and associated metrics of welding intensity used by various researchers are summarized in Section 3.2. The variation of E (or shear modulus, G), ν, and their correlations with porosity are then discussed in Section 3.3. Finally, the factors affecting the mechanical properties of specimens with various degrees of welding and lithostratigraphic features are presented in Section 3.4. It should be noted that all the mechanical properties (e.g., E, G, and ν) presented in this chapter are limited to the measurements in the small-strain range, except for the properties discussed in the section related to strain amplitude effect (Section 3.4.5). The small-strain range is often defined as the strain range where the mechanical properties are constant and independent of strain amplitude. Various researchers have determined the small-strain properties at different levels of strain (e.g., at axial strains less than 5×10^{-6} (Haupt et al., 1991); in the range of stresses between 10 and 50 % of the ultimate sample strength (Price, 1986); and shearing strains below 10^{-3} % (Stokoe et al, 1993)). Detailed discussions of the small-strain range are presented in Chapters 6 and 7.

3.2 DEGREE OF WELDING OF PYROCLASTIC DEPOSITS

Glassy pyroclastic materials are emplaced at high temperatures and form a deposit with various thicknesses. The central part of a thick deposit becomes welded due to the load of its overlying column and the time of residence at temperatures above the glass transition temperature (Tg) (Russell and Quane, 2004). The welding process of these materials involves their sintering, compaction and flattening processes (Quane and Russell, 2005). As welding intensifies, significant changes in physical properties of the deposits accompany as shown in Figure 3.1. In the fresh undeformed pyroclastic deposit, the Y-shaped glass shards and subspherical pumice lapilli are well preserved (Figure 3.1a). As welding intensifies, the pumice and shards are flattened (Figure 3.1b). The maximum compaction typically occurs at 35 – 40 % up from the bottom of the deposit (e.g., Regan and Sheridan, 1972) (Figure 3.1c). The resulting deformations of pumice lapilli are schematically shown in Figure 3.1d.

Smith (1960b) proposed three zones to describe a pyroclastic deposit in terms of welding intensity. The three zones are as follows: nonwelded, partially welded, and densely welded zones. The partially welded zone was further subdivided into the following four zones: upper, middle, lower, and transition zones. These classifications were qualitative and mainly based on petrographic characteristics of lapilli and ash sized fragments. Smith and Bailey (1966) started using the estimated porosities as a semiquantitative scheme to define the 6 welding zones in the Bandelier Tuff: from the nonwelded zone having porosities greater than 45 % to the densely welded zone having porosities less than 10 %. Porosity contours were constructed based on the porosity measurements along various stratigraphic vertical sections located in the emplacement area of the Valles Calder as shown in Figure 3.2. The contours show how welding decreases away from the caldera source while the total cooling unit thickens. The authors discussed that this lateral decrease in welding is related to heat loss toward the distal end of the sheet during emplacement of the ash flows. The thickness of the zone of crystallization relative to the thickness of the cooling unit also decreases away from the caldera confirming the heat loss.

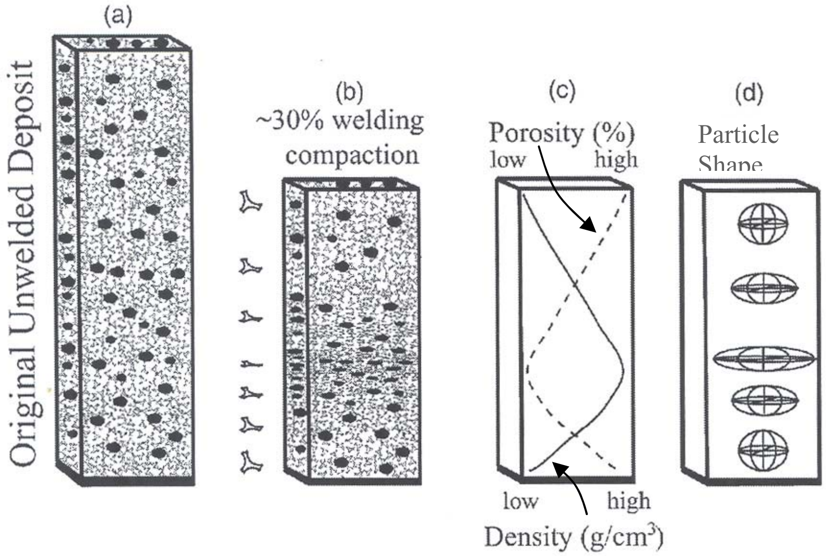

Figure 3.1 Schematic Illustration of the Welding Process: (a) An Initial Undeformed Pyroclastic Deposit, (b) the Deposit Deformed after about 30 % Compaction, (c) Profiles of Porosity and Density when about 30 % Compaction has Occurred and (d) Shapes of Pumice Lapilli when about 30 % Compaction has Occurred (after Quane and Russell, 2003)

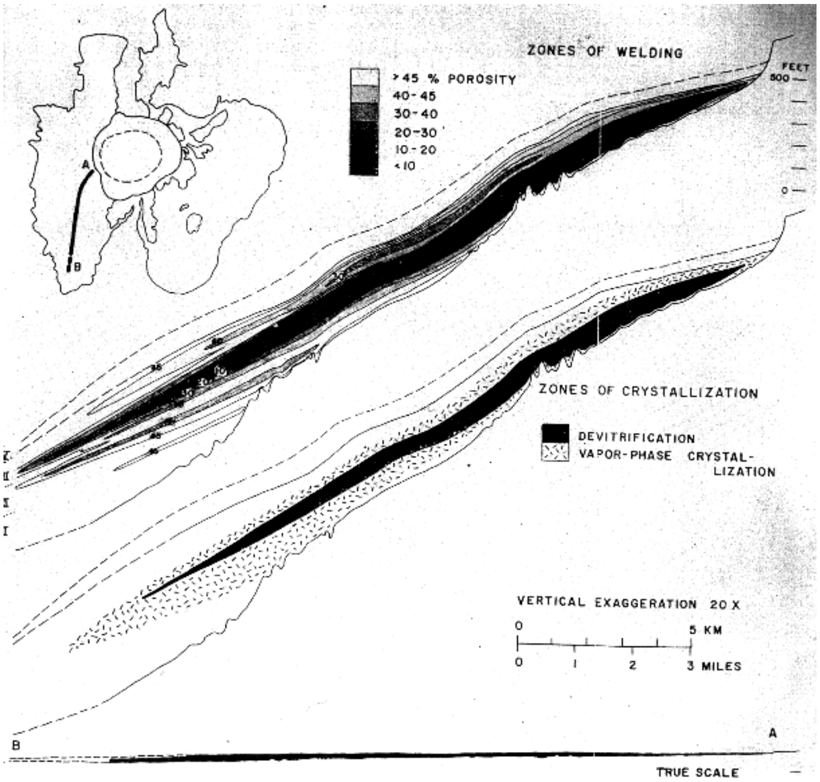

Figure 3.2 Zone of Welding and Zone of Crystallization on the Cross Section of the Upper Member of the Bandelier Tuff in San Diego Canyon, Jemez Plateau, NM (after Smith and Bailey, 1966)

Peterson (1979) studied the flattening of pumice fragments within the Apache Leaf Tuff to define degree of welding. The tuff is a Miocene ash-flow tuff (about 20 Ma) that was emplaced over an area of at least 1000 km^2. Figure 3.3 illustrates the ways of defining the amount of flattening of pumice fragments of the tuff. The “apparent flatness” was defined by the ratio of the length parallel to the flattening to the height perpendicular to the flattening. The “flattening ratio” was determined by taking the means of the apparent flatness measurements on at least 30 pumice fragments at each locality. The author discussed that the logarithmic mean reduces the influence that highly deviatory fragments may have on the mean value. The author argued that postemplacement crystallization and deposition of diagenetic minerals through time result in the decrease in porosity on nonwelded to partially welded zones in older rocks; moreover, since deformation of pumice fragments after primary welding is normally unchanged with time, the flattening ratio of the pumice fragments serves better than porosity to identify the degree of welding.

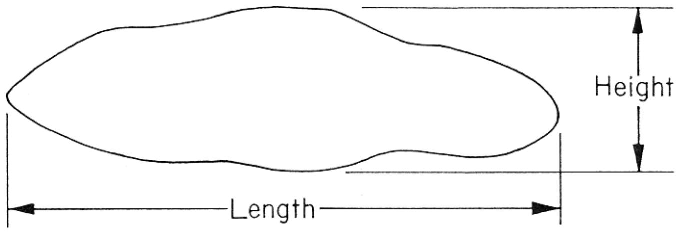

Apparent flatness: $F_a = \frac{\text{Length}}{\text{Height}}$

Number of fragments measured: n

Arithmetical flattening ratio: $F_R = \frac{\Sigma F_a}{n}$

Logarithmic flattening ratio: $F_L = \text{antilog} \frac{\Sigma \log F_a}{n}$

Figure 3.3 Apparent Flatness and Determination of Flattening Ratios of Pumice Fragment (after Peterson, 1979)

Wilson and Hildreth (2003) used the bulk density and welding textures observed in the field as shown in Table 3.1. The authors classified five different welding facies for the 0.76 Ma Bishop Tuff in the Owens River Gorge, California. The authors pointed out the any obvious local concentrations of lithic or pumice clasts might skew the density measurements. Therefore, their samples were collected from representative blocks or cored from typical matrix material. The weight of the samples used in the determination of density ranged from 300 to 1800 g. The authors reported that the lithic proportions of the samples were less than 10 % by weight, mostly less than 5 % by weight.

Table 3.1 Field Descriptive Terms for Welding Textures in the Bishop Tuff (after Wilson and Hildreth, 2003)

Welding Term	Density (g/cm^3)	Nature of Deposit
Nonwelded	1.09 - 1.47	Noncoherent; can be disaggregated between fingers
Sintered	1.22 - 1.57	Coherent; requires hammer to fracture; no eutaxitic texture
Poorly Welded	1.49 - 1.81	Some pumice flattening, highly porous and soft
Moderately Welded	1.74 - 2.00	Clear eutaxitic texture, still relative soft
Densely Welded	>2.00	Strong eutaxitic texture, dark color if glassy

Quane and Russell (2003) utilized rock strengths to track degree of welding in a section of the Bandelier Tuff (Cooling Unit 4 in Tshirege Member). The authors specifically used the point load strength test (PLST) (see ASTM D5731 for details) since it is a relatively portable and efficient method to measure rock strength in the field. Furthermore, the authors developed empirical relationships to convert the PLST measurements to uniaxial compressive strength (USC) as follows:

$$\mathrm{UCS} = 3.86 \cdot \mathrm{PLST}^2 + 5.65 \cdot \mathrm{PLST} \qquad (3.1)$$

where, PLST is the point load strength and UCS is the uniaxial compressive strength. The coefficients of Eq. (3.1) were obtained based on least squares fitting of measurements on various manufactured isotropic materials (e.g., chalk, graphite rod) and natural rock samples including samples of the Bandelier Tuff. The converted USC is used to determine the rock strength rating (RSR) defined by Hoek and Brown (1980). The RSR is as follows: a strength rating of 0 for rocks with strengths from 1 - 3 MPa, a rating of 1 for rocks with strengths from 3 - 10 MPa, a rating of 2 for rocks with strengths from 10 – 25 MPa and a rating of 4 for rocks with strength 25 – 50 MPa. The authors identify four discrete zones of welding intensity based on the RSR as shown in Table 3.2. The authors discussed that this classification scheme provides an objective means to determine the welding intensity quantitatively in the field.

Table 3.2 Four Welding Zones and Associated Strengths and Strength Rating (after Quane and Russell, 2003)

Welding Zone	Welding Intensity (Descriptive)	Suggested Range of PLST (Mpa)	RSR*
I	Unwelded	0 - 0.5	0
II	Incipiently welded	0.5 - 1.0	1
III	Partially or moderately welded	1.0 - 1.95	2
IV	Densely Welded	>1.95	4

Note: *rock strength ratings (RSR) defined by Hoek and Brown (1980)

Quane and Russell (2005) later combined petrographic characteristics and physical properties of ignimbrites for ranking welding intensity in pyroclastic deposits. Their classification comprises six ranks of welding intensity ranging from unconsolidated (Rank I) to obsidian-like vitrophyre (Rank VI). The ranks were defined by discrete ranges in physical properties (porosity, density and strength) and measurable petrographic features (oblateness (OB) and fabric angle (FA)). The authors defined the oblateness (OB) as one minus the reciprocal of pumice flattening ratio and the fabric angle (FA) as the average angle from horizon of fabrics that were formed by ash shards aligned during the welding process. The ranges of the physical properties associated with the six ranks are tabulated in Table 3.3 and specific petrographic characteristics for the ranks are listed in Table 3.4.

Table 3.3 Range of Physical Properties for Six Ranks (after Quane and Russell, 2005)

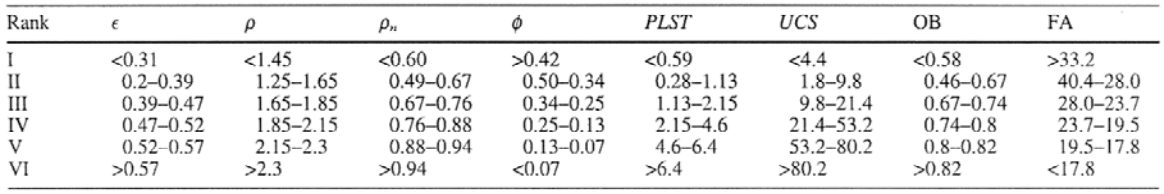

Rank	ϵ	ρ	ρ_n	ϕ	*PLST*	*UCS*	OB	FA
I	<0.31	<1.45	<0.60	>0.42	<0.59	<4.4	<0.58	>33.2
II	0.2–0.39	1.25–1.65	0.49–0.67	0.50–0.34	0.28–1.13	1.8–9.8	0.46–0.67	40.4–28.0
III	0.39–0.47	1.65–1.85	0.67–0.76	0.34–0.25	1.13–2.15	9.8–21.4	0.67–0.74	28.0–23.7
IV	0.47–0.52	1.85–2.15	0.76–0.88	0.25–0.13	2.15–4.6	21.4–53.2	0.74–0.8	23.7–19.5
V	0.52–0.57	2.15–2.3	0.88–0.94	0.13–0.07	4.6–6.4	53.2–80.2	0.8–0.82	19.5–17.8
VI	>0.57	>2.3	>0.94	<0.07	>6.4	>80.2	>0.82	<17.8

Table 3.4 Petrographic Characteristics Used for Ranking Welding Intensity (after Quane and Russell, 2005)

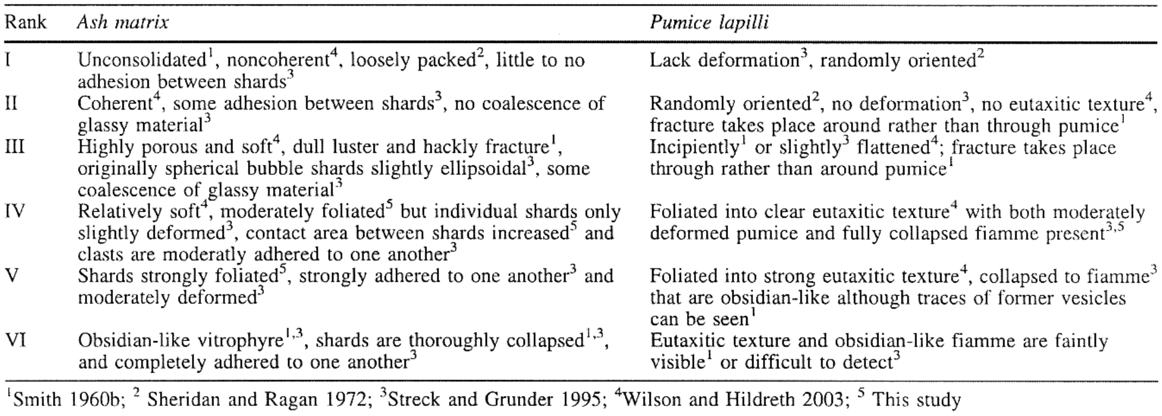

Rank	*Ash matrix*	*Pumice lapilli*
I	Unconsolidated[1], noncoherent[4], loosely packed[2], little to no adhesion between shards[3]	Lack deformation[3], randomly oriented[2]
II	Coherent[4], some adhesion between shards[3], no coalescence of glassy material[3]	Randomly oriented[2], no deformation[3], no eutaxitic texture[4], fracture takes place around rather than through pumice[1]
III	Highly porous and soft[4], dull luster and hackly fracture[1], originally spherical bubble shards slightly ellipsoidal[3], some coalescence of glassy material[3]	Incipiently[1] or slightly[3] flattened[4]; fracture takes place through rather than around pumice[1]
IV	Relatively soft[4], moderately foliated[5] but individual shards only slightly deformed[3], contact area between shards increased[5] and clasts are moderatly adhered to one another[3]	Foliated into clear eutaxitic texture[4] with both moderately deformed pumice and fully collapsed fiamme present[3,5]
V	Shards strongly foliated[5], strongly adhered to one another[3] and moderately deformed[3]	Foliated into strong eutaxitic texture[4], collapsed to fiamme[3] that are obsidian-like although traces of former vesicles can be seen[1]
VI	Obsidian-like vitrophyre[1,3], shards are thoroughly collapsed[1,3], and completely adhered to one another[3]	Eutaxitic texture and obsidian-like fiamme are faintly visible[1] or difficult to detect[3]

[1]Smith 1960b; [2] Sheridan and Ragan 1972; [3]Streck and Grunder 1995; [4]Wilson and Hildreth 2003; [5] This study

The authors discussed that the proposed ranking scheme provides great sensitivity or precision and allows for reproducible mapping of subtle variations in welding intensity between different deposits. However, the authors also pointed out that the ranks are based on the properties of fresh pyroclastic rock samples that preserve their vitroclastic texture. The properties have not been significantly affected by secondary crystallization processes (e.g., lithophysae, spherulites; Streck and Grunder,1995). For the deposit where these processes are significant, the authors suggested relying only on petrographic criteria to rank welding intensity of the deposit.

3.3 EFFECT OF POROSITY ON YOUNG'S MODULUS AND POISSON'S RATIO

Earlier studies of tuffs from Yucca Mountain show that the elastic and strength properties of the tuffs are predominantly dependent upon porosity (Price, 1983; Price and Bauer, 1985). Figure 3.4a shows the variation of Young's modulus (E) with functional porosity (n) of fully saturated ash-flow tuff samples from Yucca Mountain as determined from unconfined compression tests (Price, 1983). The n was defined as the volume fraction of clay (montmorillonite) material in addition to the actual porosity. The author examined the variation of E with respect to n, since the strength and Young's modulus of montmorillonite are relatively insignificant (Olson, 1974). The n values range from about 21 to 43 % leading to a wide variation in E, with E ranging from about 3.5 to 29 GPa as shown in Figure 3.4a. The variation of E with n is fitted with a straight line on the log-log scale and the equation of the best-fit line is shown in Figure 3.4a. The specimens were recovered from the Calico Hills, Bullfrog and Tram tuffs at Yucca Mountain and had a nominal diameter of 1 in. (2.5 cm). All tests were performed under unconfined, at room temperature (about 23°C) and at a constant axial strain rate (10^{-5} s^{-1}). These conditions for the tests are later called a standard set of conditions for baseline testing (Price et al., 1991), especially when a specimen with a diameter of 2 in. (5.1 cm) is tested.

While E exhibit a strong relationship with n, Poisson's ratio (ν) does not show any discernable trend with n as illustrated in Figure 3.4b. The values of ν varies randomly from 0.08 to 0.38 for the tuff specimens.

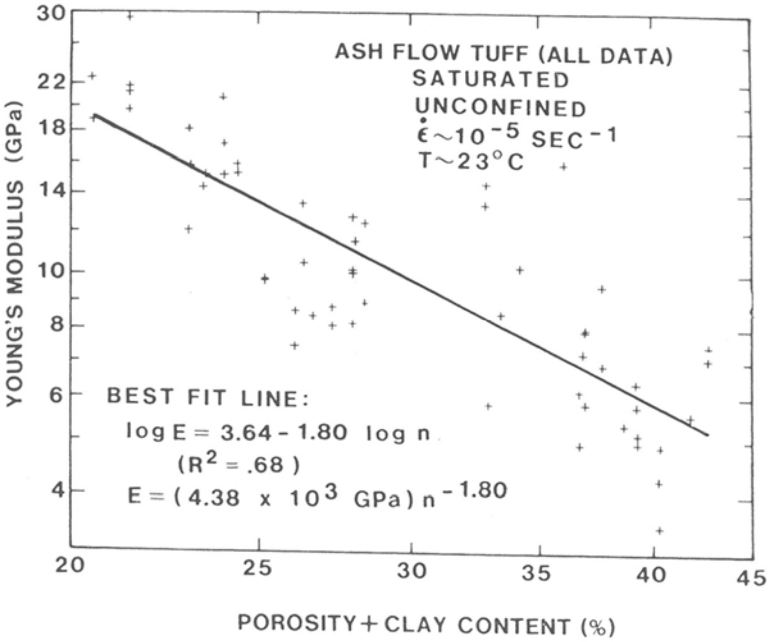

(a) Young's Modulus versus Functional Porosity

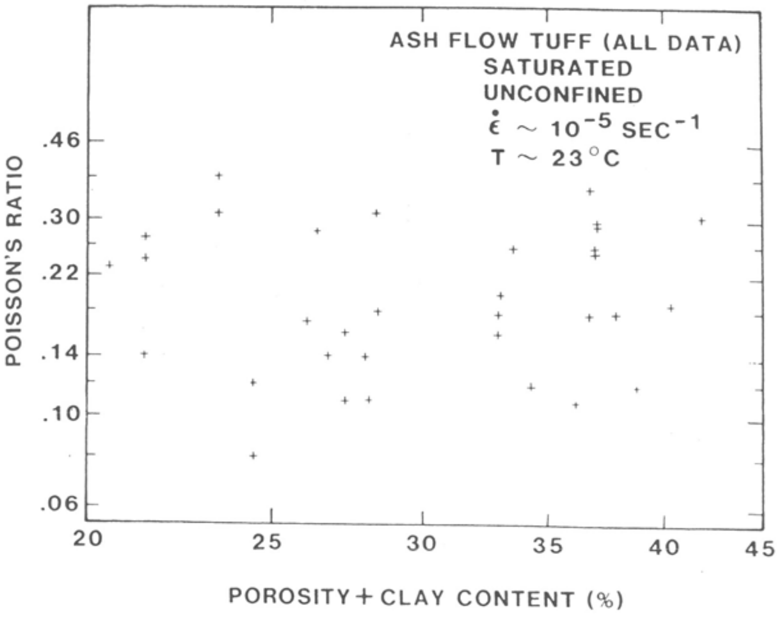

(b) Poisson's Ratio versus Functional Porosity

Figure 3.4 Variation of (a) Young's Modulus (E) and (b) Poisson's Ratio (ν) with Functional Porosity (n) of Saturated Samples from the Calico Hills, Bullfrog and Tram Tuffs at the Yucca Mountain (after Price, 1983)

Price and Bauer (1985) extended their study on porosity effects to include the data for the specimens from the Topopah Spring Tuff as shown in Figure 3.5. The properties of the test specimens ranged more widely with the additional data; n ranged from 10.3 to 40.9 %. The E data have been analyzed as a function of n as previously defined; however, a linear trend on a semi-log plot (instead of log-log plot as previously used) was determined as shown in Figure 3.5. The following best-fit line was found:

$$E = 85.5e^{-6.96n} \tag{3.2}$$

where, E is Young's modulus in GPa and n is functional porosity. In addition, one additional Yucca Mountain Tuff sample with an n-value of 63.8 % is included in the analysis to examine the fit for a higher porosity tuff. The E measured on this sample was about 20 % of the predicted E value (about 0.8 GPa smaller) indicating that the trend line may have limited in use.

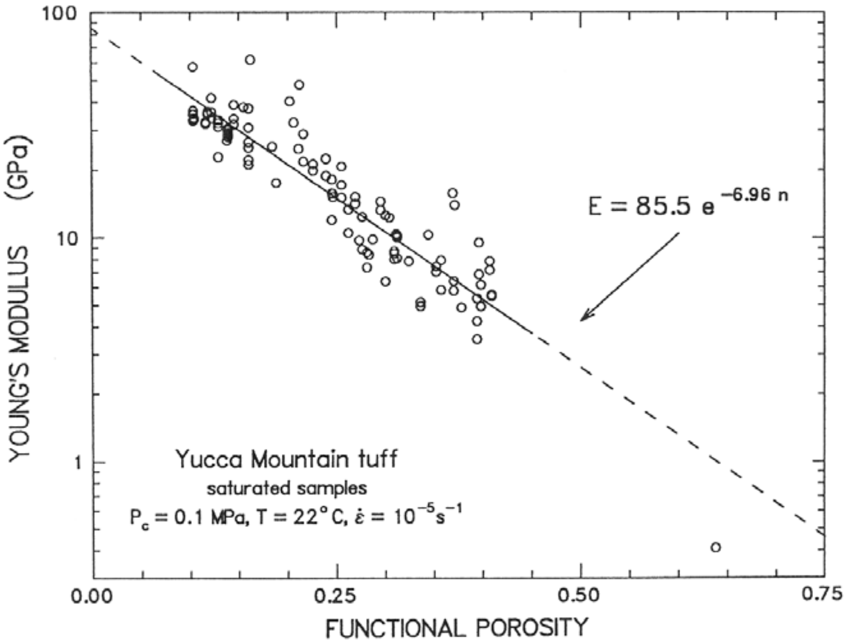

Figure 3.5 Variation of Young's Modulus (E) with Functional Porosity (n) of Saturated Nonlithophysal Specimens from the Calico Hills, Bullfrog, Tram, and the Topopah Spring Tuff at the Yucca Mountain Site (after Price and Bauer, 1985)

Price et al. (1994) reported data from a series of drill holes along the proposed alignment of the Exploratory Study Facilities (ESF) north ramp. The elastic properties on nonlithophysal samples from five of the drill holes are analyzed and compared with the previous trend line in Figure 3.6: the relationship between (a) E and (b) ν with porosity (or functional porosity). All tests were performed at the standard set of conditions for baseline testing. However, the specimen diameter in this case was 2 in. (5.1 cm). The trend found along the new data for E is approximately parallel to the trend from the earlier study (Price and Bauer, 1985) as seen in Figure 3.6a. The new best-fit line is:

$$E = 65.5e^{-7.12\phi} \tag{3.3}$$

where porosity (ϕ) is used instead of n. The new trend line represents the new data quite well, indicating porosity (ϕ) alone can be a good predictor of E. The new data covers the ϕ range from about 10 to 50 %. In this case, E ranged from about 0.3 to 42 GPa. A few data points that fell relatively far below the best-fit line were explained with the possibility of higher montmorillonite content in porous non-welded tuffs by the authors. Poisson's ratio (ν) exhibits little correlation with ϕ of the larger diameter (2 in. (5.1 cm)) specimens as shown in Figure 3.6b. The scatter in ν was quite significant, between about 0.01 to 0.49, with an average value of about 0.2.

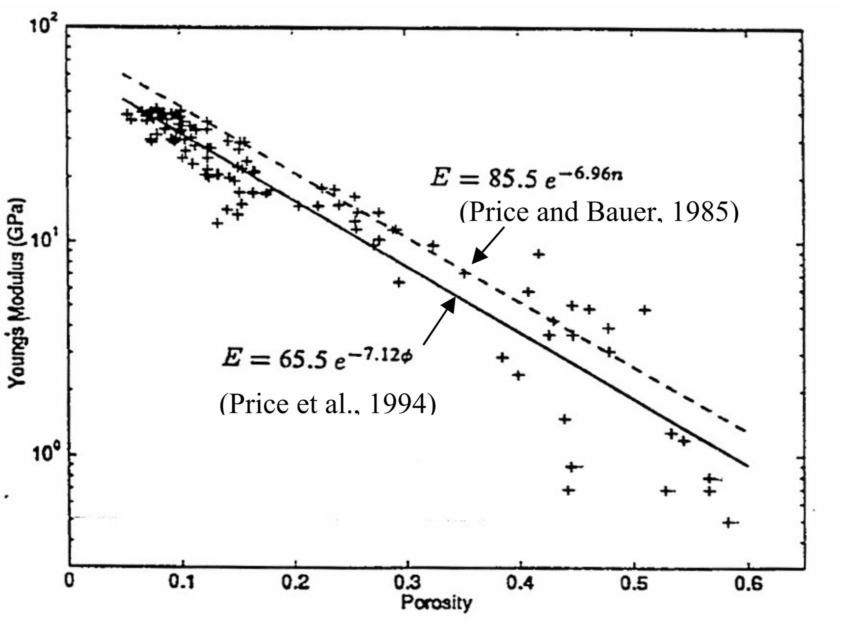

(a) Young's Modulus versus Porosity

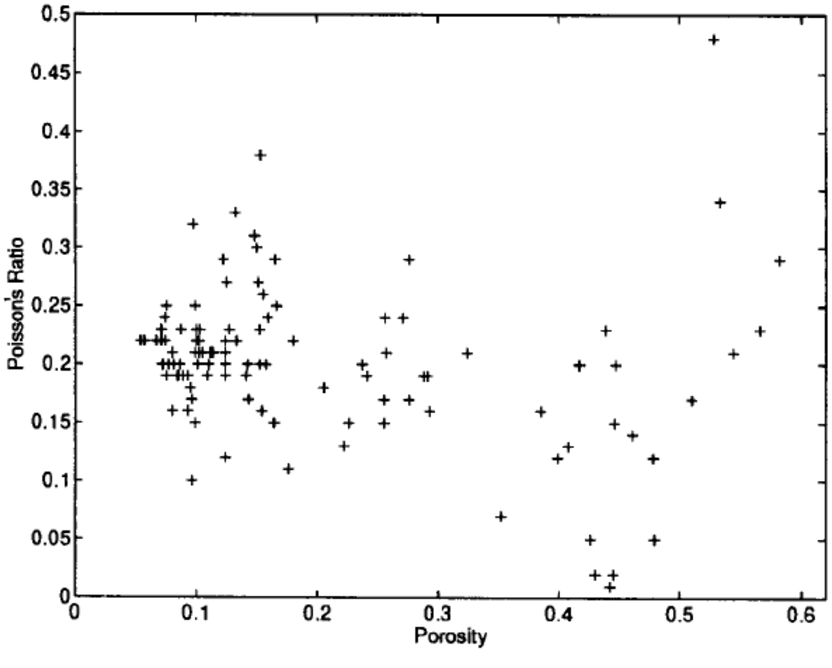

(b) Poisson's Ratio versus Porosity

Figure 3.6 Variation of (a) Young's Modulus (E) and (b) Poisson's Ratio (ν) with Porosity (ϕ) of Saturated Nonlithophysal Specimens from the Nonlithophysal Specimens from Drill Holes along the Explaratory Study Facilities (ESF) North Ramp (after Price et al., 1994)

3.4 FACTORS AFFECTING YOUNG'S MODULUS AND POISSON'S RATIO

The elastic properties (Young's modulus (E) and Poisson's ratio (ν)) discussed in Section 3.3 are influenced by many factors. These factors are directly related to physical characteristics of the test samples and various testing conditions. The physical characteristics of the test samples include bulk properties (e.g., porosity, density, grain density, lithophysal cavities, mineralogy), specimen size, and specimen anisotropy. Testing conditions include, for example, confining pressure, strain rate (loading frequency), saturation, and strain amplitude. The major findings for ignimbrites that are currently available and closely related to this research are summarized in this section.

3.4.1 Confining Pressure

In general, previous experimental studies have indicated that confining pressure has little to no effect on the elastic properties of welded tuffs like the Topopah Spring Tuff (e.g., Olson and Johnes (1980); Martin et al. (1992); Price et al. (1994); Martin (1997a)). However, a few of data sets for nonwelded tuffs (like the Bandelier Tuff) show relatively large pressure dependency on the properties (e.g., Price et al. (1994); Stokoe et al., (1993)).

Martin et al. (1992) reported small pressure dependence of the welded specimens from the Topopah Spring formation. A small specimen was cored from a larger core obtained from the Busted Butte outcrop. The axis of the larger core (Specimen 10/AE/78) was approximately normal to the bedding plane observed in the outcrop. Three specimens were prepared with the following orientations to the core axis for further study on the effect of anisotropy (discussed later): normal, parallel, and 45°. Each specimen had dimensions of about 1 in. (2.54 cm) in both diameter and length. The ultrasonic velocities of the compressional wave (V_P) and two shear waves (V_S) with orthogonal polarizations were measured on the cores. The wave velocities were measured at 8 effective confining pressures including the unconfined state (0, 2.5, 5.9, 7.5, 10, 15, 20 and 25 MPa (3.6 ksi)). Figure 3.7 shows the velocities measured on one of the small cores (Specimen 10/AE78B) that was cored normal to the fabric. The specimen was dry and its dry bulk density and porosity of the specimen were 2.33 g/cm^3 (145 lb/ft^3) and 0.075, respectively. As clearly seen in the figure, both compression and shear wave velocities do not change with pressure, and in turn, Poisson's ratio remains constant (about 0.21). The authors reported that this lack of influence of confining pressure on the elastic properties was observed again when the specimen was fully saturated; 0.37 % increase in V_P and average 0.34 % increase in both V_S values when pressure increased from zero to 20 MPa (2.9 ksi). In addition, the other two specimens cored in different orientation to the fabric exhibited nearly no pressure effects, but they show slight anisotropy especially for the specimen cored parallel to the fabric (about 6 % higher V_P and 3.5 % higher V_S on average than the specimen cored perpendicular to the fabric at the unconfined state and in the dry condition). Note the specimen cored at 45^o to the fabric exhibited the smaller difference in V_S (less than 1 %) and V_P (less than 0.4 %) at the unconfined state and in the dry condition compared with the specimen cored normal to fabric.

Price et al. (1994) reported a small effect of confining pressure based on the ultrasonic V_P and V_S measurements on a dry welded Tiva Canyon Tuff specimen as shown in Figure 3.8a. The specimen had dimensions of about 1 in. (2.54 cm) in both diameter and length. The welded tuff had a bulk density of 2.33 g/cm^3 (145 lb/ft^3) and a porosity of 0.019. This porosity is similarly small as determined for the Topopah Spring welded Tuff specimen tested by Martin et al. (1992). In addition, it is worth noting that these two specimens were stiff in terms of velocity measurements; for example, V_S values

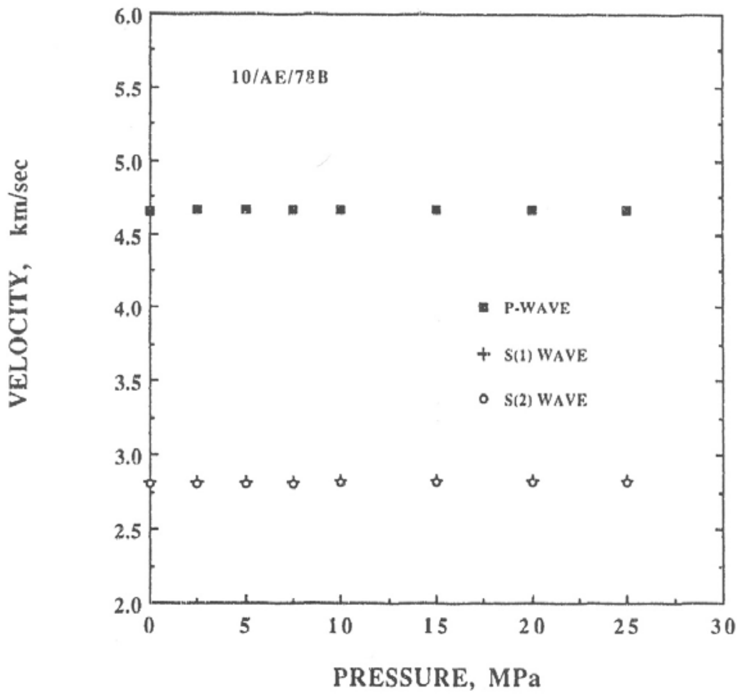

Figure 3.7 Variation of Elastic Wave Velocities in Compression (V_P) and Shear (V_S) of a Dry Welded Specimen from the Topopah Spring Tuff Collected from the Busted Butte Outcrop (after Martin et al., 1992)

of these tuff specimens were about 2.8 km/s (9186 ft/sec) and 2.9 km/s (9514 ft/sec) at the lowest confining pressures for the Topopah Spring Tuff specimen and Tiva Canyon Tuff specimen, respectively, when they were dry. Price et al. (1994) also tested a nonwelded vitric tuff specimen from the Paintbrush Group between the Tiva Canyon Tuff and Topopah Spring Tuff. This specimen had a low dry bulk density of 1.265 g/cm^3 (78.9 lb/ft^3) and a high porosity of 48.1 %. This low density tuff also had a lower stiffness in terms of velocity measurements compared with the two welded tuffs discussed above; for example, V_S of the dry nonwelded tuff was about 1.0 km/sec (3280 ft/sec) at the lowest confining pressure (1 MPa). This low value of V_S is only about 1/3 of the V_S values of the two welded tuffs. The wave velocities measured on this specimen exhibit some dependency on confining pressure as shown in Figure 3.8b. Especially, the V_P of the dry

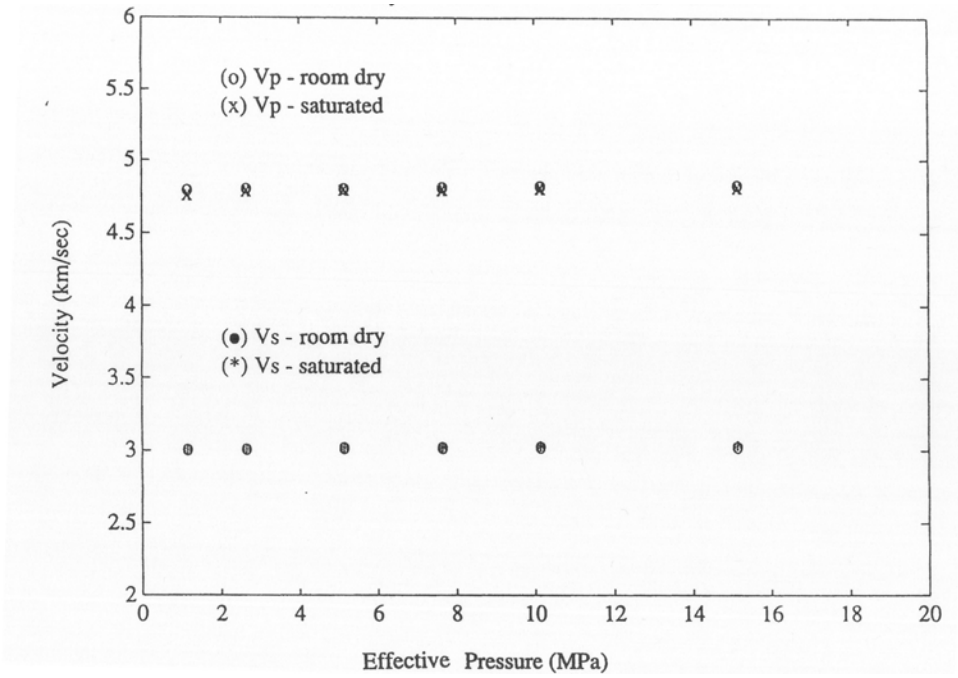

(a) Tiva Canyon Welded Tuff

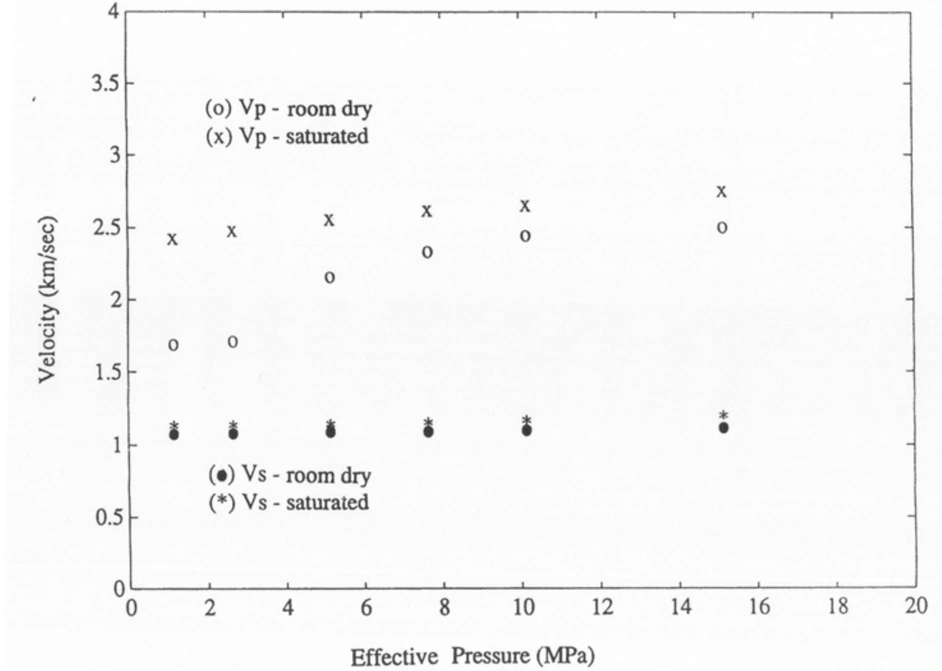

(b) Paintbrush Nonwelded Tuff

Figure 3.8 Variation of Elastic Wave Velocities of (a) Tiva Canyon Welded Tuff and (b) Paintbrush Nonwelded Tuff with Effective Confining Pressure (after Price et al., 1994) specimen increased by about 50 % when the confining pressure increased from 1 MPa (145 lb/in^2) to 15 MPa (2179 lb/in^2).

It is worth noting that all attenuation (Q^{-1}; Q=1/2D, where Q is a quality factor and D is material damping ratio) values in compression (Q_P^{-1}) and in shear (Q_S^{-1}) decrease with confining pressure as shown in Figures 3.9a and 3.9b for the stiff and soft specimens, respectively. The largest pressure dependency was observed on the Qp^{-1} of the saturated nonwelded Paintbrush tuff. The Q_P^{-1} drops by about 27 % from 0.313 to 0.228 when the effective confining pressure increases from 1 to 15 MPa (145 to 2176 psi) as shown in Figure 3.9a. It is also worth noting that the nonwelded tuff has the larger attenuation values (smaller Q) in compressional motion compared with the welded and stiffer tuff. The Q^{-1} value of the saturated nonwelded tuff is about 3.6 times higher than the Q^{-1} value of the saturated welded tuff at an effective confining pressure of 1 MPa (145 psi).

Three specimens from the Bandelier Tuff were tested at room temperature by Stokoe et al. (1993). Two specimens (Specimens HQ5 and HQ30) were from the Tshirege member (Qbt3U and Qbt2, respectively) and one specimen (Specimen HQ114) was from the Otowi member (Qbo) of the Bandelier Tuff. Specimens HQ5 and HQ30 were rock-like specimens with small water contents (0.15 and 0.12 %, respectively) and a relatively large dry density (91.9 and 115.9 lb/ft^3 (1.47 and 1.86 g/cm^3), respectively). Specimen HQ114 was soil-like with a water content of 24.0 % and a dry density of 82.3 lb/ft^3 (1.32 g/cm^3). The denser specimens exhibit larger small-strain shear moduli (G_{max} at shearing strain less than 0.0005 %) throughout entire test pressure range than the porous specimen as shown in Figure 3.10a. They also exhibited less pressure dependency. The specimen from the Qbo unit (Specimen HQ114) exhibited a pronounced

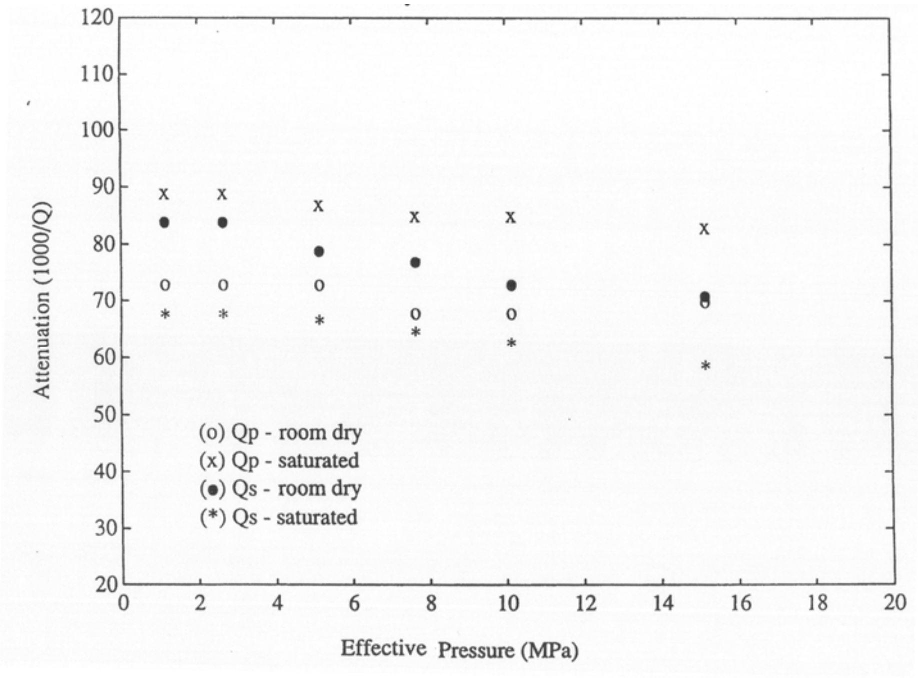

(a) Tiva Canyon Welded Tuff

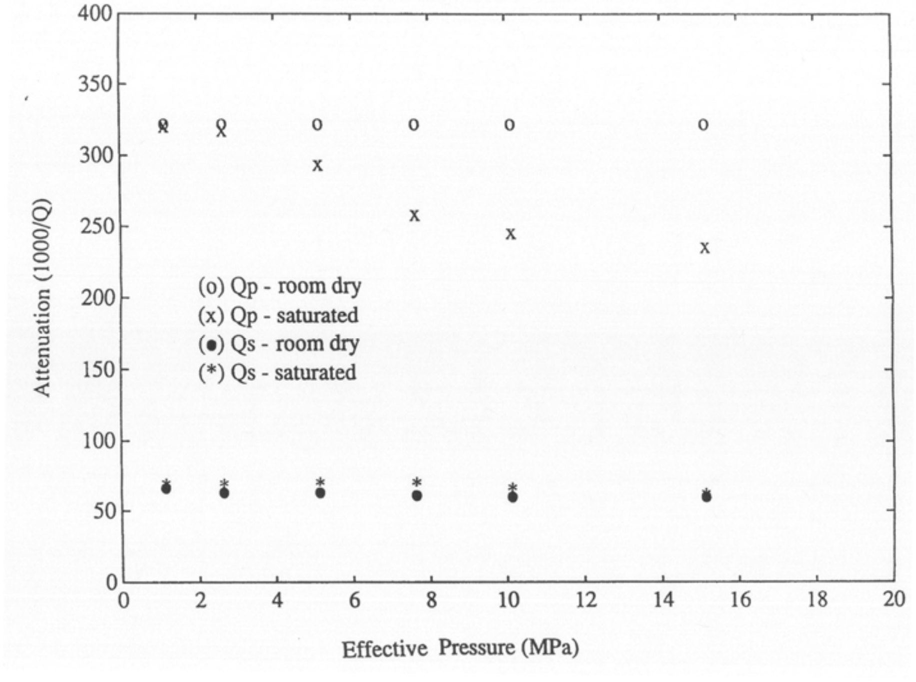

(b) Paintbrush Nonwelded Tuff

Figure 3.9 Variation of Attenuation of (a) Tiva Canyon Welded Tuff and (b) Paintbrush Nonwelded Tuff with Effective Confining Pressure (after Price et al., 1994)

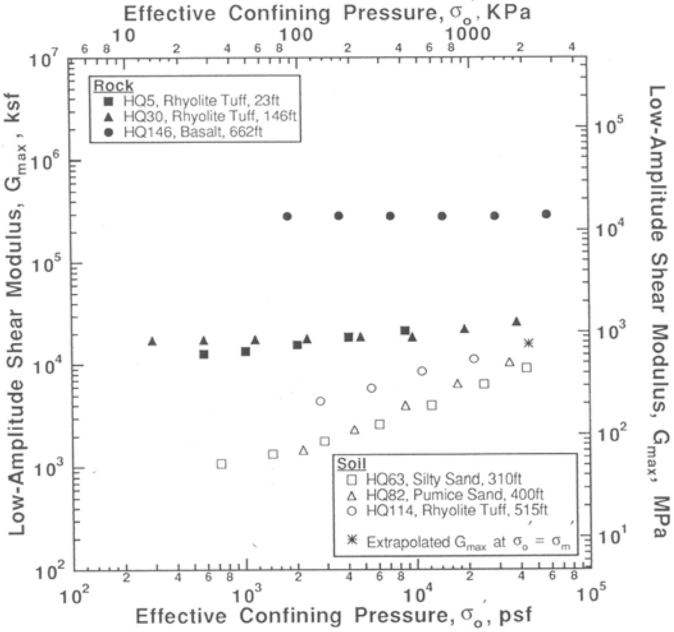

(a) Low-Amplitude Shear Modulus versus Confining Pressure

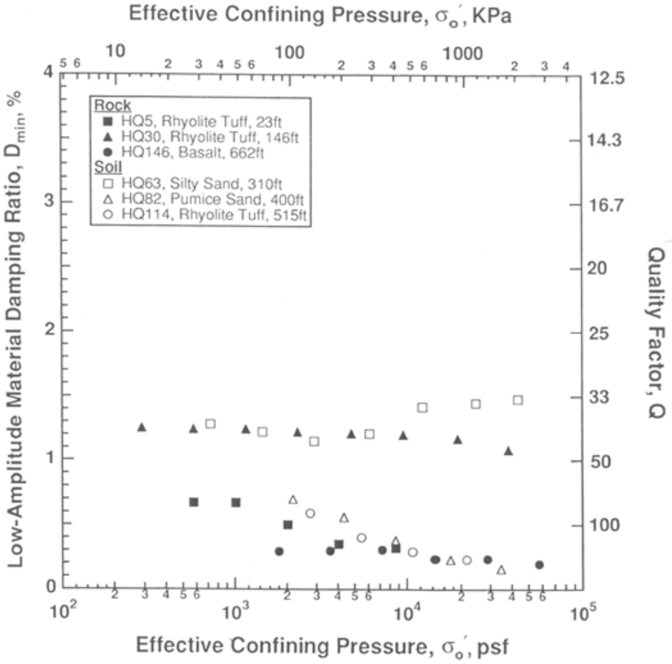

(b) Low-Amplitude Material Damping Ratio versus Confining Pressure

Figure 3.10 Variation of (a) Small-Strain Shear Modulus (G_{max}) and (b) Small-Strain Material Damping Ratio (D_{min}) of the Welded and Nonwelded Bandelier Tuff Specimens with Effective Confining Pressure (after Stokoe et al., 1993) pressure dependency on modulus like the sand specimens (Specimens HQ63 and HQ82). The shear modulus of Specimen HQ114 linearly increased on a log-log scale by about 2.4 times when the confining pressure increased from 0.1 to 1.0 MPa (0.21 to 21 ksf). As shown in Figure 3.10b, the small-strain material damping ratio (D_{min}) of Specimen HQ114 exhibits the largest change with pressure.

3.4.2 Strain Rate (or Loading Frequency)

Haupt et al. (1991) tested both dry and saturated welded tuff from the Topopah Spring formation with four different testing methods to cover wide ranges of peak strain amplitude (about 10^{-8} to 10^{-4}) and frequency (about 10^{-2} to 10^{6} Hz). Table 3.5 presents the four methods and corresponding frequency ranges. The ultrasonic velocity, resonant bar, and waveform inversion measurements utilize pulse propagation techniques with peak strain amplitudes on the order of 10^{-8} to 10^{-6}. Above this small-strain range, the effect of strain amplitude was studied with cyclic loading experiments at a single frequency of 0.1 Hz (discussed in later section). The dimensions of the test samples are also listed in Table 3.5. It should be noted that the cyclic loading tests were completed first and then the sample was subdivided into smaller specimens for the wave propagation measurements. The authors discussed the potential differences in characteristics between the cores due to the inherent heterogeneity in the tuff.

Figures 3.11a and 3.11b illustrate the results of the four different tests for Young's modulus (E) and the extensional attenuation (Q_E^{-1}), respectively. The moduli of the specimens in both dry and saturated conditions increase very slightly with frequency for frequencies between 0.01 and 50 Hz (by less than 2 % for the dry condition and by less than 6 % for the saturated condition). The saturated specimen exhibited a slightly larger increase in modulus at frequencies between 50 and 100 Hz, but still the increase was small in comparison with the range of variation in data collected with different techniques that mainly resulted from the sample heterogeneity. The authors discussed that the relatively small subsamples used for the wave propagation measurements probably contained different quantities of inhomogeneities (e.g., pores, lithics, vapor phase altered zones, pumice fragments, and lithophysae), producing scatter in measurements between different techniques. When the specimen was dry, its attenuation (Q_E^{-1}) is relatively low and independent of frequency below 50 Hz as shown in Figure 3.11b. When the specimen was saturated, Q_E^{-1} increased significantly above 10 Hz. The authors discussed that the inconsistent results between different testing methods were likely due to the sample heterogeneity in the samples with different sizes. These data were only used to compare the effect of saturation on attenuation characteristics of the tuff (discussed in the following section). The porosity of the tuff sample was about 7 %. All the tests were performed at the unconfined state and room temperature.

Table 3.5 Frequency Ranges for Four Test Methods and Dimensions of Welded Specimens from the Topopah Spring Formation (after Haupt et al., 1991)

Technique	Frequency	Length (mm)	Diameter (mm)
Cyclic Loading	0.01 - 19 Hz	210	55
Rosonant Bar	1 - 200 kHz	201	13
Waveform Inversion	1 - 200 kHz	40	15
Ultrasonic Velocity	700 kHz	40	55

The three Bandelier Tuff specimens discussed in the previous chapter were tested at various loading frequencies as shown in Figure 3.12. The tests were performed in the small-strain range (shearing strain equal to or less than 0.001 %) at or somewhat below

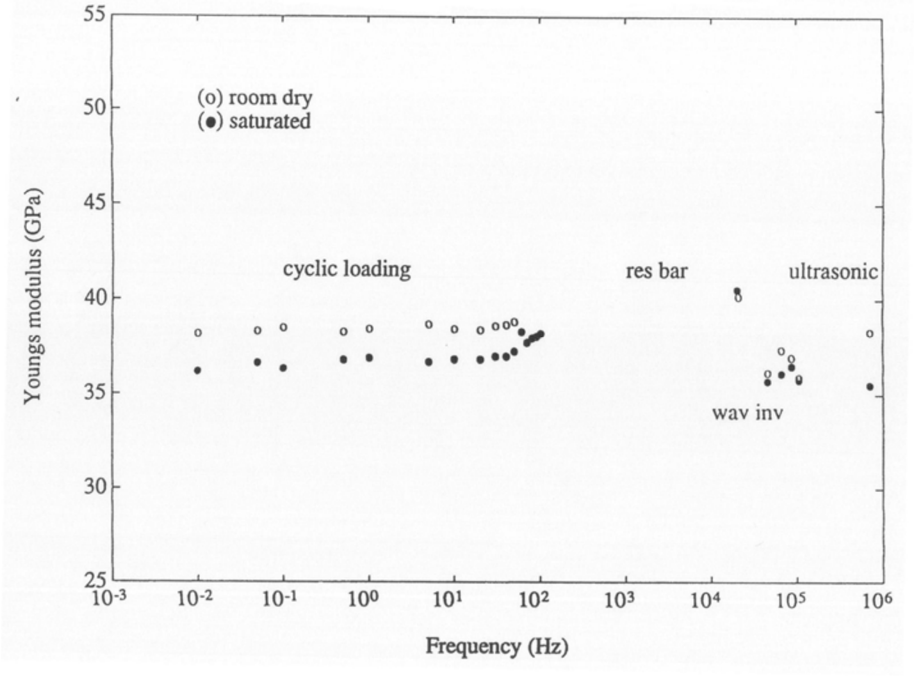

(a) Young's Modulus (E) versus Frequency (f)

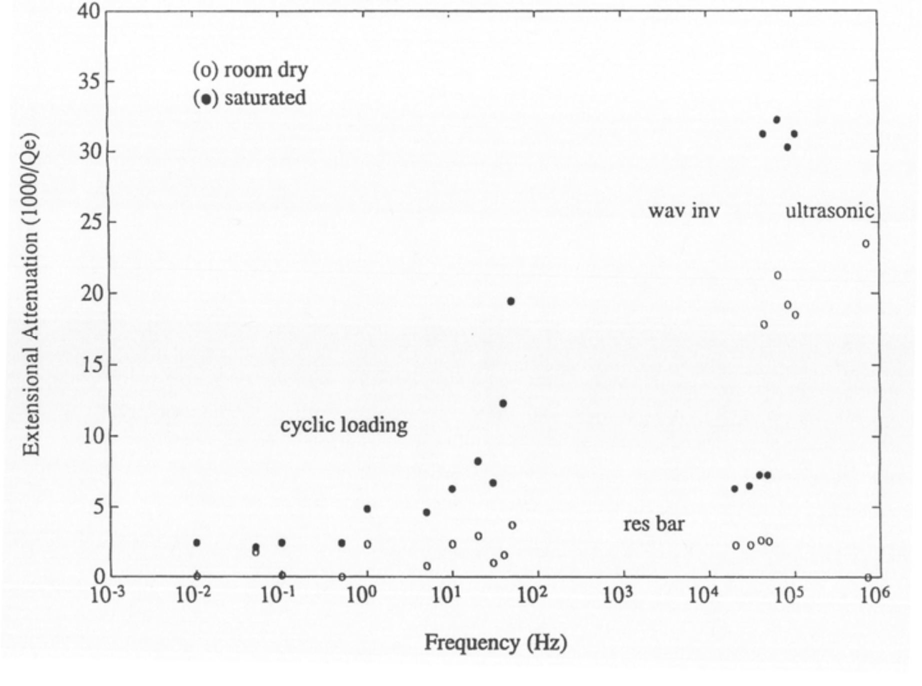

(b) Extensional Attenuation (Q_e^{-1}) versus Frequency (f)

Figure 3.11 Variation of (a) Young's Modulus (E) and (b) Extensional Attenuation (Q_E^{-1}) of the Welded Topopah Spring Tuff as Determined Four Different Methods (after Haupt et al., 1991)

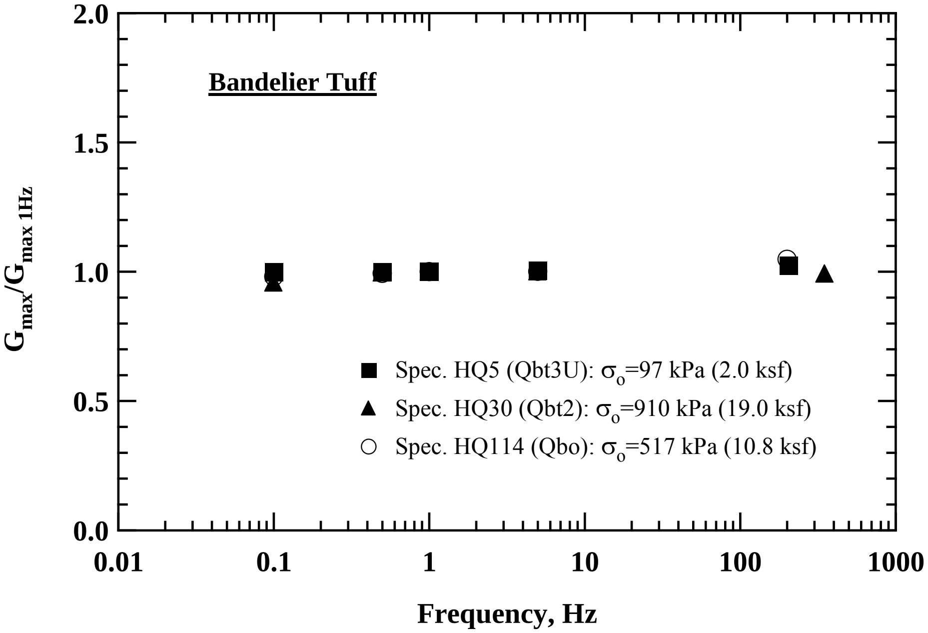

(a) Normalized G_{max} by G_{max} at 1 Hz versus Frequency

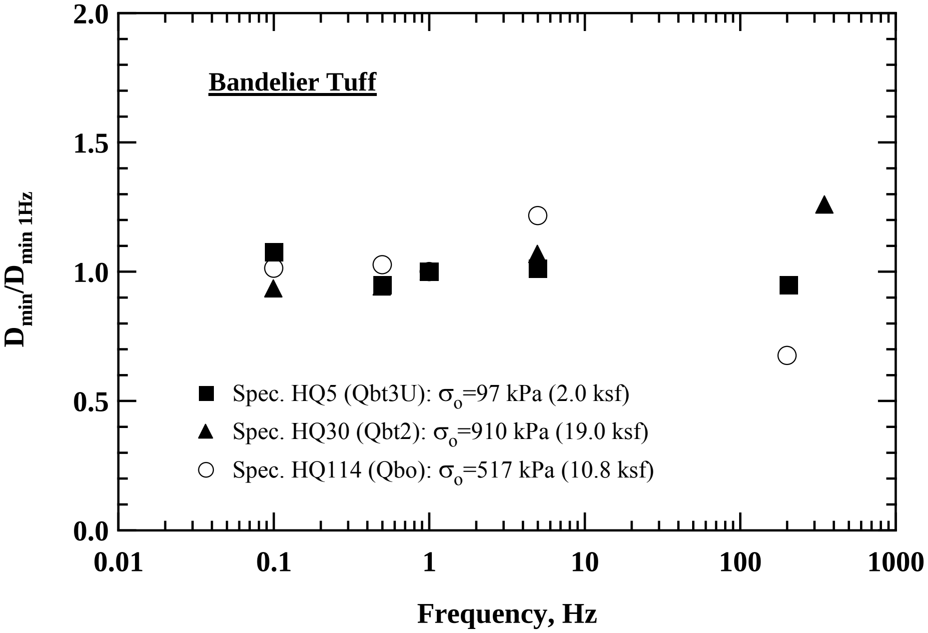

(b) Normalized D_{min} by D_{min} at 1 Hz versus Frequency

Figure 3.12 Variation of (a) Small-Strain Shear Modulus (G_{max}) and (b) Small-Strain Material Damping Ratio (D_{min}) of the Bandelier Tuff Specimens (Normalized with Measurements at 1 Hz) (after Stokoe et al., 1993) their estimated in-situ mean effective stresses, σ_m'. All measurements were normalized with the measured values at 1 Hz. There was no noticeable tend with frequency regardless of the specimen or test condition. The G_{max} values stayed almost constant as the loading frequency ranged between 0.1 to about 300 Hz. The D_{min} values varied somewhat at the highest frequency but no noticeable trend is shown, with the average result represented by frequency independent damping.

3.4.3 Saturation

Test results of Haupt et al. (1991) discussed in the previous section clearly show the effect of saturation on the elastic Young's modulus (E) and attenuation (Q_E^{-1}). In general, the dry tuff specimens exhibit somewhat larger E values than the saturated tuff specimens as shown in Figure 3.11a. However, the increases were not significant (less than 6 %). The effect of saturation on Q_E^{-1} is just the opposite to the effect on E; in other words, Q_E^{-1} increases when the specimens were saturated as shown in Figure 3.11b. The increases in Q_E^{-1} with saturation, with Q_E^{-1} values more than doubling in the 1 to 100 Hz range.

The influences of saturation on shear modulus and Poisson's ratio were studied in experiments performed on five welded tuffs from the Topopah Spring Tuff exposed on the Busted Butte outcrop (Martin et al., 1993). The porosities of the specimens were a bit larger than the porosities of the specimens tested by Haupt et al. (1991); but they were generally uniform (ranged from 0.090 to 0.108). As shown in Figure 3.13a, shear wave velocity (V_S) decreased by about 4 % on average when the specimens were saturated. This decrease in shear wave velocity corresponds to about 8.4 % decrease in shear modulus on average. On the other hand, the compressional wave velocity (V_P) values for all specimens remained almost constant. Therefore, Poisson's ratio calculated based on

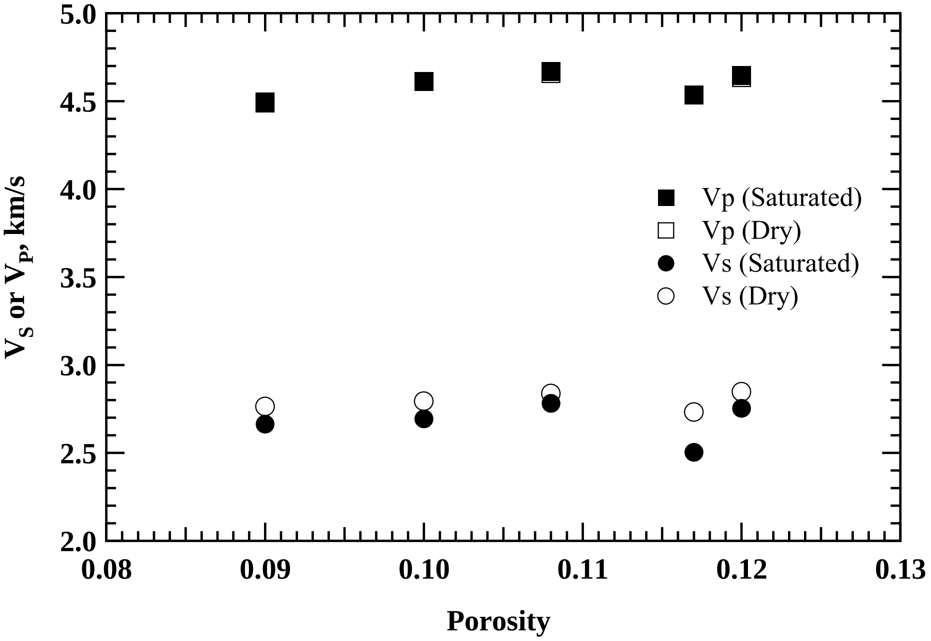

(a) Elastic Wave Velocities (V_S or V_P) versus Porosity (ϕ)

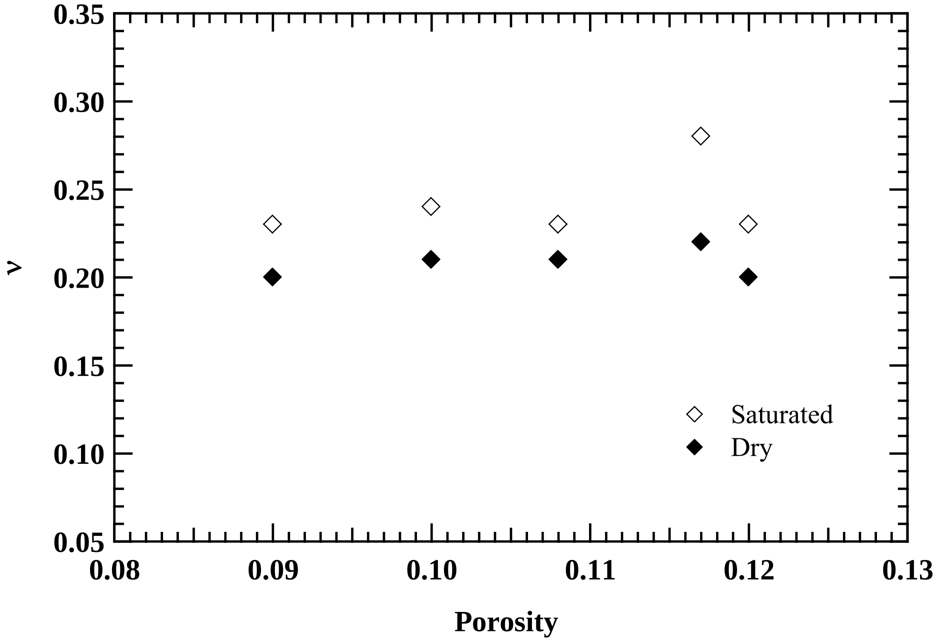

(b) Poisson's Ratio (ν) versus Porosity (ϕ)

Figure 3.13 Variation of (a) Elastic Wave Velocities (V_S and V_P) and (b) Poisson's Ratio (ν) of Five Welded Topopah Spring Tuff Specimens (after Martin et al., 1993) the compressional and shear wave velocities increased by about 16 % for the dry specimens as shown in Figure 3.13b.

Recently Price (2004) tested a total of 71 specimens cored from four large boulders taken from the southeast flank of Busted Butte. The large blocks were classified as the lower lithophysal zone of the Topopah Spring Tuff (Tptpll). Each boulder initially had dimensions of about 1 m by 0.75 m by 0.5 m with weighted about 3 kN (674 lb). A total of 120, right-circular cylindrical specimens were cored from the boulders with nominal diameters of 26, 51, 82 and 121 mm to study the effect of specimen size on mechanical properties of the tuffs (discussed in Section 3.4.4). All specimens have a length-to-diameter ratio (L:D) of about 2:1 (with a range of 1.9 to 2.1:1). It is important to note that 71 specimens with a diameter of 51 mm were tested under the following conditions: room dry, oven dry and saturated. All other testing conditions for the specimens were same; testing at a room temperature with a constant strain rate of 10^{-5} s^{-1} under the unconfined condition. Figure 3.14 illustrates the variation of the mean values of E and ν with sample diameter observed in the 71 specimens. The statistical variations (± 1 standard deviation) in these measurements are also shown in the figure. Although the variations are somewhat large, the trend of the mean values with specimen conditions are clearly shown in the figure; the mean value of E increases by about 4 % when the specimens went from room dry to saturated conditions and by about 8 % when the specimens went from oven dried to saturated conditions. As a result, the mean value of ν decreased by about 9 % when the specimens were from room dry to saturated conditions and by about 13 % when the specimens went from oven dried to saturated conditions. The author discussed that all four original large boulders had relatively little amount of lithophysae; less than a half dozen lithophysal cavities were evident in each boulder. Therefore, the measurements were not affected significantly by severe lithophysae.

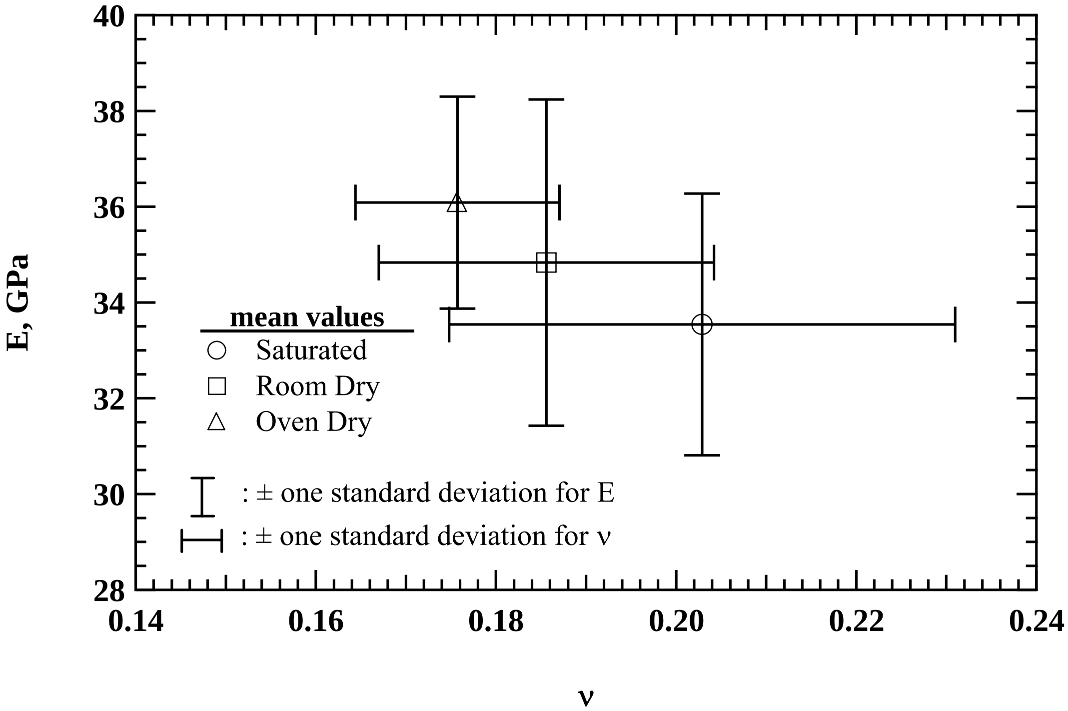

Figure 3.14 Variations of Young's Modulus (E) and Poisson's Ratio (ν) of Seventy-One Lithophysal Specimens from the Topopah Spring Tuff (Tptpll) with Different Degrees of Saturation (after Price, 2004)

3.4.4 Specimen Size

Price (1986) tested 34 nonlithophysal samples from the Topopah Spring Tuff (Tptpmn). The samples were collected from large boulders from Busted Butte, in the southwest corner of the NTS, southwest of Yucca Mountain. Cylindrical samples with five different diameters were tested: 25.4, 50.8, 82.6, 127.0 and 228.6 mm. All tests were performed at the baseline set of conditions. The E and ν values determined from uniaxial compression tests are shown in Figure 3.15. Neither property exhibited a dependency of sample size. The average E values for these five sample sizes ranged from 35.3 GPa to

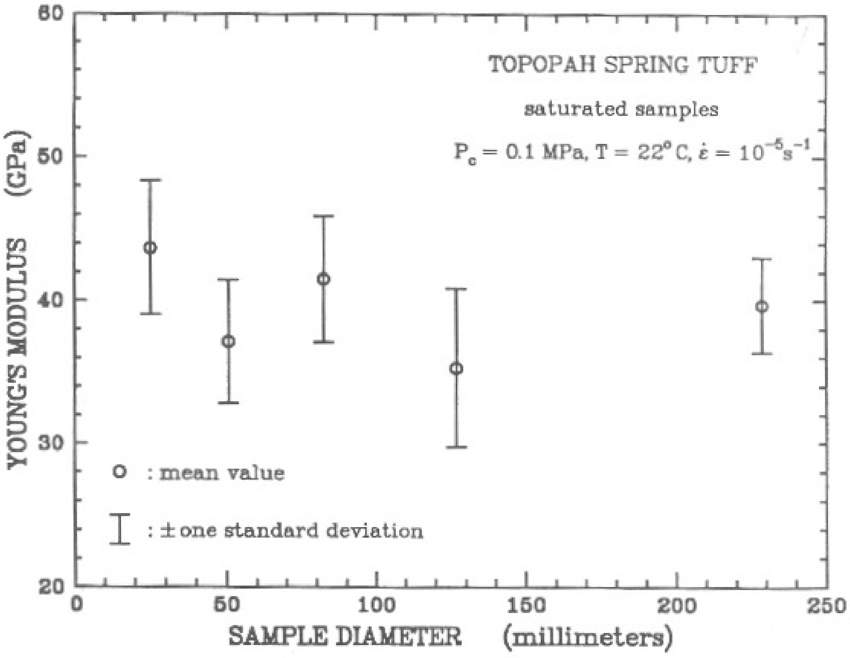

(a) Young's Modulus (E) vs Sample Diameter

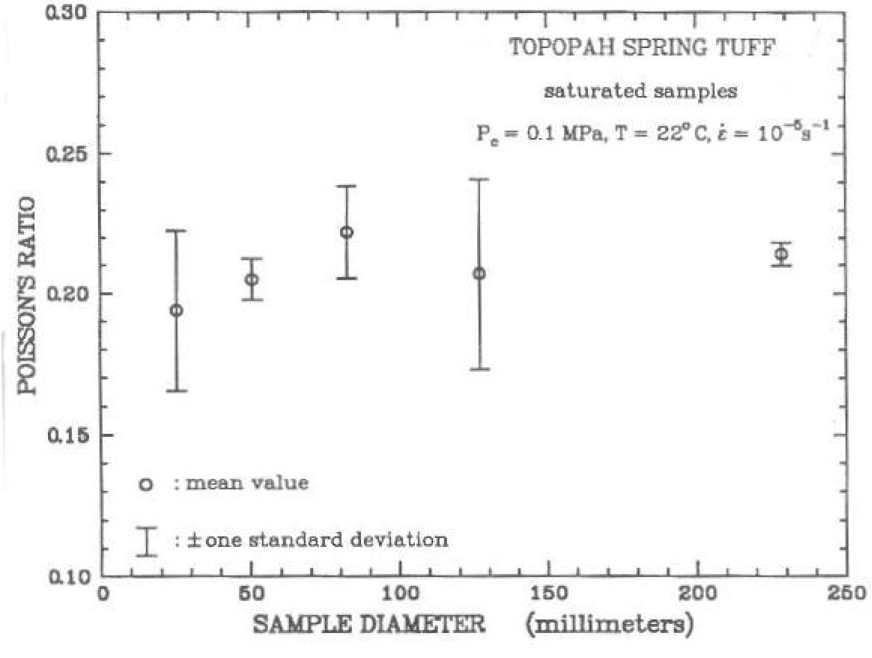

(b) Poisson's Ratio (ν) vs Sample Diameter

Figure 3.15 Variations of (a) Young's Modulus (E) and (b) Poisson's Ratio (ν) of Thirty-Four Nonlithophysal Specimens from the Topopah Spring Tuff, Tptpmn (after Price, 1986)

43.7 GPa and the average ν values ranged from 0.19 to 0.22. The standard deviation for the measurements with each diameter is also presented in the Figure 3.15.

More recently, Price (2004) tested 101 lithophysal specimens from the Topopah Spring Tuff (Tptpll). The nominal diameters of the specimens are 25, 51, 82 and 121 mm and an average L:D ratio of 2:1. All specimens were tested as follows: room dry under ambient pressure and temperature at a nominal strain rate of 10^{-5} s^{-1}. The E and ν values for these lithophysal specimens seem to be independent of sample size, as was found by Price (1986) for the nonlithophysal specimens. The average E values have a smaller span than before, ranging from 31.6 GPa to 35.9 GPa and the average ν values range from 0.17 to 0.19 as illustrated in Figure 3.16.

3.4.5 Strain Amplitude

Haupt et al. (1991) also studied the effect of strain amplitude on E and ν of a welded specimen from the Topopah Spring Tuff that was discussed in Sections 3.4.2 and 3.4.3. The specimen was tested at various axial strains ranging from about 2×10^{-4} % to 8×10^{-3} % by cyclic loading (hysteresis loop) technique. The values of E and D stayed constant within the strain range for both dry and saturated conditions as shown in Figure 3.17. Again, this rock was a welded tuff with low porosity (about 7%) having an E of 38 GPa at an axial strain amplitude of about 3×10^{-4} % when it was tested dry and unconfined. If ν is assumed to be in the range from 0.1 to 0.4, G will be from 13.6 to 17.3 GPa. This range in G values gives very high shear moduli compared with the three Bandelier Tuff specimens discussed in Section 3.4.1; the small-strain shear moduli of the

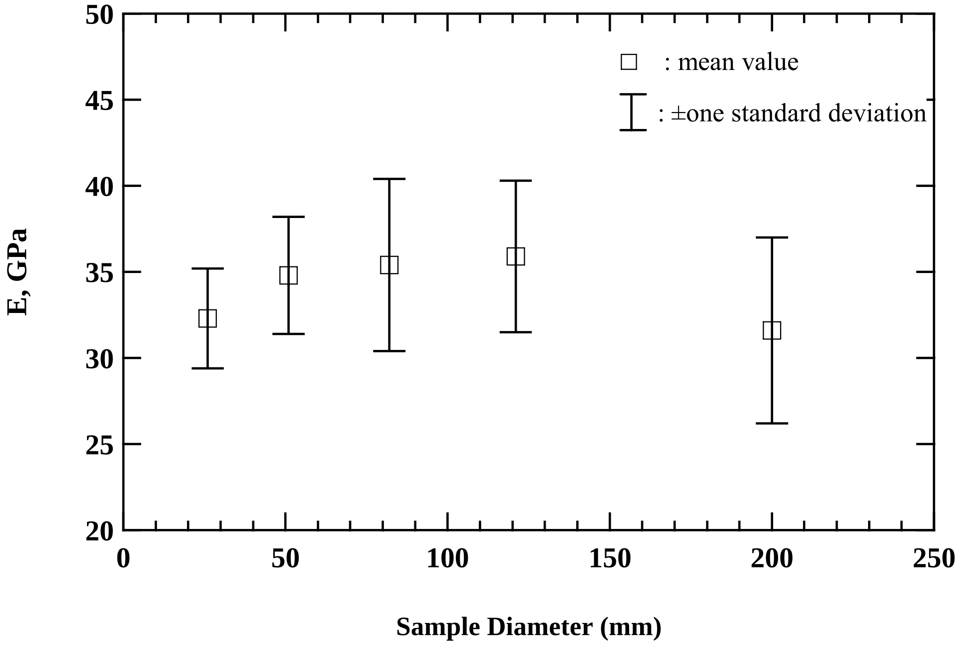

(a) Young’s Modulus (E) versus Sample Diameter

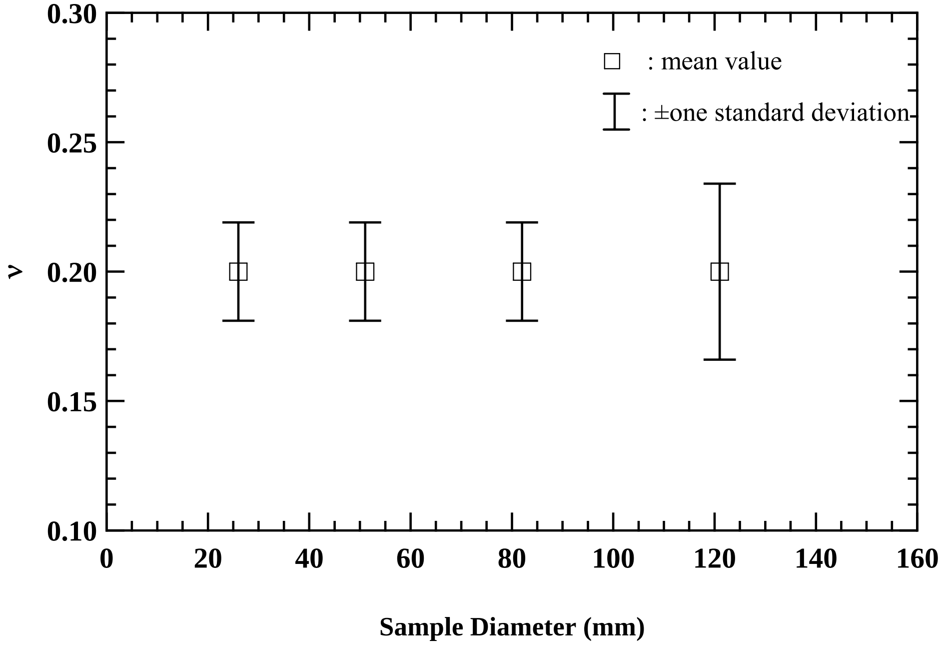

(b) Poisson’s Ratio (ν) versus Sample Diameter

Figure 3.16 Variations of (a) Young’s Modulus (E) and (b) Poisson’s Ratio (ν) of Seventy-One Lithophysal Specimens from the Topopah Spring Tuff, Tptpll (after Price, 2004)

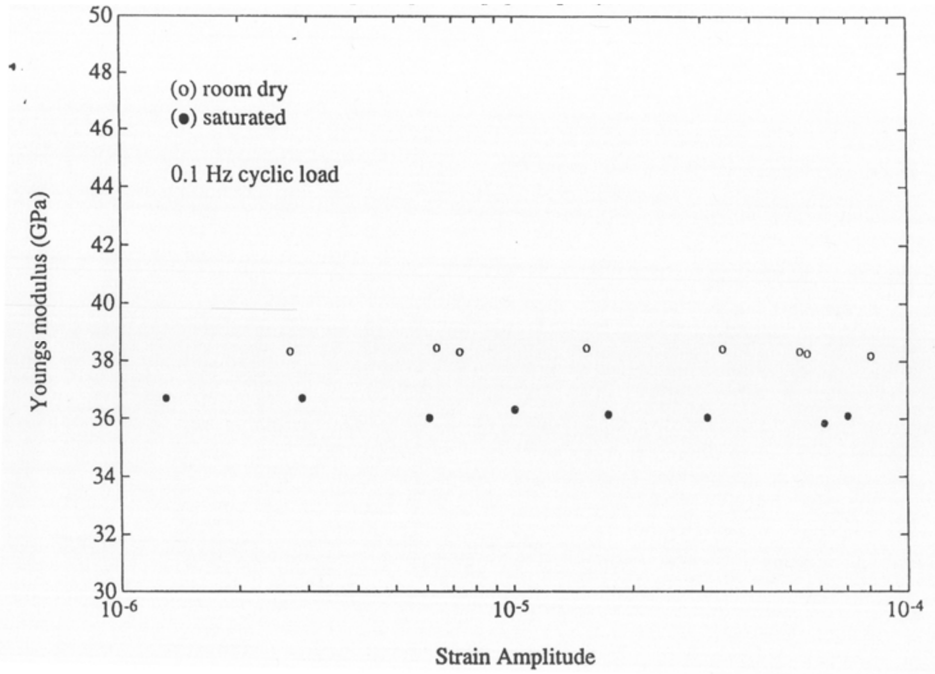

(a) Young's Modulus versus Strain Amplitude

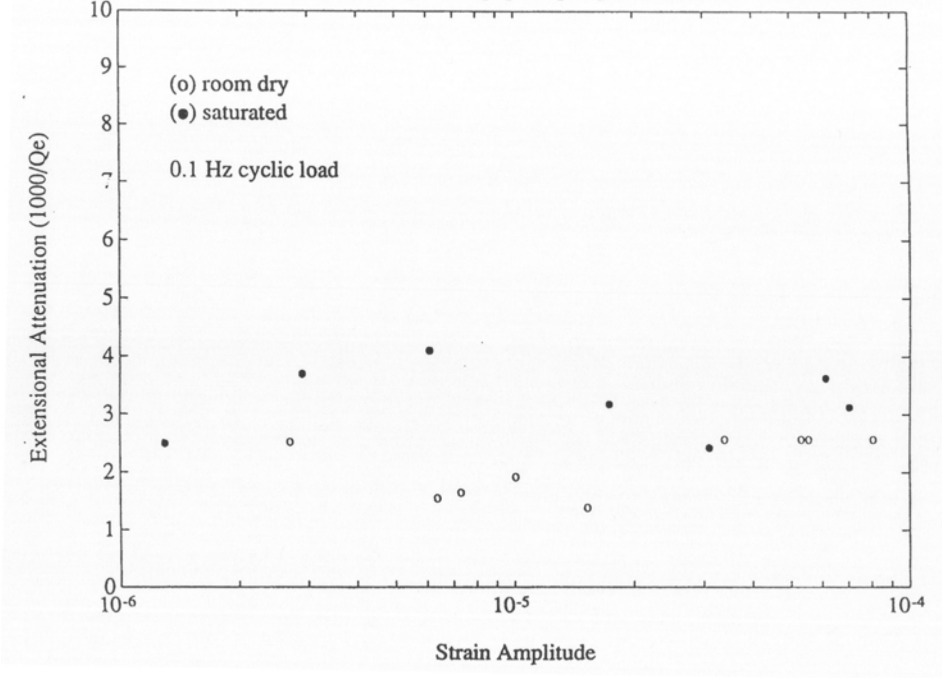

(b) Extensional Attenuation versus Strain Amplitude

Figure 3.17 Variations of (a) Young's Modulus (E) and (b) Extensional Attenuation (Q_e^{-1}) of Welded Topopah Spring Tuff Specimen (after Haupt et al., 1991)

Bandelier Tuff specimens ranged from 0.54 to 1.25 GPa at their highest test pressures. In addition, the damping ratio values of the Topopah Spring Tuff were about 0.1 % and 0.2 % for the dry and saturated conditions, respectively. These small values are indicative of very sound conditions of the specimens (few flaws such as cracks). The Topopah Spring welded tuff having a high modulus, a small material damping ratio and an independency of pressure on the properties is very similar to the Basalt specimen shown in Figure 3.18 (Specimen HQ146). The Basalt specimen had an average G_{max} of 13.7 GPa and an average D_{min} of 0.26 %, with very little variations in these values throughout the test pressure range (although this is not shown).

Figure 3.18 illustrates the nonlinear characteristics observed in the softer rocks from the Bandelier Tuff at or somewhat below the estimated in-situ mean effective stress, σ_m'. The shear modulus (G) normalized with G_{max} and material damping ratio (D) at various shearing strain (γ) amplitudes are presented in the Figure 3-18. The mean trend line with upper and lower bound curves for sands proposed by Seed and Idriss (1970) are presented for comparison purposes. The relationships between the normalized shear modulus (G/G_{max}) and log γ for the soft rocks follow the upper bound curve (Stokoe et al., 1993) as shown in Figure 3.18a. On the other hand, the relationships between D and log γ make a somewhat wider range from around the upper bound for sands at small strains to below the lower bound for sands at large strains. All measurements were obtained from the resonant column (RC) test at frequencies that ranged from about 190 to 357 Hz. The authors discussed that the frequency effects on these nonlinear characteristics were not significant. It is worth noting that the sound and stiff basalt specimen exhibited no effect of strain amplitude on both modulus and damping over the range of strains tested (equal to and less than 10^{-2} %).

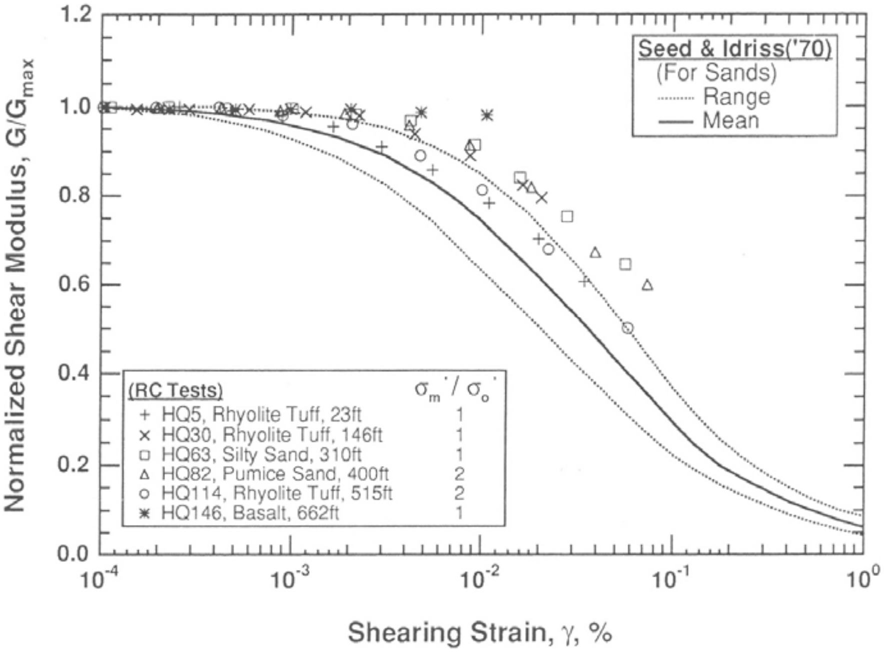

(a) Normalized Shear Modulus versus Shearing Strain

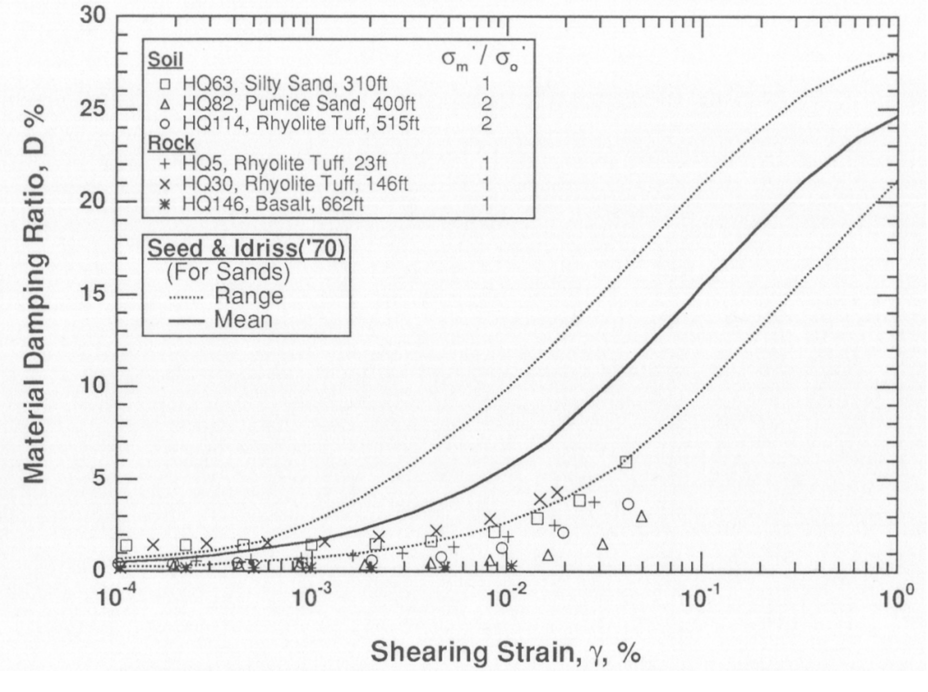

(b) Material Damping Ratio versus Shearing Strain

Figure 3.18 Variations of (a) Normalized Shear Modulus (G/G_{max}) and (b) Material Damping Ratio (D) of Specimens from the Bandelier Tuff (after Stokoe et al., 1993)

Price et al. (1986) reported that the axial strain amplitude at failure, $(\varepsilon_{ax})_u$, is related to sample size of the nonlithophysal tuffs (Tptpmn) from the Topopah Spring Tuff. As the diameter of the specimen increases, the failure strain decreases as illustrated in Figure 3.19. The authors argued that the trend was to be expected because the specimen was essentially linear elastic until they failed and their moduli were not affected by sample size while strength and sample size were inversely related. Figure 3.19 presents the recent findings for the specimen size effect on the lithophysal tuffs from the Topopah Spring Tuff studied by Price (2004). The same trend ($(\varepsilon_{ax})_u$ decreases with increase in sample size) was observed. It is interesting to note that the nonlithophysal and lithophysal specimens had very similar average E values when their sizes were big (about 229 mm and 200 mm, respectively) whereas the average E for lithophysal specimens was about 50 % higher than the average E for nonlithophysal specimens for their smallest sizes (25 mm and 26 mm, respectively). The author discussed that the higher E values are attributed to the difference in saturation states between the two sets of samples All the lithophysal specimens tested in 2004 were dry at room temperature, while all the nonlithophysal specimens tested in 1986 were fully saturated with water. The ultimate strengths of the room dry lithophysal specimens were also higher than the saturated nonlithophysal specimens.

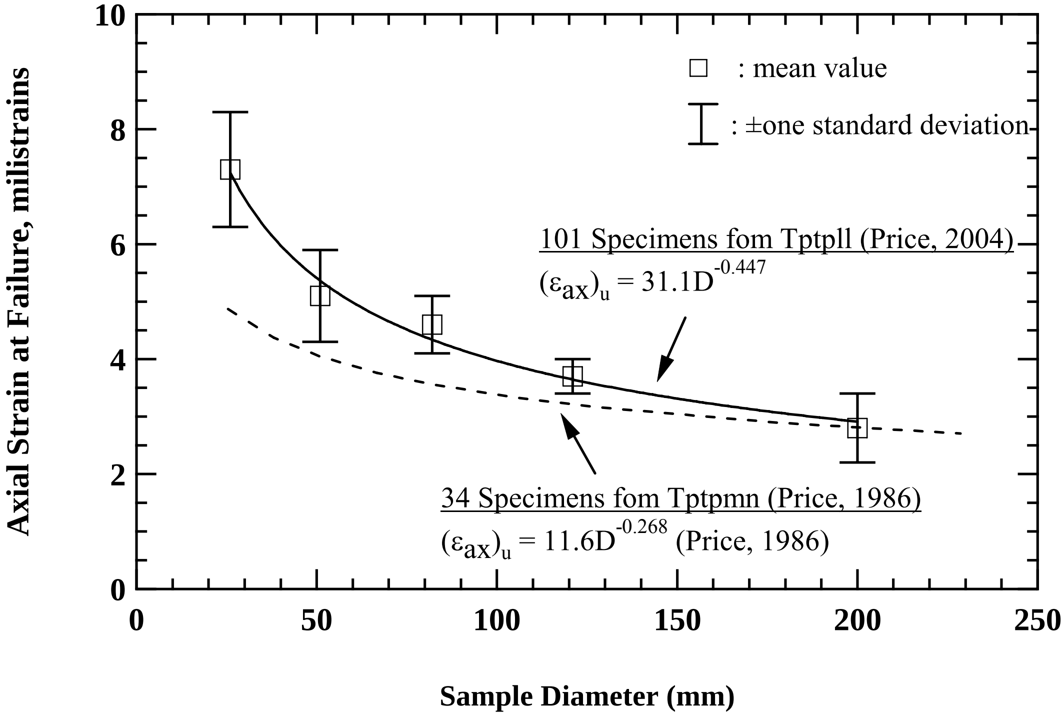

Figure 3.19 Variations of Axial Strain at Failure ($(\varepsilon_{ax})_u$) with Sample Diameter for the Specimens of the Topopah Spring Tuff (after Price, 1986; Price 2004)

3.5 SUMMARY

Published literature discussing the geologic characteristics of pyroclastic deposit and mechanical properties of its major component (ash-flow tuffs) are presented in this chapter. The classification schemes for the deposit in terms of welding intensity and relating the geologic and/or physical properties proposed by various researchers are summarized. The variation of E (or shear modulus, G), ν, and their correlations with porosity are then discussed. Finally, the factors that affect the mechanical properties of specimens with various degrees of welding and lithostratigraphic features are discussed. The factors include confining pressure, strain rate, saturation, and strain amplitude.

Chapter 4

Laboratory Test Equipment and Test Program

4.1 INTRODUCTION

Two different test devices were used in this research: (1) the combined resonant column (RC) and torsional shear (TS) device (generally denoted as RCTS device), and (2) the unconfined, free-free, resonant column (URC) device. Various test parameters can be controlled when evaluating the dynamic properties in shear of intact and/or reconstituted soil or rock specimens with the RCTS device. Most importantly, the effects of confining pressure, strain amplitude, and excitation frequency can be studied with the RCTS device. With the URC device, both compression and shear modes can be studied. However, all testing is performed at the unconfined state and only at small strains. By using both devices, studies of the linear and nonlinear dynamic properties of various types of tuff were performed in this study.

The equipment and the results of parametric studies with the equipment have been discussed by Stokoe et al. (1994a) and Stokoe et al. (1999). The RCTS equipment is of the fixed-free type, with the bottom of the specimen fixed and torsional excitation applied to the top. The interaction between coils and magnets generates harmonic torsional excitation at various amplitudes and frequencies. This excitational force is transferred to the soil column (right cylindrical specimen) through the drive plate and top cap. The displacement and acceleration of the motion due to the force are recorded with proximetors for the TS test and with an accelerometer for the RC test as illustrated in Figure 4.1. The equipment has two important attributes. First, both resonant column (RC) and torsional shear (TS) tests can be performed with the same piece of equipment. Switching from one type of test to the other is simply done outside the confining chamber by changing: (1) the input excitation frequency used to drive the specimen, and (2) the motion monitoring devices used to record the specimen response. As a result, variability due to testing different specimens is eliminated so that results from both types of tests can be compared effectively. Second, the loading frequency in the torsional shear test can be easily changed from 0.1 to about 5 Hz (generally lower than 10 Hz). Therefore, the effect of frequency and number of loading cycles on the deformational characteristics in shear (G and D) of intact specimens can be conveniently investigated.

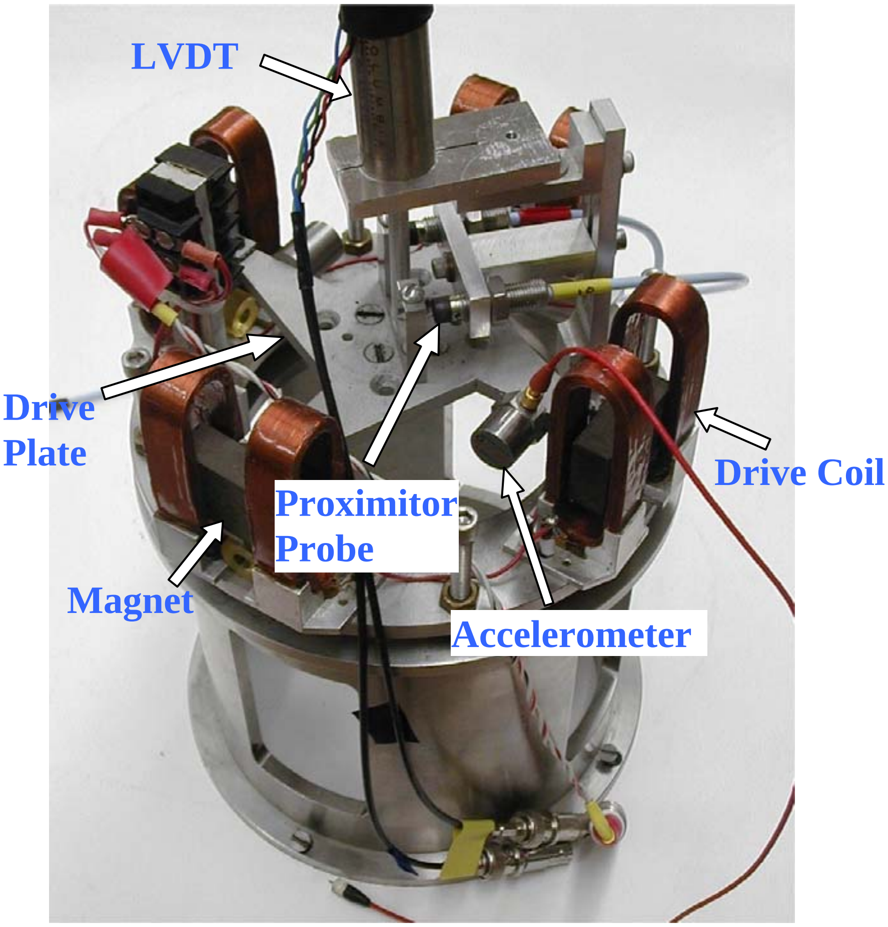

Figure 4.1 Photograph of Combined Resonant Column (RC) and Torsional Shear (TS) Device (Confining Chamber not Shown)

Figure 4.2 shows photographs of an unconfined, free-free, resonant column (URC) test set-up used to evaluate the stiffnesses and material damping ratios of soil and rock specimens at small strains. The measurements in both shear and compression can be performed on the same specimen by changing the orientation of the sensors (accelerometers) and the seismic source. These measurements in both motions provide valuable comparisons with measurements from the combined Resonant Column and Torsional Shear (RCTS) tests and from filed seismic measurements by tests such as the Spectral Analysis of Surface Waves (SASW), crosshole, downhole, and P-S logging tests. The simplicity of the URC set-up eliminates potential compliance problems such as fixity of the bottom platen in a fixed-free configuration and equipment-induced damping in a torsional electrical motor (Stokoe et al., 1994b). Moreover, the changes in properties due to coring and trimming processes or inherent inhomogeneity of test specimens can be studied with URC device.

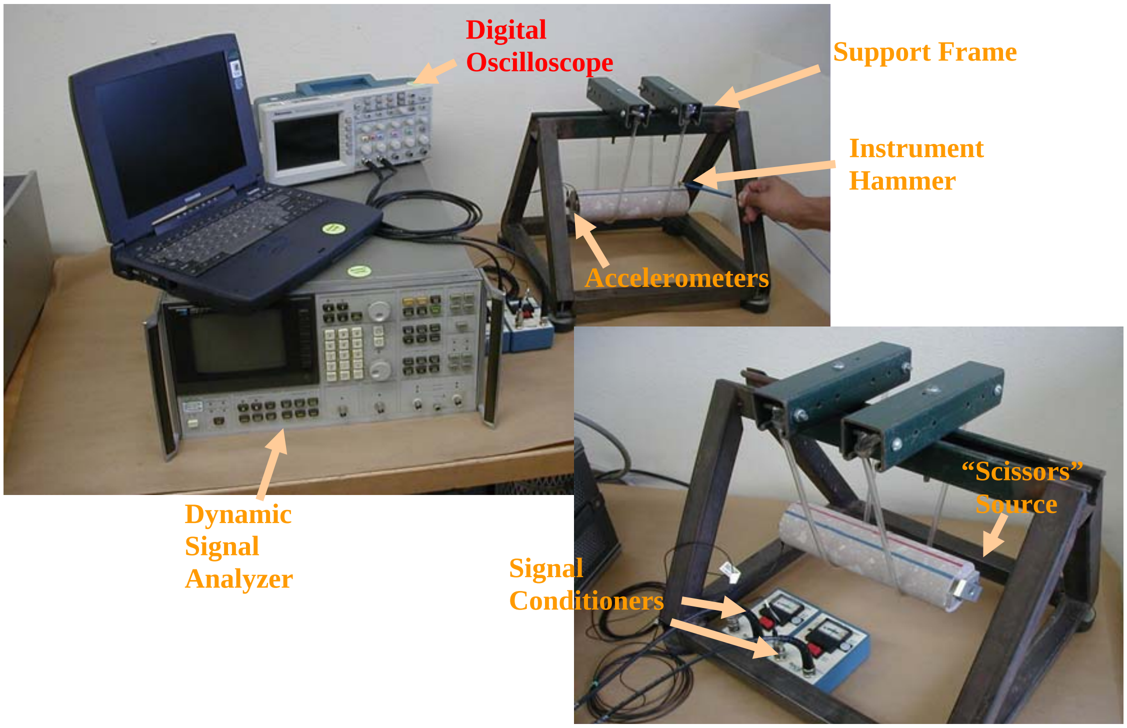

Figure 4.2 Photograph of Unconfined, Free-Free, Resonant Column (URC) Set-Up

The basic operational principles of the RCTS and URC tests are described in this section followed by testing programs on the intact ignimbrite specimens for this research (Sections in 4.2 and 4.3, respectively). Note that the new large RC device recently developed to invest the large-strain range with larger specimens is introduced and described in Chapter 5.

4.2 TESTING WITH THE RCTS DEVICE

4.2.1 Brief Background on RCTS Measurements

Laboratory determination of dynamic material properties employs combined resonant column and torsional shear (RCTS) testing. The RCTS apparatus can be idealized as a fixed-free system as shown in Figure 4.3. The bottom end of the specimen is fixed against rotation at the base pedestal, and the top end of the specimen is connected to the driving system. The driving system can rotate freely to excite the specimen in cyclic torsion.

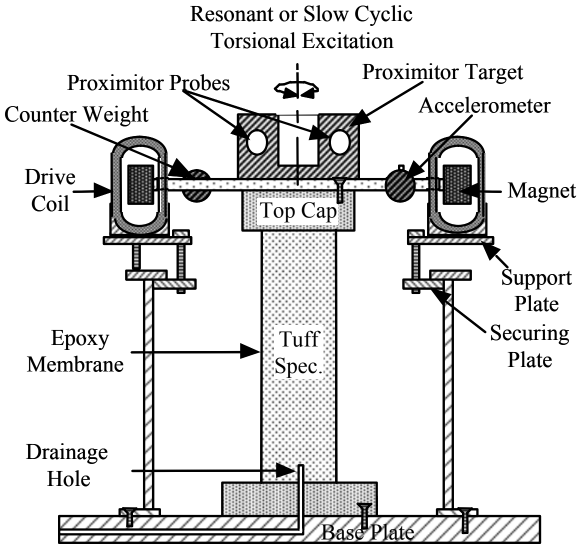

Note: confining chamber not shown

Figure 4.3 Simplified Diagram of a Combined Resonant Column (RC) and Torsional Shear (TS) Device (after Stokoe et al., 1999)

The basic operational principle of the fixed-free resonant column (RC) test is to vibrate the cylindrical specimen in first-mode torsional motion. Harmonic torsional excitation is applied to the top of the specimen over a range in frequencies, and the variation of the acceleration amplitude of the specimen with frequency is obtained (frequency response curve) as shown in Figure 4.4. Once the frequency response curve at the first-mode resonance is established, shear-wave velocity, shear modulus, and shearing strain are calculated using the resonant frequency and amplitude of motion. These calculations are based on the equipment characteristics and specimen size using one-dimensional wave propagation theory. Material damping ratio is determined either from the width of the frequency response curve (half-power bandwidth method) or from the free-vibration decay curve as illustrated in Figures 4.5 and 4.6, respectively.

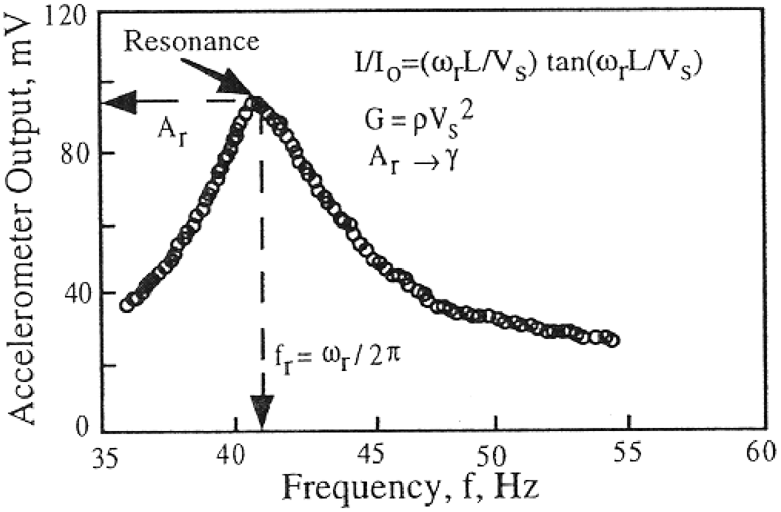

Notes:
I = mass polar moment of inertia of specimen,
I_o = mass polar moment of inertia of drive plate,
ω_r = circular resonant frequency,
L = height of specimen,
V_S = shear wave velocity
G = shear modulus,
ρ = density of specimen,
A_r = peak amplitude of motion at resonance, and
γ = shearing strain

Figure 4.4 Frequency Response Curve Determined in the Resonant Column (RC) Test (after Stokoe et al., 1999)

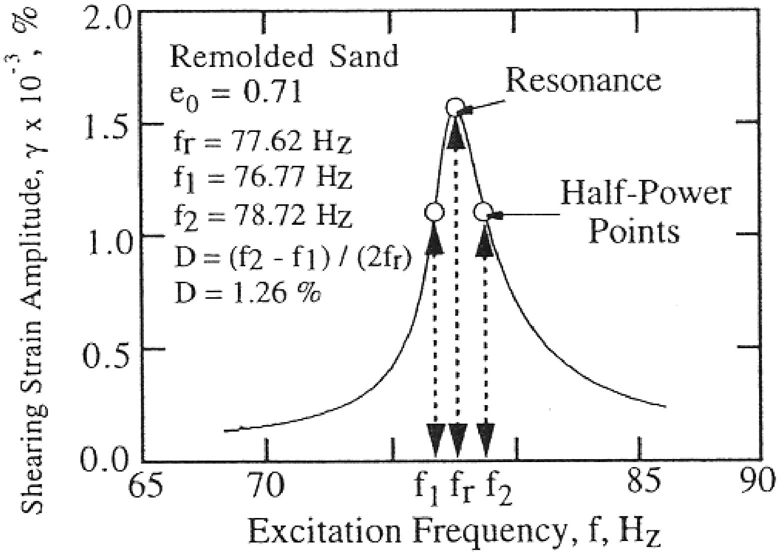

Figure 4.5 Material Damping Ratio as Determined from Half-Power Bandwidth Method in the Resonant Column (RC) Test (after Stokoe et al., 1999)

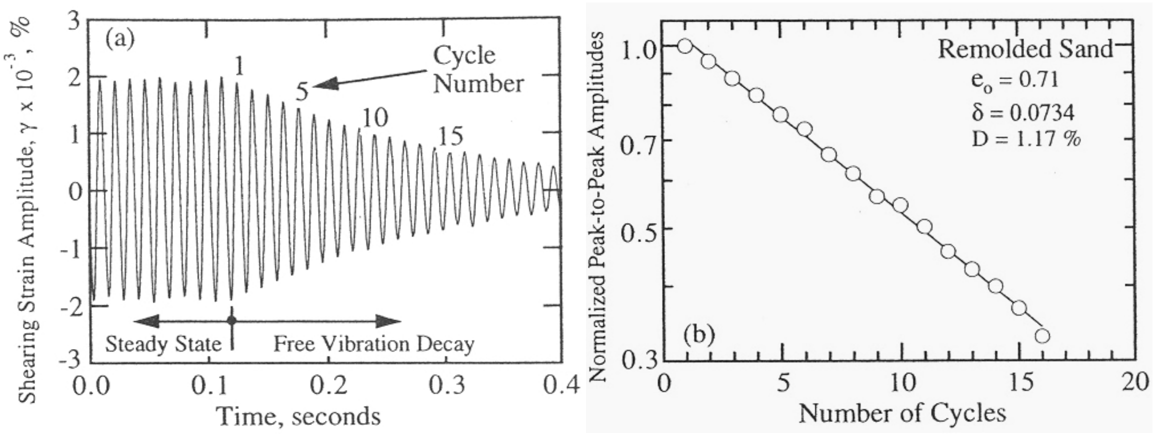

(a) Free Vibration Decay Curve (b) Normalized Peak-to-Peak Amplitude

Figure 4.6 (a) Free-Vibration Decay Curve and (b) Logarithmic Decrements of Normalized Peak-to-Peak Amplitude Determined in the Resonant Column (RC) Test (after Stokoe et al., 1999)

The torsional shear (TS) test is another method to determine shear modulus and material damping ratio. The same RCTS equipment is used for the TS test but its operation is different. A cyclic torsional force with a given frequency, generally below 10 Hz, is applied at the top of the specimen. Instead of determining the resonant frequency, the stress-strain hysteresis loop is determined from measuring the torque-twist response of the specimen. Proximitors are used to measure the angle of twist while the voltage applied to the coil is calibrated to yield torque. Shear modulus is calculated from the slope of a line through the end points of the hysteresis loop, and material damping ratio is obtained from the area of the hysteresis loop as illustrated in Figure 4.7.

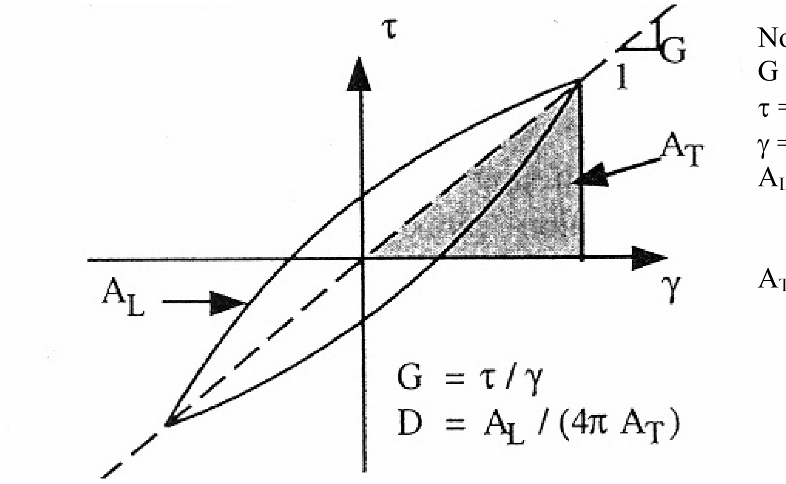

Notes:
G = shear modulus
τ = shear stress
γ = shearing strain
A_L = Area of the hysteresis loop (energy dissipated in one cycle of oscillation), and
A_T = Area of the shadowed triangle (strain energy stored in the system at maximum displacement).

Figure 4.7 Hysteresis Loop Determined from the Torsional Shear (TS) Test (after Stokoe et al., 1999)

4.2.2 Stage Testing with the RCTS Device

Tests at several confinement stages and strain levels, called stage testing, are typically performed with the RCTS device. First, each rock specimen is inspected for defects and a URC test is performed before any RCTS testing was performed. The dimensions of the original cores may be changed through the re-coring, cutting and/or trimming processes. Free-Free resonant column tests are again performed after these processes are done. Following this work and URC tests, the specimens are affixed in the RCTS device.

More than three isotropic confining pressures, σ_o, on a loading sequence were used in this study during RCTS stage testing of each tuff specimen. These pressures generally ranged from below, to equal to, to above the estimated in-situ mean effective stress, σ_m'. Low-amplitude resonant column testing was performed at each level of σ_o to determine the effects of magnitude of confinement and time of confinement on the small-strain shear modulus, G_{max}, and small-strain material damping ratio, D_{min} or $D_{S\,min}$. Low-amplitude dynamic tests are defined as those tests in which the resonant amplitude did not exceed 0.0005 % and was often below this level. Each confining pressure in the loading sequence is listed in Tables 4.1 and 4.2 for the specimens from the Topopah Spring Tuff and from the Bandelier Tuff, respectively. The estimated in-situ mean effective stress, σ'_m, for each specimen was calculated based on the depth and unit weight of the specimen, the depth of the water table, and an assumption of the value of the in-situ coefficient of lateral earth pressure at rest, K_o. For weak rock masses that are unable to support large deviatoric stress differences during confining, it was assumed that the vertical and horizontal stresses had equalized over time; hence, $K_o = 1.0$. This assumption is in accordance with Heim's Rule (Hoek and Brown, 1980), as often applied in the field of tunneling. Thus lithostatic stress and a K_o of 1.0 were assumed for Qbt3L, Qbt1v, Qbt1g, and Qbo materials from the Bandelier Tuff. The remaining units for the Bandelier Tuff, namely Qbt3U and Qbt2, are generally moderately to strongly welded. These materials are assumed to exhibit a behavior that is more linear and more constrained from deforming horizontally. Assuming a Poisson's ratio of 0.33, which is an average test value determined in tests on samples from the previous project nearby, a

Table 4.1 Summary of Test Performed on the Specimens from the Topopah Spring Tuff

Spec. No.	Specimen ID	Type	Initial Specimen Size		Total Unit Weight, lb/ft^3 (g/cm^3)	Isotropic Test Pressures		
			Height, in. (cm)	Diameter, in. (cm)		Low-Amplitude RC and TS Tests ksf (kPa)	High-Amplitude RC Tests ksf (kPa)	High-Amplitude TS Tests ksf (kPa)
Tuff1	UTA-42-A (1G-1)	Tptrl	1.81 (4.6)	0.83 (2.1)	136 (2.2)	0, 7.2, 15.8 (0, 345, 759)	15.8 (759)	15.8 (759)
Tuff2a	UTA-42-B (2B-3)	Tptpul	4.13 (10.5)	1.77 (4.5)	135 (2.2)	0, 1.4, 2.9, 5.8, 11.5, 23.0 (0, 69, 138, 276, 552, 1105)	5.8, 23.0 (276, 1105)	5.8, 23.0 (276, 1105)
Tuff2b	UTA-42-B (2C-2)*	Tptpul	1.81 (4.6)	0.83 (2.1)	141 (2.3)	0, 1.4, 2.9, 5.8, 11.5, 23.0 (0, 69, 138, 276, 552, 1105)	5.8, 23.0 (276, 1105)	5.8, 23.0 (276, 1105)
Tuff3a	UTA-42-C (3C-2)	Tptpmn	4.02 (10.2)	1.57 (4.0)	144 (2.3)	0, 5.2, 10.4, 20.7, 41.5, 64.8 (0, 249, 497, 994, 1988, 3106)	20.7, 64.8 (994, 3106)	20.7, 64.8 (994, 3106)
Tuff3b	UTA-42-C (3K-2)**	Tptpmn	1.97 (5.0)	0.83 (2.1)	147 (2.4)	0, 5.2, 10.4, 20.7, 41.5, 64.8 (0, 249, 497, 994, 1988, 3106)	0, 20.7, 64.8 (0, 994, 3106)	0, 20.7, 64.8 (0, 994, 3106)
Tuff4	UTA-42-D (4C-2)	Tptrn	4.57 (11.6)	1.57 (4.0)	145 (2.3)	0, 13.8, 27.4, 54.4, 64.8 (0, 663, 1312, 2609, 3106)	0, 54.4, 64.8 (0, 2609, 3106)	0, 54.4, 64.8 (0, 2609, 3106)
Tuff5	UTA-42-E (5C-2)	Tptpll	3.35 (8.5)	1.57 (4.0)	138 (2.2)	0, 3.6, 7.2, 14.4, 28.8, 57.6 (0, 173, 345, 690, 1381, 2761)	0, 14.4, 57.6 (0, 690, 2761)	0, 14.4, 57.6 (0, 690, 2761)
Tuff6	UTA-42-F (6C-2)	Tptpln	4.84 (12.3)	1.57 (4.0)	147 (2.4)	0, 3.6, 7.2, 14.4, 28.8, 57.6 (0, 173, 345, 690, 1381, 2761)	0, 14.4, 57.6 (0, 690, 2761)	0, 14.4, 57.6 (0, 690, 2761)
Tuff7	UTA-42-I (9A-2)	Tptpll	5.24 (13.3)	1.77 (4.5)	136 (2.2)	0, 3.6, 7.2, 14.4, 28.8, 57.6 (0, 173, 345, 690, 1381, 2761)	0, 14.4, 57.6 (0, 690, 2761)	0, 14.4, 57.6 (0, 690, 2761)

Notes: *UTA-42-B (2C-2) was cored from Specimen UTA-42-B (2B-3)
**UTA-42-C (3K-2) was cored from Specimen UTA-42-C (3D)

Table 4.1 Continued - Summary of Test Performed on the Specimens from the Topopah Spring Tuff

Spec. No.	Specimen ID	Type	Initial Specimen Size		Total Unit Weight, lb/ft^3 (g/cm^3)	Isotropic Test Pressures		
			Height in. (cm)	Diameter in. (cm)		Low-Amplitude RC and TS Tests ksf (kPa)	High-Amplitude RC Tests ksf (kPa)	High-Amplitude TS Tests ksf (kPa)
Tuff8	UTA-42-J (10A-2)	Tptpll	3.78 (9.6)	1.77 (4.5)	138 (2.2)	0, 3.6, 7.2, 14.4, 28.8, 57.6 (0, 173, 345, 690, 1381, 2761)	0, 14.4, 57.6 (0, 690, 2761)	0, 14.4, 57.6 (0, 690, 2761)
Tuff9	UTA-42-K (11C-1)*	Tptpul	2.91 (7.4)	1.57 (4.0)	139 (2.2)	0 (0)	0 (0)	0 (0)
Tuff10	UTA-42-L (12C-1)*	Tptpul	3.90 (9.9)	1.57 (4.0)	137 (2.2)	0 (0)	0 (0)	0 (0)
Tuff11	UTA-42-M (13C-2)	Tptpmn	5.98 (15.2)	1.57 (4.0)	144 (2.3)	0, 3.6, 7.2, 14.4, 28.8, 57.6 (0, 173, 345, 690, 1381, 2761)	0, 14.4, 57.6 (0, 690, 2761)	0, 14.4, 57.6 (0, 690, 2761)
Tuff12	UTA-42-N (14C-2)	Tptpmn	4.72 (12.0)	1.57 (4.0)	145 (2.3)	0, 3.6, 7.2, 14.4, 28.8, 57.6 (0, 173, 345, 690, 1381, 2761)	0, 14.4, 57.6 (0, 690, 2761)	0, 14.4, 57.6 (0, 690, 2761)
Tuff13	UTA-42-O (15C-3)	Tptpll	5.55 (14.1)	1.57 (4.0)	143 (2.3)	0, 3.6, 7.2, 14.4, 28.8, 57.6 (0, 173, 345, 690, 1381, 2761)	0, 14.4, 57.6 (0, 690, 2761)	0, 14.4, 57.6 (0, 690, 2761)
Tuff14	UTA-42-P (16C-2)	Tptpll	4.13 (10.5)	1.57 (4.0)	138 (2.2)	0, 3.6, 7.2, 14.4, 28.8, 57.6 (0, 173, 345, 690, 1381, 2761)	0, 14.4, 57.6 (0, 690, 2761)	0, 14.4, 57.6 (0, 690, 2761)

Note: *Tested only without confinement because of many large voids detected on the specimen surface.

Table 4.2 Summary of Test Performed on the Specimens from the Bandelier Tuff

Spec. No.	UT Spec. ID	Geologic Unit	Mid-Depth ft (m)	Mean Effective Stress* ksf (kPa)	Initial Specimen Size		Isotropic Test Pressures		
					Height in. (cm)	Diameter in. (cm)	Low-Amplitude RC and TS Tests ksf (kPa)	High-Amplitude RC Tests ksf (kPa)	High-Amplitude TS Tests ksf (kPa)
Tuff3	3C	Qbt3U	29.6 (9.0)	1.9 (92)	4.03 (10.23)	1.48 (3.77)	0, 0.1, 0.4, 0.9, 1.9, 3.7, 7.5 (0, 7, 21, 41, 90, 179, 359)	0, 0.1, 1.9, 7.5 (0, 7, 90, 359)	1.9, 7.5 (90, 359)
Tuff5	5E	Qbt3U	69.1 (21.1)	4.4 (212)	3.80 (9.66)	1.51 (3.84)	0.3, 0.4, 1.0, 2.2, 4.5, 8.9, 17.9 (14, 21, 48, 104, 214, 428, 856)	4.5, 17.9 (214, 856)	4.5, 17.9 (214, 856)
Tuff11	15C	Qbt3L	100.6 (30.7)	7.2 (344)	6.36 (16.16)	2.86 (7.27)	0.9, 1.7, 3.6, 7.2, 14.4, 28.8 (41, 83, 172, 345, 690, 1379)	7.2, 28.8 (345, 1379)	7.2 (345)
Tuff12	16C	Qbt3L	114.0 (34.7)	8.3 (398)	6.44 (16.37)	2.71 (6.89)	0.4, 1.0, 2.0, 4.2, 8.4 (21, 48, 97, 200, 400)	2.0, 8.4 (97, 400)	8.4 (400)
Tuff14	18C	Qbt3L	91.6 (27.9)	6.2 (298)	7.45 (18.92)	3.00 (7.63)	0.7, 1.4, 3.0, 6.2 (34, 69, 145, 296)	1.4, 6.2 (69, 296)	6.2 (296)
Tuff15	19C	Qbt3L	102.8 (31.3)	7.2 (347)	6.87 (17.44)	2.99 (7.60)	0.4, 0.9, 1.7, 3.6, 7.2, 1.7^+, 0.4^+, $1.7^\#$, $7.2^\#$, (21, 41, 83, 173, 345, 83^+, 21^+, $83^\#$, $345^\#$, $690^\#$)	1.7, 7.2, $7.2^\#$ (83, 345, $345^\#$)	7.2 (345)
Tuff18	22C	Qbt3L	121.6 (37.1)	8.8 (422)	6.41 (16.29)	3.01 (7.64)	0.4, 1.0, 2.2, 4.3, 8.8 (21, 48, 104, 207, 421)	2.2, 8.8 (104, 421)	8.8 (421)
Tuff13	17C	Qbt3L	83.4 (25.4)	5.6 (267)	4.60 (11.68)	2.02 (5.12)	0.7, 1.4, 2.9, 5.6 (34, 69, 138, 269)	1.4, 5.6 (69, 269)	5.6 (296)
Tuff16	20C	Qbt3L	105.4 (32.1)	7.5 (360)	5.25 (13.34)	2.00 (5.08)	0.4, 1.0, 1.9, 3.7, 7.5 (21, 48, 90, 179, 359)	1.9, 7.5 (90, 359)	7.5 (359)
Tuff17	21C	Qbt3L	117.6 (35.8)	8.5 (407)	6.48 (16.45)	3.02 (7.67)	1.0, 2.2, 4.3, 8.5 (48, 103, 207, 407)	2.2, 8.5 (103, 407)	8.5 (407)

Notes: *estimated mean effective stress provied by Kleinfelder

$^+$unloading pressure

$^\#$reloading pressure

Table 4.2 Continued - Summary of Test Performed on the Specimens from the Bandelier Tuff

Spec. No.	UT Spec. ID	Geologic Unit	Mid-Depth ft (m)	Mean Effective Stress* ksf (kPa)	Initial Specimen Size		Isotropic Test Pressures		
					Height in. (cm)	Diameter in. (cm)	Low-Amplitude RC and TS Tests ksf (kPa)	High-Amplitude RC Tests ksf (kPa)	High-Amplitude TS Tests ksf (kPa)
Tuff2	2G	Qbt2	155.4 (47.4)	11.7 (562)	4.85 (12.32)	1.56 (3.95)	0, 2.9, 5.9, 11.8, 23.6, 47.2 (0, 138, 283, 566, 1132, 2264)	0, 11.8, 47.2 (0, 566, 2264)	11.8, 47.2 (566, 2264)
Tuff1	1G	Qbt2	136.5 (41.6)	10.3 (492)	5.42 (13.76)	1.56 (3.96)	0, 2.6, 5.2, 10.4, 20.7, 41.5 (0, 124, 249, 497, 994, 1988)	0, 10.4, 41.5 (0, 497, 1988)	10.4, 41.5 (497, 1988)
Tuff4	4H	Qbt1v	234.8 (71.6)	17.7 (847)	5.03 (12.77)	1.99 (5.05)	0.3, 0.6, 1.2, 2.3, 4.5, 8.9, 17.9 (14, 28, 55, 110, 214, 428, 856)	2.3, 17.9 (110, 856)	17.9 (856)
Tuff9	10C	Qbt1v	249.2 (76.0)	19.0 (909)	6.76 (17.16)	2.81 (7.15)	0.7, 1.4, 2.9, 4.8, 9.5, 19.0, 38.9, 57.6 (35, 69, 138, 228, 455, 910, 1862, 2758)	9.5, 19.0 (455, 910)	9.5, 19.0 (455, 910)
Tuff6	7C	Qbt1g	282.1 (86.0)	21.8 (1045)	5.94 (15.10)	2.86 (7.27)	1.4, 2.9, 5.5, 10.8, 21.7, 39.6, 57.6 (69, 138, 262, 517, 1041, 1896, 2758)	10.8, 21.7 (517, 1041)	10.8, 21.7 (517, 1041)
Tuff7	8C	Qbt1g	284.1 (86.6)	22.2 (1066)	6.38 (16.21)	2.87 (7.28)	0.3, 1.4, 2.9, 5.6, 11.4, 22.3 (14, 69, 138, 267, 545, 1069)	11.4, 22.3 (545, 1069)	11.4, 22.3 (545, 1069)
Tuff8	9C	Qbo	420.3 (128.1)	34.7 (1662)	4.39 (11.15)	1.98 (5.04)	0.7, 1.4, 2.9, 5.8, 8.6, 17.3, 34.6, 46.1, 57.6 (35, 69, 138, 276, 414, 828, 1657, 2209, 2761)	17.3, 34.6, 57.6 (828, 1657, 2761)	17.3, 34.6, 57.6 (828, 1657, 2761)
Tuff10	11C	Qbo	530.8 (161.8)	43.8 (2100)	5.83 (14.82)	2.87 (7.28)	1.3, 2.8, 5.5, 10.1, 21.9, 43.8 (62, 131, 262, 483, 1048, 2096)	10.1, 43.8 (483, 2096)	10.1, 43.8 (483, 2096)

Notes: *estimated mean effective stress provied by Kleinfelder

K_o of 0.5 was estimated for these indurated units (Kleinfelder, 2005). Because most of the rock specimens from the Topopah Spring Tuff at Yucca Mountain were recovered from large depths, RCTS tests were performed at four or five pressures up to the maximum of the system (about 400 psi (3.1 MPa)). Because of the large depth, the value of σ_m' could not be reached for these tuffs.

Strains in the RCTS tests ranged from the small-strain range, where dynamic properties of the specimens stay constant (normally less than about 0.0005 %) to rather large strain amplitudes where the specimens can exhibit nonlinear behavior. Testing of rock specimens in this research was performed over this strain range. The high-amplitude testing was composed of two series of tests: cyclic torsional shear (TS) tests and high-amplitude resonant column (HARC) tests. These tests for the samples from the Bandelier Tuff were performed at the estimated in-situ mean effective stress, σ'_m, and at one or more pressures below and sometimes at a pressure equal to four times σ'_m. The rocks from the Topopah Spring Tuff did not show significant pressure dependency. Thus, two large pressures, apart from each other by a factor of 2 or 4, were selected for the HARC tests on the specimens from the Topopah Spring formation.

Torsional shear (TS) tests were performed to estimate the effects of strain amplitude, loading frequency and number of loading cycles on the dynamic properties of most specimens. Ten cycles of loading were used in the TS test followed by about 1000 cycles in the resonant column (RC) test. The majority of the measurements were performed at 0.5 Hz. However, TS tests at two or three different levels of shearing strain, γ, were also conducted to evaluate the effect of excitation frequency on G and D at these strains. In these tests, ten cycles of loading were applied at four different frequencies ranging from 0.1 Hz to 5 Hz (the maximum frequency in the TS test was ≤ 0.1 times the resonant frequency in the RC test). The frequency associated with resonance in the RC test varied with material stiffness and strain amplitude and ranged from about 48 Hz to 525 Hz for these specimens.

After the TS tests were completed, confinement of the specimen was continued at the given pressure. A series of high-amplitude resonant column (HARC) tests was performed following the TS tests. However, before the HARC tests commenced, small-strain RC tests were performed to determine if any changes in the coupling of the rock specimen with the top cap and/or base pedestal might have occurred from the TS tests. No significant changes were measured. Significant changes are defined as a change of 5 % in G_{max} and 10 % in D_{min}.

Since significant time dependent changes in dynamic properties were not found in the tuff specimens from both formations, low-amplitude tests (defined as testing at shearing strains less than about 0.0005 %) were performed at confinement times less than about 100 minutes.

4.3 TESTING WITH THE URC DEVICE

An unconfined, free-free, resonant column (URC) test set-up was also used to evaluate the stiffness and material damping of specimens that could be handled like rock cores. These specimens were: four moderately to densely welded specimens from the Bandelier Tuff (two Qbt2 and two Qbt3U cores) and all thirty eight specimens from the Topopah Spring Tuff that have higher welding intensities than tuffs from the Bandelier Tuff formation. The testing was performed only at small strains and only in the unconfined state. All tests were performed on the complete core specimens before smaller test specimens were cut from them. The ends of each core were cut with a rock saw to achieve a square shape at the ends. The dimensions of the specimens tested in the URC set-up are presented in Table 4.3 for the specimens from the Bandelier Tuff. Note

Table 4.3 Initial Characteristics of the Core Specimens from the Bandelier Tuff Dynamically Tested Using an Unconfined, Free-Free, Resonant Column Set-Up at the University of Texas at Austin

Free-Free Spec. No.	UT Spec. ID	Boring No. *	Sample No.*	Geologic Unit*	Sample Type*	Depth (ft)		Height	Diameter	Weight	Total Unit Weight, γ_t,	Description/ Sample Condition*
						Top	Bottom	in. (cm)	in. (cm)	lb (g)	lb/ft^3 (g/cm^3)	
FrF1	1C	DSC-2	R29	Qbt2	HQ core	136.1	137.0	9.52 (3.75)	2.49 (0.98)	3.13 (1418)	117.0 (1.87)	Moderately welded tuff
FrF2	1G	DSC-2	R29	Qbt2	HQ core	136.2	136.7	5.42 (2.13)	1.56 (0.61)	0.71 (322)	118.9 (1.91)	Moderately welded tuff
FrF3	2C	DSC-1A	R40	Qbt2	HQ core	155.0	155.7	7.53 (2.96)	2.46 (0.97)	2.45 1111	117.8 (1.89)	Strongly welded tuff
FrF4	2G	DSC-1A	R40	Qbt2	HQ core	155.2	155.6	4.85 (1.91)	1.56 (0.61)	0.63 (286)	118.2 (1.89)	Strongly welded tuff
FrF5	3A	DSC-2	R6	Qbt3U	HQ core	28.9	29.8	10.22 (4.02)	2.45 (0.96)	2.67 (1212)	95.8 (1.54)	Moderately welded tuff
FrF6	5C	DSC-1A	R14	Qbt3U	HQ core	68.5	69.2	8.62 (3.39)	2.16 (0.85)	1.81 (819)	99.0 (1.59)	Moderately welded tuff

Notes: Specimens 1C, 2C, 3A, and 5C are the larger cores that were only tested in the free-free RC test.
Specimens 1G and 2G were tested in both the free-free and fixed-free RC tests.
*information provided by Kleinfelder

that the information on the specimens from the Topopah Spring Tuff is presented in Table 2.2 in Chapter 2.

One purpose of the URC tests was to measure V_S, G_{max} and D_{min} in a simpler configuration than the RCTS device so that these values can be compared as independent measurements with similar values measured in the RCTS tests. In addition, other compressional measurements can be also conducted for comparison with the field downhole and suspension logging measurements.

4.3.1 URC Test Set-Up

The dynamic tests in the URC set-up consist of two general types of small-strain seismic tests: (1) free-free resonance tests and (2) direct-travel-time tests. Shear wave velocity, V_S, shear modulus, G_{max}, and material damping ratio in shear, D_{min} or $D_{S\ min}$ can be measured in free-free resonance tests in torsional motion. Unconstrained compression wave velocity, V_C, Young's modulus, E_{max}, and material damping ratio in unconstrained compression, $D_{C\ min}$ can be measured in free-free resonance tests in longitudinal motion. Direct-travel-time measurements of compression waves also provide an estimation of the constrained compression wave velocity, V_P, and constrained modulus, M_{max}. A sketch illustrating these three measurements is shown in Figure 4.8. In all cases, the specimens were unconfined (that is, no confining pressure was applied during testing) and all strain levels were in the small-strain or linear range.

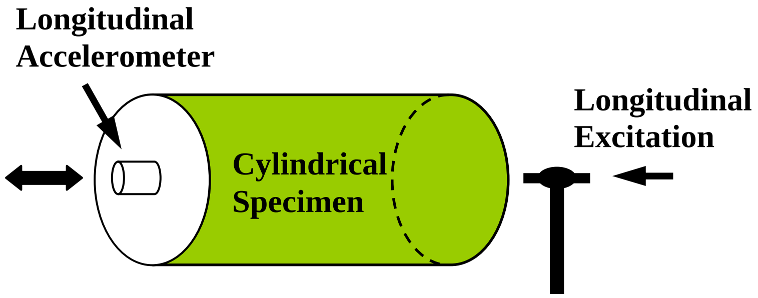

a. Compressional (Longitudinal) Resonance Test

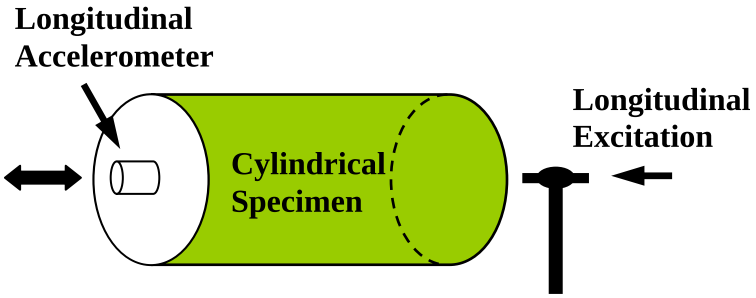

b. Direct-Travel-Time of Constrained Compression Waves Measurement

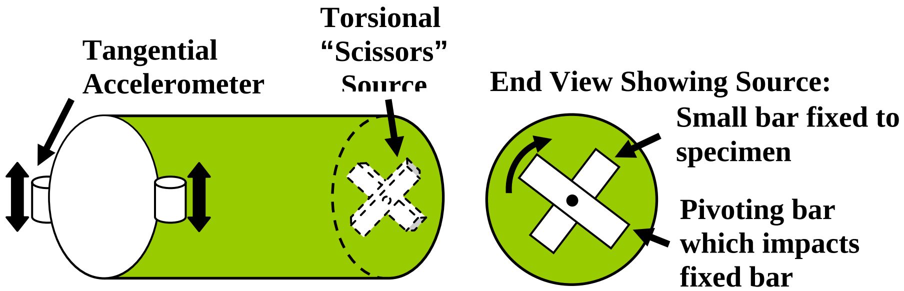

c. Torsional Resonance Test with a "Scissors" Source

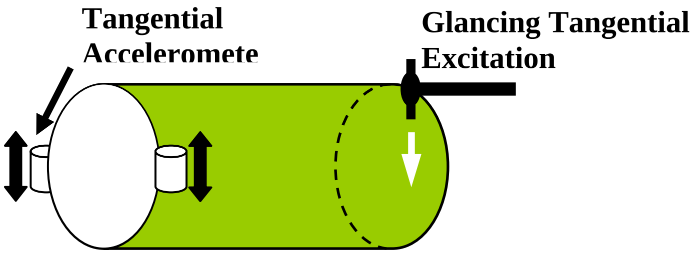

d. Torsional Resonance Test with a Tangential Impact

Figure 4.8 General Test Set-Up Configurations for: (a) Compressional (Longitudinal) Resonance Test, (b) Direct-Travel-Time Measurement, and (c) and (d) Torsional Resonance Test on Unconfined Cylindrical Specimens (after Stokoe et al. 1994)

Free-free resonance tests are performed by establishing longitudinal and torsional resonant vibrations to evaluate the dynamic properties of the tuff specimens. Free-free boundary conditions are created by laying the tuff specimens on soft cushions, in order to minimize the restriction of movements of the specimen. The excitation is created by different types of impact devices: (1) a small hand-held hammer for longitudinal vibration and (2) a "scissors" source or a tangential impact for torsional vibration. Resonant motions of the specimen created by the impacts are measured by accelerometer(s) on the free end opposite the source as illustrated in Figure 4.8. The output(s) of the accelerometer(s) are monitored with a dynamic signal analyzer which provides data acquisition and signal processing operations. All time-domain and frequency-domain data are saved in a data logger which is connected to the analyzer. Figure 4.9 illustrate the configuration of the equipment for the compressional (longitudinal) resonance tests and direct-travel-time measurements and Figure 4.10 illustrates the configuration for the torsional resonance tests.

4.3.2 Typical URC Measurements

The frequencies of the normal modes and geometrical shape of the frequency response curves (or power spectrum) are used in determining the dynamic properties of the soil and rock specimens as shown in Figure 4.11. First-mode resonant frequencies are measured and recorded in longitudinal and torsional motions. Unconstrained compression wave velocity, V_C, is determined from Eq. (4.1) and shear wave velocity, V_S, from Eq. (4.2), as follows:

$$V_C = f_l\lambda/(C/C_B) \tag{4.1}$$

$$V_S = f_l\lambda \tag{4.2}$$

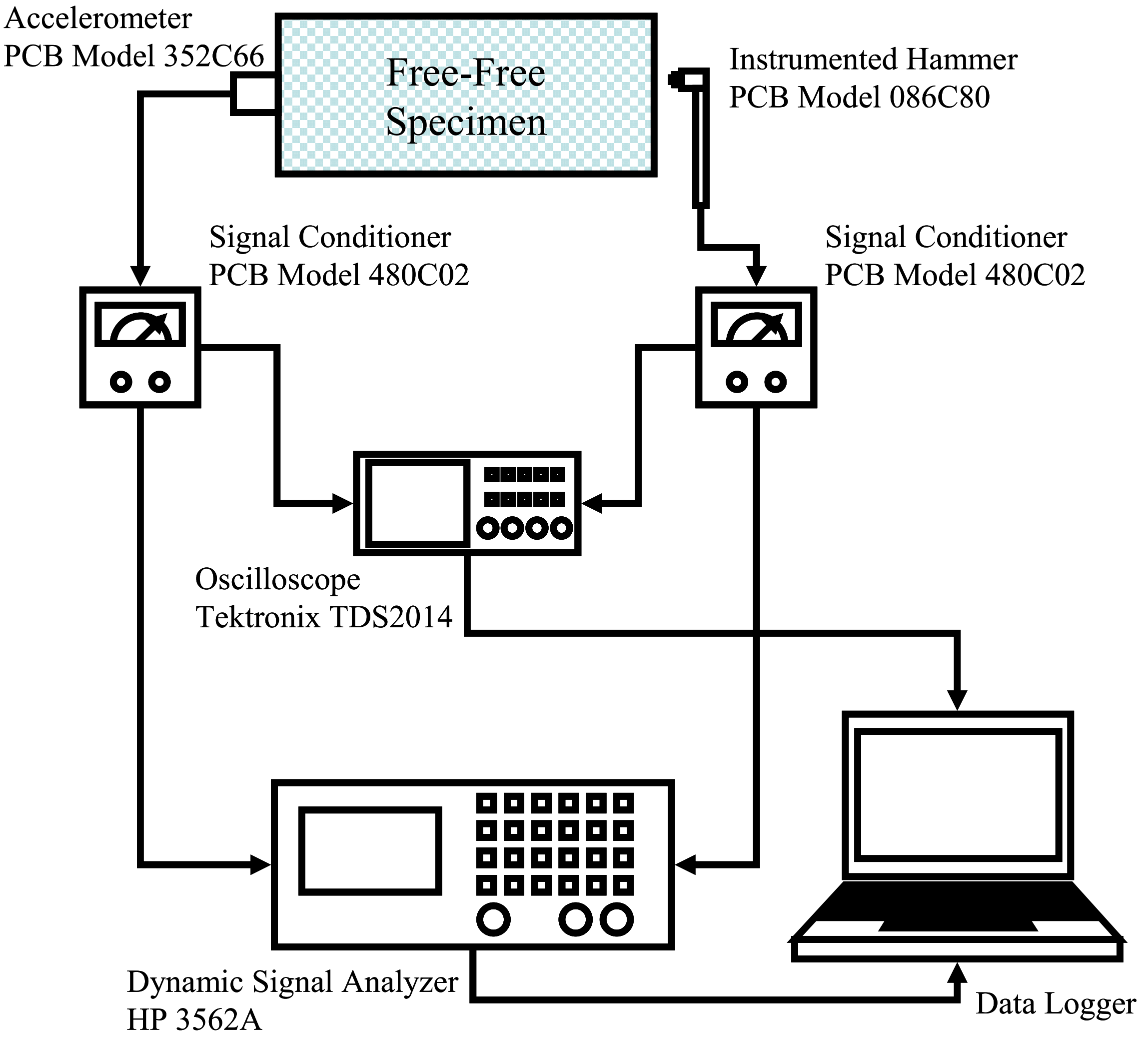

Figure 4.9 Configuration of URC Equipment for Compressional (Longitudinal) Resonance Testing and Direct-Travel-Time Measurements

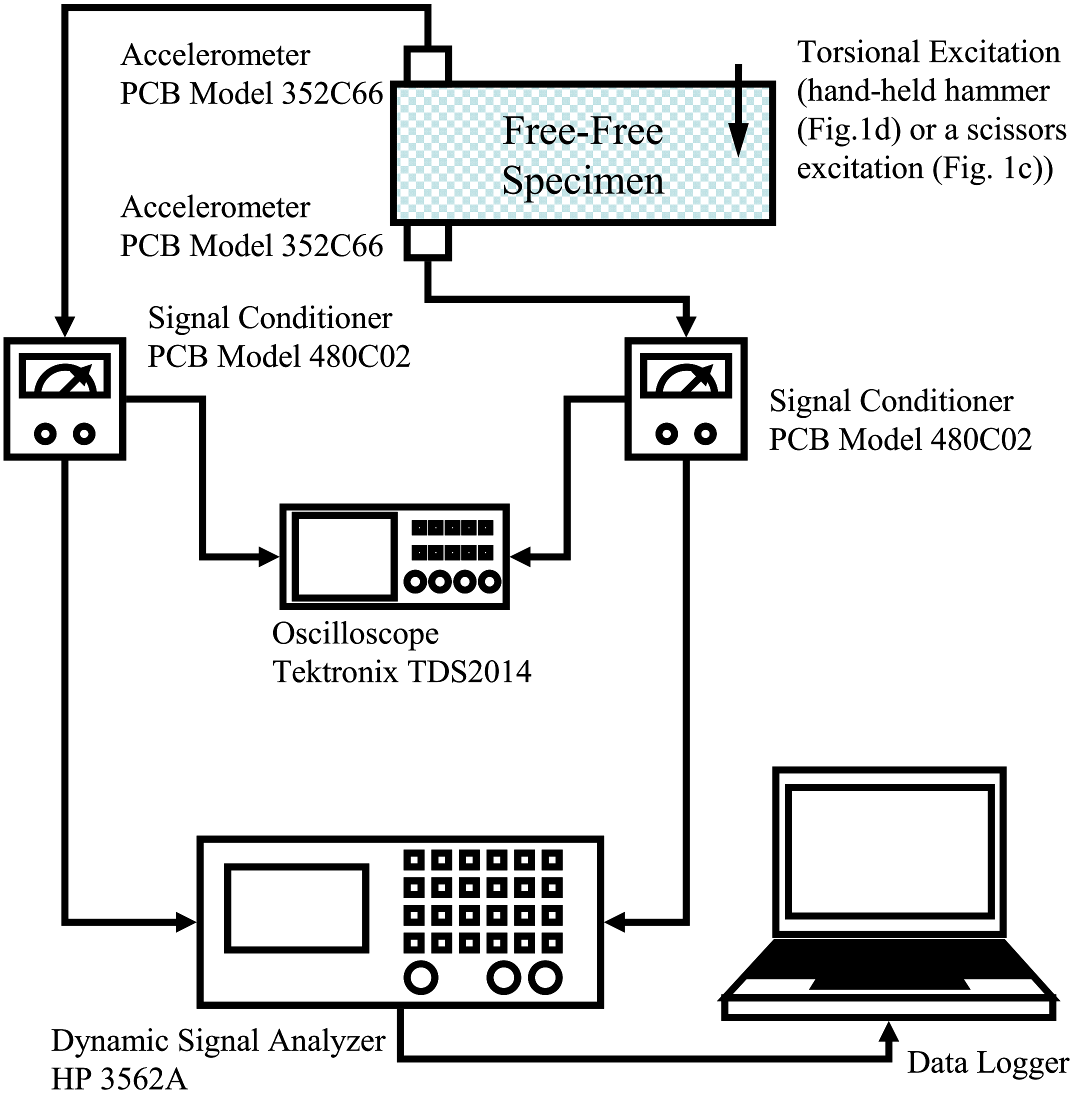

Figure 4.10 Configuration of URC Equipment for Torsional Resonance Testing

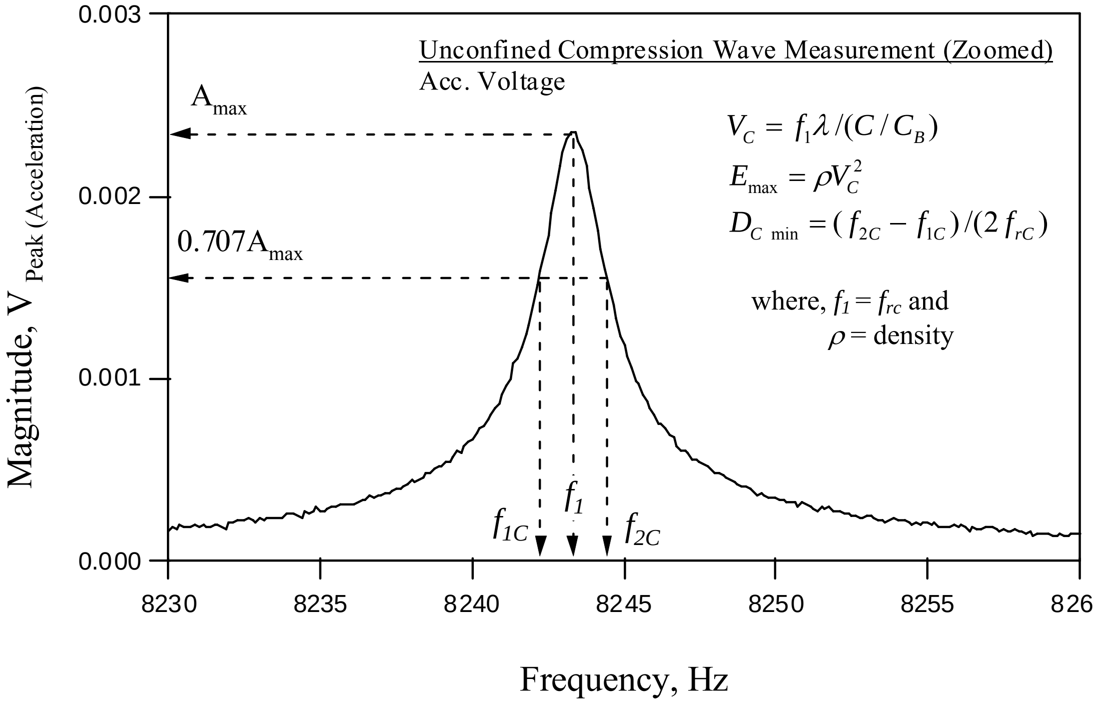

Figure 4.11 Extended Power Spectrum of First-Mode Unconstrained Compressional Resonance; Aluminum Specimen

where, f_l = first-mode resonant frequency (in longitudinal excitation for V_C and in torsional excitation for V_S),

λ = wavelength = 2L (for first-mode resonance),

L = the length of the specimen, and

C/C_B = dimensionless velocity (a dimensionless correction factor for wavelength. See Figure 4.12).

In the case of the V_C evaluations, correction for specimen length is not required if the first-mode wavelength is more than four times the diameter of the test specimen (Stokoe et al., 1994). When the wavelength is less than four times the diameter, the correction factor shown in Figure 4.12 is used (Lewis, 1990). Material damping ratios in both unconstrained compression ($D_{C\min}$) and torsion ($D_{S\min}$) are determined from the half-

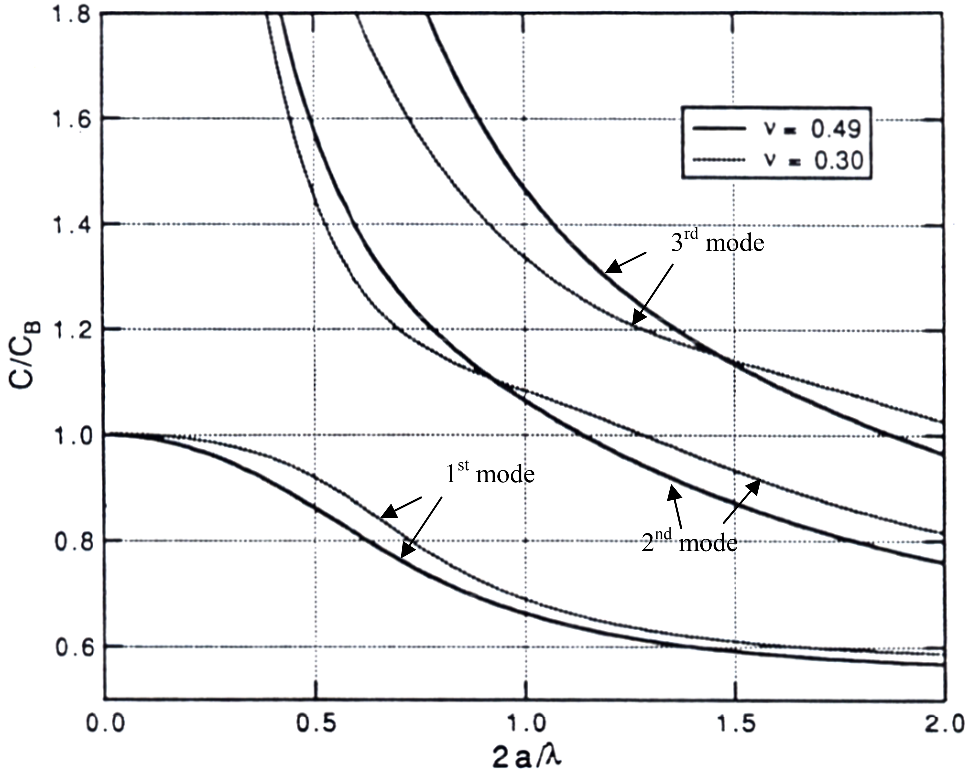

Notes: C = phase velocity,
C_B = bar velocity = V_C
C/C_B = dimensionless velocity,
a = radius of specimen,
λ = wavelength determined in the measurement mode, and
2a/λ = dimensionless wave number.

Figure 4.12 Frequency Spectrum for Longitudinal Waves in Resonance in a Cylindrical Rod as a Function of Dimensionless Wave Number (after Lewis, 1990)

half-power bandwidth method (see Figure 4.11) for each mode of vibration using Eqs. (4.3) and (4.4), respectively, as follows:

$$D_{C\,min} = D_{hp,C\,min} \cong \frac{f_{2C} - f_{1C}}{2 \times f_{rC}} \tag{4.3}$$

$$D_{S\,min} = D_{hp,S\,min} \cong \frac{f_{2S} - f_{1S}}{2 \times f_{rS}} \tag{4.4}$$

where, f_{rC} = the 1st mode resonant frequency in compression,

f_{1C} = the lower frequency at $1/\sqrt{2}$ times the resonant amplitude in compression,

f_{2C} = the higher frequency at $1/\sqrt{2}$ times the resonant amplitude in compression.

f_{rS} = the 1st mode resonant frequency in torsion,

f_{1S} = the lower frequency at $1/\sqrt{2}$ times the resonant amplitude in torsion, and

f_{2S} = the higher frequency at $1/\sqrt{2}$ times the resonant amplitude in torsion.

In addition to resonance testing, constrained compression wave velocity, V_P, can be measured between the free ends of the specimen using the direct-travel-time as presented in Figure 4.13. The set-up for this measurement is identical to the set-up for the free-free resonance tests in longitudinal motion as shown in Figures 4.8a and 4.8b. The value of V_P is calculated using the Eq. (4.5) as:

$$V_P = L/t \tag{4.5}$$

where L is the length of the specimen and t is the time shift between the input and output signals, which is the difference in time between the start point of the hammer impact (input signal) and the arrival point observed in the arrival wave.

4.3.3 Evaluating the URC Device with Metal Specimens

Metal specimens were used as reference specimens to evaluate the system compliance in the URC set-up (Stokoe et al., 1994). The tests of the metal specimens provide the proper selection of the wavelength-to-diameter ratio and resonance mode used to evaluate the stiffnesses of rock and stiff soil samples. An appropriate way of digitization and resolution needed in the spectrum can be also provided by evaluating the material damping ratio of metal specimens.

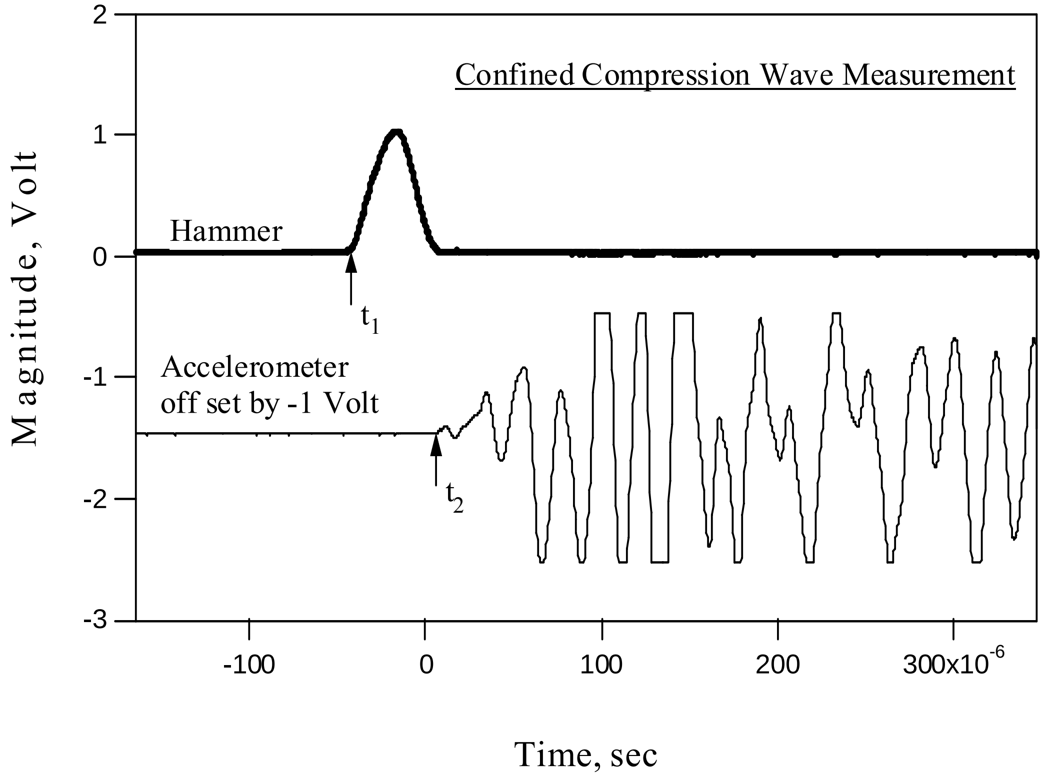

Figure 4.13 Measurements of Direct P-Wave Arrival; Aluminum Specimen

Three different aluminum specimens were used. One specimen was 30.5 cm (12.0 in.) in length and had a diameter of 15.2 cm (6.0 in.). The other two specimens were 15.2 cm (6.0 in.) and 45.7 cm (18.0 in.) long, with the same diameter of 7.6 cm (3.0 in.). Figure 4.14 illustrates the influence of wavelength on calculated wave velocities for the three aluminum reference specimens. The unconstrained compression wave velocity, V_C, decreases as the wavelength-to-diameter ratio (λ/d) decreases, while the shear wave velocity shows little change with this ratio. The decrease in the value of V_C results from the violation of the plane wavefront assumption and excitation of more complex modes of vibration as the wavelength is close to the diameter of the specimen as suggested by

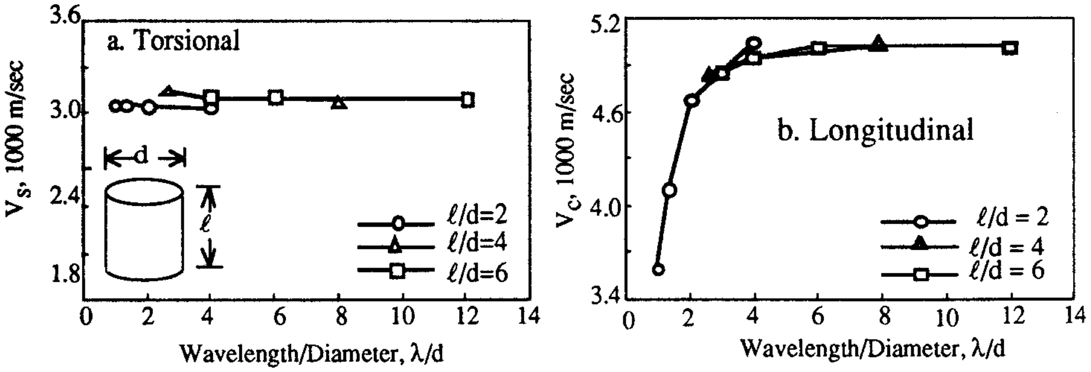

Figure 4.14 Influence of Wavelength on Calculated Wave Velocities for Three Aluminum Reference Specimens (after Stokoe et al. 1994)

Lewis (1990). The first mode is the proper mode to evaluate both V_C, E_{max}, V_S and G_{max}. The further corrections for the specimen with (λ/d) < 2 can be made by using the correction factor discussed in Section 5.3.2 and shown in Figure 4.12.

The small-strain material damping ratio values of the aluminum reference specimens measured using different frequency bandwidths and first-mode resonance are presented in Figure 4.15. The small-strain material damping ratio is overestimated when a large frequency bandwidth is used. However, it is shown that for frequency bandwidths less than about 3 kHz, the damping ratios in both unconstrained compression and shear become nearly constant. It should be also noted that these values are between 0.02 and 0.06 %, and they were accurately measured and agree well with values reported in the literature (Sun, 1993).

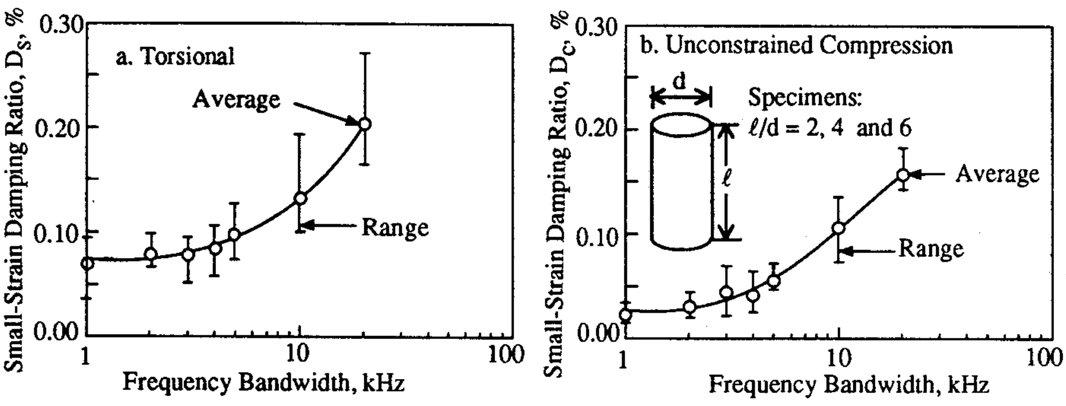

Figure 4.15 Influence of Frequency Bandwidth on Measured Values of Material Damping for Three Aluminum Reference Specimens (after Stokoe et al. 1994)

4.4 SUMMARY

Various test parameters were controlled to evaluate the dynamic properties of the tuffs in this research by using: (1) the combined resonant column and torsional shear (RCTS) device, and (2) the unconfined, free-free, resonant column (URC) device. The effects of confining pressure, strain amplitude, and excitation frequency were studied with the RCTS device. With the URC device, both compression and shear modes were studied.

More than three isotropic confining pressures, σ_o, on a loading sequence were used during RCTS stage testing of each tuff specimen. These pressures generally ranged from below, to equal to, to above the estimated in-situ mean effective stress, σ_m'. The σ_o applied for the tests are tabulated in Tables 4.1 and 4.2 for the specimens from the

Topopah Spring Tuff and from the Bandelier Tuff, respectively. Strains in the RCTS tests ranged from the small-strain range (normally less than about 0.0005 %) to large strain (normally larger than about 0.02 %). To evaluate the effect of strain amplitude, the cyclic torsional shear (TS) tests and high-amplitude resonant column (HARC) tests were performed at the σ'_m and one or two more pressures for the specimens from the Bandelier Tuff and at two large pressures apart from each other by a factor of 2 or 4 for the specimens from the Topopah Spring formation. Majority of the measurements in the torsional shear (TS) tests were performed at 0.5 Hz with ten loading cycles while about 1000 cycles were used in the RC test. Ten cycles of loading were applied at four different frequencies ranging from 0.1 Hz to 5 Hz to evaluate the effect of loading frequency.

The dynamic tests in the URC set-up consist of two general types of small-strain seismic tests: (1) free-free resonance tests and (2) direct-travel-time tests. The free-free resonance tests involve the measurements in both shear mode in torsional motion and compression in longitudinal motion. In torsional motion, shear wave velocity, V_S, shear modulus, G_{max}, and material damping ratio in shear, D_{min} or $D_{S\ min}$ are measured. In longitudinal motion, unconstrained compression wave velocity, V_C, Young's modulus, E_{max}, and material damping ratio in unconstrained compression, $D_{C\ min}$ are measured. Direct-travel-time measurements of compression waves are performed to estimate the constrained compression wave velocity, V_P, and constrained modulus, M_{max}.

Chapter 5

Development of a Large Resonant Column (LgRC) Device

5.1 INTRODUCTION

The traditional fixed-free Resonant Column and Torsional Shear (RCTS) device has been used for several decades to evaluate dynamic properties of soils and rocks. However, the device has limitations in specimen size and the potential problem of the lack of fixity at the bottom of the specimen when the specimen is large and stiff (Menq, 2003). The maximum particle size of specimen tested in the RCTS device is limited simply because the maximum torque of the device limits the maximum diameter of specimen. In addition, dynamic testing on materials such as rock, concrete and heavily cemented gravely material requires a substantially robust base pedestal and reaction block to satisfy the fixed-boundary condition. By freeing the fixity at the specimen base and increasing the capacity of the coil-magnet system, materials with a wider range of dimensions and stiffnesses can be tested dynamically up to larger strain levels.

There have been researchers who developed the supporting system to achieve free-free boundary conditions; e.g. Lewis (1990), Vaghela (1995), Western (1996) etc. Menq (2003) recently developed a Multi-Mode, Free-Free, Resonant Column (MMD) device. As shown in Figure 5.1, the vertically oriented specimen is hung by four thin wires with soft springs. The weight of the test specimen is supported by connecting these wires to the bottom pedestal and the support plate. The MMD is capable of supporting a 6-in. (15 cm) diameter by 12-in. (30-cm) tall specimen, thus gravely soils having the maximum particle size of 1-in. (2.5 cm) can be tested dynamically.

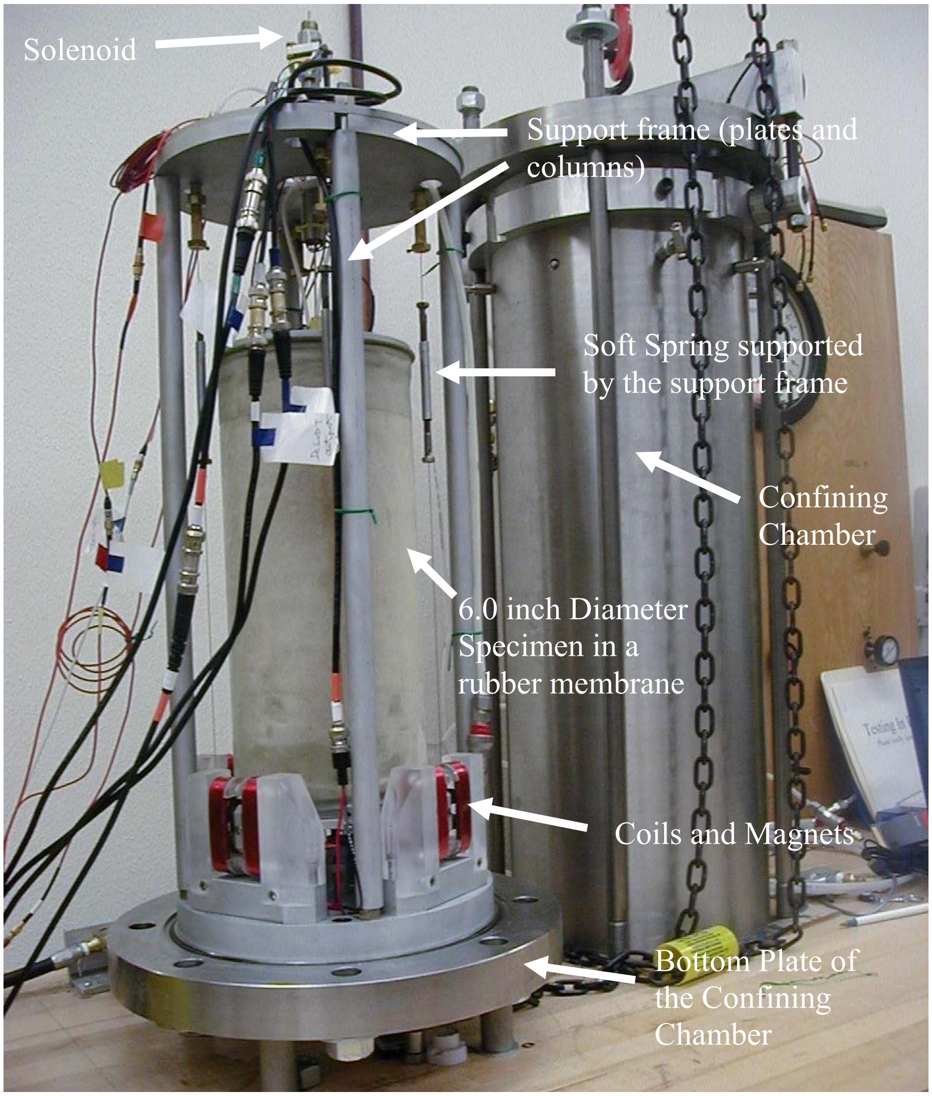

Figure 5.1 Six Inch Sand Specimen in the Large-Scale, Multi-Mode, Free-Free, Resonant Column (MMD) Device with the Confining Chamber (After Menq, 2003)

While the MMD allows large-scale testing using the free-free boundary condition, the test specimen size is limited to about 6.0 in. (15 cm) because the distance between the centers of the two magnets on the bottom of the specimen is fixed to 8.0 in. (20 cm). Just as with the fixed-free RCTS device, the test specimen is placed inside a supporting system, so that a larger system would have to be built to accommodate specimens larger than originally targeted. This inherent limitation can be overcome by placing the specimen on a table that supports the specimen weight and vibrates in torsional direction. Flexure bearings employed in the new device developed in this research allows this configuration. Figure 5.2 shows the cutaway of the cantilever-type flexure bearing. While axial loading is supported by sturdy outer sleeves, two thin metal beams flex to support the rotational loading. Therefore, this configuration of flexure bearing provides both high axial and radial stiffnesses and nearly frictionless angular travel.

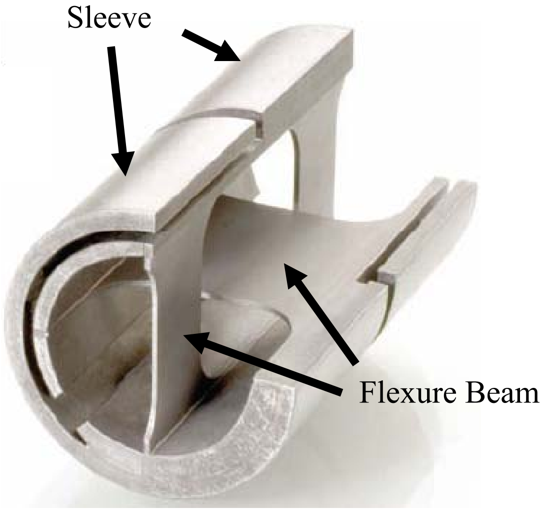

Figure 5.2 Cutaway of Cantilever-Type Flexure Bearing

Figure 5.3 shows the torsional shaker (RVC 400 Rotary Vibration System manufactured by TEAM Corporation (Burlington, WA) used in this study. A rotary voice coil actuator unit is equipped in the torsional shaker. As current flows into voice coils, a magnetic field is produced (induction). This magnetic field causes the voice coils to react to the magnetic field from a permanent magnet that is fixed to the actuator frame. The rotational movement of the coils (coil assembly) is transferred to the flexure bearing assembly, which consists of its axis plate, shaft, travel stop arm, and drive adapter directly connected to the coil assembly as shown in Figure 5.3. The torsional excitation is applied to the test specimen through this unit.

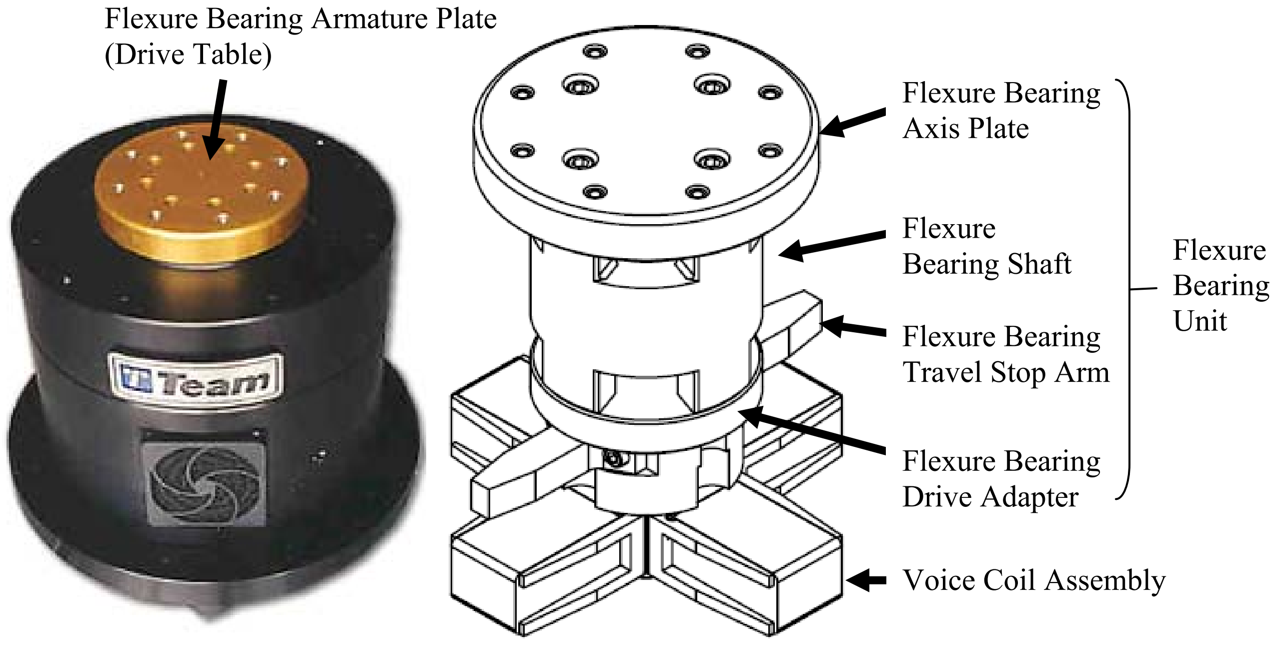

Figure 5.3 Torsional Shaker and Its Rotational Mass Assembly

The overview of the equipment set-up used in this study is shown in Figure 5.4. This set-up mainly consists of the torsional shaker with its controlling device and motion monitoring devices. The set-up is generally referred to as the Large Resonant Column or LgRC device, hereafter. The dynamic signal analyzer creates sinusoidal waveforms at various amplitudes and frequencies. A power amplifier amplifies the signal from the analyzer. It is worthwhile to note that this power amplifier has a high capacity of a current with 18 amps that is much higher than the capacity of a traditional amplifier with a current limit of 1 amp. Two metal plates are built: one is the connection plate between the drive table of the torsional shaker and the base pedestal of the specimen and the other is a top mass plate. It is worth noting that this top mass plate is used to reduce the resonant frequency of specimen as well as to house the top accelerometers. Accelerometers are placed on these metal plates to monitor relative displacement and phase difference along the specimen length. The plates are considered as rigid masses, so the accelerometers are considered to measure the pure motion of the specimen. The schematic illustration of the LgRC device is shown in Figure 5.5. The model and serial numbers of each component of the device are shown in the figure. It should be noted that the LgRC device presently has no confining chamber.

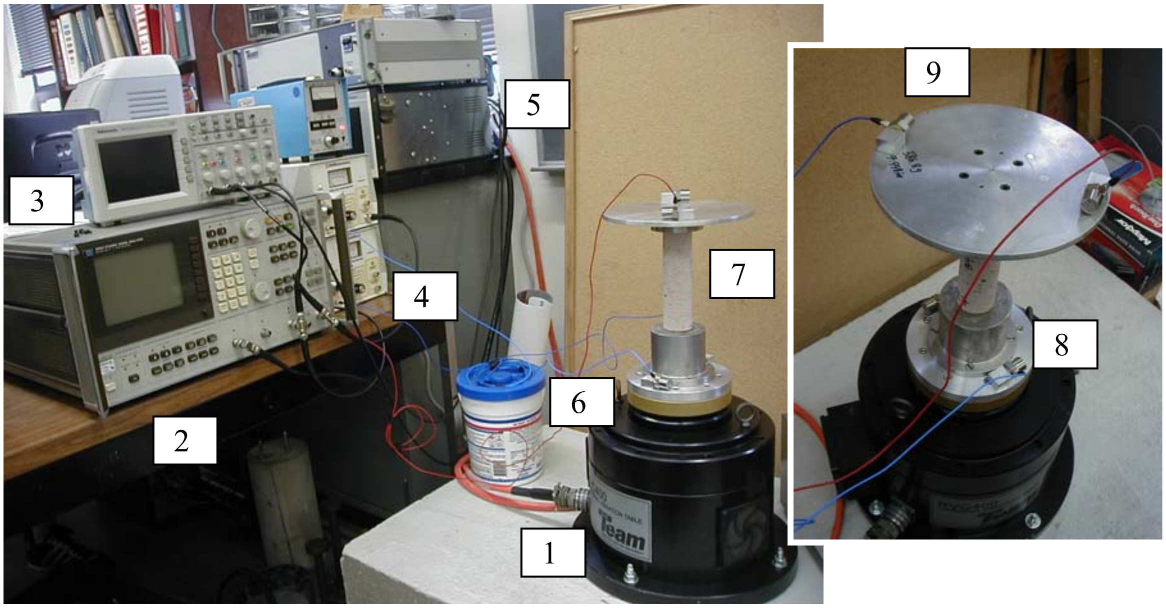

Notes: 1. torsional shaker
2. dynamic signal analyzer
3. oscilloscope
4. charge amplifier for top and bottom accelerometers
5. power amplifier
6. connection plate
7. top mass plate (Added Mass (AM) No. 6)
8. bottom accelerometers and
9. top accelerometers

Figure 5.4 General Overview of the Large Scale Resonant Column (LgRC) Device

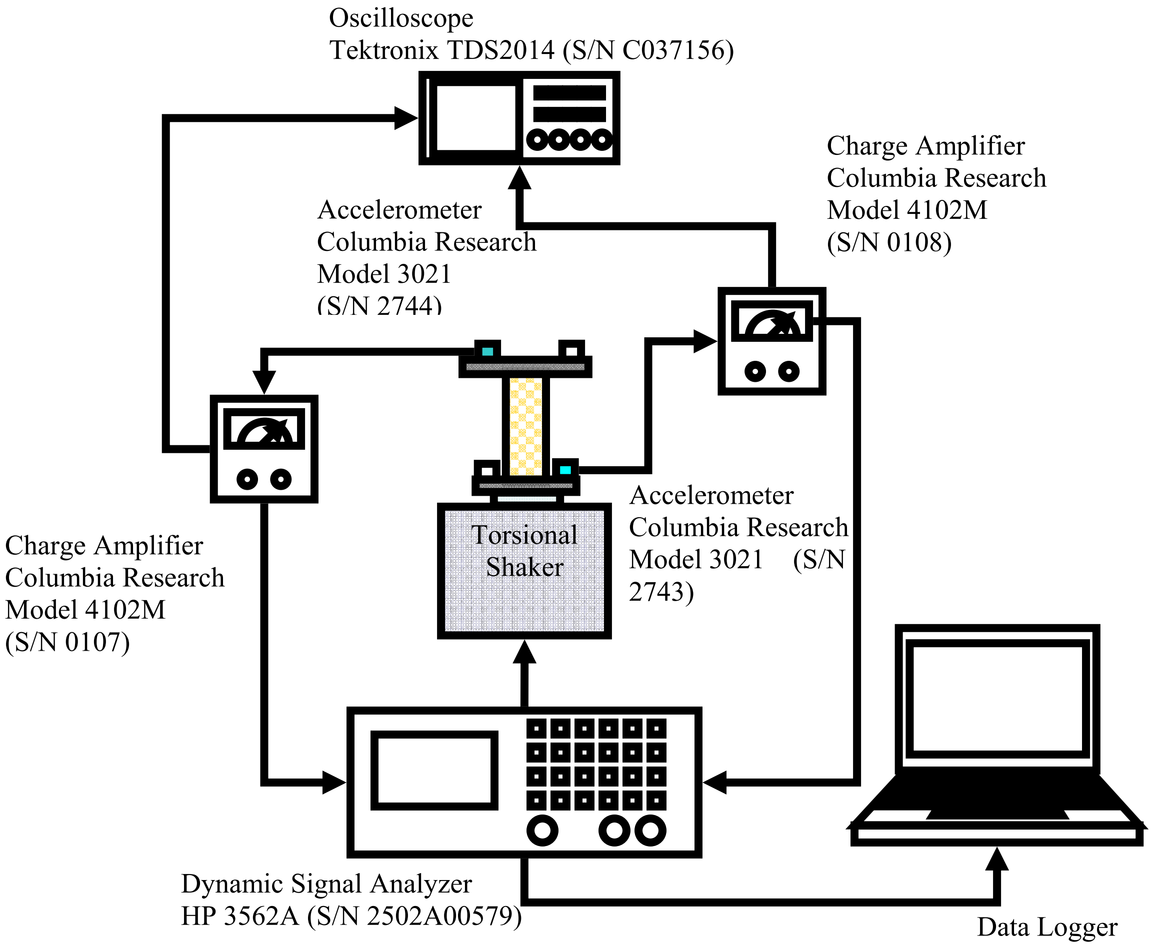

Figure 5.5 Configuration of Equipment for the Large Resonant Column (LgRC) Tests

A general description of the background related to the LgRC test is described in Section 5.2. The proposed theoretical approach to estimate mass polar moment of inertia of the system, shearing strain estimation in free-free boundary condition, and equipment generated damping estimation are also discussed in Section 5.2. Validation of the system with the results from two different known materials is discussed in Section 5.3.

5.2 BACKGROUND THEORY AND CALIBRATION OF THE LgRC TEST

When torsional waves travel through a rod, each finite segment of the rod rotates about its longitudinal axis as shown in Figure 5.6. Particle motion occurs in cross-sectional planes perpendicular to the direction of wave propagation. The one-dimensional torsional wave equation can be expressed as:

$$\frac{\partial^2 \phi}{\partial t^2} = V_S^2 \frac{\partial^2 \phi}{\partial x^2} \tag{5.1}$$

where, ϕ = angle of twist,
V_S = shear wave velocity ($=\sqrt{G/\rho}$),
t = time, and
x = location along x axis.

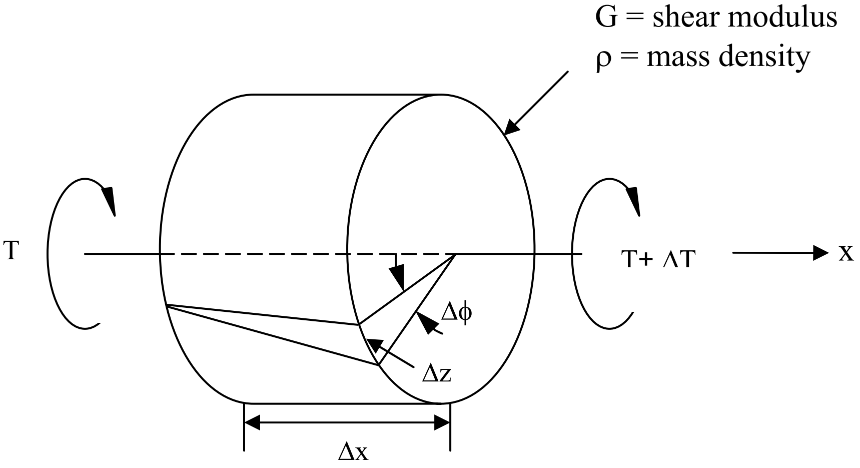

Figure 5.6 Torque and Rotation in a Cross-Sectional Element of a Rod in Torsional Vibration

By assuming sinusoidal motion, the angle of twist can be expressed as:

$$\phi(x,t) = \theta(x) e^{i\omega t} \tag{5.2}$$

Therefore, Eq. (5.1) can be rewritten as:

$$\frac{\partial^2 \theta(x)}{\partial x^2} + \frac{\omega^2}{V_S^2} \theta(x) = 0 \tag{5.3}$$

The solution of Eq. (5.3) can be expressed as:

$$\theta(x) = C_1 \sin\frac{\omega_n x}{V_S} + C_2 \cos\frac{\omega_n x}{V_S} \tag{5.4}$$

To satisfy the no-constraint (free) boundary condition at both ends of a rod with a finite length, l, the strain must be zero on the end planes as follows:

$$\frac{d\theta(0)}{dx} = 0 \text{ and } \frac{d\theta(l)}{dx} = 0 \tag{5.5}$$

By evaluating Eq. (5.4) with end conditions in Eq. (5.5) and by assuming a nontrivial solution, one obtains:

$$\sin\frac{\omega_n l}{V_S} = 0 \tag{5.6}$$

Therefore the circular frequencies of the natural modes of vibration of the free-free rod satisfying Eq. (5.6) are:

$$\omega_n = \frac{n\pi V_S}{l},\ n = 1,\ 2,\ 3,\ \ldots \tag{5.7}$$

Figure 5.7 shows the mode shapes at the first three resonances. Corresponding values of the wavelength at resonance can be determined as:

$$\lambda = \frac{2l}{n},\ n = 1,\ 2,\ 3,\ \ldots \tag{5.8}$$

which indicates the decrease of wavelength by ½ and 1/3 at higher modes from the wavelength at the first resonance mode or the increase of frequency by 2 and 3 times at higher modes from the one at the first resonance mode.

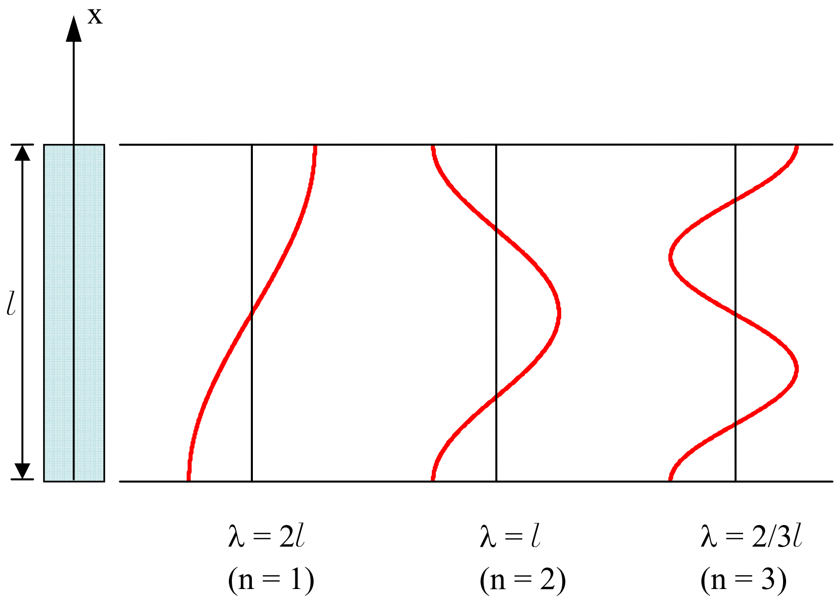

Figure 5.7 Rotation of a Rod in Torsional Vibration

For dynamic tests, instrumentation such as accelerometers and/or end platens is attached at either or both ends. The added masses may have a large enough mass or moment of inertia to alter the boundary condition in Eq. (5.5); that is, forces at the ends are not zero but equal to the inertia forces of the added masses. For the torsional excitation, Eq. (5.5) changes to:

$$GJ\frac{\partial\phi(0)}{\partial x} = I_1\frac{\partial^2\phi(0)}{\partial t^2} \text{ and } GJ\frac{\partial\phi(l)}{\partial x} = -I_2\frac{\partial^2\phi(l)}{\partial t^2} \qquad (5.9)$$

where, J = polar moment of inertia of the rod,

I_1 = mass polar moment of inertia of the added mass at x = 0, and

I_2 = mass polar moment of inertia of the added mass at x = l.

By combining Eq. (5.4) with Eq. (5.9) and assuming a nontrivial solution, we get:

$$\frac{(\mu_1+\mu_2)\beta_n}{\mu_1\mu_2\beta_n^2-1} = \tan\beta_n \qquad (5.10)$$

where, $\mu_1 = I_1/I$, where I = mass polar moment of inertia of the rod,

$\mu_2 = I_2/I$, and

$\beta_n = \omega_n l/V_S$.

The values of β_n satisfying Eq. (5.10) with the added mass conditions (I_1 and I_2) can be found by trial and error or graphically. Once the values of β_n are found, corresponding values of the wavelength can be determined as:

$$\lambda = \frac{2l}{\beta_n / \pi},\ n = 1, 2, 3, \ldots \tag{5.11}$$

In comparison with Eq. (5.8), the wavelength at resonance is $n\pi/\beta_n$ (n = 1, 2, 3, …) times that for the case without any added mass. In other words, the wavelength at resonance can be longer or shorter depending on the value of β_n; that is, when the value of β_n/π is larger than n (or β_n larger than $n\pi$), the added masses lead to a shorter wavelength (larger resonant frequency), and vise versa. To investigate the range of β_n, Eq. (5.10) can be rearranged as follows:

$$\frac{(\mu_1 + \mu_2)}{\dfrac{\mu_1\mu_2\beta_n^2 - 1}{\beta_n}} = \tan\beta_n \tag{5.12}$$

Furthermore, by assuming a nontrivial solution ($\beta_n = \omega_n l/V_S \neq 0$), the left hand side of this equation can be expressed as:

$$\frac{A}{B\beta_n - \dfrac{1}{\beta_n}} = \tan\beta_n \tag{5.13}$$

where, A and B are any positive values including zero and represent $\mu_1 + \mu_2$ and $\mu_1\,\mu_2$, respectively. It should be noted that if there is no added mass, the value of A ($=\mu_1 + \mu_2$) and B ($=\mu_1\,\mu_2$) are zero, then Eq. 5.13 becomes:

$$0 = \tan\beta_n \tag{5.14}$$

which means $\beta_n = n\pi$ (n = 1, 2, 3, …). Therefore, Eq. (5.11) becomes the same as Eq. (5.8). Moreover, if a mass is added to only one side, the value of B is zero and the left hand side of Eq. (5.13) becomes a function that linearly decreases with β_n. In the meanwhile, tan β_n on the right side of Eq. (5.13) is a function that increases from negative infinity to zero when β_n is between (2n-1)π/2 and (2n)π/2 (n = 1, 2, 3, …). Therefore, the intercepts of the two functions are always in this β_n range, and the β_n values at the intercepts are smaller than nπ (smaller than (2n)π/2), so that the added mass increases the wavelength at any resonance modes. If added masses are placed on both ends of the specimen and they have sufficiently large mass polar moments of inertia, the denominator of the left hand side of the Eq. (5.13) is positive in general (ignoring trivial cases of a very small β_n) and a continuously increasing function as β_n increases. Therefore, the left hand side of Eq. (5.13) should continuously decrease with β_n approaching zero at very high β_n because A is also positive. Since tan β_n increases from zero to infinity when β_n is between (2n-2)π/2 and (2n-1)π/2 (n = 1, 2, 3, …), the β_n values satisfying Eq. (5.13) are always smaller than (2n-1)π/2 (also smaller than nπ automatically) resulting in the increase of the wavelength at any resonance modes. The value of β for the first resonance mode is generally about 0.13 for the rock specimens studied in this research with the configuration of the added masses (details given in Section 5.3.2). The resulting wavelength at the first resonant mode becomes about $48.3l$. This is about 24 times longer wavelength compared with the wavelength in the case of no added mass.

5.2.1 Mass Polar Moment of Inertia of the Flexure Bearing Unit of the LgRC Device

As can be seen in Eq. (5.10), values of the mass polar moment of inertia for added masses on both ends of the specimen must be known to calculate the value of β_n. For parts machined in a regular shape, their mass polar moment of inertia (I_1 and/or I_2) can be easily calculated. When their shapes are irregular, it may be very hard to apply simple mathematical equations to the estimation of I_1 and/or I_2 value. For example, the drive plate for the combined resonant column and torsional shear (RCTS) device has a complex shape with various instrument and cables on top of the plate. Estimation of the mass polar moment of inertia for the drive plate (I_o) is performed experimentally. The value I_o is estimated based on the changes in resonant frequencies with added masses with simple shapes and known weights. In this estimation, the system is idealized as a single degree of freedom (SDOF) system and the relationship between resonant frequency and I_o is from the equation of motion of a SDOF system. The simple configuration of the fixed-free specimen allows this process to be reasonable; that is, the drive plate and added masses are located at only one end of the test specimen and they have a sufficiently larger mass polar moment of inertia. However, masses are added to both ends of the LgRC test specimen and their I_1 and I_2 values are not necessarily same, which means displacements at the top and bottom of the specimen can be different. Therefore, the approach with a SDOF system is not appropriate for the LgRC specimen and a new calibration method is needed.

In the section below, the procedures to estimate the value of I_o in a fixed-free configuration is reviewed first. The new calibration approach to estimate the value of mass polar moment of inertia of the drive table and associated mass assembly for the configuration of the LgRC device is then proposed.

5.2.1.1 Mass Polar Moment of Inertia of Drive Plate for Fixed-Free Specimen Configuration for the RCTS Device

The determination of the mass polar moment of inertia of the drive plate of the RCTS device is performed by using brass specimens. Figure 5.8 shows the brass specimens used to calibrate the RCTS device. The metal specimens are either solid or tube-type-rods connected to the top and bottom plates by welding. The purpose of the top and bottom plates is merely to allow the metal rod to be attached to the fixed base and the drive plate of the RCTS device. The metal specimen is placed in the position of the soil specimen in this configuration. It is worthwhile noting that the dimensions and sitffnesses of the metal specimens were selected to cover the various frequency ranges encountered in fixed-free RCTS testing of geomaterials (Hwang, 1997). The brass specimens are used in calibration as a standard material because its dynamic properties are independent of testing conditions such as loading frequency, shearing strain and time.

Figure 5.8 Metal Specimens Used in Calibration of the Fixed-Free Resonant Column and Torsional Shear (RCTS) Device

After the base plate of the brass specimen is fixed to the test table, the drive plate of the RCTS device is rigidly connected to a brass specimen using four screws. This configuration is considered to represent a single-degree-of-freedom (SDOF) system; that is, a mass with a rotational spring and a damper. The equation of motion of this system without a forcing function can be expressed as:

$$I_{tm}\ddot{\phi} + c\dot{\phi} + k\phi = 0 \tag{5.15}$$

where, I_{tm} = mass polar moment of inertia of the top mass,

c = damping coefficient of the torsional spring (test specimen),

k = the torsional spring constant (torsional stiffness of test specimen),

ϕ = rotational displacement (angle of twist),

$\dot{\phi}$ = the first derivative of rotational displacement, and

$\ddot{\phi}$ = the second derivative of rotational displacement.

The resonant frequency (f_r) measured by the fixed-free resonant column (RC) test is:

$$f_r = f_n\sqrt{1-D^2} \tag{5.16}$$

where, f_n = natural frequency of the brass specimen

D = material damping ratio of the brass specimen.

Assuming small damping of the brass specimen, Eq. (5.16) is close to be:

$$f_r \cong f_n = \frac{1}{2\pi}\sqrt{\frac{k}{I_o + I_t}} \tag{5.17}$$

where, k = torsional stiffness of the brass specimen

I_o = mass polar moment of inertia of drive plate, and

I_t = mass polar moment of inertia of the top plate of the brass specimen.

Another fixed-free RC test is then performed with an additional mass. This additional mass has a regular shape and its mass polar moment of inertia (ΔI) of this mass has been calculated based on its dimensions and weight. The measured resonant frequency (f_{r1}) with this mass is:

$$f_{r1} \cong \frac{1}{2\pi}\sqrt{\frac{k}{I_o + I_t + \Delta I}} \tag{5.18}$$

By combining Eq. (5.17) and Eq. (5.18), one can find:

$$\frac{f_r}{f_{r1}} = \sqrt{\frac{I_o + I_t + \Delta I}{I_o + I_t}} \tag{5.19}$$

Since I_o is the only unknown in Eq. (5.19), the value of I_o can be obtained as:

$$I_o = \frac{\Delta I}{(f_r / f_{r1})^2 - 1} - I_t \tag{5.20}$$

5.2.1.2 Mass Polar Moment of Inertia of Drive Table for Free-Free Specimen Configuration of the LgRC Device

The same brass metal specimen used for the fixed-free resonant column system is used to estimate (determine) the mass polar moment of inertia of the drive table and the associated added mass assembly for the LgRC device. The bottom plate of the brass specimen is screwed to the connection plate that is attached to the drive table of the torsional shaker as shown in Figure 5.9. The plate is made of Aluminum Alloy 2024, and it provides a rigid connection between the specimen and the drive table. The motion at the specimen bottom is monitored with an accelerometer attached to the connection plate. Another circular metal plate made of the same material, Aluminum Alloy 2024, is coupled on top of the brass specimen for the purpose of reducing the resonant frequency of the specimen as shown in Figure 5.9. The motion at the top end of the metal specimen is monitored with an accelerometer attached to this top mass plate.

When the specimen is twisted about its longitudinal axis, both top and bottom ends of the specimen rotate and rotational displacements within the specimen occur. The magnitude of the displacements can be different and out-of phase as discussed in previous section. Therefore, this configuration is idealized as a two degree of freedom system (2DOF) for this research, as illustrated in Figure 5.9. The first rotational mass with the mass polar moment of inertia of I_{bo} represents a combination of masses connected to the bottom of the brass specimen, which consists of the connection plate, the drive table, accelerometers and their cables, the flexure bearing unit, and the voice coil assembly. The support of this combined bottom mass is considered as a torsional spring with a stiffness of k_1. This spring is fixed to the shaker body. The second spring represents the brass specimen and the mass on top of the brass specimen has a mass polar moment of inertia of I_{tp} as seen in Figure 5.9. Note that the brace specimen and the support of the combined bottom mass have small material damping ratios as discussed earlier, thus dampers are not included in the system.

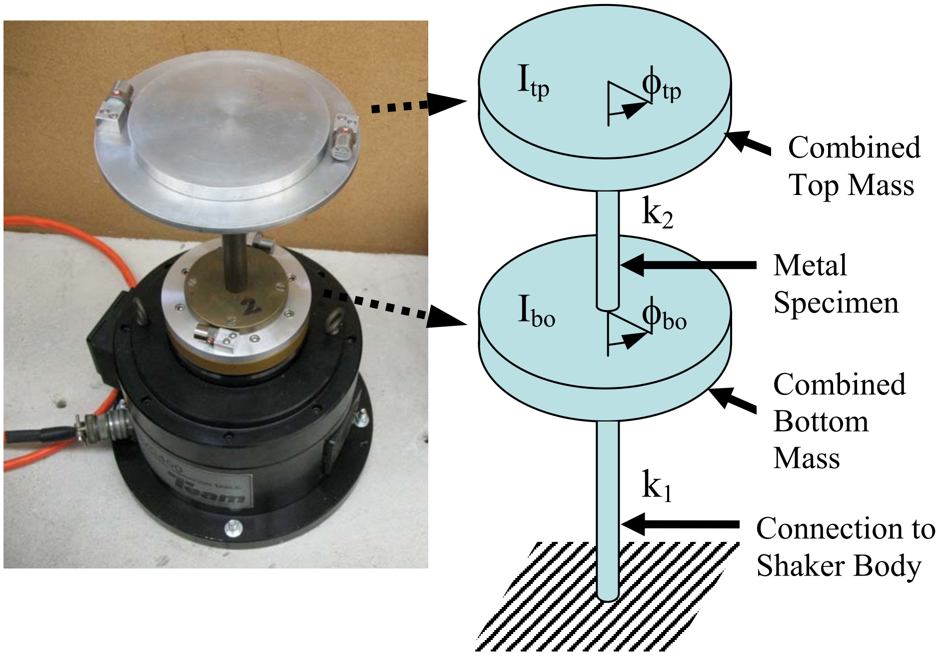

Figure 5.9 Idealized Two-Degree-of-Freedom System for the LgRC Test Set-Up with Metal Specimen No. 2

By considering the free-vibration case, the equations of motion for this system can be expressed as:

$$I_{bo}\ddot{\phi}_{bo} + (k_1 + k_2)\phi_{bo} - k_2\phi_{tp} = 0 \tag{5.21}$$

$$I_{tp}\ddot{\phi}_{tp} + k_2(\phi_{tp} - \phi_{bo}) = 0 \tag{5.22}$$

where, I_{bo} = mass polar moment of inertia of the combined bottom mass,

I_{tp} = mass polar moment of inertia of the combined top mass,

k_1 = torsional spring constant for the connection of the bottom mass to the shaker body,

k_1 = torsional spring constant for the metal specimen,

ϕ_{bo} and ϕ_{tp} = rotational displacement of the combined bottom mass and the combined top mass, respectively,

$\dot{\phi}_{bo}$ and $\dot{\phi}_{tp}$ = the first derivative of ϕ_{bo} and ϕ_{tp}, respectively, and

$\ddot{\phi}_{bo}$ and $\ddot{\phi}_{tp}$ = the second derivative of ϕ_{bo} and ϕ_{tp}, respectively.

By assuming a nontrivial solution of these equations of motion, the resonant circular frequencies must satisfy the following:

$$(k_1 + k_2 - I_{bo}\omega_n^2)(k_2 - I_{tp}\omega_n^2) - k_2 = 0 \tag{5.23}$$

The torsional stiffness of the first spring is negligibly small compared with the one of the metal specimen. By eliminating k_1 in Eq. (5.23), the solution for ω_n becomes:

$$\omega_n = \sqrt{\left(\frac{1}{I_{bo}} + \frac{1}{I_{tp}}\right)k_2} \tag{5.24}$$

Furthermore, if I_{tp} is $I_{tm}/2$ (where I_{tm} is the mass polar moment of inertia of the top mass in the fixed-free RC test in Eq. (5.15)), I_{bo} is proportional to I_{tp} by a factor of α, and replace k_2 with k (where k is the torsional spring constant of the fixed-free RC test), Eq. (5.24) becomes:

$$\omega_n = \sqrt{\frac{2(\alpha+1)}{\alpha}}\sqrt{\frac{k}{I_{tm}}} \tag{5.25}$$

Figure 5.10 illustrates the variation of ω_n with the value of α. It is very interesting to point out that ω_n becomes $\omega_n = 2\sqrt{k / I_{tm}}$ when the value of α is unity. This frequency is two times higher than that of the SDOF system for the fixed-free resonant column test.

In other words, if the added mass of fixed-free SDOF system (I_{tm}) splits into two equal masses ($I_{tm}/2$ for each) and they are placed at each end, the resonant frequency of the specimen increases to the double in the free-free condition. When a larger mass is added at either side of specimen (hence, a larger α in Eq. (5.25)) and if the mass polar moments of inertia of the other mass is one half of the added mass of fixed-free SDOF system ($I_{tm}/2$), ω_n approaches $\sqrt{2}\sqrt{k/I_{tm}}$. This circular frequency is the one of the fixed-free SDOF system with an added mass on top having a mass polar moment of inertia of $I_{tm}/2$. Therefore, the free-free 2DOF system becomes a fixed-free SDOF system. Note that adding a mass at either side of the specimen does not make any difference in these observations because I_{bo} and I_{tp} can be interchangeable in Eq. (5.25).

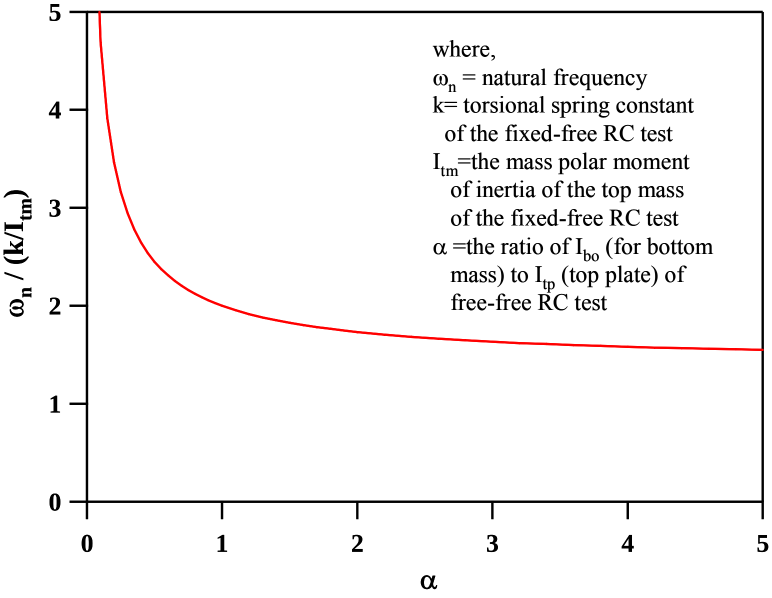

Figure 5.10 Change in Natural Frequency with Added Mass

For general cases where the added mass has an arbitrary value of the mass polar moment of inertia (I_a) and is added to I_{tp}, the reduced resonant frequency (ω_{nr}) of a specimen can be expresses as:

$$\omega_{nr} = \sqrt{\left(\frac{1}{I_{bo}} + \frac{1}{I_{tp} + I_a}\right) k_2} \tag{5.26}$$

The ratio of the two frequencies before and after adding I_a becomes:

$$\left(\frac{\omega_n}{\omega_{nr}}\right)^2 = \frac{(I_{bo} + I_{tp})(I_{tp} + I_a)}{I_{tp}(I_{bo} + I_{tp} + I_a)} \tag{5.27}$$

By solving Eq. (5.27) for I_{bo}, the value can be expressed as:

$$I_{bo} = I_{tp} \frac{(I_{tp} + I_a)\left((\omega_n / \omega_{nr})^2 - 1\right)}{I_{tp} + I_a - (\omega_n / \omega_{nr})^2 I_{tp}} \tag{5.28}$$

By using this equation, the mass polar moment of inertia of the added mass at the bottom of the specimen is determined based on the change in resonant frequency.

This process described above was followed in the calibration of the LgRC. Four different added masses are added to the top of a brass specimen as listed in Table 5.1. As shown in Table 5.1, the resonant frequency decrease from 112.73 Hz to 87.65 Hz as the mass polar moment of inertia at the top of the brass specimen increase by adding more added masses. The calculated value of I_{bo} is consistent and has a value of 1.062E-0.2 lb-ft-sec^2.

Table 5.1 Four Added Masses and Mass Polar Moment Inertia of Bottom Mass Assembly from Changes in the Resonant Frequency in Free-Free LgRC Tests

Added Mass No.	I_a (lb-ft-sec2)	$\sum I_a$ (lb-ft-sec2)	f_r, Hz	I_{bo} (lb-ft-sec2)
1	2.243E-03	2.243E-03	112.73	-
2	5.192E-04	2.762E-03	103.82	1.062E-02
3	1.365E-03	4.127E-03	89.43	1.062E-02
4	2.425E-04	4.370E-03	87.65	1.062E-02

5.2.2 Equivalent Shear Strain in the LgRC Test Specimen

As shown in Figure 5.6, the LgRC test specimen experiences shear strains during torsional vibration. The shear strain on the perimeter of the specimen can be expressed as:

$$\gamma = \frac{dz}{dx} \tag{5.29}$$

As with the fixed-free resonant column test, the configuration with the large added masses on the ends of the LgRC specimen allows an assumption that the shear strain on the specimen perimeter is constant and the torsional displacement is linearly distributed along the specimen length. At the first-mode resonant frequency of the specimen, the displacements at the top and bottom ends of the specimen are 180^{o} out of phase. Based on the assumption of constant shear strain, the shear strain can be considered as the change of relative displacement of the specimen top to the bottom along the specimen height as shown in Figure 5.11. Therefore, the shear strain at the perimeter of the specimen can be estimated from the summation of the rotational angles at the top and bottom of the specimen and can be written as:

$$\gamma_{\max} = \frac{r \cdot \left(\phi_{1\ \max} + \phi_{2\ \max}\right)}{H_t} \tag{5.30}$$

While the shear strain is constant along the specimen length, it varies along specimen radius. The shear strain at the center of the cylindrical specimen is zero simply because no displacement occurs at the specimen center. The shear strain increases as the distance from the center increases and reaches its maximum on the perimeter of the specimen. These characteristics of shear strain in torsion indicate a material whose stiffness varies with γ would also have stiffness varying along the specimen radius. Chen and Stokoe (1979) suggested a concept of an equivalent radius, r_{eq}, to average this variation.

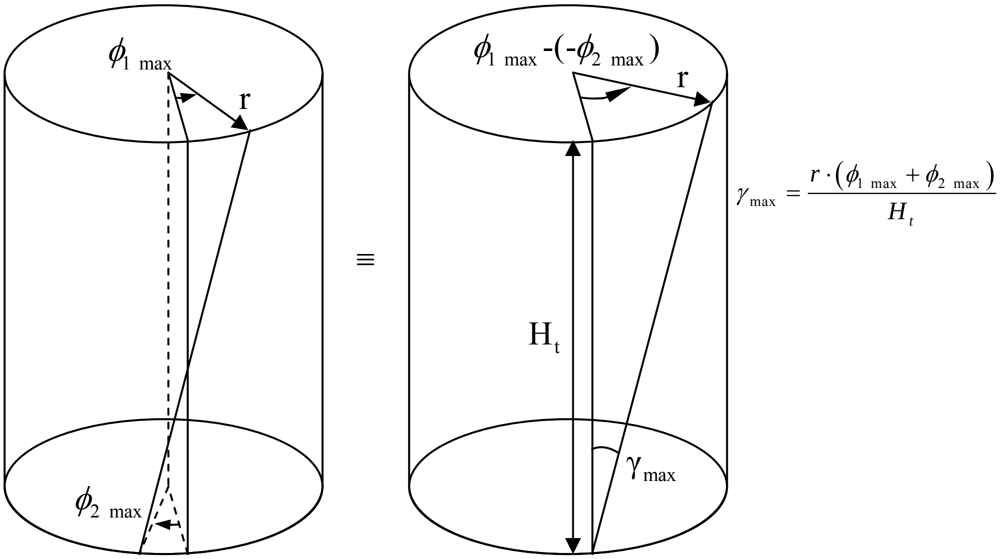

Figure 5.11 Shear Strain on the Perimeter of the Specimen in the LgRC Test

The authors suggested using an equivalent radius of 0.79 for the fixed-free specimens of soil. The same value is used for the LgRC test specimen when soil is tested and is as expressed below:

$$\gamma_{eq} = C\gamma_{\max} \tag{5.31}$$

where, γ_{eq} = equivalent shearing strain

C = the ratio of the equivalent radius to radius of the specimen (r_{eq}/r)

The displacement at the perimeter of the specimen is estimated based on the acceleration measured with an accelerometer. The accelerometer is located at the distance of d_a from the center of the specimen. The value of peak displacement measured by the accelerometer is:

$$Z_a = \frac{1}{(2\pi f_r)^2} \frac{32.2V_a}{F_a} \tag{5.32}$$

where, Z_a = peak displacement measured by the accelerometer (ft),

f_r = resonant frequency of the specimen (1/sec),

V_a = accelerometer output voltage (V), and

F_a = accelerometer calibration factor (V/g).

Furthermore the maximum rotation can be calculated using the value of Z_a as:

$$\phi_{\max} = \frac{Z_a}{d_a} \tag{5.33}$$

where, $\phi_{\max}$= maximum rotation, and

d_a = distance to the accelerometer from the center of specimen (ft).

By combining Eqs. (5.31), (5.32), and (5.33), the equivalent shear strain of the LgRC test specimen can be expressed as:

$$\gamma_{eq} = C\frac{r}{H_t}\frac{32.2}{\left(2\pi f_r\right)^2}\left(\frac{V_{a1}}{d_{a1}F_{a1}} + \frac{V_{a2}}{d_{a2}F_{a2}}\right) \tag{5.34}$$

where, V_{a1} and V_{a2} =output voltages of the accelerometers at the top and bottom of the specimen, respectively,

d_{a1} and d_{a2} = distances to the accelerometers at the top and bottom of the specimen, respectively, and

F_{a1} and F_{a2} = accelerometer calibration factors for the accelerometers at the top and bottom of the specimen, respectively.

It should be noted the γ_{eq} is related to the C value as shown in Eqs. (5.31 and 5.34). As noted earlier, the C of 0.79 for the fixed-free test specimens of soil is used for the LgRC specimen, so that comparisons of the results of a specimen tested with two different devices can be easily assessed. However, for competent rocks, γ_{eq} should be larger because of their large linear range until failure. Further study on this is required.

5.2.3 Equipment-Generated Damping in the LgRC Device

The forcing system of the torsional shaker relies on a voice coil actuator unit. The unit consists of four rotary voice coil actuators manufactured by BEI Kimco Magnetics.

The voice coil actuators are direct drive devices that utilize a permanent magnet field and coil winding (conductor) to produce a force that is proportional to the current applied to the coil. These non-commutated electromagnet devices are widely used in linear and rotary motion applications that require linear force or torque output over a wide range of frequencies and accelerations. On the other hand, the conductor moving through a magnetic field will have a voltage potential across the conductor. The voltage potential is called the back electro-magnetic force or back EMF. The current induced by the back EMF creates an additional magnetic force to the system. When a specimen is excited at different frequencies, the phase shift between the electro-magnetic force (EMF) used to drive the system and the specimen displacement (or coil displacement) varies; that is, it starts from zero at static excitation to 180^o out of phase at an infinitely high frequency of excitation. However, the back EMF is 180^o out of phase to the velocity of the coil regardless of frequency. Furthermore, the direction of the back EMF is just opposite to the EMF at resonance where the EMF is 90^o out of phase with the coil displacement. Therefore the back EMF acts like a viscous damper of the system throughout the resonance testing conducted in the LgRC. The back EMF is considered as a major component of equipment generated damping in the fixed-free resonant column and torsional shear (RCTS) device (Hwang, 1997).

Since the magnitude of back EMF is proportional to the velocity of the coil, the damping coefficient of the fixed-free resonant column system can be considered as a linear combination of the viscous damping coefficient for the specimen ($c_{specimen}$) and the back EMF ($c_{back\ EMF}$) (Menq. 2003). If a metal (brass) specimen is tested, the $c_{specimen}$ is small enough to ignore, so the measured material damping ratio is possibly considered to be the equipment generated damping ratio (D_{eq}). Therefore, the material damping ratio of the single degree of freedom system for a metal specimen can be written as:

$$D = \frac{c_{back\ EMF}}{2\sqrt{kI_s}} = D_{eq} \tag{5.35}$$

where, I_s is the sum of the mass polar moment of inertia of drive plate (I_o) and top cap (I_t) of the RCTS device. As seen in Eq. (5.35), equipment generated damping decreases as the stiffness of a test material increases. Note that the values of $c_{back\ EMF}$ and I_s are constant in a system. Since the stiffness of a test material is directly related to the resonant frequency of the material, equipment generated damping is inversely related to the resonant frequency. The trend of the change is linear on a log-log scale as can be seen in Eqs. (5.17) and (5.35). In summary, equipment-generated damping, expressed as an equipment-generated damping ratio, of a specific drive plate can be estimated by testing metal specimens having various resonant frequencies. Hwang (1997) reported that the equipment-generated damping in the fixed-free RC tests decreases with loading frequency with a slope of about negative one on a log-log scale.

For the LgRC tests, it is a bit more complicated to estimate the equipment-generated damping ratio from an equation like the fixed-free system that can be easily idealized as a SDOF system. Having the concept described above, equipment-generated damping for the LgRC device is determined experimentally. Six different brass specimens were tested in the condition with the Added Mass No 6 as shown in Figure 5.4. The weights and dimensions of these metal specimens are listed in Table 5.2. The equipment-generated damping ratio, D_{eq}, measured from the half-power bandwidth method linearly decreases as the resonant frequency of the specimen increases on a log-log scale, as shown in Figure 5.12 for frequencies between 50 and 100 Hz. This linear trend is similar to the one for the fixed-free RC test, but D_{eq} for the LgRC tests shows a faster decrease (larger negative slope) in D_{eq} with frequency; in other words, the slope of the trend line obtained with Added-Mass No. 6 is about -1.9 while the one for the fixed-

Table 5.2 Six Metal Specimens Used in Calibration of the LgRC Device

Metal Spec. No.	Height, inch (cm)	Outside Diameter, inch (cm)	Inside Diameter, inch (cm)	Weight, lb (g)
2	6.961 (17.68)	0.875 (2.223)	0.813 (2.064)	0.177 (80.36)
6	6.961 (17.68)	0.625 (1.588)	0.560 (1.423)	0.129 (58.45)
3	8.488 (21.56)	0.875 (2.223)	0.813 (2.064)	0.214 (97.07)
4	6.969 (17.70)	0.750 (1.905)	0.687 (1.746)	0.156 (70.72)
5	8.492 (21.57)	0.750 (1.905)	0.687 (1.746)	0.189 (85.87)
13	6.988 (17.75)	0.750 (1.905)	0.0 0.0	0.947 (429.52)

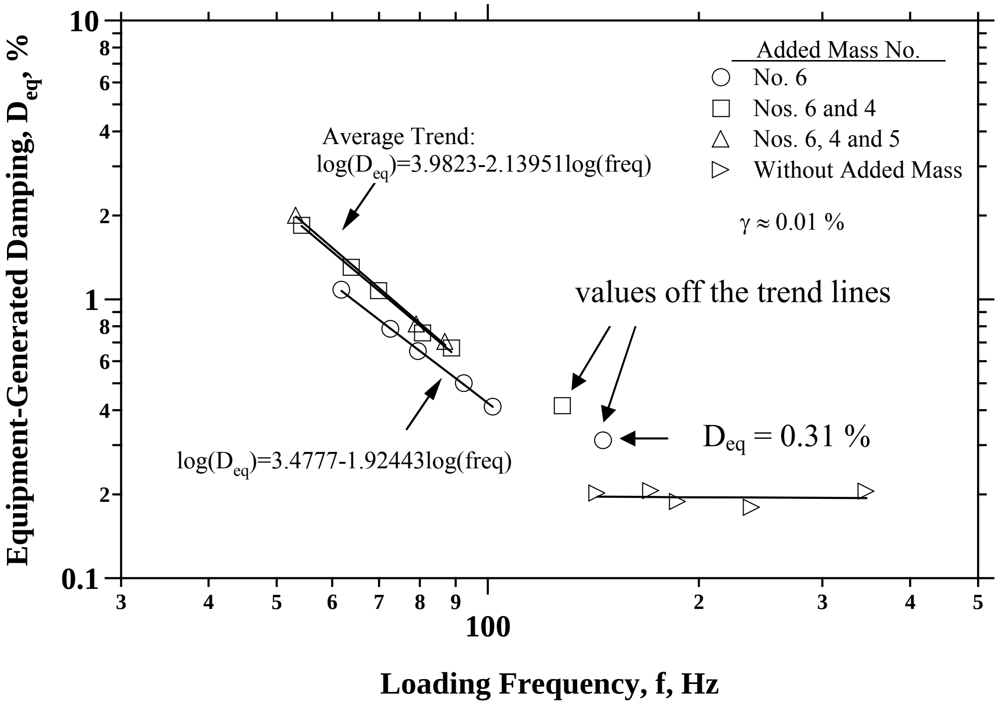

Figure 5.12 Change in Equipment-Generated Damping with Loading Frequency Using Half-Power Bandwidth Method

free RCTS device is about -1.0. It should also be noted that the least-squares fit line is shifted slightly upward when more masses are added. However, the slope of the line does not vary much. The slopes for the relationship with Added Mass Nos. 6 and 4 and Added Mass Nos. 6, 4, and 5 were -2.1142 and -2.1649, respectively. There is another important observation in D_{eq}; that is, the values of D_{eq} at frequencies higher than 100 Hz are off the trends as shown in Figure 5.12. Tests without any added mass exhibit negligible change in D_{eq} in the high frequency range. As a summary, since all tests in this study are being performed with Added Mass No. 6, the fitting equation shown in Figure 5.12 is used in determining the damping ratio from the half-power bandwidth method for the LgRC tests at frequencies below 100 Hz. For frequencies higher than 100 Hz, it is assumed that the D_{eq} is constant as a single value of 0.31 %.

Figure 5.13 shows the D_{eq} measured from free-vibration decay method for various metal specimens with various added-mass conditions. As observed in the half-power bandwidth method, equipment-generated damping decreases as loading frequency increases on a log-log scale. The slope of this linear trend is a bit stiffer than the one for D_{eq} from the half-power bandwidth method; when Added Mass No. 6 is used, the slope from the free-vibration decay curve is slightly larger, changing from -1.92443 to -2.4211. In addition, the value of D_{eq} increases when larger masses are added, but does not increase as much as the values of D_{eq} from the half-power bandwidth method. As observed in Figure 5.12, the values of D_{eq} at frequencies higher than 100 Hz are off the trends as shown in Figure 5.13. Tests without any added mass also show a negligible change in D_{eq} at frequencies above 143 Hz. As a summary, since all tests in this study are performed with Added Mass No. 6, the fitting equation shown in Figure 5.13 is used to determine the damping ratio from the free-vibration decay curve for the LgRC tests at

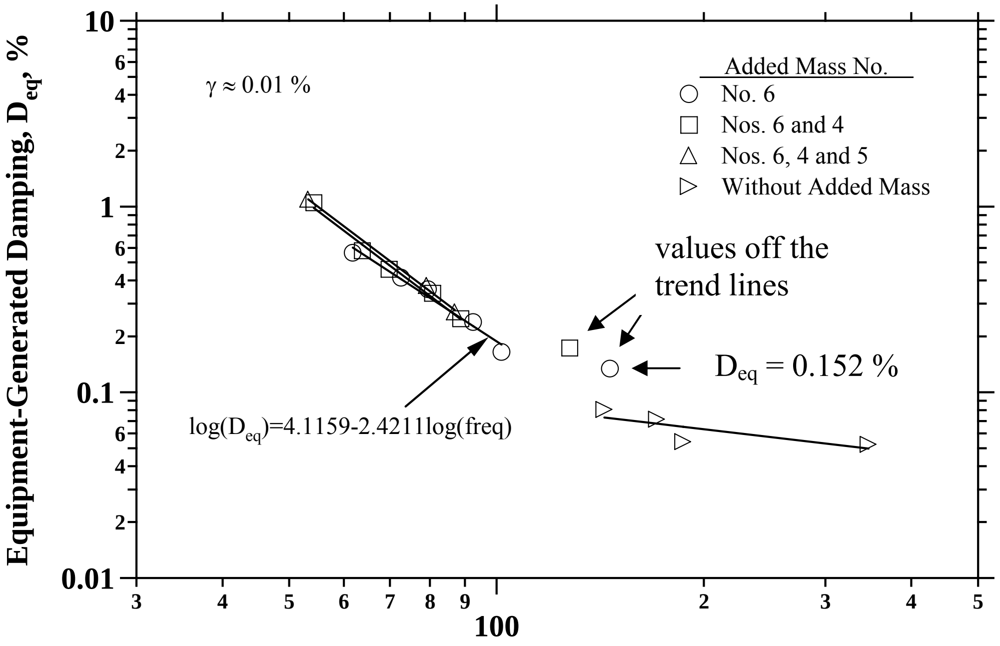

Figure 5.13 Change in Equipment Generated Damping in Free Vibration Decay with Loading Frequency

frequencies below 100 Hz. For the frequency range higher than 100 Hz, it is assumed that the D_{eq} is constant as a single value of 0.15 %.

It should be noted that the D_{eq} values of these metal specimens are independent of shearing strain (Hwang, 1997). However, the measured values of D_{eq} in the LgRC device exhibit a moderate dependency in the small-strain range of the metal specimens. The variation of the resonant frequency (f_r) and damping ratio (D) with shearing strain measured with Metal No.2 are illustrated in Figure 5.14 (a) and (b), respectively. As shearing strain increases, both values of f_r and D_{eq} decrease. These values, however, become stable when the shearing strain exceeds about 0.003 %. The driving input voltage (V_{in}) used for each strain level is shown in Figure 5.14 since it is directly related

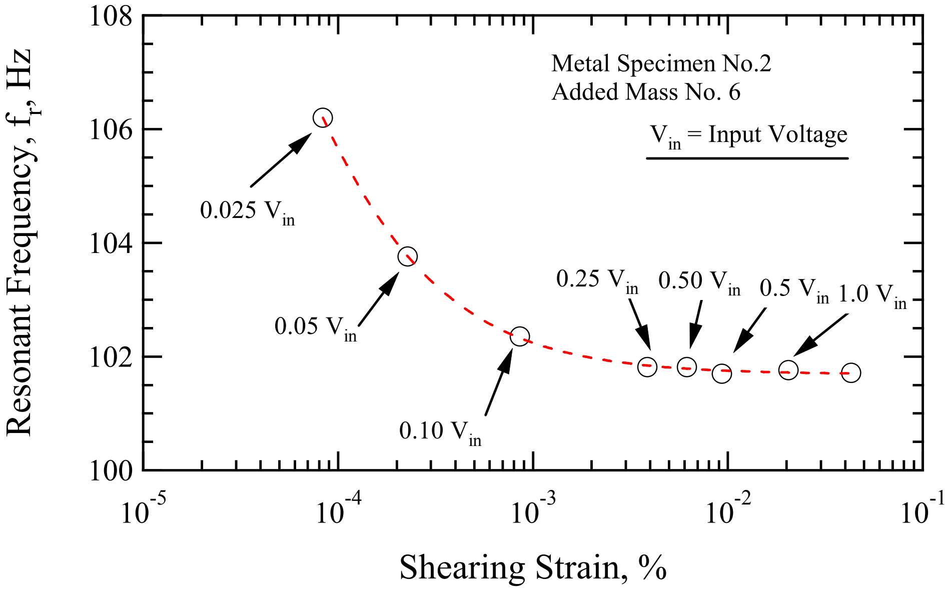

(a) Variation of Resonant Frequency with Shearing Strain Amplitude

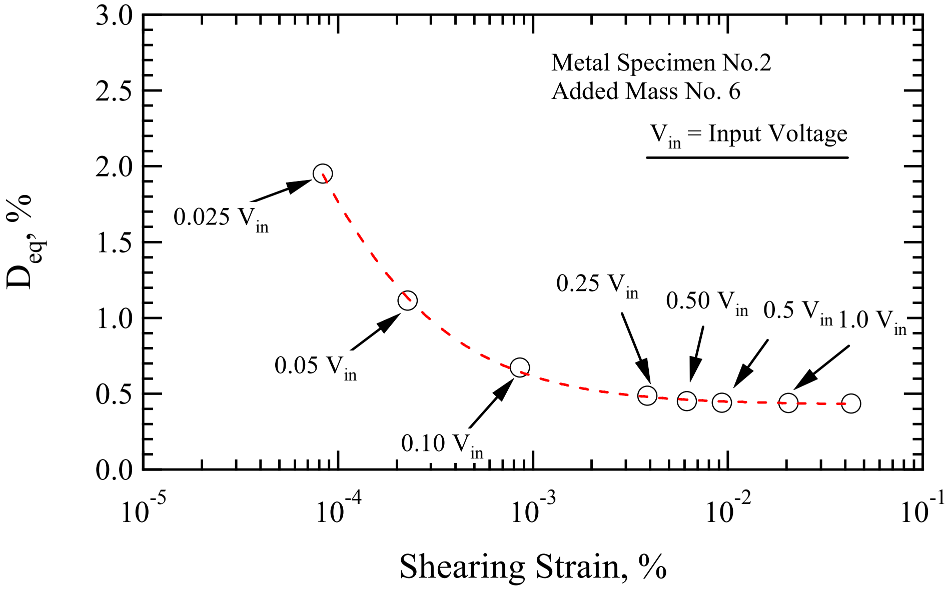

b) Variation of Equipment-Generated Damping Ratio with Shearing Strain Amplitude

Figure 5.14 Variation of Resonant Frequency and Equipment-Generated Damping Ratio in Free-Vibration Decay with Shearing Strain Amplitude to the shearing strain. It is observed that the values of f_r and D become independent or driving voltage (or shearing strain) when V_{in} is higher than 0.25 Volt. It is interesting to see the shape of the response curve when small input voltages are applied to drive the specimen. Figure 5.15 illustrates the response curves when tests were performed with four of the different driving voltages shown in Figure 5.14. It is thought that the metal specimen cannot be properly resonated at small input levels; therefore, the measured response curve is distorted (not smooth or nonsymmetrical about the f_r); in turn, the measured values of f_r and D may not properly represent the material properties for the metal specimens. This behavior is thought to be a part of the drive system compliance. All D_{eq} values used to obtain the trend discussed previously were measured at the shearing strain of about 0.01 % with about an input voltage of about 0.5 Volt.

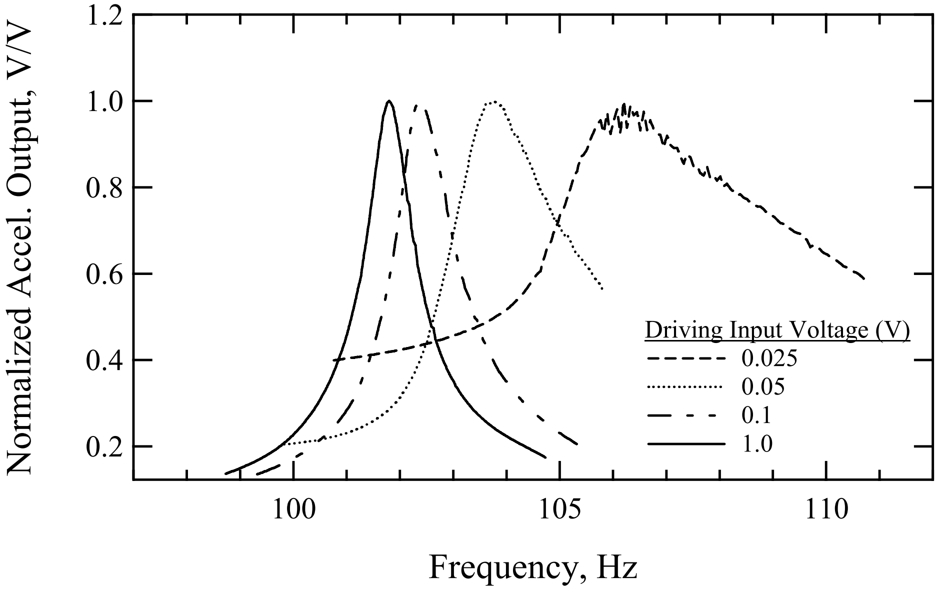

Figure 5.15 Variation of Frequency Response Curve with Driving Input Voltage

5.3 VALIDATION OF THE LgRC DEVICE

The LgRC device was set-up based on the background theory and calibration results discussed in the previous sections. The results obtained using the LgRC device are carefully reviewed and compared with ones obtained using the fixed-free resonant column tests on the same specimens. Two different specimens were used for the comparisons: a brass metal specimen and a tuff specimen from the Yucca Mountain site.

5.3.1 Validation with a Metal Specimen

Besides of the calibrations for equipment-generated damping ratio and mass polar moment of inertia of the drive table, tests on a metal specimen provides a verification of system compliance and any calculations associated with the test results; in other words, testing with a metal specimen has several benefits such as: (1) the material of the metal specimen, brass, is a common material and its mechanical properties are well-known and available in the literature, (2) the effects of testing conditions on the measured values (shear modulus and material damping ratio) are negligible as discussed in previous sections, and (3) the test results can be verified once again by comparing with the test results obtained with a different and independent device. The elastic characteristics in a large linear strain range of metal and their consistency with time allow this comparison to be made without other complications.

Metal Specimen No. 2 was dynamically tested using the LgRC device as shown in Figure 5.14. Metal Specimen No.2 has also been used to verify the system of the combined Resonant Column and Torsional Shear (RCTS) device. The mass polar moment of inertia of the drive plate and equipment-generated damping of the device are estimated using this metal specimen. The Metal Specimen No.2 is tube type (a hollow specimen) connected to the top and bottom plates by welding. The information on Metal

Specimen No.2 is listed in Table 5.3. The drive table and the connection plate of the LgRC device have the same screw-hole patterns as the drive plate and the base plate of the RCTS device. Therefore, the metal specimen can be set-up without any additional connecting material as shown in Figure 5.16. The mass polar moment of inertia (I) values for all materials of the set-up shown in the figure were for the calculation of the β value. These values are listed in Table. 5.4. As shown in the table, the sum of the I values for the masses added to the top of the specimen is about 0.00281 ft-lb-sec^2. This value is only about 27 % of the sum of the I values for the masses connected to the specimen bottom, which is about 0.0106 ft-lb-sec^2. Therefore, the top end of the specimen rotates more than the bottom end of specimen, and, in turn, the nodal point at the first mode of resonance is located below the center of the specimen. The calculated displacements at both ends and location of the nodal point are discussed below.

(a) Metal Specimens with the Torsional Shaker

(b) Metal Specimen No.2

Figure 5.16 Metal Specimen No. 2 Used in Validation Tests

Table 5.3 Information on Metal Specimen No. 2

Material	Brass	
Height, inch (cm)	6.961	(17.7)
Outside Diameter, inch (cm)	0.875	(2.22)
Inside Diameter, inch (cm)	0.813	(2.06)
Weight, lb (g)	31.64	(80.4)
Unit Weight, pcf (g/cm^3)	530.0	(8.49)

Table 5.4 Mass Polar Moment of Inertia Values of Metal Specimen No.2 and Top and Bottom Added Masses

Mass	I, ft-lb-sec^2
Top Plate + Top Accelerometer	2.76E-03
Top Plate of Metal Spec. No. 2	5.25E-05
Metal Spec. No. 2	6.81E-06
Bottom Plate of Metal Spec. No. 2	8.24E-04
Bottom Mass* + Bottom Accelerometer	9.79E-03

Note: *drive table, flexure bearing unit and coil assembly of the torsional shaker

The response curves obtained from the output of the top and bottom accelerometers are shown in Figure 5.17. Both response curves are smooth and symmetric about their resonant frequencies. The resonance frequencies and material damping ratio values from the curves are identical as 103.8 Hz and 0.42 %, respectively.

It should be noted that the charge amplifier setting of the top accelerometer was 10 times higher (top accelerometer output signal is attenuated by a factor of 10) is than that (no attenuation) of the bottom accelerometer. Therefore, the peak voltage output from the bottom accelerometer is actually higher than that from the top accelerometer in the figure. The phase shift of the signal at the top of the specimen relative to its base is about 180 degree throughout the swept-range, as shown in Figure 5.18. However, the phase values shown in the figure are about zero because the top and bottom accelerometers are physically oriented in opposite directions (180 degree out-of-phase).

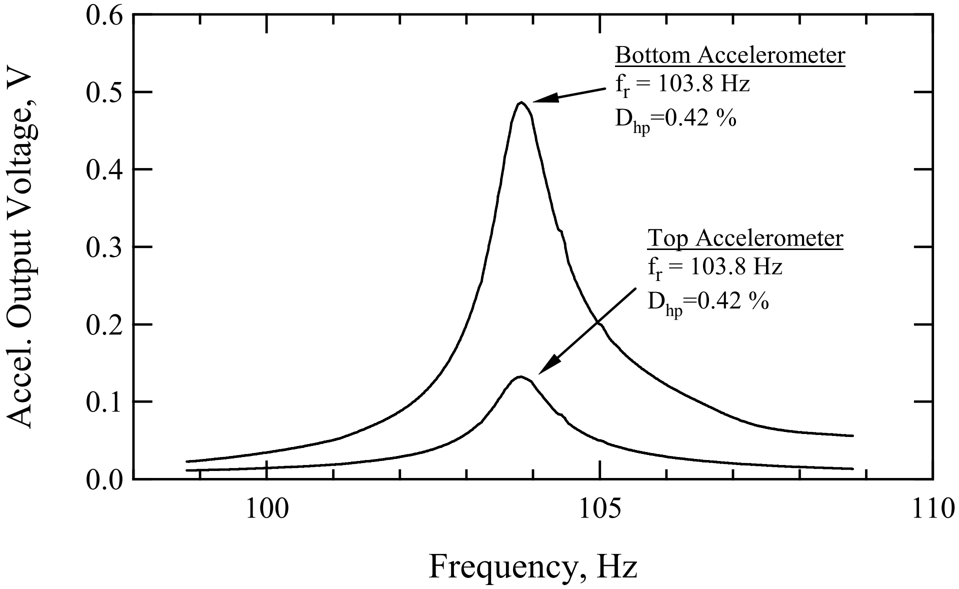

Figure 5.17 Response Curves from Outputs of Accelerometers Located at the Top and Bottom of Metal Specimen No. 2

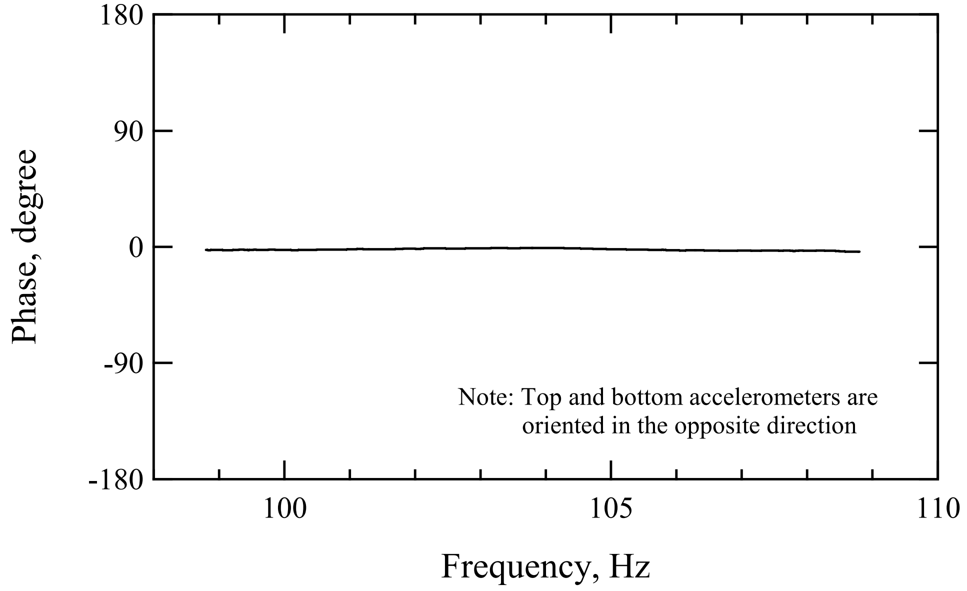

Figure 5.18 Phase Shift between Outputs of the Top and Bottom Accelerometers

On the other hand, displacements on the specimen perimeter at the top and bottom are estimated based on the locations of accelerometers and their measured peak voltage output values. The β value calculated from the configuration of the specimen itself and added masses is about 0.0553. This low β value leads to a long wavelength of 114L. Therefore, it can be assumed that the displacement on the perimeter of the specimen changes linearly as shown in Figure 5.19. The location of the nodal point is about 1.50 in. above the base of the specimen based on the geometry of displacement values and specimen length.

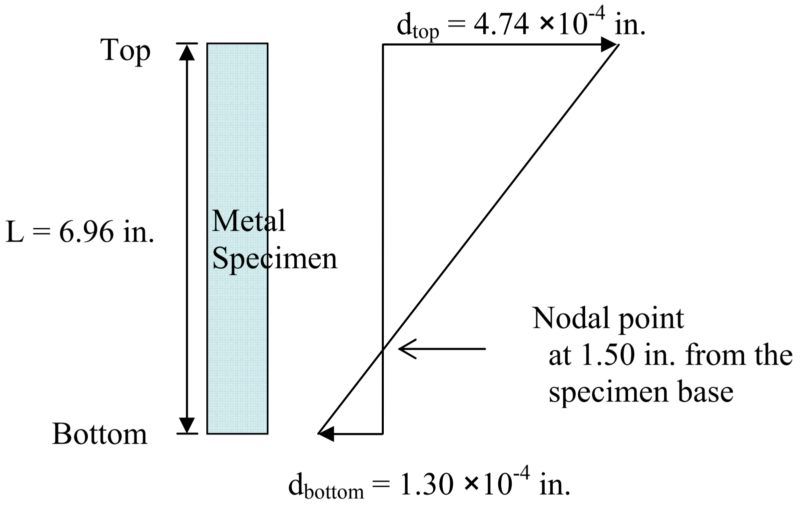

Figure 5.19 Displacement on the Perimeter of Metal Specimen No. 2 at Resonance

Figure 5.20 shows free-vibration decay curves measured from the top and bottom accelerometers. The first ten free-vibration cycles are used for the material damping ratio in each decay. The calculated values are identical and are equal to 0.21 %.

The resulting parameters obtained from the LgRC tests are listed in Table 5.5 along with ones obtained from the fixed-free RC tests. Shear wave velocity was calculated based on the resonant frequency measured from the response curve in each device. Note that the response curve obtained from the top accelerometer of the LgRC device was used although there is no difference in top and bottom responses as discussed previously. Most of the values obtained from the two different devices are very close to each other. Shear wave velocity and shear modulus values are almost identical and even the material damping ratio from the half-power bandwidth method (D_{hp}) are very close in each device. The major difference is the material damping ratio obtained from the free-vibration decay (D_{fv}). The D_{fv} value is about the half of the D_{hp} value in LgRC tests, while those from the fixed-free RC tests show small difference. (0.1 %). The difference

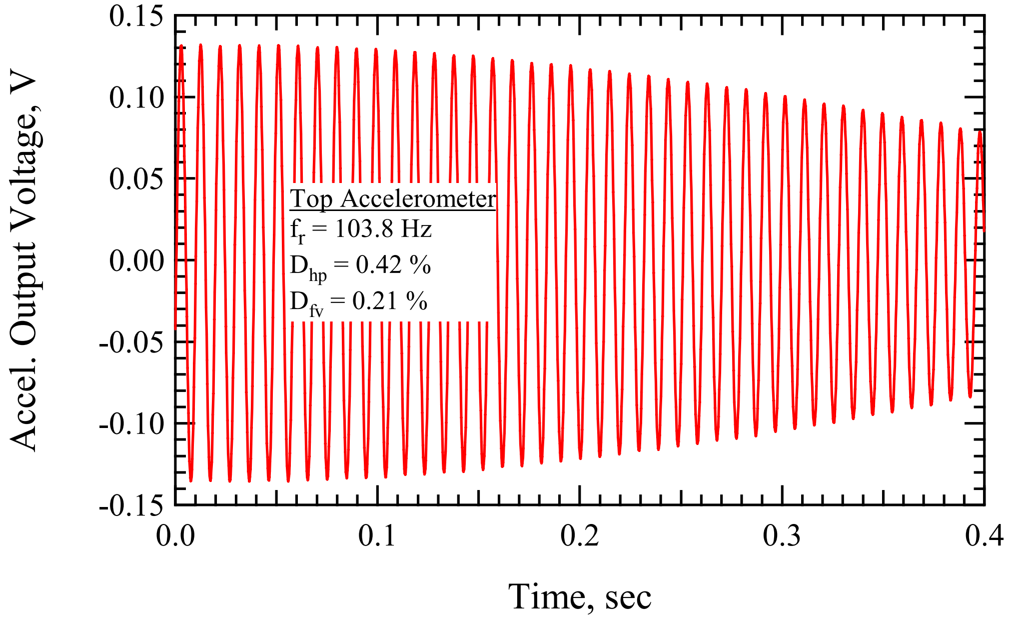

(a) Free-vibration decay curve measured with the top accelerometer

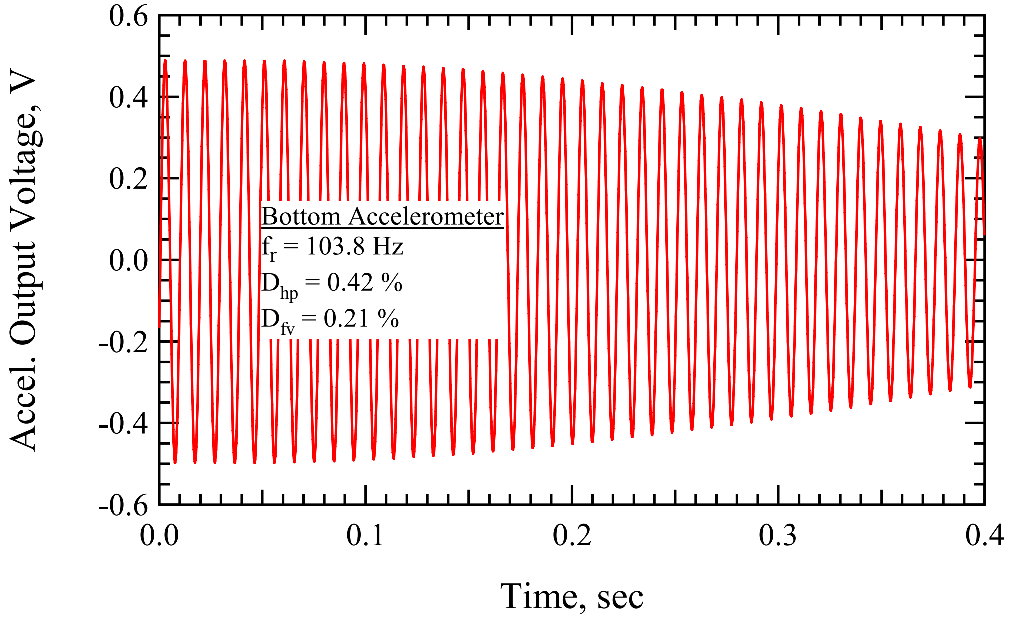

(b) Free-vibration decay curve measured with the bottom accelerometer

Figure 5.20 Free-Vibration Decay Curves Measured on Metal Specimen No. 2 by: (a) top accelerometer and (2) bottom accelerometer

Table 5.5 Comparison of Test Results from the LgRC Device with Test Results from the RCTS Device

Test Device	f_r, Hz	V_S, ft/sec (m/sec)	G_{max}, lb/ft^2 (Gpa)	D_{hp}, %	D_{fv}, %
RCTS	104.1	6842 (2085)	7.71E+08 (36.9)	0.48	0.47
LgRC	103.8	6840 (2085)	7.71E+08 (37.0)	0.42	0.21

was observed with different metal specimens as discussed previously in the discussion about the equipment-generated damping of the LgRC device. Further discussion of this point is presented in following section where the test results with a rock specimen are shown.

5.3.2 Validation with a Rock Specimen

As with the metal specimen, a rock specimen was tested to verify the LgRC test and procedure. The main purpose of rock testing is measurement in the nonlinear range of a real geotechnical material. The metal specimen is nearly elastic and has a large linear range, so that the changes in modulus and material damping ratio with strain are not observed in the testing range. Moreover, rock specimens are the material to be tested in the new device. By testing a rock specimen, one can evaluate any potential effects associated with the coupling issue between rock and the top cap and base pedestal, inhomogeneity in the material, and/or resonant frequencies and nonlinearities.

A rock specimen from the Calico Hill (Tac) formation at the Yucca Mountain site was selected and tested with both RCTS and LgRC devices. The rock from this formation is relatively homogeneous and has fewer fractures. In addition, the rock exhibits a bit lower stiffness compared with nonlithophysal units in the Topopah Spring formation, so that higher shearing strains can be reached even if their dimensions are similar to stiffer test specimens. Figure 5.21 shows the Tac specimen set-up in the LgRC device with Added Mass No. 6 and top and bottom accelerometers. The mass polar moment of inertia values for all the materials were determined prior to the tests and the values are listed in Table. 5.6. The β value from these configuration of specimen and added mass is about 0.125. This low β value leads to the long wavelength of about 50L. Therefore, it can be assumed that the displacement on the perimeter of the specimen changes linearly as in the case for the metal specimen.

The $G - \log \gamma$, $G/G_{max} - \log \gamma$, and $D - \log \gamma$ relationships determined using the two different devices are presented in Figures 5.22 through 5.24, respectively. The fixed-free RC tests were performed first. The small-strain shear modulus determined from the fixed-free RC test was about 86400 ksf (4137 MPa) at γ of about 0.0005 %. As γ increased, G decreased. When γ value reached about 0.02 %, G value was about 82700 ksf (3960 MPa) as shown in Figure 5.22. The corresponding normalized shear modulus (G/G_{max}) at this strain level was about 0.96. Tests were stopped at this γ to avoid any significant de-coupling of the specimen with the top and bottom masses. The G_{max} was determined again from the fixed-free RC tests after the highest straining (0.02 %). No significant changes were measured for the specimen. Significant changes are defined as a change of 5 % in G_{max} and 10 % in D_{min}.

The G values determined using the LgRC device in general exhibited a good agreement with the G values determined using the RCTS device as shown in Figure 5.22. The G_{max} value from the LgRC tests was about 88640 ksf (4244 MPa). This is only 3 %

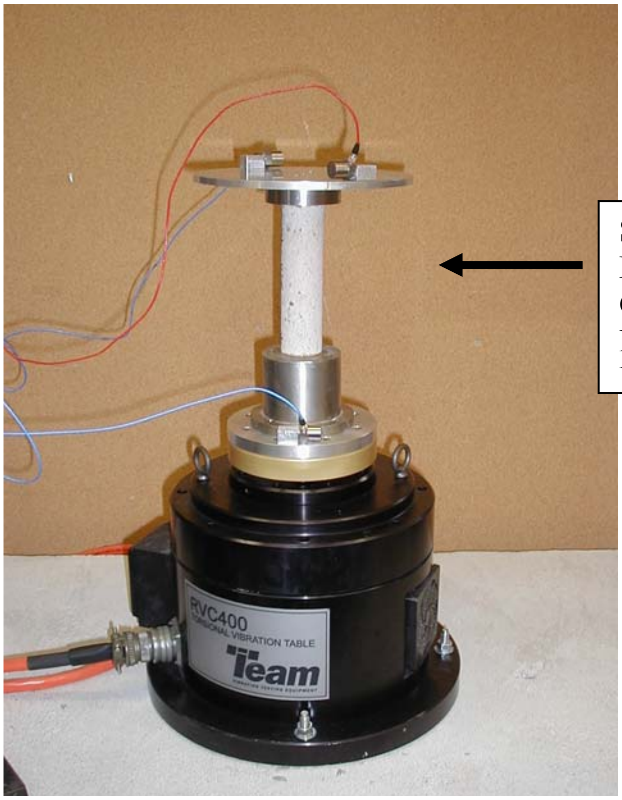

Specimen UTA-42-AH (34C):
Borehole: USW SD-12 at Yucca Mt. site
Geologic Formation: Calico Hill (Tac)
Height = 5.63 in. (14.3 cm)
Diameter = 1.56 in. (3.96 cm)

Figure 5.21 Specimen UTA-42-AH (34C) Set-Up in the Large Resonant Column (LgRC) Device

Table 5.6 Mass Polar Moment of Inertia Values of Calico Hills Specimen and Added Masses

Mass	I, ft-lb-sec^2
Top Plate + Top Accel.	2.76E-03
Top Cap	2.67E-04
Specimen	3.76E-05
Pedestal	1.70E-03
Bottom Mass + Bottom Accel.	9.79E-03

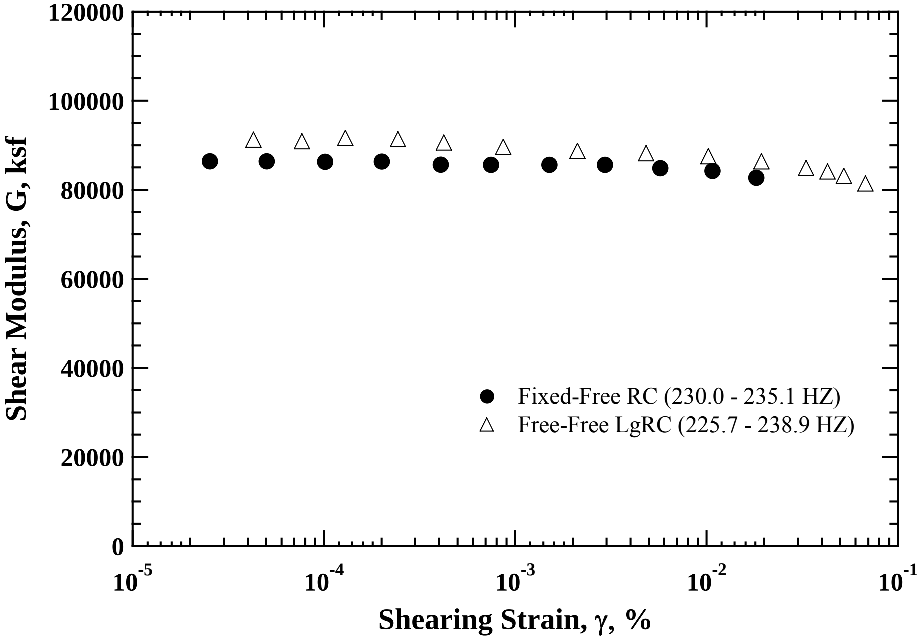

Figure 5.22 Variation of Shear Modulus with Shearing Strain Determined from Fixed-Free RC Tests and Free-Free LgRC Tests; Calico Hills Specimen

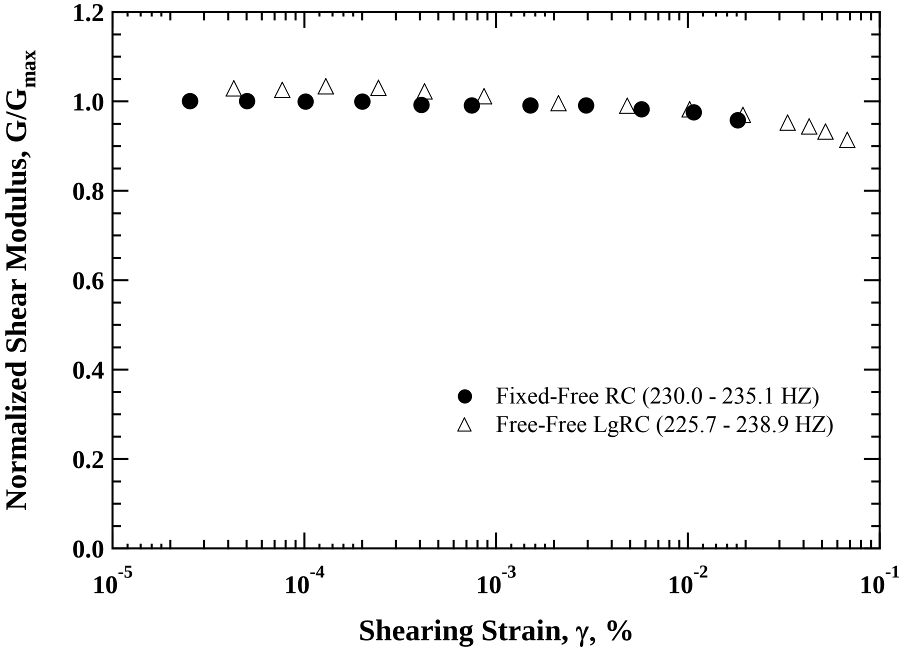

Figure 5.23 Variation of Normalized Shear Modulus with Shearing Strain Determined from Fixed-Free RC Tests and Free-Free LgRC Tests; Calico Hills Specimen

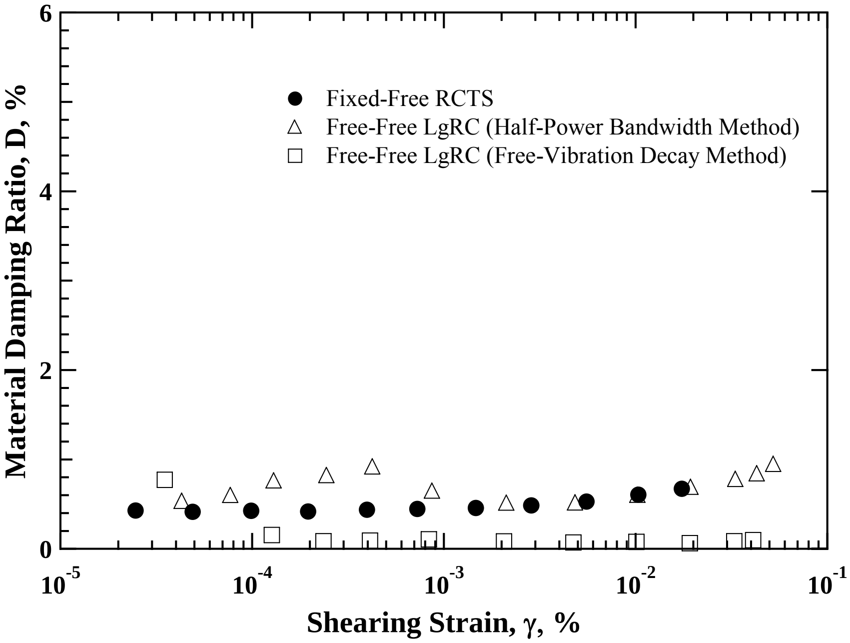

Figure 5.24 Variation of Material Damping Ratio with Shearing Strain Determined from Fixed-Free RC Tests and Free-Free LgRC Tests; Calico Hills Specimen

higher than the G_{max} from the fixed-free RC tests. It should be noted that the G value at γ of about 0.002 % was taken as G_{max} for the LgRC tests. As seen in Figure 5.22, the G values below this strain level (0.002 %) are higher than the G_{max}. This behavior is thought to be a part of the drive system compliance (see Section 5.2.3). The relatively larger material damping ratio values measured at γ below 0.002 % possibly indicate that the specimen could not be properly resonated at small input levels. When the largest input voltage was used, γ reached about 0.068 % and G/G_{max} reached about 0.91.

The D values determined from the fixed-free RC changed from 0. 42 to 0.67 % as γ increased from about 2×10^{-5} to 0.017 %. The D values determined from the LgRC tests using the half-power bandwidth method follow this trend from the fixed-free RC tests when γ is larger than 0.02 %. The D_{min} value determined from the LgRC tests at γ of about 0.002 % was about 0.51 %. This is only 0.09 % higher D_{min} in absolute value than the D_{min} from the fixed-free RC tests. However, the D values determined from the LgRC tests using the free-vibration decay method did not increase with γ as shown in Figure 5.24. It is thought that a bending mode is associated with the free-vibration decay. However, these is no measurement to support this hypothesis currently. The use of free-vibration decay method is limited and further study is required.

5.4 SUMMARY

General backgrounds related to the LgRC test is discussed in this chapter. A theoretical approach to estimate mass polar moment of inertia of the system is proposed for the LgRC device. The equations for the shearing strain estimation in free-free boundary condition and for the equipment generated damping estimation are also proposed and discussed. Validation of the system using a metal and a rock specimen is discussed.

Chapter 6

Small-Strain Dynamic Properties of Ash-Flow Tuff

6.1 INTRODUCTION

Stiffness and material damping of the ash-flow tuffs are discussed in this chapter. These dynamic material properties were evaluated based on test results only in the strain range where the dynamic properties are constant and independent of strain amplitude. This strain range is called the linear range, and measurements and dynamic properties in this strain range are often called small-strain or low-amplitude. The dynamic properties of the ash-flow tuffs are represented primarily by the values of shear wave velocity (V_S), shear modulus (G_{max}) and material damping ratio in shear (D_{min} or $D_{S,\ min}$). In addition, some small-strain measurements of Young's modulus (E_{max}), constrained compression modulus (M_{max}) and material damping ratio in unconstrained compression ($D_{C,\ min}$) were performed.

Small-strain testing was performed with both the unconfined, free-free, resonant column (URC) device and the combined resonant column (RC) and torsional shear (TS) device. The effects of lithostratigraphic characteristics were evaluated for the tuffs from the Topopah Spring Tuff formation at Yucca Mountain, Nevada and the Bandelier Tuff formation at Pajarito Plateau, New Mexico. The lithostratigraphic characteristics include lithophysal cavities, rims on lithophysae, spots, fractures, and degree of welding.

The G_{max} and D_{min} values of the tuffs measured at various confinement stages, including the unconfined state, are first discussed. The effects of lithophysal cavities, flaws (fractures and missing pieces of the core) and the degree of welding on G_{max} and D_{min} at different confinement pressures (σ_o) are discussed next. Correlations between G_{max} and γ_t and D_{min} and γ_t are studied. Then, the effects of excitation frequency (f), change in water content (w) due to specimen preparation, and large lithophysal cavities on G_{max} and D_{min} are discussed.

With the URC device, the compression mode as well as the shear mode was studied. The small-strain unconstrained compression modulus (also called Young's modulus) (E_{max}), constrained compression modulus (M_{max}), and material damping ratio in unconstrained compression ($D_{C,\ min}$) of the tuff specimens were evaluated. These data and correlations of these moduli and material damping ratios with γ_t are presented in Appendix A.

6.2 SMALL-STRAIN SHEAR MODULI OF ASH-FLOW TUFFS AT $\sigma_O = 0$

6.2.1 Topopah Spring Tuff

The small-strain shear wave velocities (V_S) of the 38 densely welded and crystallized specimens from the Topopah Spring Tuff are shown in Figure 6.1. The specimens were recovered from the six different zones of the formation (general characteristics including lithostratigraphic features in each zone are described in Chapter 2). A total of 22 specimens from the nonlithophysal zones and 16 specimens from the lithophysal zones were tested using the unconfined, free-free, resonant column (URC) device. The specimens were tested under conditions of: no confinement, air-dry and room temperature. On the whole, the values of V_S and total unit weight (γ_t) exhibit a strong correlation as shown in Figure 6.1. The values of V_S range from about 3686 to 9222 ft/sec (1123 to 2810 m/sec) for the specimens and the values of γ_t range from about 108.6 to 145.9 lb/ft^3 (1.74 to 2.33 g/cm^3). Since all specimens are densely welded, the

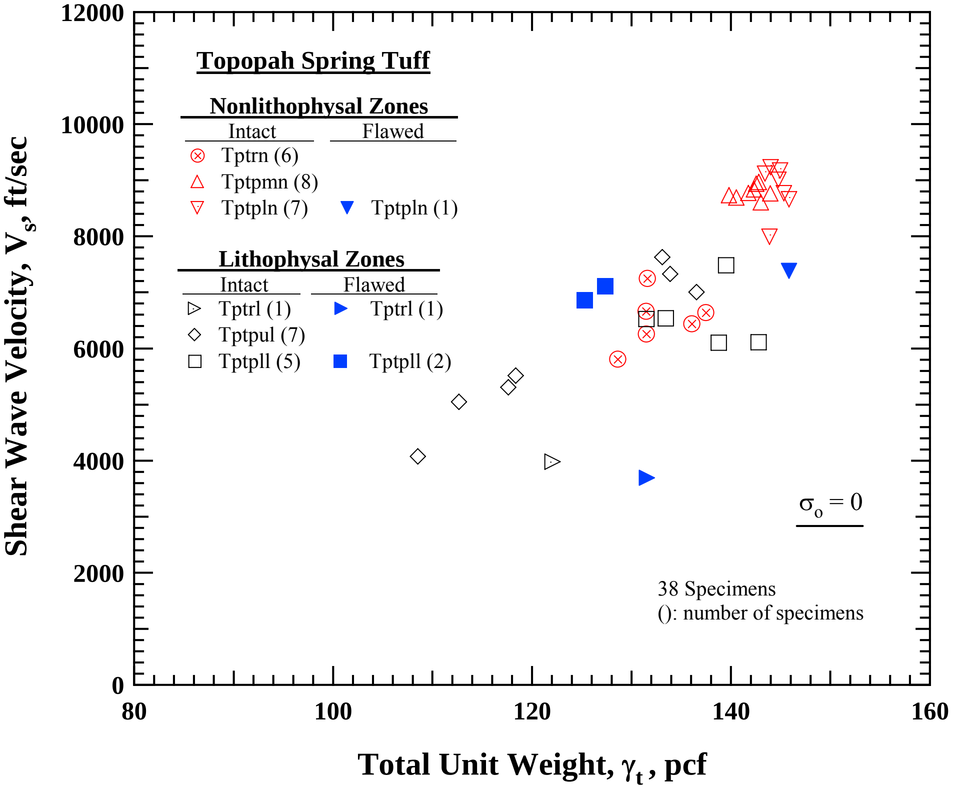

Figure 6.1 Variation of Small-Strain Shear Wave Velocity with Total Unit Weight from Unconfined, Free-Free Resonant Column (URC) Tests for Thirty-Eight Specimens from the Topopah Spring Tuff

differences in γ_t result mainly from the amount of lithophysal cavities in the specimens. As seen in the figure, nonlithophysal tuffs in the crystal-poor middle nonlithophysal zone (Tptpmn) and lower nonlithophysal zone (Tptpln) have very similar and high values of γ_t. The average value of γ_t is about 143 lb/ft^3 (2.3 g/cm^3) while the average γ_t of the lithophysal tuffs in the same crystal-poor member (the upper and lower lithophysal zones (Tptpul and Tptpll, respectively)) is about 129 lb/ft^3 (2.1 g/cm^3). The denser tuffs exhibit larger V_S values (8719 ft/sec on average) than the less dense tuffs (average V_S of 6327 ft/sec).

Tuffs in the crystal-rich nonlithophysal zone (Tptrn) have somewhat smaller γ_t and V_S values than the Tptpmn and Tptpln materials, although the Tptrn is a nonlithophysal zone. The average values of γ_t and V_S are about 132.8 lb/ft^3 (2.1 g/cm^3) and 6508 ft/sec (1984 m/sec), respectively, for the Tptrn. These values are rather close to the values of many tuffs from the upper and lower lithophysal zones in the crystal-poor member (Tptpul and Tptpll, respectively). The larger amount of vapor-phase corrosion (as defined by the corrosion of glass material in matrix-groundmass) and the larger portions of pumice clasts in these specimens contribute to the smaller values. Similarly, the tuffs from the Tptpul and Tptpll materials have generally smaller γ_t and V_S values than the Tptpmn and Tptpln materials due to the lithophysal cavities. It is interesting to note that the largest γ_t of these tuffs (142.8 lb/ft^3 (2.29 g/cm^3)) is very close to the average γ_t (143.5 lb/ft^3 (2.30 g/cm^3)) of the nonlithophysal tuffs from the Tptpmn and Tptpln materials. However, the V_S of the lithophysal specimen with the highest γ_t was only 70 % of the average V_S of the nonlithophysal rocks. This difference is indicative of the large effect of lithophysae on the small-strain dynamic properties of the specimen.

Besides the characteristics of relatively small γ_t and V_S values, the tuffs with lithophysal cavities exhibit larger variations in these values compared with the rocks with fewer (or none) lithophysal cavities as shown in Figure 6.1. The γ_t values of these specimens range from about 108.6 to 142.8 lb/ft^3 (1.74 to 2.29 g/cm^3) and their V_S values range from about 3686 to 7620 ft/sec (1123 to 2323 m/sec). The samples from the Tptpul unit have a greater range in the γ_t and V_S values than the Tptpll samples. Buesch (1996) reported a wide range in the amount of lithophysae in specimens from the Tptpul unit. Buesch found the Tptpul have lithophysae of 2 to 40 % of sample volume while the Tptpll have lithophysae of 1 to 7 % (locally 20 %) of sample volume.

Samples from the crystal-rich lithophysal zone (Tptrl) are within the ranges of γ_t in the Tptpul and Tptpll materials; however, their Vs values are slightly smaller. These relations in the Tptrl compared to the Tptpul and Tptpll are consistent with slightly increased amounts of vapor-phase corrosion in the matrix-groundmass and of pumice clasts in the Tptrl.

Variations in shear-wave velocities in samples within a specific lithostratigraphic zone, especially values that are outside the typical range for the zone, can be accounted for by the presence of specific lithostratigraphic features. Features that have the greatest effect on properties include: (1) the amount, sizes, and spacing (distribution) of lithophysal cavities, (2) small pore structures in features such as rims, spots, and the matrix-groundmass, and (3) fractures. Four samples that were affected (flawed) by these features are noted in Figure 6.1. These samples are denoted as "flawed" and were simply identified by eye. The samples are: the Tptrl sample that has missing pieces and large lithophysae; the two Tptpll samples that have fractures, missing pieces, and large lithophysae; and the Tptpln sample that has numerous small fractures. The photographs of the four samples flawed are presented in Figures 6.2a through 6.2d, respectively.

The small-strain shear moduli, G_{max}, of the specimens from the Topopah Spring Tuff are shown in Figure 6.2. Since G_{max} is directly calculated from the V_S and γ_t values and these two parameters are generally correlated, the G_{max} values are also generally correlated with the γ_t values. A semi-logarithmic (natural logarithmic) relationship between G_{max} and γ_t can be used to represent the trend as shown in Figure 6.3. The relationship can be expressed as:

$$G_{\max} = 274.2e^{0.0491\gamma_t} \qquad (6.1)$$

where G_{max} are in ksf and γ_t is in pcf. Eq. (6.1) can be expressed for SI units as:

$$G_{\max} = 13.13e^{0.00307\gamma_t} \qquad (6.2)$$

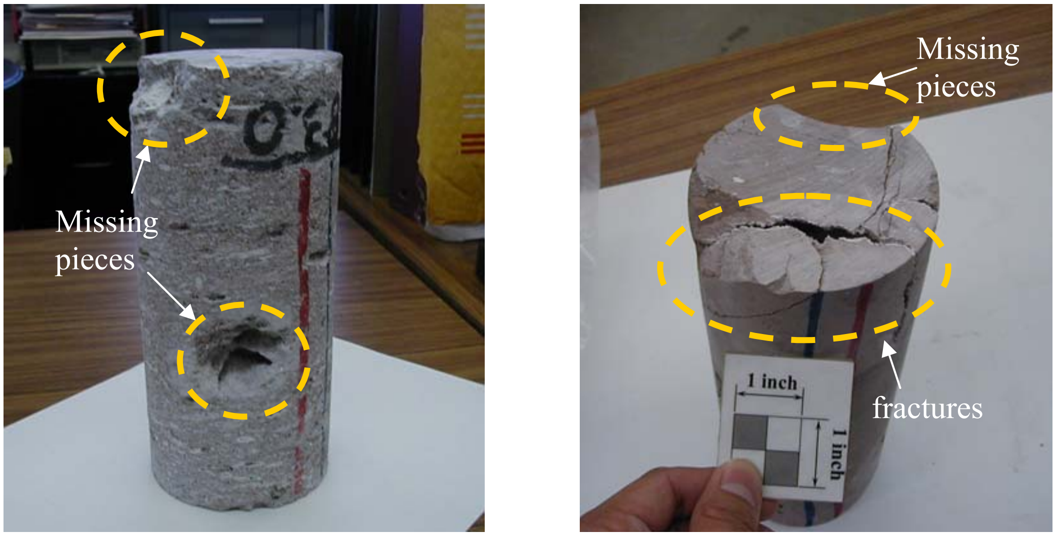

(a) Tptrl (γ_t = 131.6 pcf and V_S = 3686 fps) (b) Tptpll (γ_t = 125.3 pcf and V_S = 6862 fps)

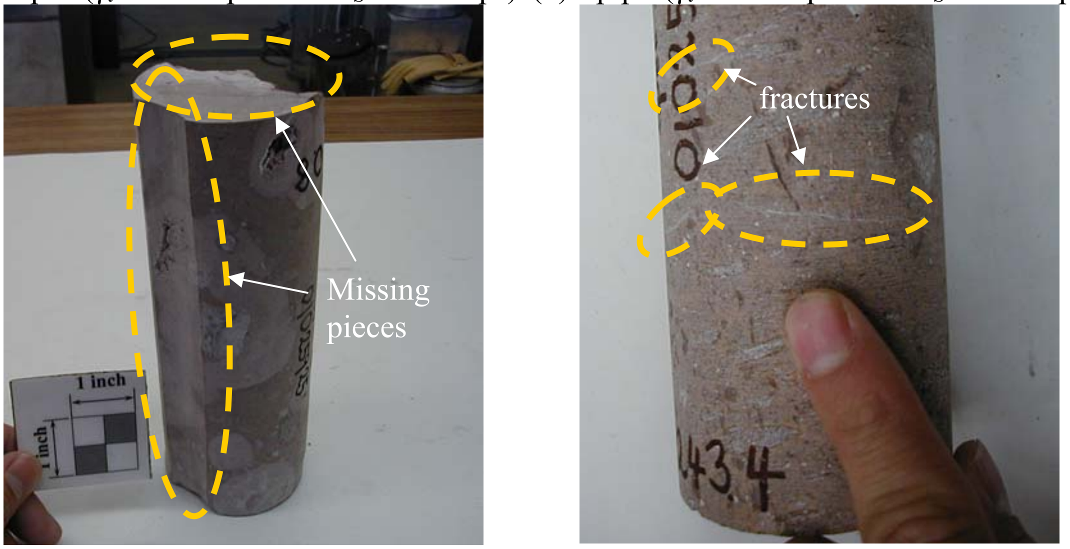

(c) Tptpll (γ_t = 127.4 pcf and V_S =7110 fps) (d) Tptpln (γ_t = 145.9 pcf and V_S = 7373 fps)

Figure 6.2 Four Flawed Samples from (a) the Tptrl (γ_t = 131.6 pcf and V_S = 3686 fps), (b Tptpll (γ_t = 125.3 pcf and V_S = 6862 fps), (c) Tptpll (γ_t = 127.4 pcf and V_S = 7110 fps), and (d) Tptpln (γ_t = 145.9 pcf and V_S = 7373 fps) Units from the Topopah Spring Tuff

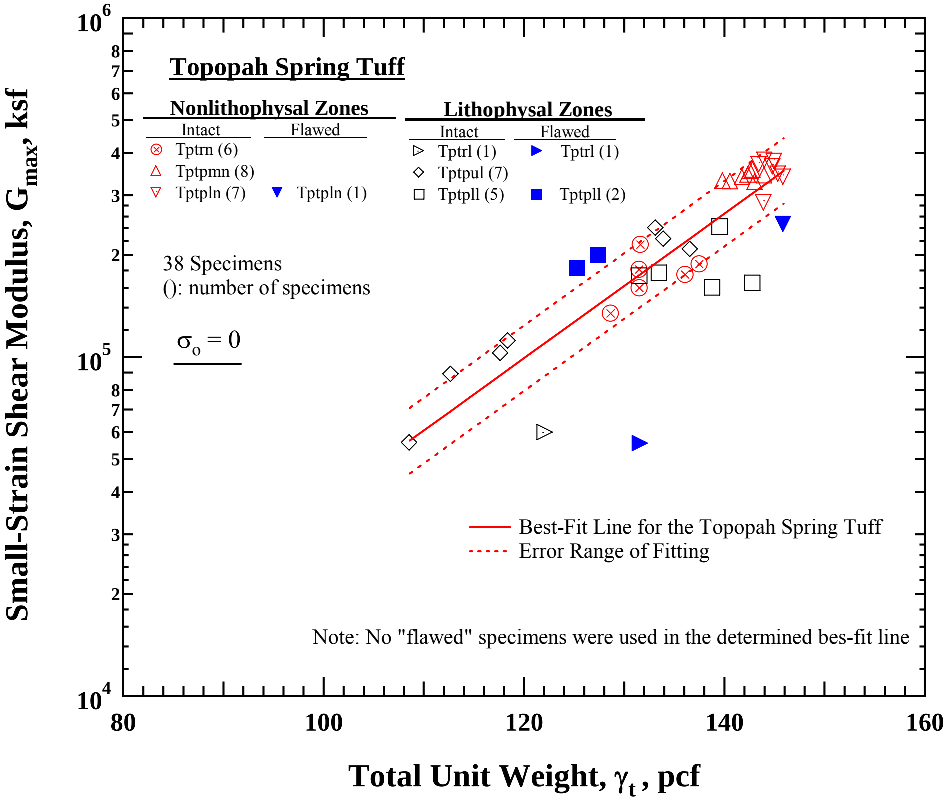

Figure 6.3 Variation of Small-Strain Shear Modulus with Total Unit Weight from Unconfined, Free-Free Resonant Column (URC) Tests for Thirty-Eight Specimens from the Topopah Spring Tuff

where G_{max} are in MPa and γ_t is in kg/m^3. The standard error of the fitting, $S_{\varepsilon,G_{max},}$ that is the standard deviation of the difference between the measured and predicted values, is about 0.222 in the semi-logarithmic (natural logarithm) relationship (Ang and Tang, 1975). It should be noted that all four flawed specimens were not included in the fitting because the flaws seemed to result from inappropriate coring processes and they do not represent the natural conditions of the specimens. Although various characteristics influence G_{max} as discussed with V_S above, the deviation of scattered data from the fitting is not very significant; most data fall in the error range covering about 20 % lower than the values on the best-fit line and 25 % higher than the values on the best-fit line based on the standard error of the fitting.

It is interesting to note that the flaws in the nonlithophysal specimen (Tptpln) decreased V_S and G_{max} but the little effect on γ_t. On the other hand, the flaws in the lithophysal specimens (Tptrl and Tptpll) affected γ_t but seemed to have a smaller effect of V_S and G_{max}.

6.2.2 Bandelier Tuff

The γ_t and V_S measured on the specimens from the Bandelier Tuff have been added to the data presented in Figure 6.1 and shown in Figure 6.4. The measurements from only two units (upper Cooling Unit 3 (Qbt3U) and Cooling Unit 2 (Qbt2)) were cored in the field. The specimens from the Qbt3U are moderately welded tuffs and the specimens from the Qbt2 are moderately to strongly welded tuffs. These tuffs are generally stiff enough to be sampled with core bits in the field. All softer Bandelier Tuff layers were sampled with steel tubes as described in Chapter 2. Two cores from each Qbt3U and Qbt2 unit were tested using the URC device. All specimens exhibit lower V_S values than the tuffs from the Topopah Spring Tuff as shown in Figure 6.4. Two specimens from the upper Cooling Unit 3 (Qbt3U) had γ_t values below 100 lb/ft^3 (1.60 g/cm^3), leading to an average V_S less than 2000 ft/sec (610 m/sec). The rocks from the Qbt2 have larger γ_t values than the Qbt3U, reflecting their higher welding intensity. However, their V_S values are smaller than the Topopah Spring Tuff specimens having similar γ_t values from the Tptpul that are strongly welded. This difference may simply result from the slight difference in welding intensity and relative degree of enduration.

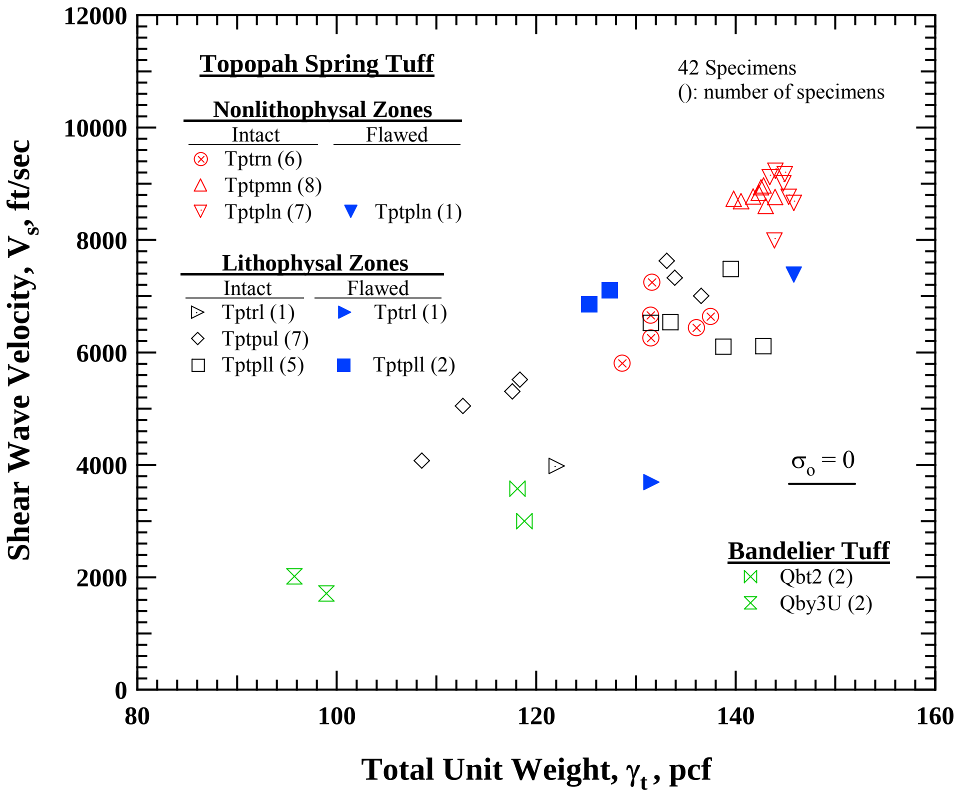

Figure 6.4 Variation of Small-Strain Shear Wave Velocity with Total Unit Weight from Unconfined, Free-Free Resonant Column (URC) Tests for Thirty-Eight Specimens from the Topopah Spring Tuff and Four Specimens from the Bandelier Tuff

However, the two projects had different criteria to define the welding intensity (see Chapter 2) and there are inherent uncertainties associated with these qualitative criteria. In addition, although more data are required to confirm this hypothesis, this difference may indicate differences in their matrix materials. The Tptpul materials have a dense matrix but their γ_t values are low because of lithophysal cavities. The Qbt2 materials do not have these lithophysal cavities. Therefore, the specimens have a more porous matrix. Furthermore, any differences related to microscopic features (minerals and/or microcracks) as products of various crystallization and cooling processes can attribute to the difference in V_S values of the densely welded tuffs from the two different sites.

Due to the limited amount of data, no correlation for V_S and γ_t or G_{max} and γ_t was determined.

6.3 Log V_S – Log σ_O AND Log G_{MAX} – Log σ_O RELATIONSHIPS OF ASH-FLOW TUFFS

6.3.1 Topopah Spring Tuff

The variations in small-strain shear wave velocity, V_S, with isotropic confining pressure, σ_o, that were measured by fixed-free resonant column (RC) testing on 16 specimens from the Topopah Spring Tuff are presented in Figure 6.5. The variations in G_{max} with σ_o for the 16 specimens are presented in Figure 6.6. Note that Specimens 11C-1 and 12C-1 were tested only at the unconfined state due to many large voids (lithophysal cavities) on their surfaces. As such no membrane could be placed on these two specimens that would allow pressure to be applied to the specimens and still be soft enough not to affect the specimen stiffness. As shown in the figure, all intact tuff specimens from the Topopah Spring Tuff exhibit little to no increase in the small-strain V_S with increasing σ_o. This (lack of) influence of confining pressure is typical of intact competent rock (Stokoe et al., 2006).

Two specimens were re-cored from larger cores. The re-cored specimens are Specimens 2C-2 and 3K-2 and they have an average diameter and height of 0.83 and 1.89 in, respectively. Based on visual inspection of the original Specimen 2B-3 and the re-cored Specimen 2C-2, the smaller re-cored specimen (2C-2) had fewer surface lithophysae. In addition, the total unit weight of the re-cored specimen was 6 lb/ft^3 (0.1

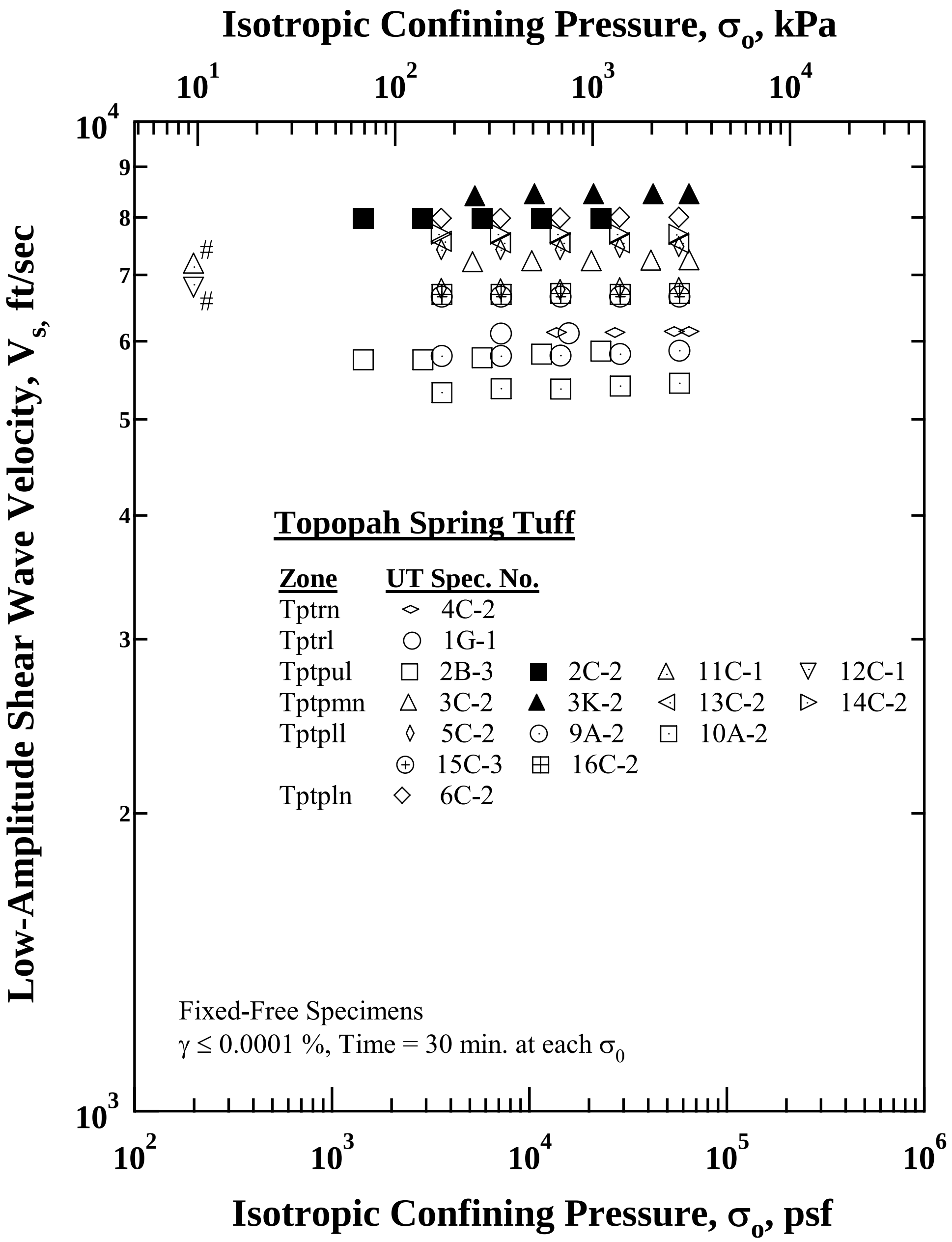

Note: #tests were performed only at unconfined state due to many large voids on specimen surface.

Figure 6.5 Variation in Low-Amplitude Shear Wave Velocity with Isotropic Confining Pressure of Sixteen Specimens from the Topopah Spring Tuff as Determined from Resonant Column (RC) Tests

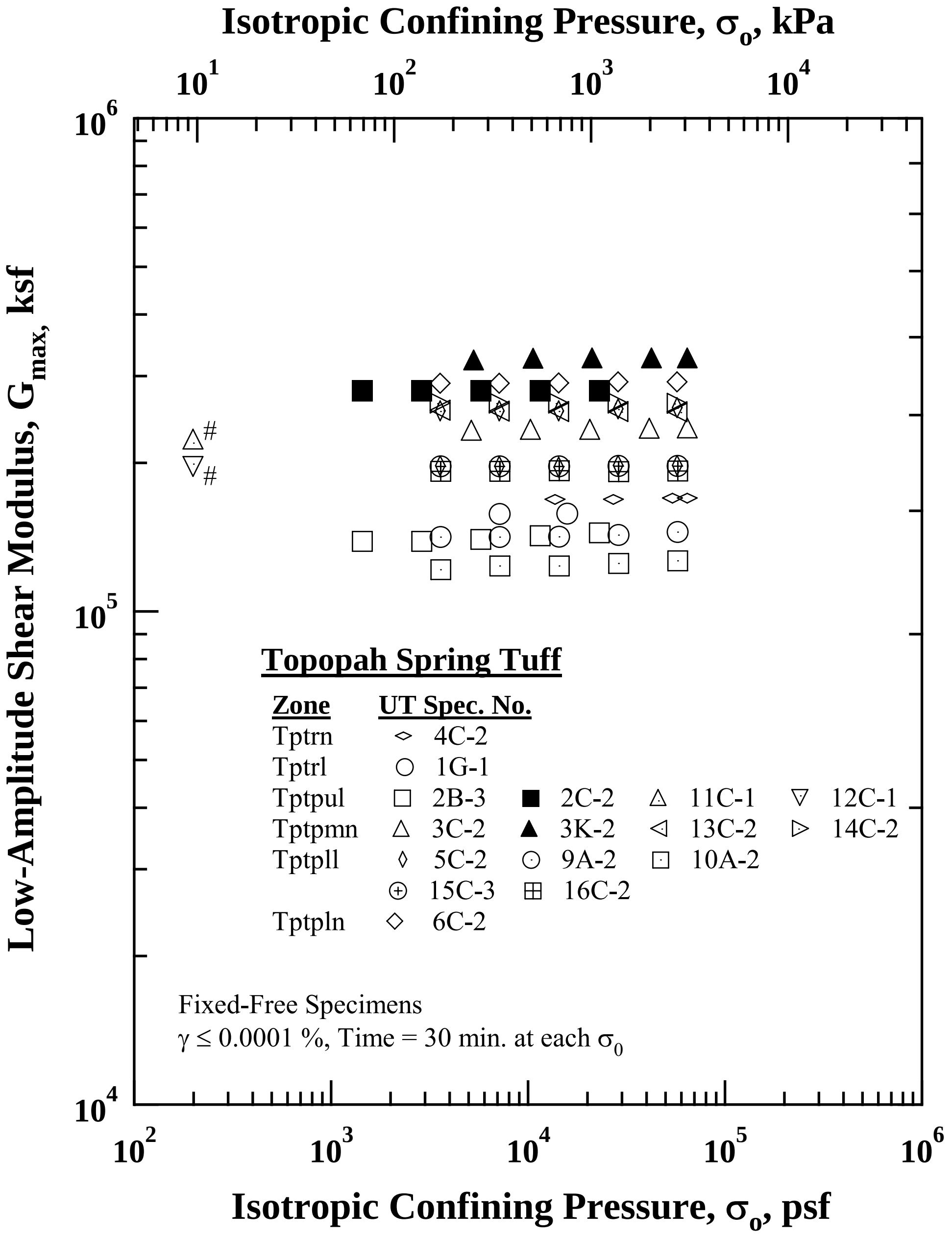

Note: #tests were performed only at unconfined state due to many large voids on specimen surface.

Figure 6.6 Variation in Low-Amplitude Shear Modulus with Isotropic Confining Pressure of Sixteen Specimens from the Topopah Spring Tuff as Determined from Resonant Column (RC) Tests g/cm^3) larger (see Table 4.1). These two factors resulted in an increase in V_S and G_{max}; V_S is 36 % higher than the V_S of lager parent specimen and G_{max} is 94 % higher than the G_{max} of the larger parent specimen at the highest confining pressure as shown in Figures 6.5 and 6.6, respectively. For original Specimen 3C-2 and re-cored Specimen 3K-2, Specimen 3K-2 was cored for the piece of core next to Specimen 3C-2. Re-cored Specimen 3K-2 had a slightly higher γ_t than original Specimen 3C-2 (higher by 3 lb/ft^3 (0.05 g/cm^3)) as shown in Table 4.1. The higher unit weight and the slightly different location resulted in an increase in V_S and G_{max} of 17 % for V_S and 39 % for G_{max} of the smaller specimen (3K-2) at the highest confining pressure.

6.3.2 Bandelier Tuff

While all densely welded rocks from the Topopah Spring Tuff exhibit pressure independency of their V_S and G_{max} values, the specimens from the Bandelier Tuff exhibit various relationships between the log V_S – log σ_o and log G_{max} – log σ_o relationships as shown in Figures 6.7 and 6.8, respectively. The V_S and G_{max} values in the figures for the 18 specimens from the Bandelier Tuff were measured by fixed-free RC testing. The relative differences between the different geologic units are clearly presented in these figures. As shown by the log V_S – log σ_o relationships in Figure 6.7, the specimens from the Bandelier Tuff can be divided into the following four groups:

1. Group 1: moderately to strongly welded tuff, Qbt2,
2. Group 2: moderately welded tuff, Qbt3U,
3. Group 3: poorly welded tuffs (Qbt1v, Qbt1g and Qbo), and
4. Group 4: poorly welded tuff, Qbt3L.

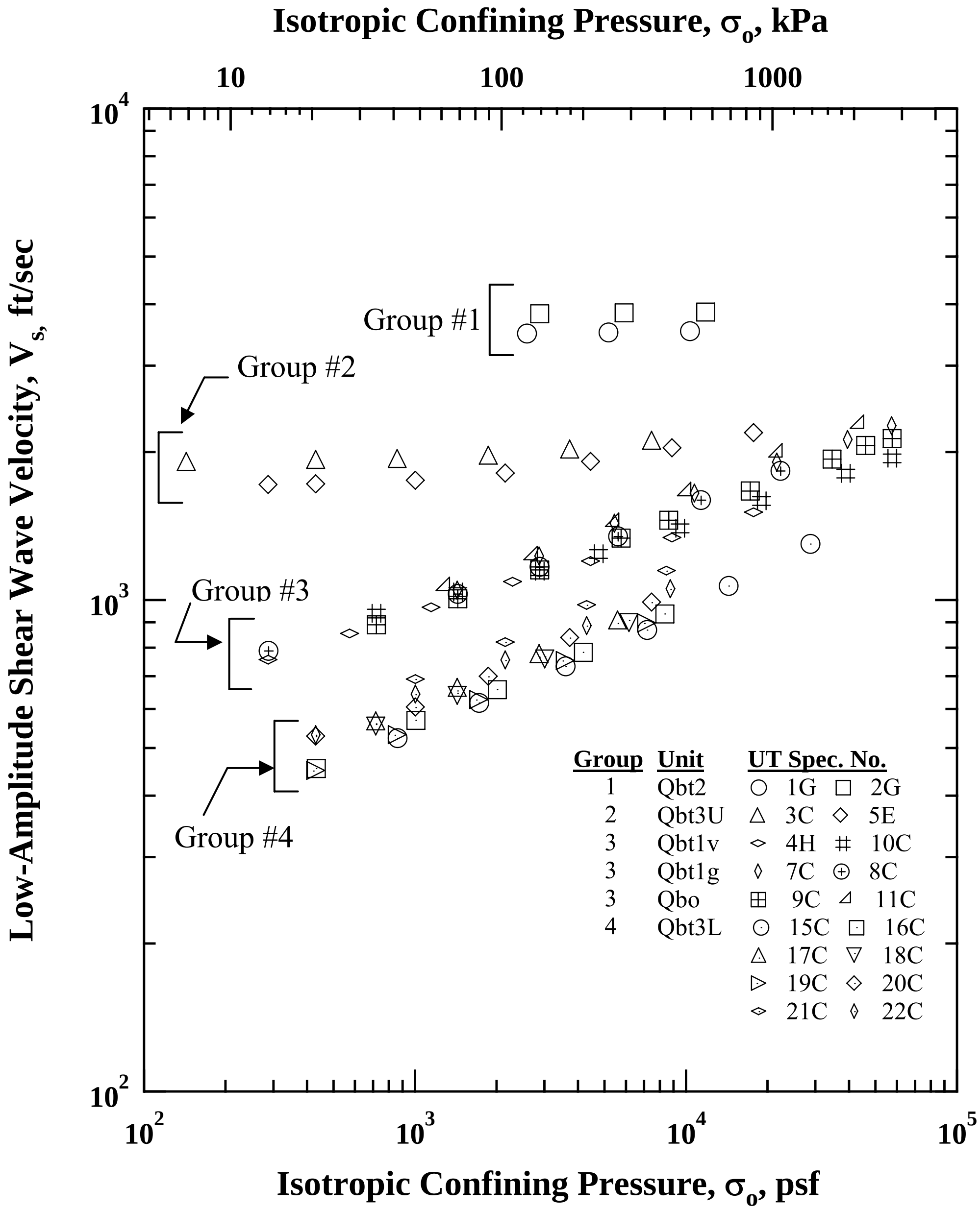

Figure 6.7 Summary Plot of the Variation in Low-Amplitude Shear Wave Velocity with Isotropic Confining Pressure of Eighteen Specimens from the Bandelier Tuff as Determined from Resonant Column (RC) Tests

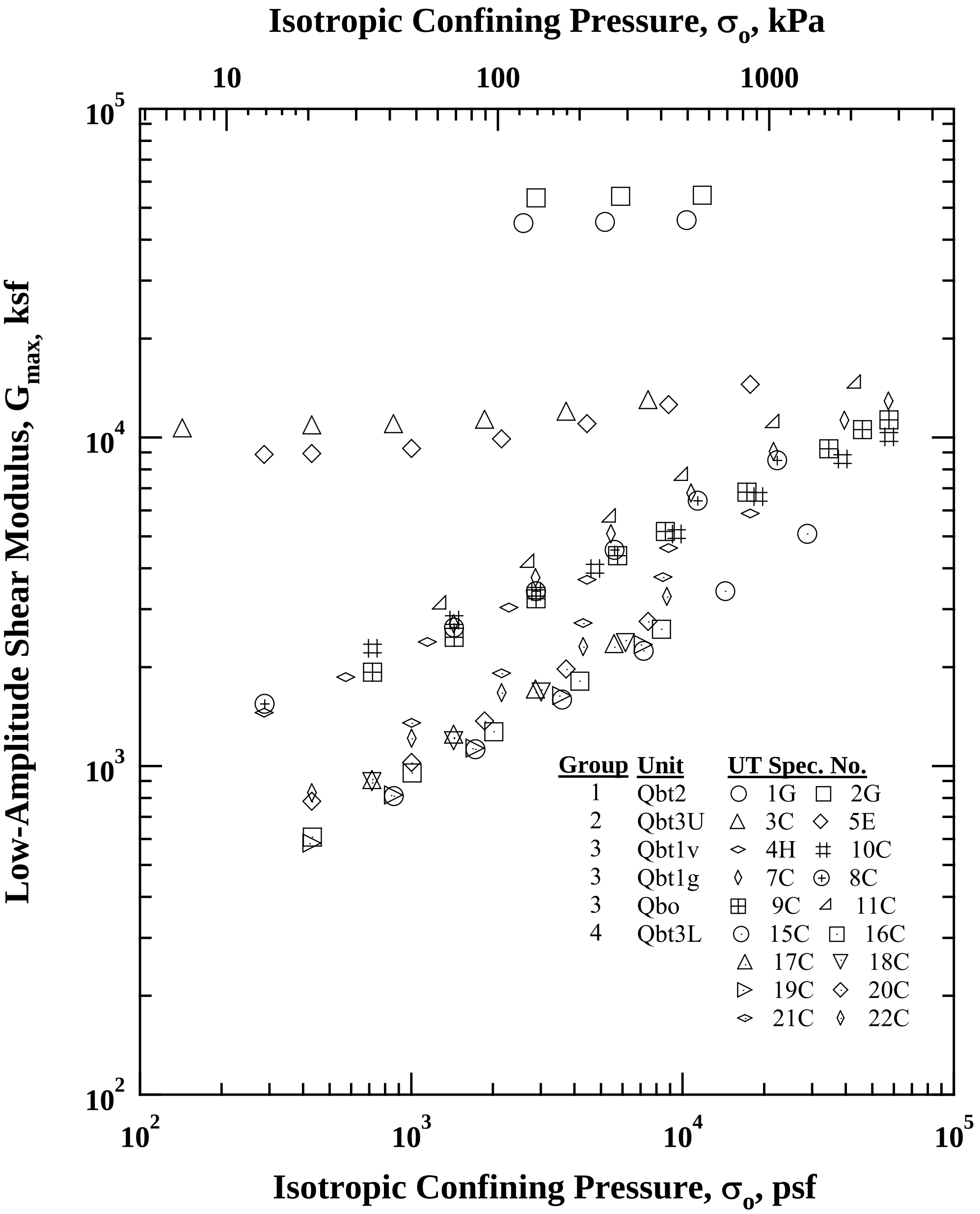

Figure 6.8 Summary Plot of the Variation in Low-Amplitude Shear Modulus with Isotropic Confining Pressure of Eighteen Specimens from the Bandelier Tuff as Determined from Resonant Column (RC) Tests

It may be noted that: (1) the differences in the V_S values of the tuffs in each group are not significant, (2) the average V_S values for each group at small σ_o are clearly different from each other, (3) the values of V_S increase markedly as effective confining pressure (σ_o) increases for the poorly welded materials in Groups 3 and 4, and (4) the effect of σ_o on V_S (and G_{max}) is small to insignificant for the tuffs with the higher welding intensity in Groups 2 and 1, respectively.

A quantitative relationship between V_S and σ_o, which expresses the trends shown in Figures 6.7, is:

$$V_S = A_V (\sigma_o / Pa)^{n_V} \tag{6.3}$$

where, A_V = small-strain shear wave velocity at σ_o = 1 atm,

σ_o = isotropic confining pressure in the same units as Pa,

Pa = one atmosphere (2117 psf or 100 kPa), and

n_V = a dimensionless exponent.

The values of A_V and n_V were obtained from least-squares fitting with Equation (6.3). Figure 6.9 shows the relationship between n_V and V_S measured at 0.3 atm (0.6 ksf). (Note that V_S is denoted as $V_{S,\,0.3\text{ atm}}$ hereafter.) The confining pressure of 0.3 atm is a small enough confining pressure that the building vacuum pressure can be used to apply it. As shown in Figure 6.9, the effect of σ_o on V_S for tuffs with poor welding conditions is well described with n_V; specimens that have a smaller value of V_S at 0.3 atm (smaller $V_{S,\,0.3\text{ atm}}$) exhibit the larger change in V_S with σ_o (larger n_V). The value of n_V decreases almost linearly down to 0.03 for a Qbt3U material ($V_{S,\,0.3\text{ atm}}$ = 1933 ft/sec (589 m/sec)) and remains very small for the Qbt2 materials from the Bandelier Tuff. The best-fit line through these data (excluding data for Group 1) found from least-squares fitting are shown

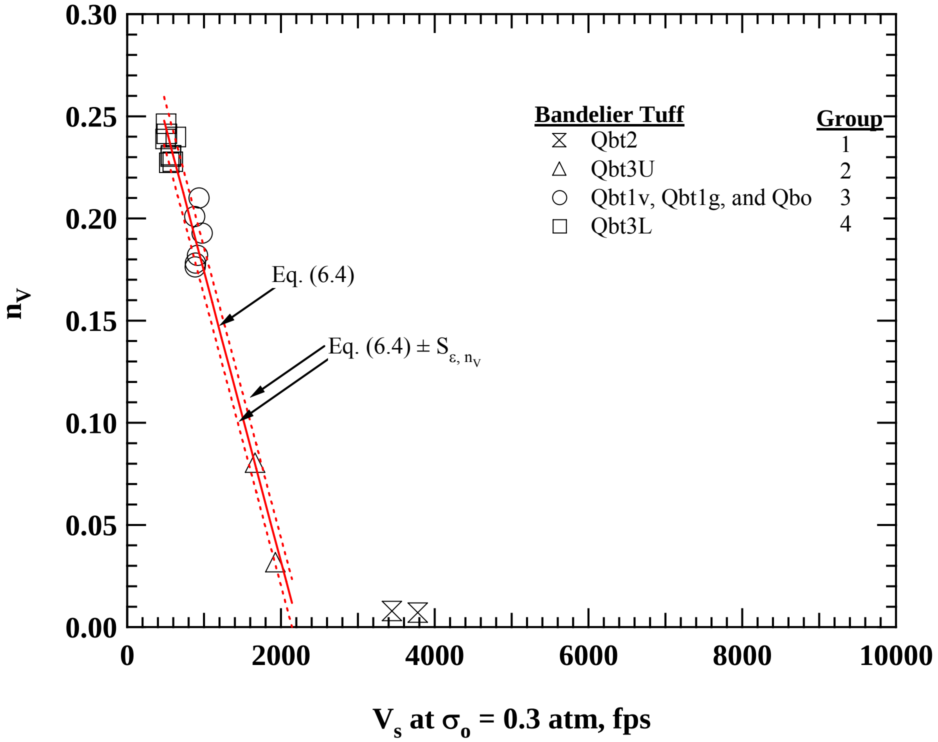

Figure 6.9 Variation of n_V with V_S at σ_o of 0.3 atm for the Bandelier Tuff Specimens

in Figure 6.9. The relationship between n_V and $V_{S,\,0.3\text{ atm}}$ for values of $V_{S,\,0.3\text{ atm}}$ less than 2000 ft/sec (610 m/sec), represented by the best-ft line, can be expressed as:

$$n_V = \frac{-0.142}{1000} V_{S,0.3atm} + 0.316 \tag{6.4}$$

where, $V_{S,\,0.3\text{ atm}}$ is in ft/sec. The standard error of this fitting, S_{ε,n_V}, is about 0.0117. The corresponding error range of the fitting line is added in the figure.

It is interesting to compare the tuffs with higher welding intensity from both the Topopah Spring Tuff and the Bandelier Tuff. This comparison of n_V with V_S at V_S of 0.3 atm is shown in Figure 6.10. All tuffs have V_S greater than 3000 ft/sec (914 m/sec). As seen in the figure, n_V ranges from 0.0077 to 0.0018 as V_S increases from about 3448 ft/sec (1050 m/sec) to about 6077 ft/sec (1852 m/sec). Above V_S of 6077 ft/sec (1852 m/sec), n_V remains between 0.0018 and zero.

It is also very interesting to note that the two lines shown in Figures 6.9 and 6.10 intersect at the $V_{S,\,0.3\text{ atm}}$ of about 2200 ft/sec (671 m/sec). This is close to the value used in the site classification for a rock site in earthquake design. For example, the International Building Code (IBC) define a rock site as having an average V_S higher than 2500 ft/sec (762 m/sec) over its top 100 ft (30 m). In other words, the variation of n_V with $V_{S,\,0.3\text{ atm}}$ possibly provides a good quantitative guideline of classifying soft and stiff rocks at shallow depth (or at unconfined state), thereby, replacing the loosely defined and vague terms (e.g., rock-like or soil-like) commonly used in the literature.

To investigate the relationship between the $V_{S,\,0.3\text{ atm}}$ and γ_t, all $V_{S,\,0.3\text{ atm}}$ for the specimens from both the Topopah Spring and Bandelier Tuffs are presented in Figure 6.11. Note that the $V_{S,\,0.3\text{ atm}}$ values for the specimens from the Topopah Spring Tuff are the same values measured at the unconfined state and shown in Figure 6.1. Based on the observation of the pressure independent characteristics of the densely welded tuffs, it was assumed that their V_S values at the unconfined state are equal to their $V_{S,\,0.3\text{ atm}}$. Along the $V_{S,\,0.3\text{ atm}}$ values, the trend line (Eq. (6.1)) determined from the relationship between G_{max} and γ_t for the Topopah Spring Tuff are converted to the relationship between V_S and γ_t and presented in the figure. The fitting equation of the converted trend line can be expressed as:

$$V_{S,0.3atm} = 100\sqrt{\frac{883e^{0.0491\gamma_t}}{\gamma_t}} \qquad (6.5)$$

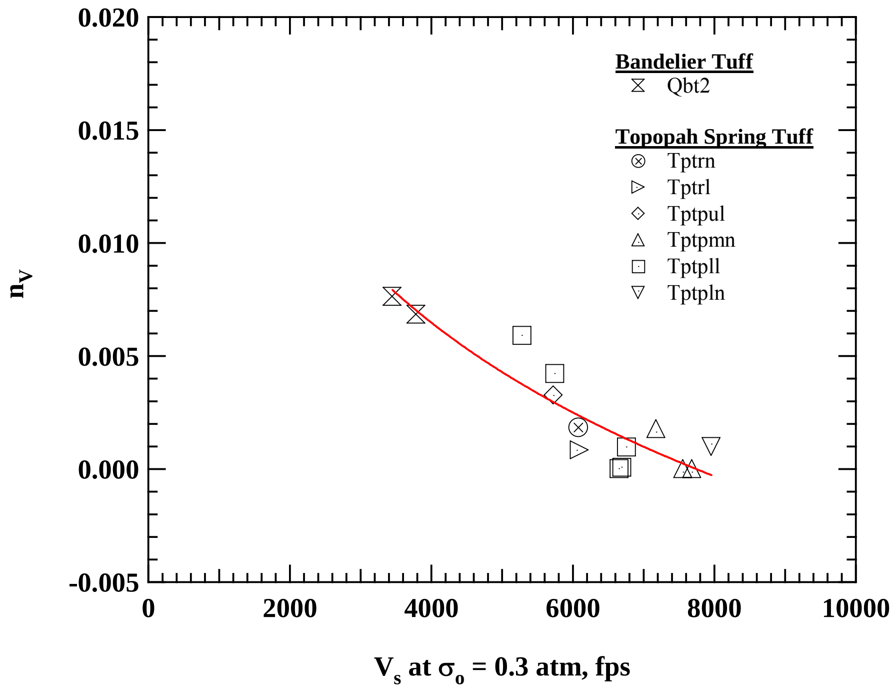

Figure 6.10 Variation of n_V with V_S at σ_o of 0.3 atm for all Ash-Flow Tuffs with $V_{S,\ 0.3\ atm} > 3000$ ft/sec

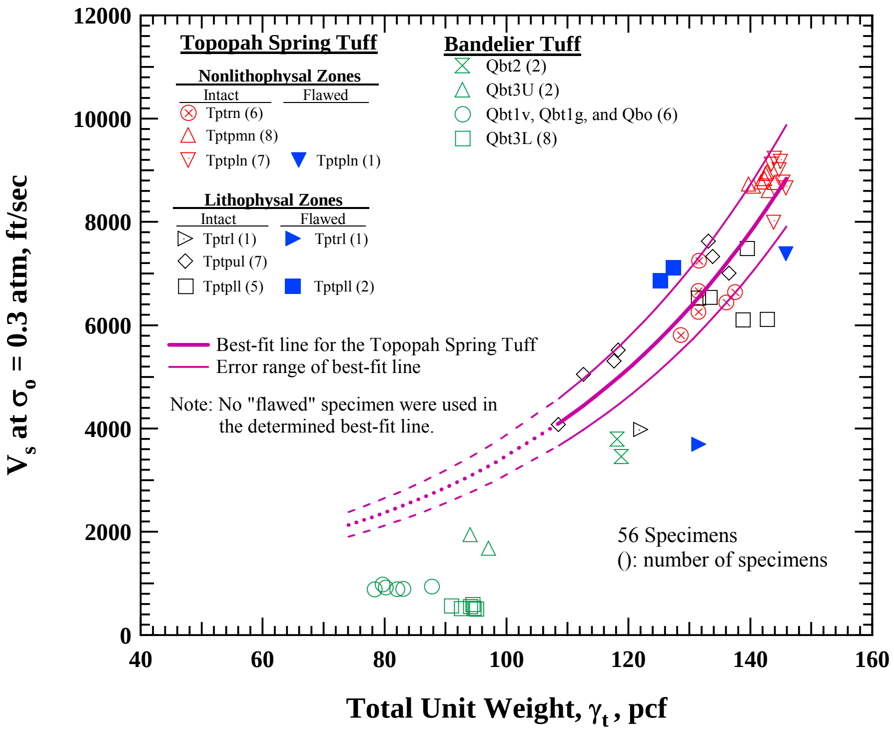

Figure 6.11 Variation of V_S at σ_o of 0.3 atm with γ_t for all Ash-Flow Tuff

where V_S is in ft/sec and γ_t is in pcf. This trend line and its error range are extended to the lower γ_t range of the Bandelier Tuff specimens. All $V_{S,\,0.3\,atm}$ values for the Bandelier Tuff specimens are lower than the lower bound of the trend line. This difference may confirm the difference in the two tuff formations including the difference in welding intensity and any microscopic features discussed previously.

As with V_S, the generalized relationship between G_{max} and σ_o can be written as:

$$G_{\max} = A_G(\sigma_o / Pa)^{n_G} \qquad (6.6)$$

where, A_G = small-strain shear modulus at σ_o = 1 atm,

σ_o = isotropic confining pressure in the same units as Pa,

Pa = one atmosphere (2117 psf or 100 kPa), and

n_G = a dimensionless exponent in the modulus relationship.

The values of n_G and A_G were obtained by least-squares fitting with Equation (6.6) for the Bandelier Tuffs. Since G_{max} is calculated with V_S ($G_{max} = \rho V_S^2$), the effect of σ_o on G_{max} is simply equal to $2n_V$. The effect of welding on n_G is again well described in Figure 6.12 by plotting the values of n_G with G_{max} at σ_o of 0.3 atm ($G_{max,\,0.3\,atm}$). Note the axis for $G_{max,\,0.3\,atm}$ is logarithmic because of its large range. As with V_S, the best-fit line through these data found from least-squares fitting of data with V_S of less than 2000 ft/sec (610 m/sec) can be expressed as:

$$n_G = \frac{-0.406}{10000} G_{\max,0.3atm} + 0.498 \qquad (6.7)$$

The standard error (standard deviation of error of the fitting) is about 0.030. The range with this value for the fitting line is added in the figure.

For all ash-flow tuffs with higher welding intensity, the n_G-log G_{max} relationship is shown in Figure 6.13. The tuffs with V_S greater than 3000 ft/sec have G_{max} larger than

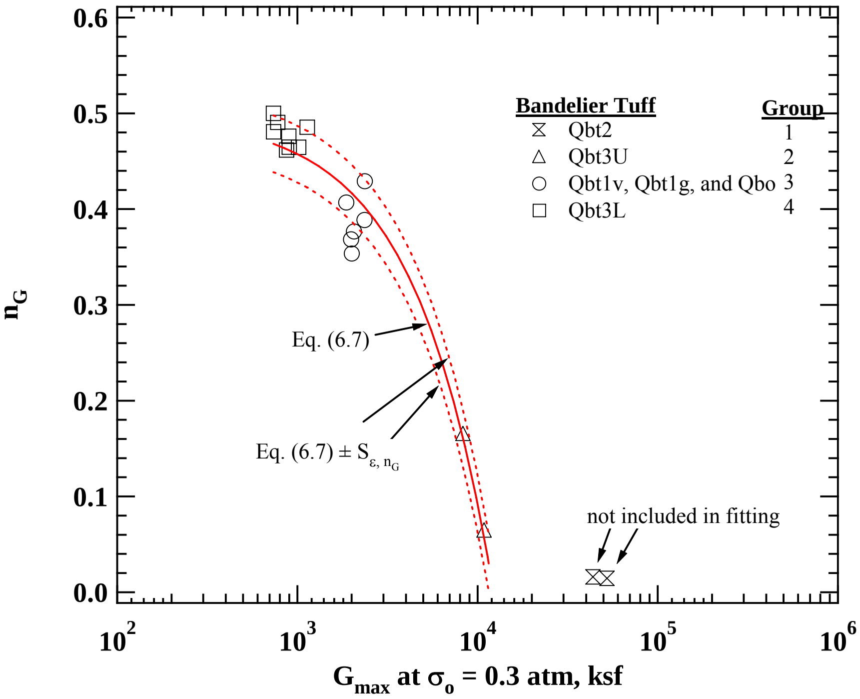

Figure 6.12 Variation of n_G with G_{max} at σ_o of 0.3 atm for the Bandelier Tuff

40000 ksf (1915 MPa). As easily recognized in the figure, the n_G values for these stiff tuffs are just close to zero indicating pressure independency. The n_G ranges from about 0.015 to 0.0046 as G_{max} increases from about 43900 ksf (2101 MPa) to about 161200 ksf (7718 MPa). Above G_{max} of 161200 ksf (7718 MPa), n_V remains between 0.0046 and zero.

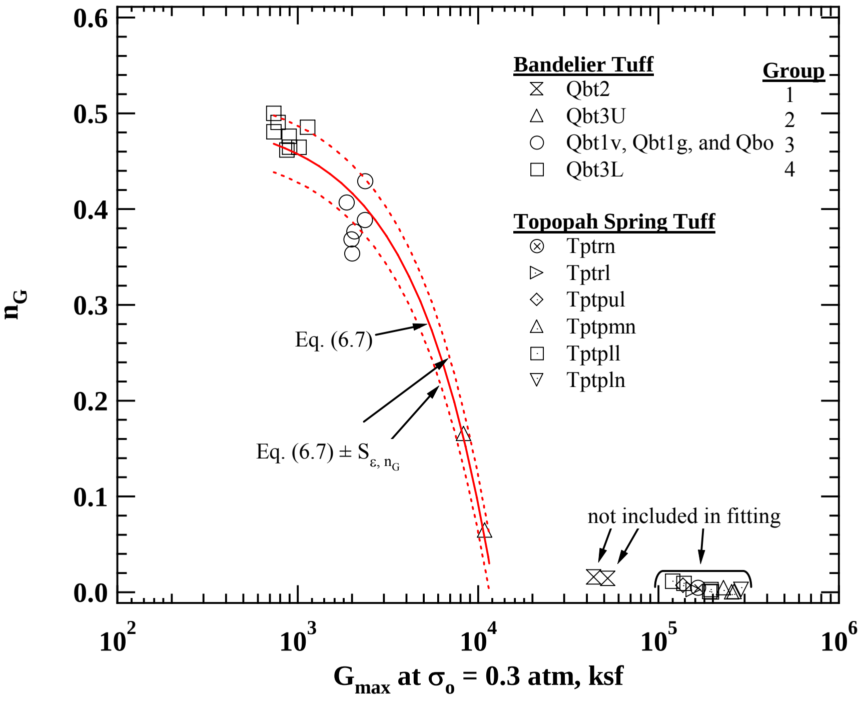

Figure 6.13 Variation of n_G with G_{max} at σ_o of 0.3 atm for all Ash-Flow Tuffs

6.4 SMALL-STRAIN MATERIAL DAMPING RATIO IN SHEAR OF ASH-FLOW TUFFS AT σ_O = 0

The variation of the small-strain material damping ratio in shear (D_{min} of $D_{S,\ min}$) of the 38 specimens from the Topopah Spring Tuff are presented in Figure 6.14. All tests were performed on the air-dried specimens at room temperature and in the unconfined state using the URC device. As clearly seen in the figure, most specimens exhibit low D_{min} values and more than half of the specimens have D_{min} values less than 0.5 %. In general, specimens with lower γ_t values exhibited higher D_{min} values. The best-fit line through the data for the Topopah Spring Tuff found by least-squares fitting can be expressed as:

$$D_{\min} = 118.7e^{-0.042\gamma_t} \tag{6.8}$$

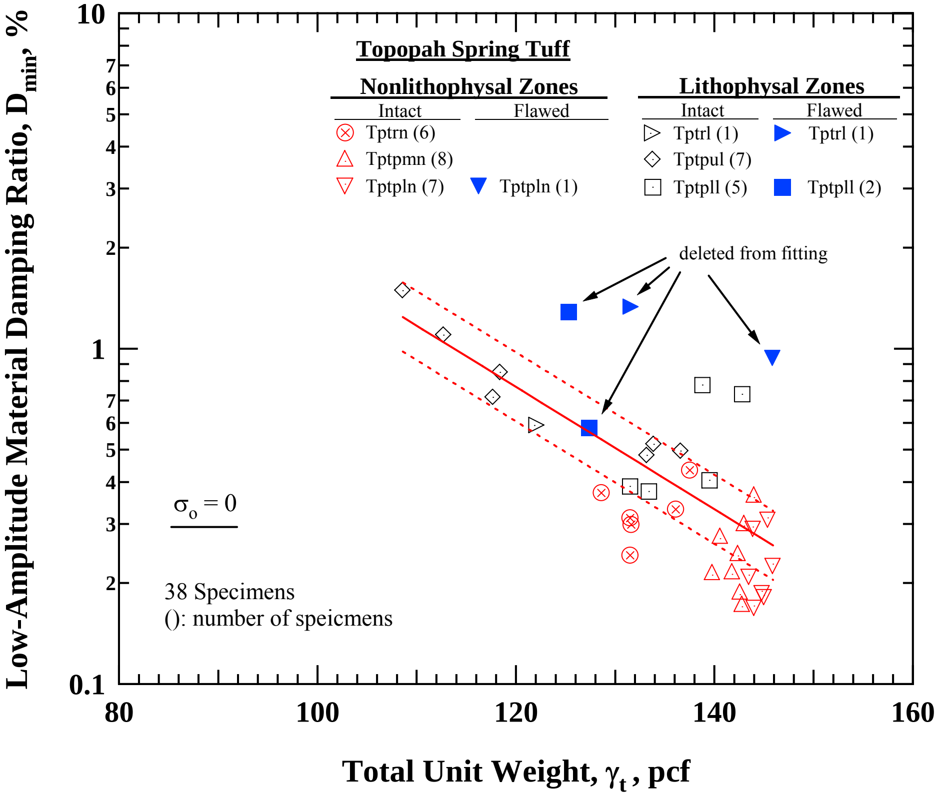

Figure 6.14 Variation of Small-Strain Material Damping Ratio with Total Unit Weight from Unconfined, Free-Free Resonant Column (URC) Tests for Thirty-Eight Specimens from the Topopah Spring Tuff

where D_{min} is in percent and γ_t is in lb/ft^3. The standard error of the fitting, $S_{\varepsilon,Dmin,}$ is about 0.237 in the semi-logarithmic relationship. It should be noted that the two flawed specimens from the Tptpll units were not included in the fitting instead of correcting their γ_t values. It is very interesting to note that the other two specimens from the Tptpln and Tptrl with significant flaws exhibit large D_{min} values deviating from the trend line. These values were also deleted from the fitting. The measured D_{min} values generally follow the trend line within the error range which is not very significant as shown in the figure.

Although the range of the measured D_{min} value is not large, there are several noticeable differences between the D_{min} values for the lithostratigraphic units as with their G_{max} values. The tuffs from the nonlithophysal units that have higher values of γ_t generally exhibit smaller D_{min} (0.29 % on average) compared with the tuffs from the lithophysal units (0.76 % on average). The Tptrn specimens have an average D_{min} of 0.33 %, which is slightly higher than the average D_{min} of 0.28 % for the other specimens from the nonlithophysal zones. As discussed previously, the tuffs from the lithophysal units have a wide range in γ_t leading to a large range in the D_{min} values. Note that most data fall in the range of error of the fitting. Two specimens from the Tptpll exhibit slightly higher D_{min} values above the upper bound as shown in the figure. It is interesting to note that these specimens also exhibited the smallest G_{max} among the rocks from the same unit although they are two of the densest specimens from the Tptpll.

The D_{min} values for the four Bandelier Tuff specimens have been added in Figure 6.15. No significant difference in the D_{min} values is observed between the units. The specimens in each unit exhibit relatively a large variation in the D_{min} values compared with the error range of the fitting line for the Topopah Spring Tuff. It should be noted that the relatively soft materials from the Bandelier Tuffs have a looser matrix as previously discussed, so that disturbance near the perimeter of the cores is more likely to occur, and in turn, can increase the sensitivity of the measurement to D_{min}. The tuffs having slightly higher G_{max} (or V_S) values in each unit of the Bandelier Tuff exhibited lower D_{min} values as shown in Figure 6.16.

The tuffs from the Topopah Spring Tuff unit also exhibit a strong relationship between V_S and D_{min} as shown in Figure 6.16. The best-fit line constructed through the data can be expressed as:

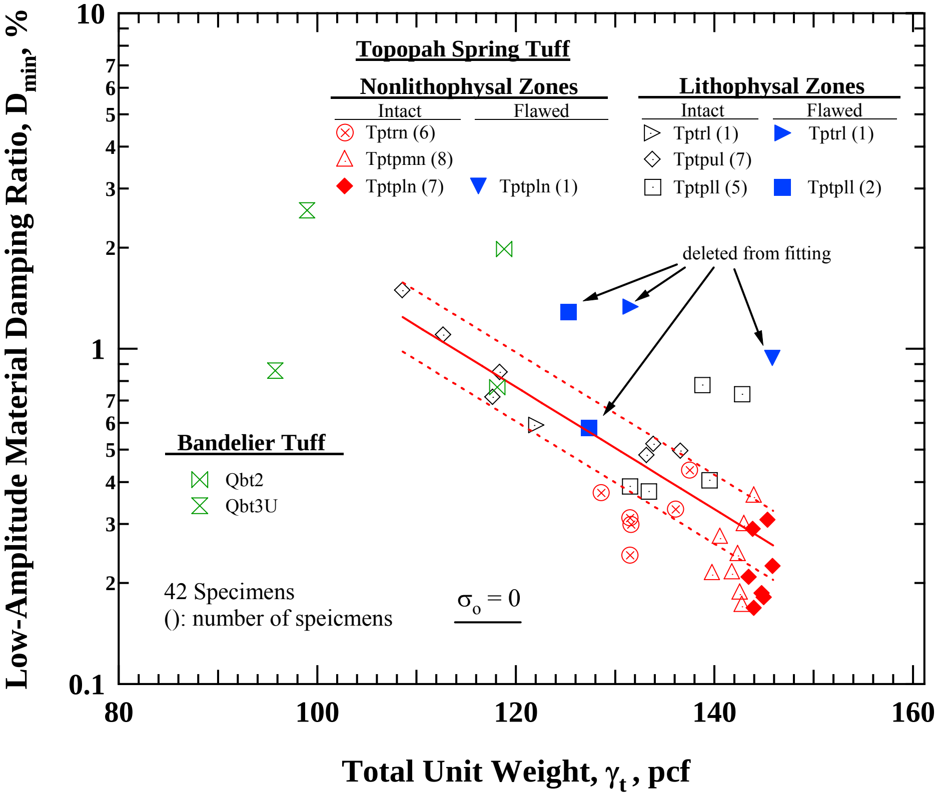

Figure 6.15 Variation of Small-Strain Material Damping Ratio with Total Unit Weight from Unconfined, Free-Free Resonant Column (URC) Tests for Thirty-Eight Specimens from the Topopah Spring Tuff and Four Specimens from the Bandelier Tuff

$$D_{\min} = 3.96e^{\frac{-0.314}{1000}V_S} \tag{6.9}$$

where D_{min} is in percent and V_S is in ft/sec. The standard error of the fitting, $S_{\varepsilon,D\min,}$ is about 0.192 in the semi-logarithmic relationship.

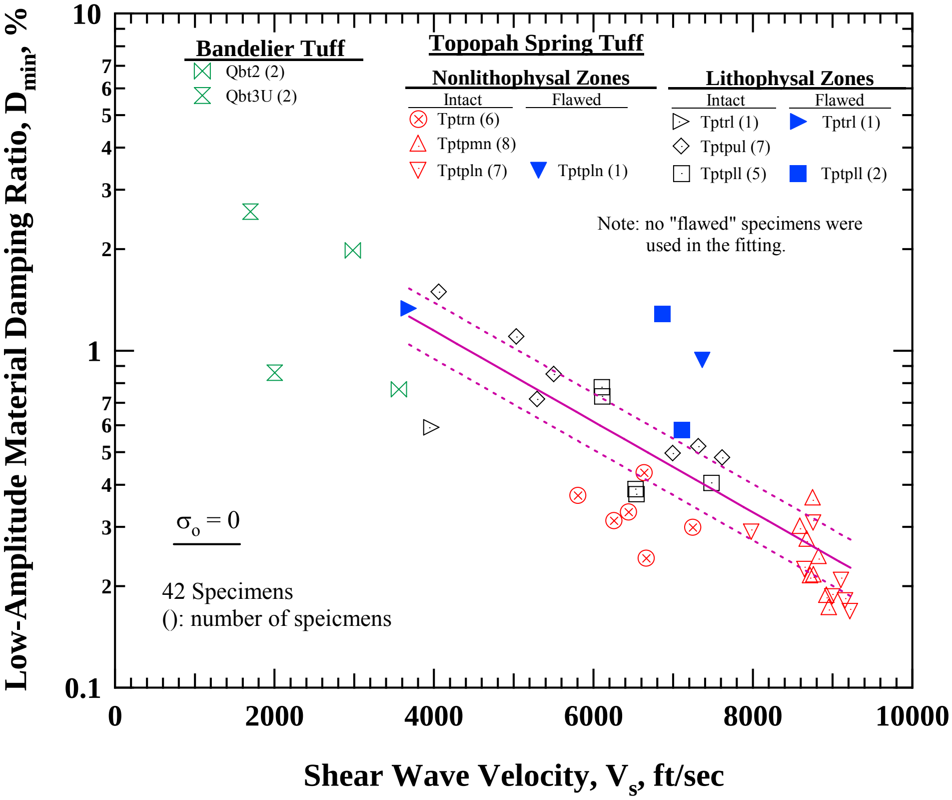

Figure 6.16 Variation of Small-Strain Material Damping Ratio with Small-Strain Shear Wave Velocity from Unconfined, Free-Free Resonant Column (URC) Tests for Thirty-Eight Specimens from the Topopah Spring Tuff and Four Specimens from the Bandelier Tuff

6.5 Log D_{min} – Log σ_o RELATIONSHIP OF ASH-FLOW TUFFS

The variation in small-strain material damping ratio, D_{min}, with isotropic confining pressure, σ_o, that were measured in the fixed-free resonant column (RC) testing on 16 specimens from the Topopah Spring Tuff are presented in Figure 6.17. As with the small-strain shear modulus, G_{max}, most tuff specimens from the Topopah Spring Tuff exhibit little to no decrease in D_{min} with increasing σ_o. Two re-cored specimens (Specimens 2C-2 and 3K-2) exhibit smaller D_{min} values compared with the original larger

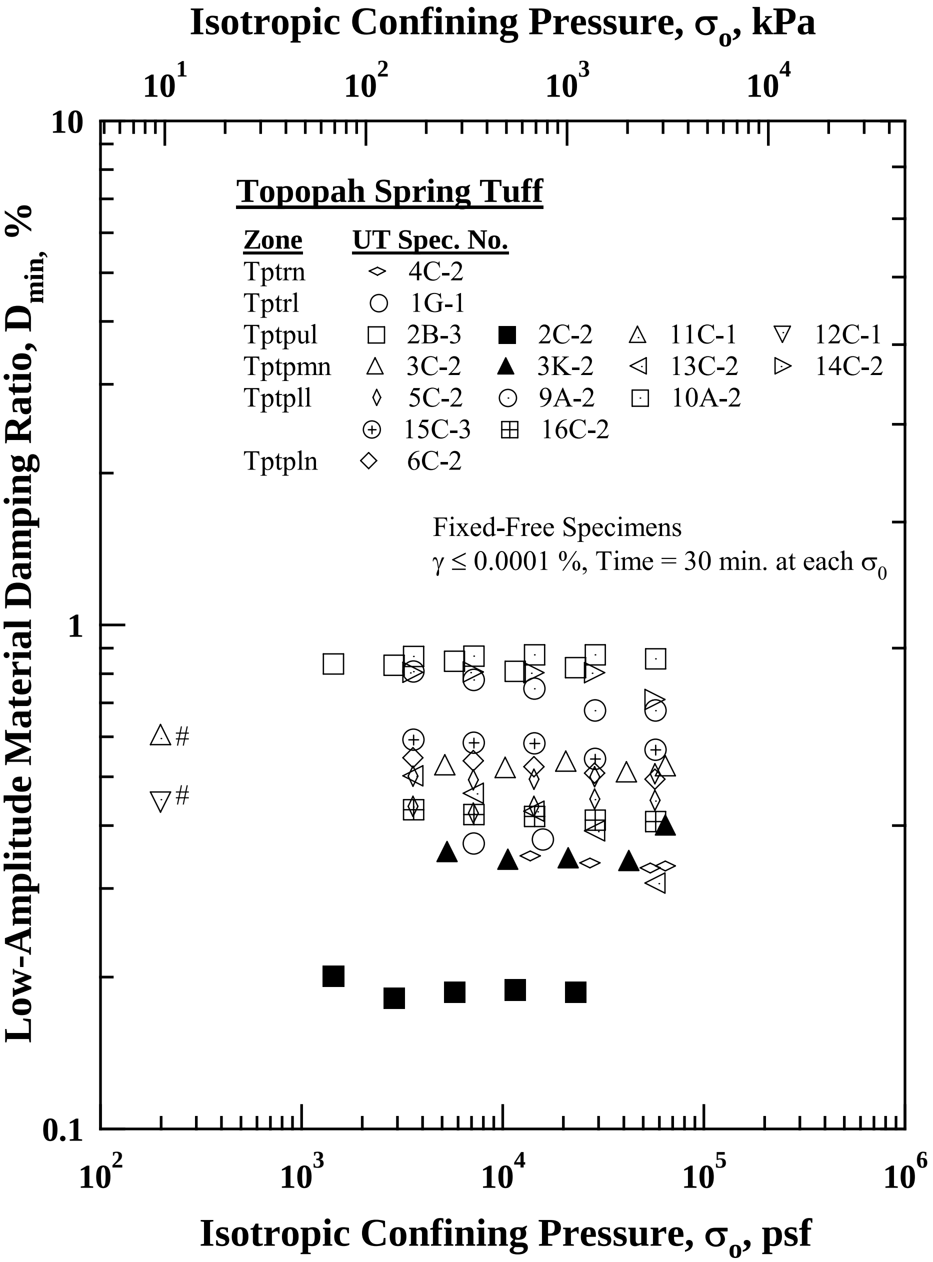

Note: #tests were performed only at unconfined state due to many large voids on specimen surface.

Figure 6.17 Variation in Low-Amplitude Material Damping Ratio with Isotropic Confining Pressure of Sixteen Specimens from the Topopah Spring Tuff as Determined from Resonant Column (RC) Tests specimens. This smaller D_{min} values support the discussion about the reduction of lithophysae and flaws during the re-coring and cutting processes used to create these small specimens. Also, the re-cored specimens have higher γ_t values than the original specimens. The specimen from the lithophysal zone exhibit a slightly larger decrease in D_{min} than the specimen from the nonlithophysal zone; Specimen 2C-2 from the Tptpul has about 77 % lower D_{min} compared with Specimen 2B-3 at the highest pressure while Specimen 3K-2 from the Tptpmn exhibit about 24 % difference compared with the D_{min} of Specimen 3C-2 at the highest test pressure.

While all densely welded tuffs from the Topopah Spring Tuff formation exhibit a small pressure dependency in their D_{min} values, the 18 fixed-free specimens from the Bandelier Tuff generally exhibit a stronger relationship between pressure and D_{min} as shown in Figure 6.18. The log D_{min} – log σ_o relationships are modeled in the same way as V_S and G_{max} using a similar quantitative relationship between D_{min} and σ_o that can be written as:

$$D_{\min} = A_D(\sigma_o / Pa)^{n_D} \tag{6.10}$$

where, A_D = small-strain material damping ratio at σ_o = 1 atm,

σ_o = isotropic confining pressure in the same units as Pa,

Pa = one atmosphere (2117 psf or 100 kPa), and

n_D = a dimensionless exponent in the material damping ratio relationship.

The behavior of D_{min} with increasing σ_o is somewhat more complex than found for V_S and G_{max} shown in Figure 6.19. As seen in the figure, there is no clear trend. A trend is better explored when n_D is plotted versus $V_{S,\ 0.3\ atm}$ as shown in Figure 6.20. Although the relationship for n_D seems to have somewhat larger relative variations at V_S values less than 2000 ft/sec (610 m/sec) than those for n_V and n_G, the effect of welding

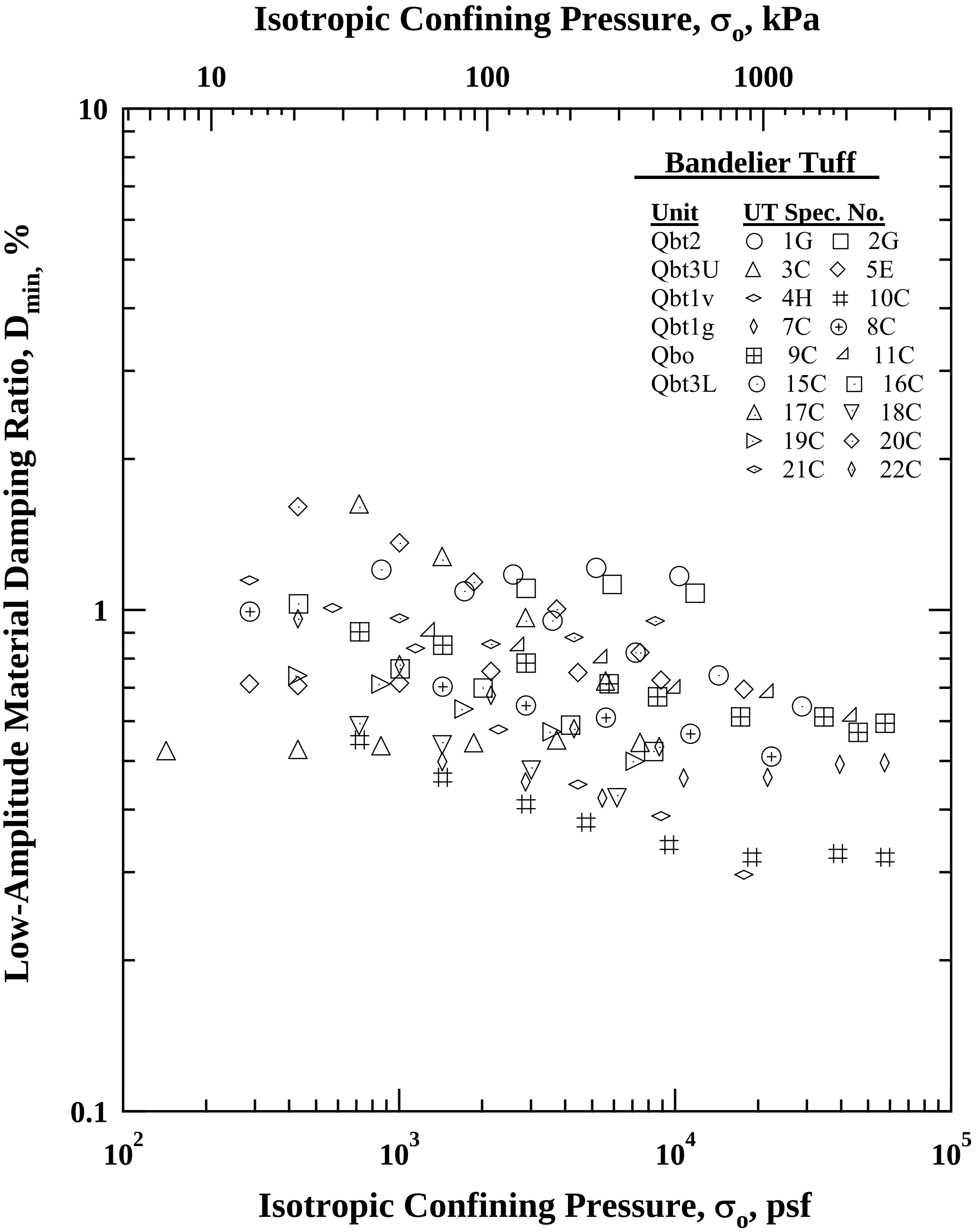

Figure 6.18 Summary Plot of the Variation in Low-Amplitude Material Damping Ratio with Isotropic Confining Pressure of Eighteen Specimens from the Bandelier Tuff as Determined from Resonant Column (RC) Tests

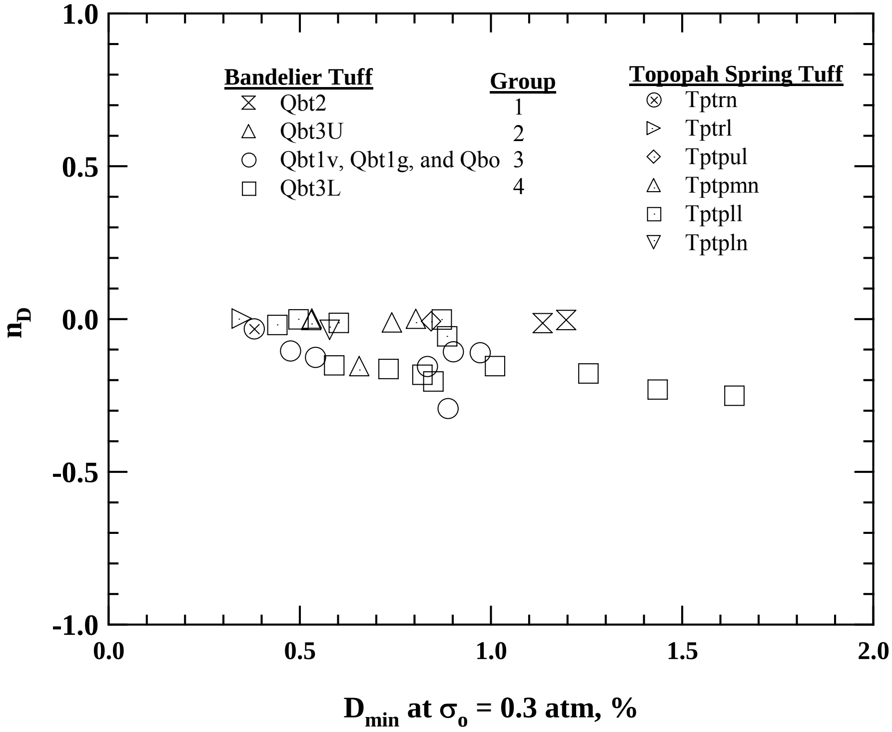

Figure 6.19 Variation of n_D with D_{min} at 0.3 atm for All Ash-Flow Tuffs

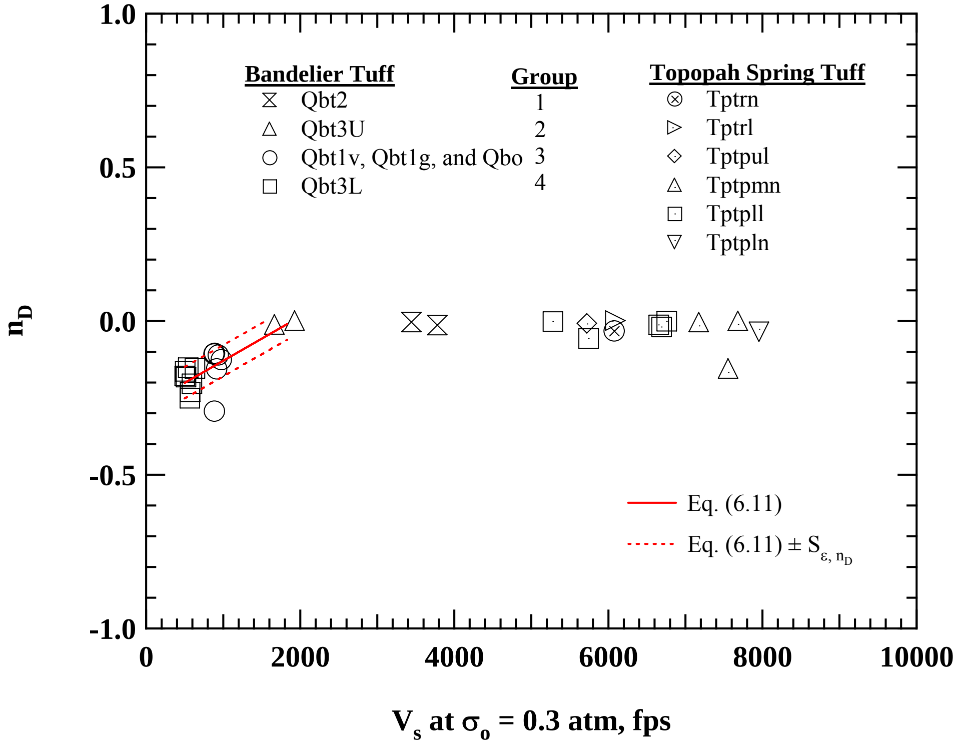

Figure 6.20 Variation of n_D with V_S at 0.3 atm for All Ash-Flow Tuffs

can be well represented with $V_{S,\ 0.3\ atm}$. The larger absolute n_D values for the Qbt3L materials are consistent with the larger n_V and n_G values for the same material observed in previous section. As with V_S and G_{max}, the best-fit line through these data found from least-squares fitting of data with V_S of less than 2000 ft/sec (610 m/sec) can be expressed as:

$$n_D = \frac{0.143}{1000} V_{S,0.3atm} - 0.272 \tag{6.11}$$

The standard error (standard deviation of error of the fitting) is about 0.051. The range with this value for the fitting line is added in the figure. All Topopah Spring tuffs which are densely welded exhibit essentially no dependency of σ_o on D_{min}.

The D_{min} and V_S values at 0.3 atm for the materials from the Bandelier Tuff are plotted with the values measured by the URC tests on the 38 specimens in Figure 6.21. As discussed previously, all samples from the Topopah Spring Tuff showed little pressure dependency in both D_{min} and V_S (and G_{max}). Therefore, the measured values at unconfined state are plotted in Figure 6.21. Most specimens from the Bandelier Tuff exhibit $D_{min\ at\ 0.3\ atm}$ smaller than 1.0 as seen earlier although their $V_{S\ at\ 0.3\ atm}$ values are small. These small values of D_{min} are taken to that: (1) the specimens are intact and do not have significant fractures, (2) the specimens were properly set-up in the fixed-free device and resonated without disturbance near the perimeter of the specimen, and (3) the extension of the fitting line for the Topopah Spring Tuff are inappropriate for intact, soft Bandelier tuffs.

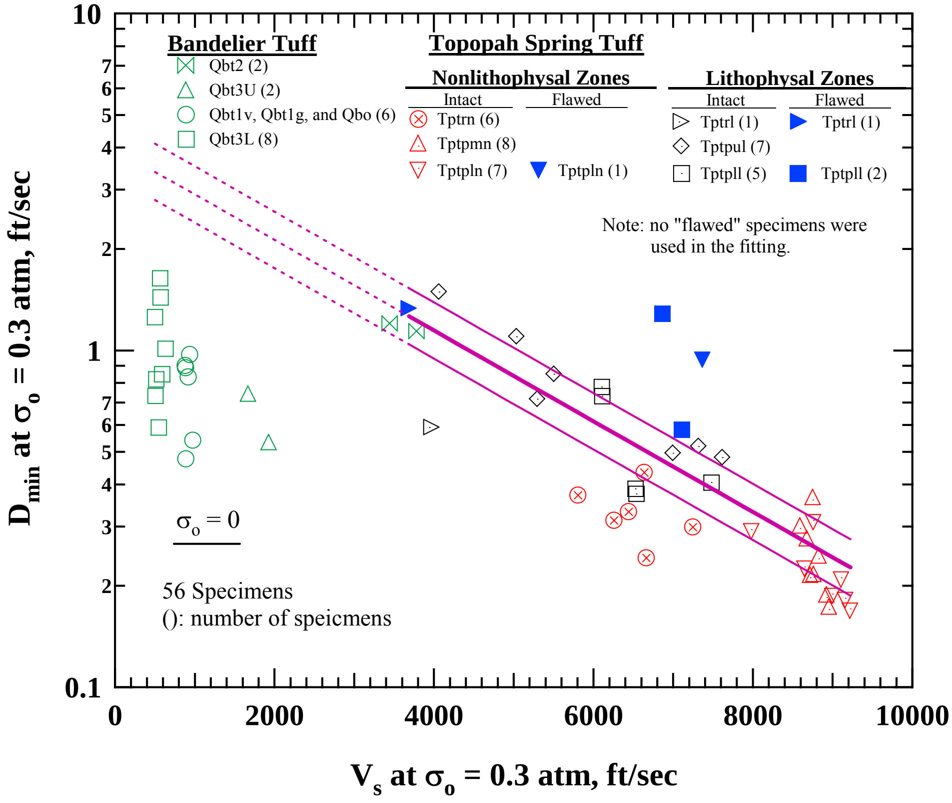

Figure 6.21 Variation of n_D with Small-Strain Shear Wave Velocity (V_S) at 0.3 atm for All Ash-Flow Tuffs

6.6 OTHER POTENTIAL FACTORS THAT MIGHT INFLUENCE SMALL-STRAIN DYNAMIC PROPERTIES OF ASH-FLOW TUFFS

In sections 6.2 through 6.5, all studies were based on RC test results with air-dried specimens. To determine if any adjustments need to be made to the RC data for use in earthquake analyses, the effects of excitation frequency, change in water content due to specimen preparation and large lithophysal cavities were studied. The results from these studies are presented in this section.

6.5.1 Effect of Frequency

The effect of *f* was investigated by performing small-strain TS tests using 10 cycles of loading at four different frequencies ranging from 0.1 to 5 Hz. Exciting slow-cyclic motion in pure torsion was more difficult than exciting resonance in torsion (RC testing) due to the impact of "flaws" (cracks, lithophysae, etc.) in the specimens. The flaws create non-uniformities within a specimen that result, to varying degrees, in bending and torsional motions occurring when torque is applied to the top of the specimen. When a specimen bends, the estimated shear strain is affected by adding some unknown component of the bending displacement to the pure torsional displacement. On the other hand, the torque applied to the specimen, hence the shear stress applied to the specimen, is only dependent on the excitation function and is independent of the specimen motion. Therefore, G_{max} and D_{min} that are estimated from the motion and torque are affected

When this complex motion occurs, it occurs together in slow-cyclic loading (TS testing). This motion distorts the values of G_{max} and D_{min} in TS testing. However, based on the experimental results, the combined motion has a larger impact on $D_{S\ min}$. An important point is that the two motions (bending and torsion) generally have different resonant frequencies which allow them to be separated in resonance testing, so that measurements in torsional resonance (RC testing) are performed with little distortion. Therefore, one set of G_{max} measurements (Specimen 10A-2) in TS testing was discarded and about one-half of the D_{min} data in TS testing were also discarded due to complications caused by bending. (No values in the RC data set were discarded.) With the remaining data, the results of the effect of *f* on G_{max} and D_{min} are presented in Figures 6.22a and 6.22b, respectively. As seen, the average change in G_{max} as excitation frequency changes from 1 to 400 Hz is less than 8%, with G_{max} decreasing slightly at the highest frequencies. The scatter in the D_{min} data is much more than in the G_{max} data as seen in Figure 6.22b. In these figures, values of normalized material damping ratio vary from about 1.6 to 0.5 times D_{min} at 1 Hz when the excitation frequency increases to about 400 Hz. The lack of consistent trends combined with the complexity of making TS measurements in specimens with varying flaws makes determining a correlation in G_{max} and $D_{S\ min}$ with frequency unclear so that a frequency independent approximation is suggested.

The effect of f on G_{max} and D_{min} of the rocks from the Bandelier Tuff are shown in Figures 6.23 and 6.24, respectively. The smaller variations of G_{max} with excitation frequency than the Topopah Spring tuffs and the similar scatter in D_{min} data observed for these specimens confirm the suggestion of the frequency independent approximation for ash-flow tuffs.

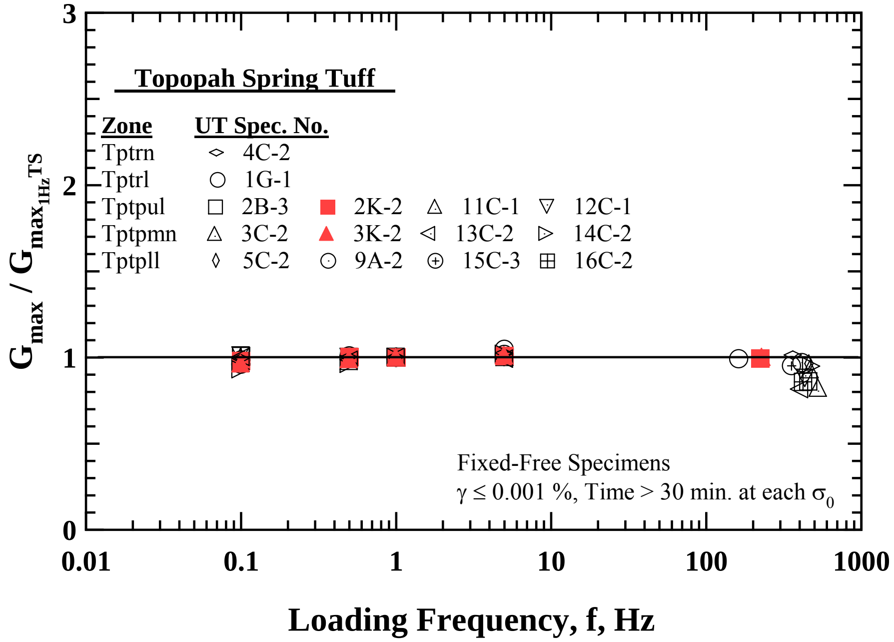

(a) Normalized G_{max} versus Loading Frequency

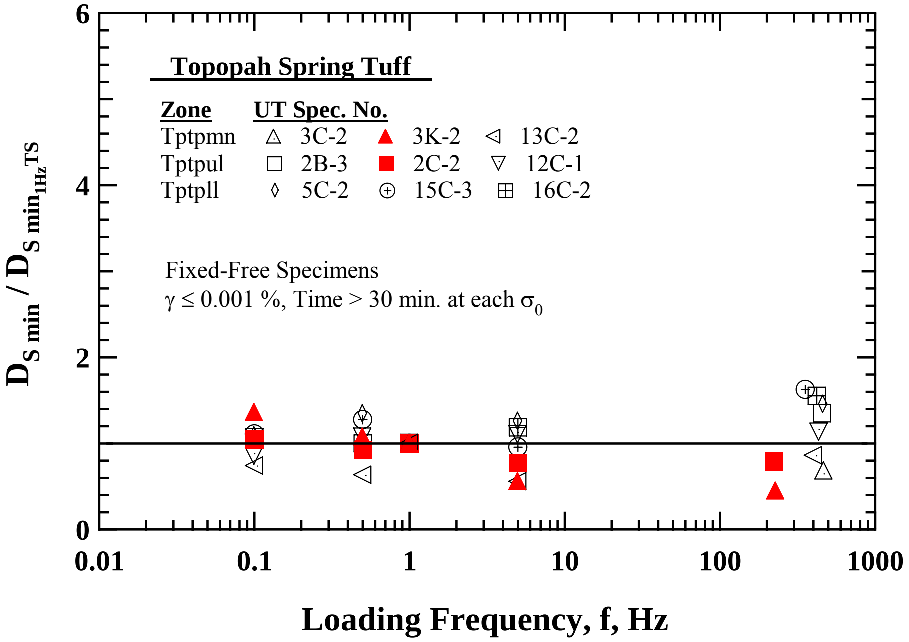

(b) Normalized D_{min} versus Loading Frequency

Figure 6.22 Variations of (a) Normalized G_{max} and (b) Normalized D_{min} with Loading Frequency of the Specimens from the Topopah Spring Tuff

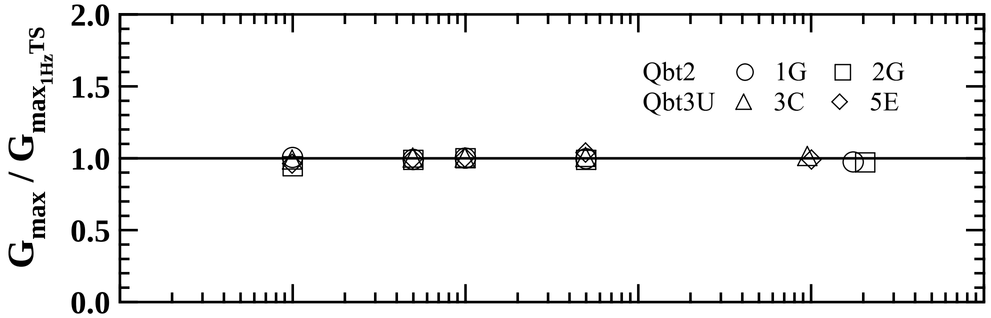

(a) Normalized G_{max} for Moderately to Strongly Welded Tuff Specimens

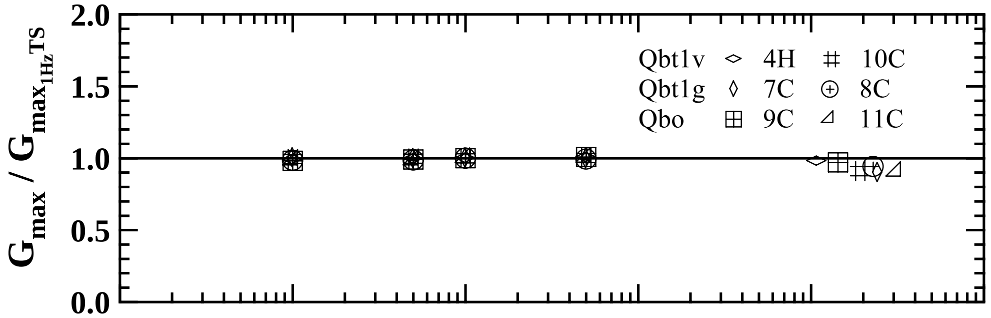

(b) Normalized G_{max} for Poorly Welded Tuff Specimens (Qbt1v, Qbt1g, and Qbo)

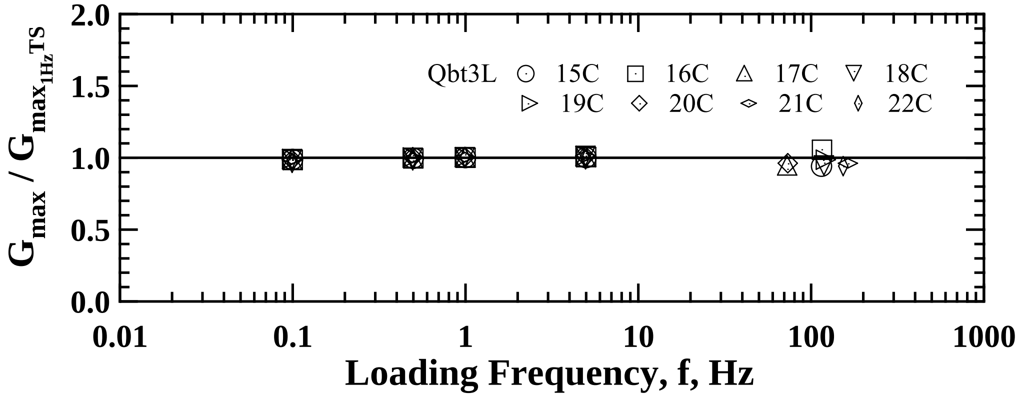

(c) Normalized G_{max} for Poorly Welded Tuff Specimens (Qbt3L)

Figure 6.23 Variation of Normalized Low-Amplitude Shear Modulus of the Specimens in (a) Groups 1 and 2, (b) Group 3 and (c) Group 4 from the Bandelier Tuff

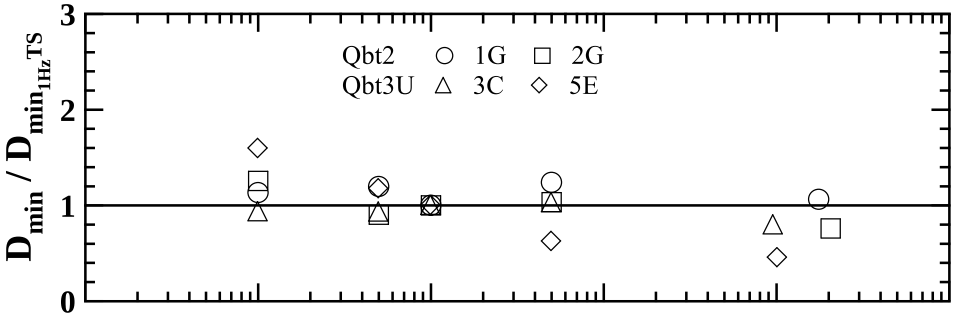

(a) Normalized D_{min} for Moderately to Strongly Welded Tuff Specimens

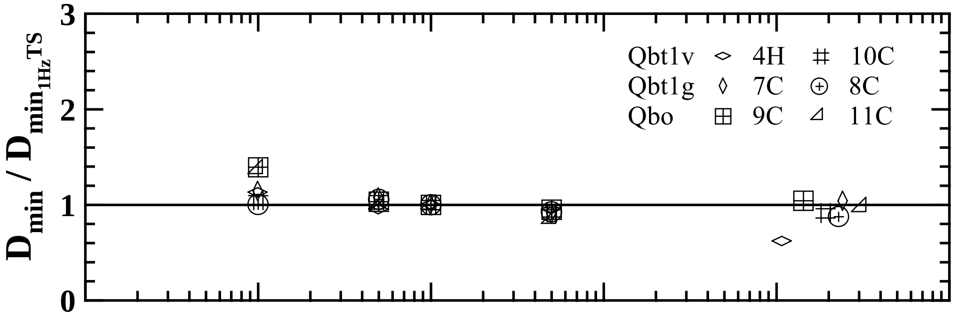

(b) Normalized D_{min} for Poorly Welded Tuff Specimens (Qbt1v, Qbt1g, and Qbo)

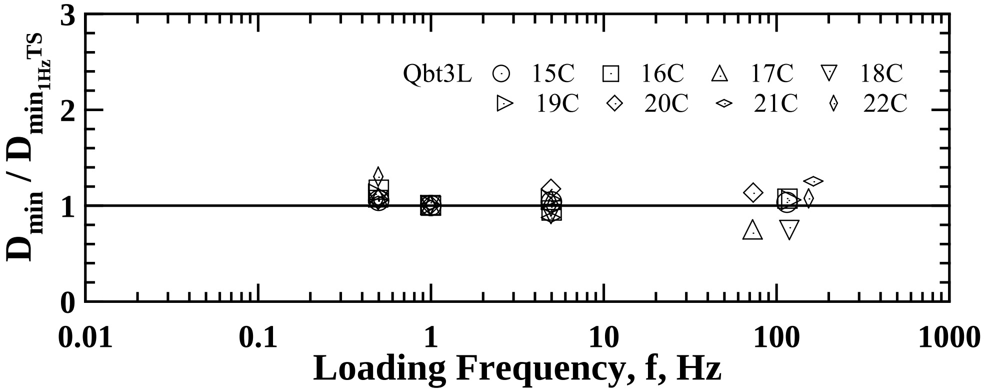

(c) Normalized D_{min} for Poorly Welded Tuff Specimens (Qbt3L)

Figure 6.24 Variation of Normalized Low-Amplitude Material Damping Ratio of the Specimens in (a) Groups 1 and 2, (b) Group 3 and (c) Group 4 from the Bandelier Tuff

6.5.2 Change in Water Content due to Specimen Preparation

Six additional samples were cored for investigating the effect of the change in water content on the G_{max} and D_{min}. As listed in Table 6.1, one sample from each unit in the Topopah Spring Tuff was selected and five specimens were tested using the URC device. Note one specimen from the Tptpul was not tested after coring because of a large lithophysa on the bottom end of the specimen. All specimens were cored so that they had a diameter of 1.6 in. (4.1 cm) and were cut so they had a length of about 5 to 6 in. (13 to 15 cm). Water was used as lubricant during the coring process. In addition to the wet-coring process, the samples were soaked in water for about thirty minutes to increase initial water contents of the specimens to permit the effect of an increased water content to be evaluated on the dynamic measurements. It is realized that the complete specimen would not come into equilibrium but that the material around the perimeter of the specimen would have an increased water content. In common practice and in this study, specimens are tested after at least one day of drying following the wet-coring with water. The tests with the additional five specimens are not intended to investigate the effect of degree of saturation or water content with precise measurements of the parameters. Instead, the tests were used to simulate the normal testing processes and to see if the one-day drying period is sufficient in a practical sense.

Several measurements of both G_{max} and D_{min} were made with the URC device during the first day of drying followed by additional measurements up to about five to six days. The change in the unit weights of the six specimens was generally not significant after about a day as shown in Figure 6.25a. The largest change of the total unit weight in the period (between the last four to six days) was observed for the specimen from the Tptpll. Its γ_t decreased by about 1.03 lb/ft^3 (0.81 % decrease) for about 4 days. The two specimens from the crystal-rich member (the Tptrn and Tptrl) exhibit decreases in γ_t of

Table 6.1 Initial Characteristics of Six Specimens Used for Effect of Change in Water Content Due to Specimen Preparation

Spec. No.	Specimen ID	Type	Mid-Depth, ft (m)	Initial Specimen Size		Initial Total Unit Weight*, lb/ft^3 (g/cm^3)
				Height, in. (cm)	Diameter, in. (cm)	
Tuff15	UTA-42-AN (40C)	Tptrn	341.4 (104.0)	5.95 (15.1)	1.56 (3.96)	137.3 (2.20)
Tuff16	UTA-42-AO (41C)	Tptrl	666.5 (203.1)	5.71 (14.5)	1.56 (3.96)	136.9 (2.19)
Tuff17	UTA-42-AP (42C)	Tptpul	495.7 (151.1)	5.16 (13.1)	1.56 (3.96)	122.1 (1.96)
Tuff18	UTA-42-AQ (43C)	Tptpmn	812.9 (247.8)	5.91 (15.0)	1.56 (3.96)	144.2 (2.31)
Tuff19	UTA-42-AR (44C)	Tptpll	992.0 (302.4)	5.42 (13.8)	1.56 (3.96)	133.8 (2.14)
Tuff20	UTA-42-AS (45C)	Tptpln	6.9 (2.1)	4.86 (12.3)	1.56 (3.96)	145.7 (2.33)

Note: *the first measument after coring (less than 100 min.)

about 0.77 and 0.99 lb/ft^3 (0.57 and 0.68 % decrease), respectively, and the specimens from the Tptpul exhibit a decrease in γ_t of about 0.45 lb/ft^3 (0.36 % decrease). The two specimens from the crystal-poor, nonlithophysal units (the Tptpmn and Tptpln) exhibit only about 0.20 and 0.16 lb/ft^3 (0.14 and 0.11 % decrease), respectively, during the period.

Water content, w, of each specimen was estimated by assuming that the specimen dried on the last day and its γ_t became close to the dry unit weight, γ_d. The estimated average w values of the six specimens are shown in Figure 6.25b. As expected, the three specimens from the lithophysal units exhibited the larger w values initially and decrease with time. While the two specimens from the crystal-poor members (Tptpmn and Tptpln) have small w values initially, the rock from the Tptrn had somewhat larger

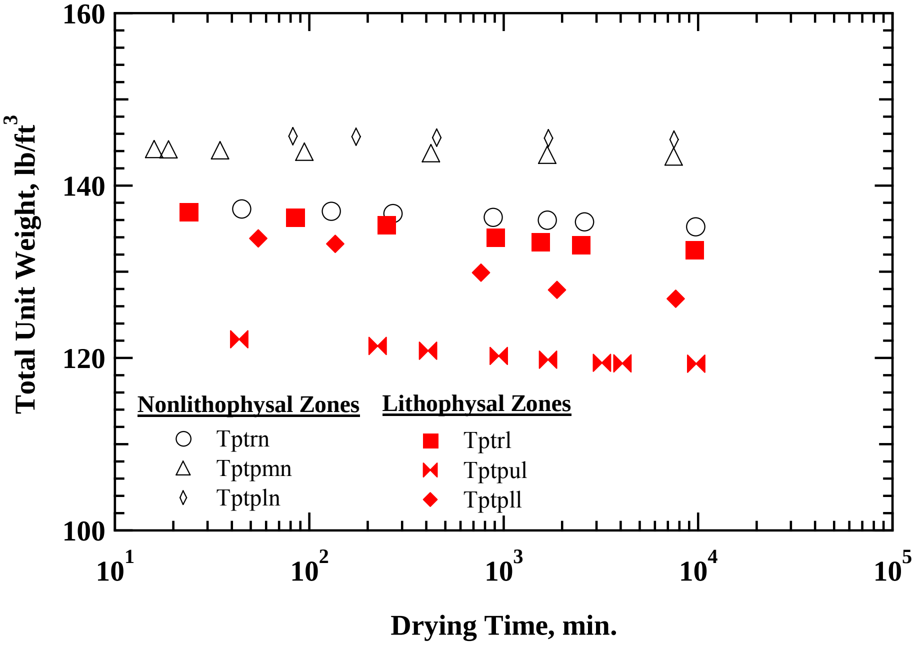

(a) Total Unit Weight versus Drying Time after Coring and Trimming

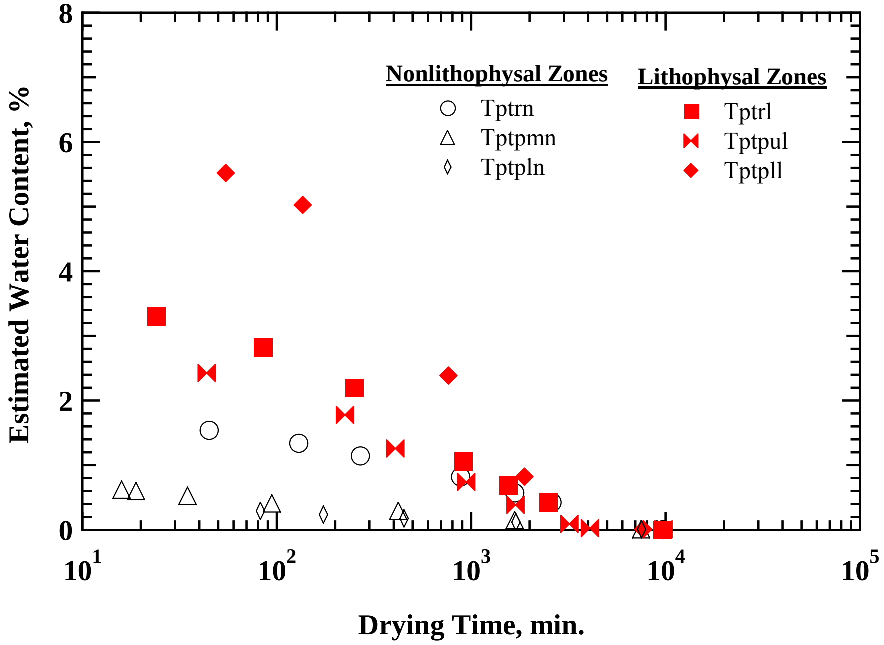

(b) Estimated Average Water Content versus Drying Time after Coring and Trimming

Figure 6.25 Changes in (a) Total Unit Weight and (b) Estimated Average Water Content of Six Specimens from the Topopah Spring Tuff initial w value. This agrees with the fact that the larger porosity and larger amount of pumice clasts and vapor-phase corrosion for the rocks in Tptprn compared with the crystal-poor nonlithophysal rocks. After about a day after the wetting, the w values of the specimens are close to 1 % or less as shown in the figure.

As drying of the specimens progressed, G_{max} increased and their D_{min} decreased as shown in Figure 6.26a and 6.26b, respectively. The measured values scattered during the first 100 minutes but they become stable. After a day of drying, the small-strain properties did not change significantly considering the range of scattering in measurements.

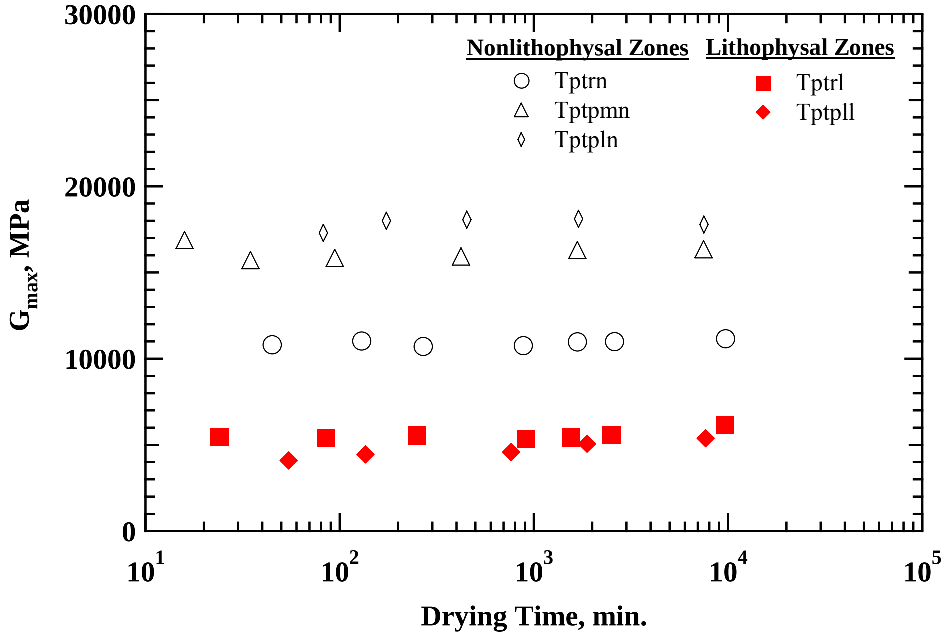

(a) Low-Amplitude Shear Modulus versus Drying Time after Coring and Trimming

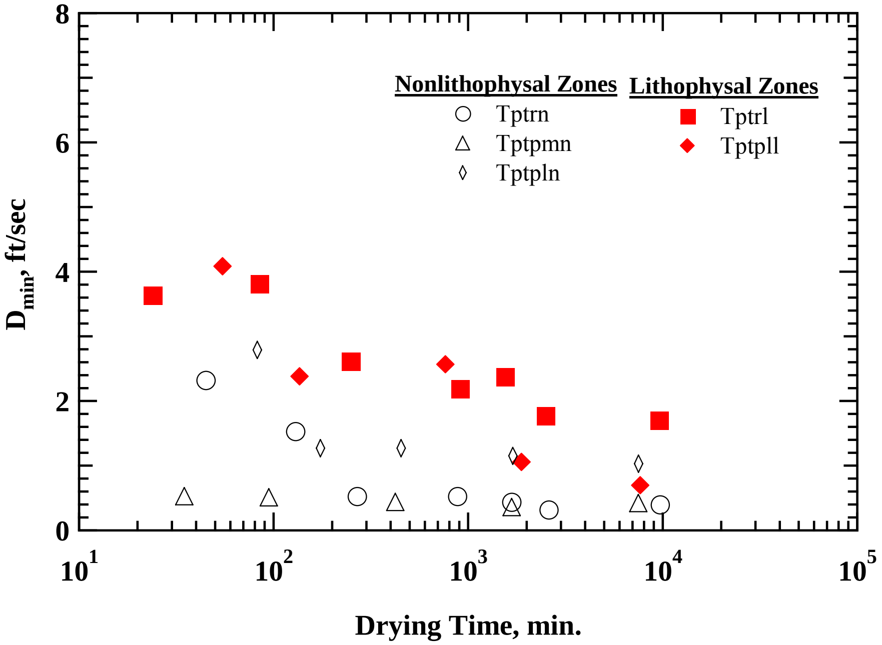

(b) Low-Amplitude Material Damping Ratio versus Time after Coring and Trimming

Figure 6.26 Changes in (a) Low-Amplitude Shear Modulus (G_{max}) and (b) Loa-Amplitude Material Damping Ratio (D_{min}) of Five Specimens from the Topopah Spring Tuff

6.4.3 Effect of Lithophysal Cavities

Two specimens were dynamically tested using the RCTS device to investigate the effect of the lithophysal cavities on their dynamic properties in both the linear and nonlinear ranges. These specimens were selected since they were free from significant flaws and imperfections based on visual inspection. The initial dimensions, the small-strain shear modulus (G_{max}) and material damping ratio (D_{min}) measured in the unconfined state are presented in Table 6.2. One specimen was from the Calico Hills (Tac) formation at Yucca Mountain. The other specimen was from the Topopah Spring Tuff formation at Yucca Mountain.

The specimen from the Calico Hills (Tac) formation had an initial value of γ_t that was about 93.7 lb/ft^3 (1.5 g/cm^3). This is similar to the average γ_t of the poorly to moderately welded tuffs of the Bandelier Tuff. However, the G_{max} value of the specimen from the Tac (4900 MPa) is about 9.6 times larger than the G_{max} of the stiffest moderately welded tuff (508 MPa) at unconfined state for both specimens. The specimen from the Tac also had a small D_{min} value (0.28 %) compared with the D_{min} of the stiffest moderately welded tuff (0.52 %). Moreover, this specimen had a larger linear range for both the shear modulus, G, and material damping ratio, D (see Chapter 8). Therefore, it was expected that the specimen can withstand the multiple processes of drilling (discussed later) and the high-amplitude straining. The G_{max} and D_{min} values were checked after high-amplitude straining in each stage of testing to assure that the interface between the specimen and the top cap and/or base pedestal were not damaged. There was no significant change in the values (less than 1 % in G_{max} and less than 15 % in D_{min}).

The other competent specimen (large G_{max}, small D_{min}, and a large linear range) that was tested was recovered from the Tptpmn. This specimen has much a larger γ_t

Table 6.2 Initial Characteristics of Specimens 8C-2 and 13C-2

UT Spec. No.	Rock Formation	Litho.Unit	Height, in.(cm)	Diameter, in. (cm)	Initial Total Unit Weight, γ_t, lb/ft^3 (g/cm^3)	Initial G_{max}, ksf (Mpa)	Initial D_{min}, %
8C-2	Calico Hills	Tac	5.67 (14.4)	1.56 (4.0)	93.7 (1.5)	102346 (4900)	0.28
13C-2	Topopah Spring	Tptpmn	6.00 (15.2)	1.56 (4.0)	144.0 (2.3)	253601 (12143)	0.52

compared with the specimen from the Tac formation. This specimen represents the tuffs from the nonlithophysal zones in the Topopah Spring Tuff.

To simulate the lithophysal cavities, the length of each specimen was equally divided by drilling seven holes that have a uniform size and shape. This hole is called the Artificial Void Segment (AVS) hereafter. The drilling pattern and four different sizes of AVS used for Specimen 8C-2 are illustrated in Figures 6.27a and 6.27b, respectively. Each AVS penetrates the specimen horizontally in the direction perpendicular to the next AVS using a drill press. All seven holes were drilled before the tests were performed for each AVS size. Figure 6.28a and 6.28b show the photographs of two specimens tested with the seven drilled holes.

For Specimen 8C-2, a total of six different sizes of AVS were drilled using. The diameter of the AVS ranged from 0.13 to 0.56 in. (0.33 to 1.42 cm). Similarly, for Specimen 13C-2, a total of eight sizes of AVS were drilled. The diameter of the AVS ranged from 0.13 to 0.63 in. (0.33 to 1.60 cm). The volume fractions (total volume of eight AVS / total volume of specimen with no AVS) created by these various sizes were

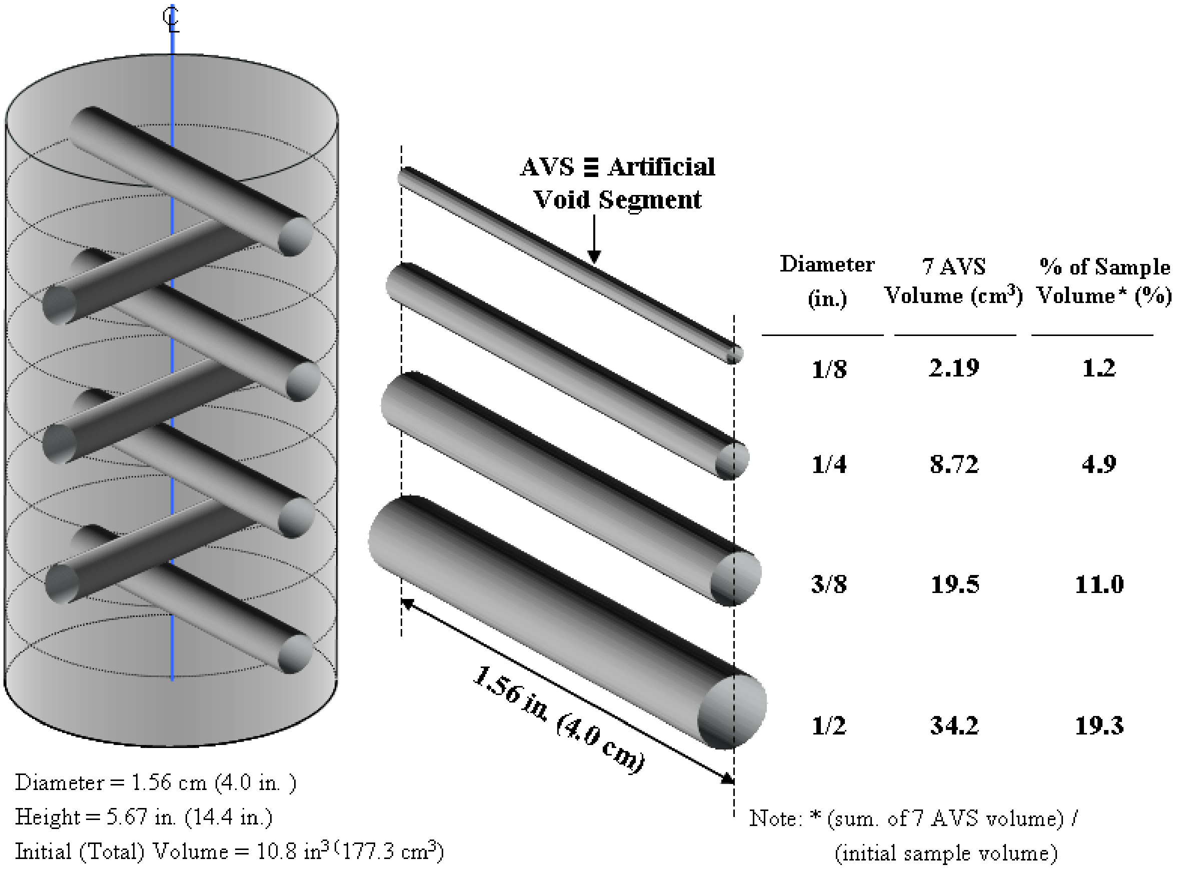

Diameter (in.)	7 AVS Volume (cm^3)	% of Sample Volume* (%)
1/8	2.19	1.2
1/4	8.72	4.9
3/8	19.5	11.0
1/2	34.2	19.3

Note: * (sum. of 7 AVS volume) / (initial sample volume)

(a) Drilling Pattern (b) Four Difference Size of AVS

Figure 6.27 (a) Drilling Pattern and (b) Four Different Size of Artificial Void Segment (AVS) Used for Specimen 8C-2

1.24 to 24.2 % for Specimen 8C and 1.16 to 28.0 % for Specimen 13C-2 as shown in Figure 6.29a. The γ_t decreased by about 24 and 28 % for Specimens 8C-2 and 13C-2, respectively as shown in Figure 6.29b.

The G_{max} of both specimens decreased as γ_t decreased as shown in Figure 6.30a. As the largest size of the AVS was drilled, the G_{max} of Specimen 13C-2 (Tptpmn) decreased by about 47 % from its initial G_{max} without any AVS. The initial G_{max} was

(a) Specimen 8C-2

(b) Specimen 13C-2

Figure 6.28 Specimens with Seven Artificial Void Segments (AVS): (a) Specimen 8C-2 with 1/2-in. Diameter AVS and (b) Specimen 13C-2 with 5/8-in. Diameter AVS

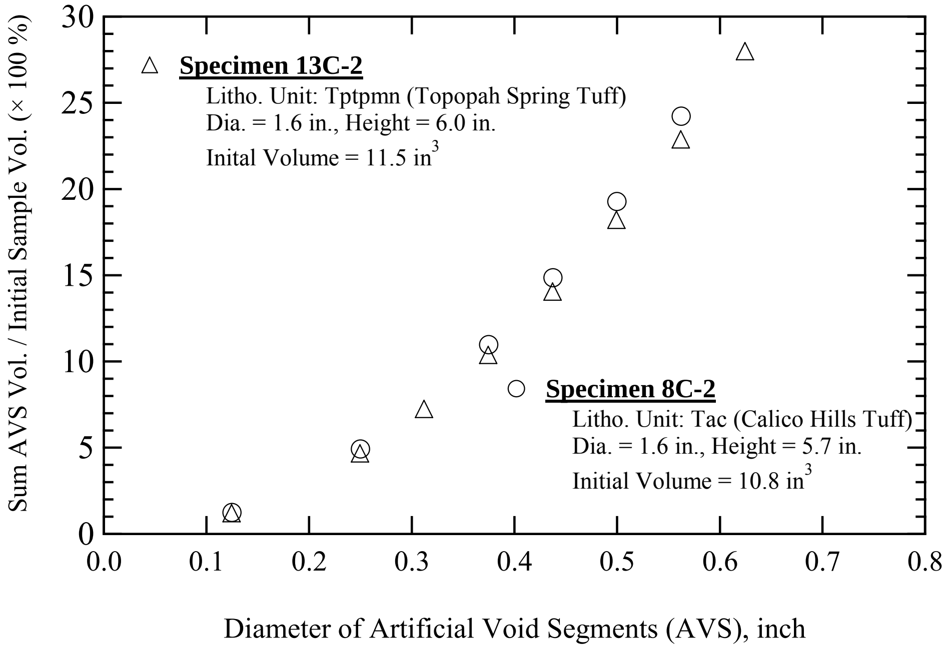

(a) Volume Change versus AVS Diameter

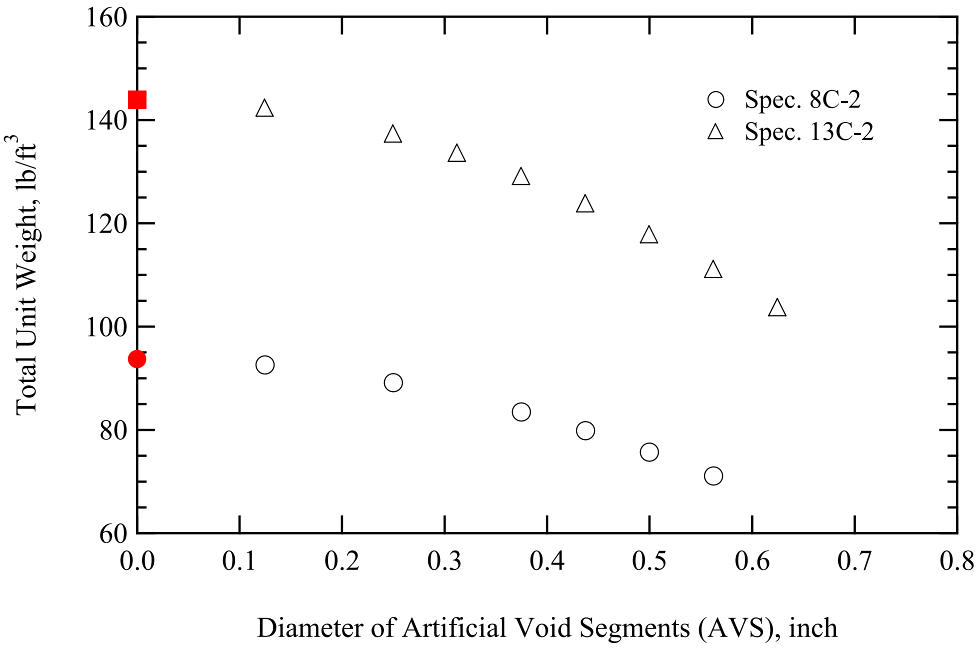

(b) Total Unit Weight versus AVS Diameter

Figure 6.29 Changes in: (a) Volume and (b) Total Unit Weight of Specimens 8C-2 and 13C-2 with Seven Artificial Void Segments (AVS) with Different Diameter Sizes

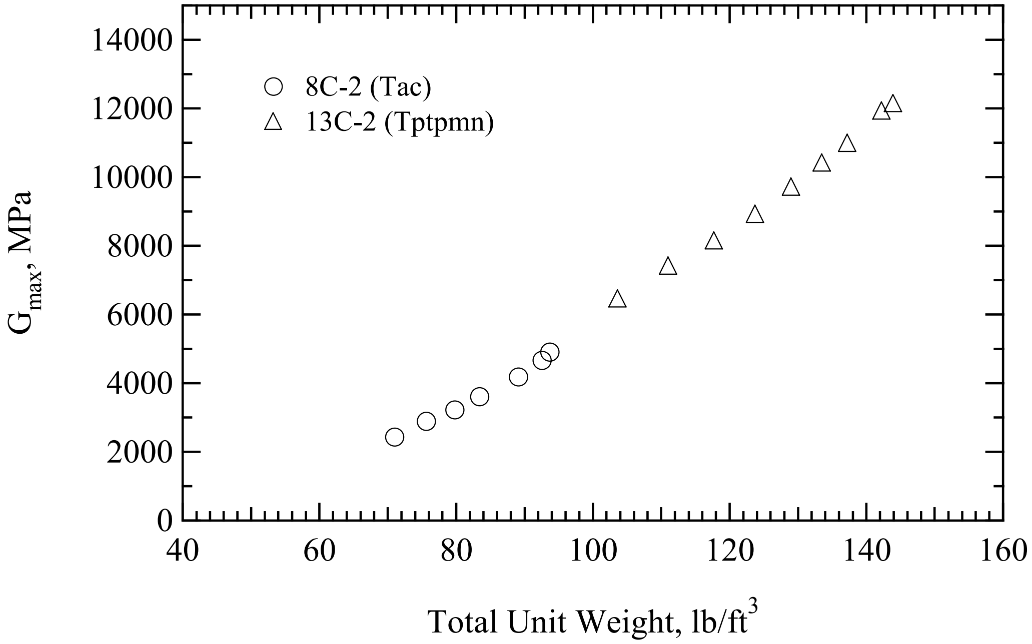

(a) Small-Strain Shear Modulus (G_{max}) versus Total Unit Weight

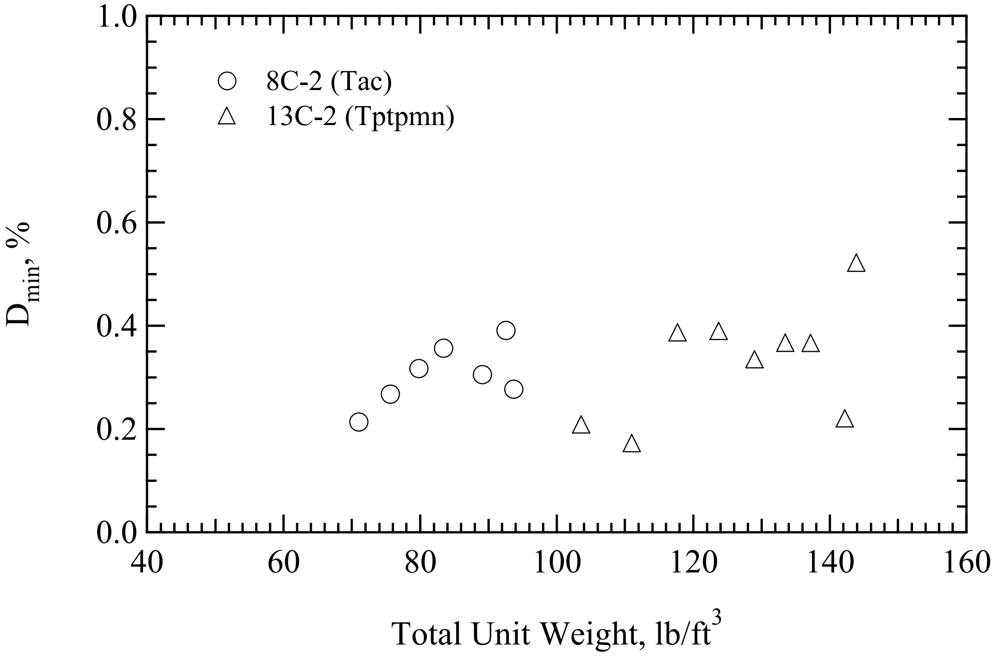

(b) Small-Strain Shear Material Damping Ratio (D_{min}) versus Total Unit Weight

Figure 6.30 Changes in: (a) Small-Strain Shear Modulus (G_{max}) and (b) Small-Strain Material Damping Ratio (D_{min}) of Specimens 8C-2 and 13C-2 with Total Unit Weight about 2.5 times higher than the G_{max} of Specimen 8C-2. For Specimen 8C-2, (Tac), the G_{max} decreased by about 50 % as the size of the AVS increased to the final dimension. The change in γ_t resulting from the change in the volume of the AVS is similar to the variations in γ_t with various amount of lithophysal cavities in the densely welded rocks in the Topopah Spring Tuff because the tuffs from the lithophysal and nonlithophysal zones have very similar matrix-groundmass (Price, 2004). The changes in the G_{max} values were used to represent the effect of the sizes of lithophysal cavities in the tuffs. In addition to the sizes of the lithophysal cavities, their shape and distribution can influence the G_{max} values. Associating with the effect of additional flaws such as fractures, the G_{max} of the rocks in the lithophysal units can be lower with larger scatter than the trend observed with the AVS.

As shown in Figure 6.30a, the G_{max} of the two specimens exhibited a strong relationship with the change in γ_t. The trend in the D_{min} values with γ_t was not as clear as shown in Figure 6.30b. Initially small D_{min} values of the specimens indicate that any imperfections in the specimens do not significantly affect the values. However, the scattering in the trend was taken to be indicative of the sensitivity of D_{min} to the changes in the imperfections and this trend requires more study in the future.

The trends observed with the AVS of the two specimens are compared with the trend found in the natural specimens with real variations in γ_t in Figure 6.31. The γ_t range created with the AVS covers the range of γ_t for the entire data set. However, the trend with AVS is much flatter than the trend with real specimens with natural pore spaces. This flatter trend indicates that the effects of other factors (such as matrix material, relative locations of lithophysae and fractures, etc) can be more significant and the trends with AVS can be an upper bound of these tuffs.

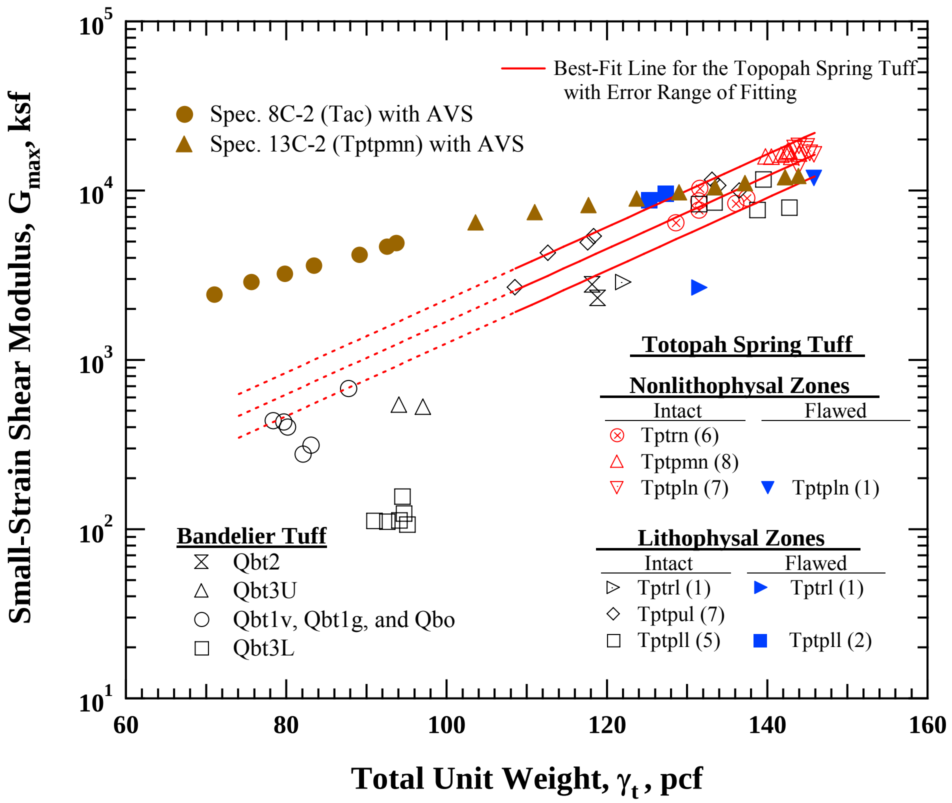

Notes: 1. the data for the Bandelier Tuff were determined at their estimated in-situ pressure and data for the Topopah Spring Tuff were determined at unconfined state.
2. no “flawed” data were not used in the fitting for the Topopah Spring Tuff.

Figure 6.31 Comparison between Trends with AVS and Trends in Natural Specimens with Real Variations in Total Unit Weight

6.5 SUMMARY

Small-strain shear modulus (G_{max}) and small-strain material damping ratio (D_{min}) of the ash-flow tuffs determined using the URC and RC devices are discussed in this chapter. The effects of lithophysal cavities, flaws (fractures and missing pieces of the core) and the degree of welding on G_{max} and D_{min} at different confinement pressures (σ_o) are discussed. Correlations between G_{max} and γ_t and D_{min} and γ_t are studied. Empirical relationships are proposed to describe the small-strain dynamic properties of ash-flow tuffs at various conditions. The effects of excitation frequency (f), change in water content (w) due to specimen preparation, and large lithophysal cavities on G_{max} and D_{min} are also discussed in this chapter.

Chapter 7

Comparisons of Laboratory Tuff Measurements with Field V_S Measurements and Laboratory Granular Soils Measurements

7.1 INTRODUCTION

Comparison of small-strain shear wave velocity (V_S) values measured in the laboratory and in situ provides valuable information on potential problems in the use of laboratory measurements for site characterization. The problems are related to disturbance in the sampling process for soils and rocks, biases in the selection of laboratory specimens, and/or the effect of sample size. Densely welded tuff specimens containing cavities and fractures might not represent site characteristics properly unless the specimens are sufficiently large enough to represent the features without distorting the laboratory measurements. On the other hand, poorly welded tuff specimens have the possibility of experiencing disturbance in the sampling operation unless proper sample methods are used. The V_S values determined in the laboratory from the RCTS and URC devices are compared with V_S values determined in the field from Spectral-Analysis-of-Surface-Wave (SASW), crosshole and downhole tests in this chapter.

In addition to the comparison between the laboratory and field velocity measurements, the small-strain dynamic properties of the poorly welded ash-flow tuffs from the Bandelier Tuff are compared with the dynamic properties of granular soils that are currently available in the literature in later portion of this chapter. In summary, the typical ranges of n_G, n_D and $V_{S,\,0.3\,\text{atm}}$ of granular soils are presented with those ranges of the poorly welded ash-flow tuffs.

7.2 COMPARISON OF FIELD AND LABORATORY V_S MEASUREMENTS

7.2.1 Topopah Spring Tuff

Comparisons between the field and laboratory V_S values for the Topopah Spring Tuff are shown in Figure 7.1. The field data come from Spectral-Analysis-of-Surface-Wave (SASW) tests that were performed in the ESF and ECRB tunnels beneath Yucca Mountain (Lin, 2007). The general locations of the sites are shown in Figure 7.2. About 7-m-long test arrays (or transects) were used in the SASW tests in these tunnels (Lin, 2007). SASW profiling along the tunnel walls was performed with small accelerometers that were attached to a series of nails that were driven into shallowly drilled holes. The accelerometers were attached to the nails using magnets such that various transect lengths could be sampled. The applied energy source was from different-sized hammers. Rayleigh wave velocities over a wide range of frequencies were measured (Lin, 2007). With this information, forward modeling of the Rayleigh wave velocities versus frequency characteristics was used to determine the V_S versus depth profile behind the tunnel wall (Stokoe et al., 1994).

The lithostratigraphic units and their V_S values measured in the laboratory exhibit a good correlation, as discussed in Chapter 6. This correlation between lithostratigraphic units and the field V_S values is not as strong as shown in Figure 7.1. Also, the difference between the field and laboratory V_S values is substantial. The mean V_S values from the laboratory measurements are about 28, 59 and 72 % higher than the mean field V_S values for the Tptpul, Tptpmn and Tptpll units, respectively. The standard deviations (σ) in the field V_S values from the Tptpmn and Tptpll units are much larger than the σ in the laboratory data from these units. Only the Tptpul unit shows a σ value in the laboratory compared with the field data. The differences in mean V_S values likely indicate that the

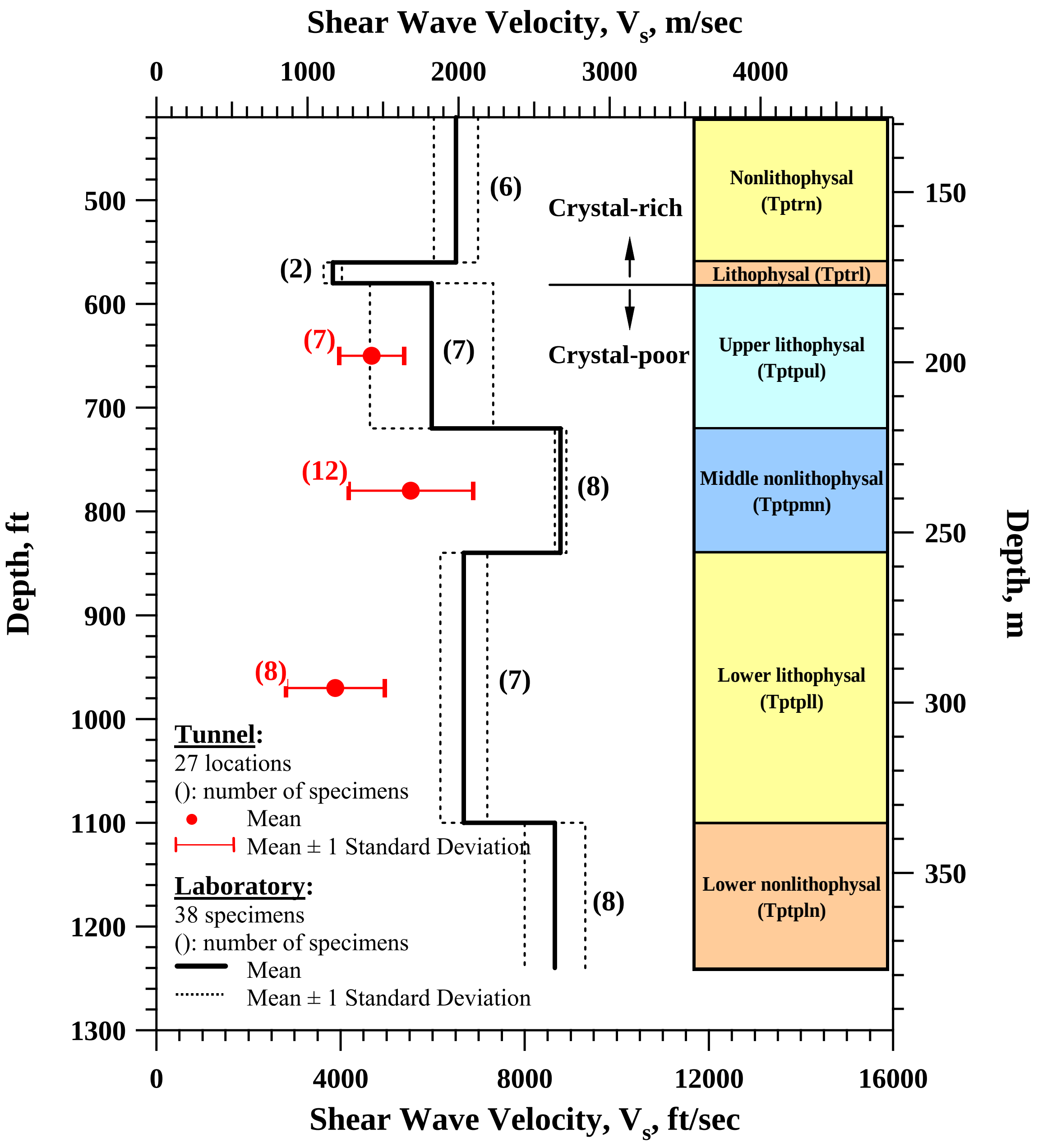

Figure 7.1 Comparison of Vs Values Measured in the Laboratory and In-Situ for the Topopah Spring Tuff

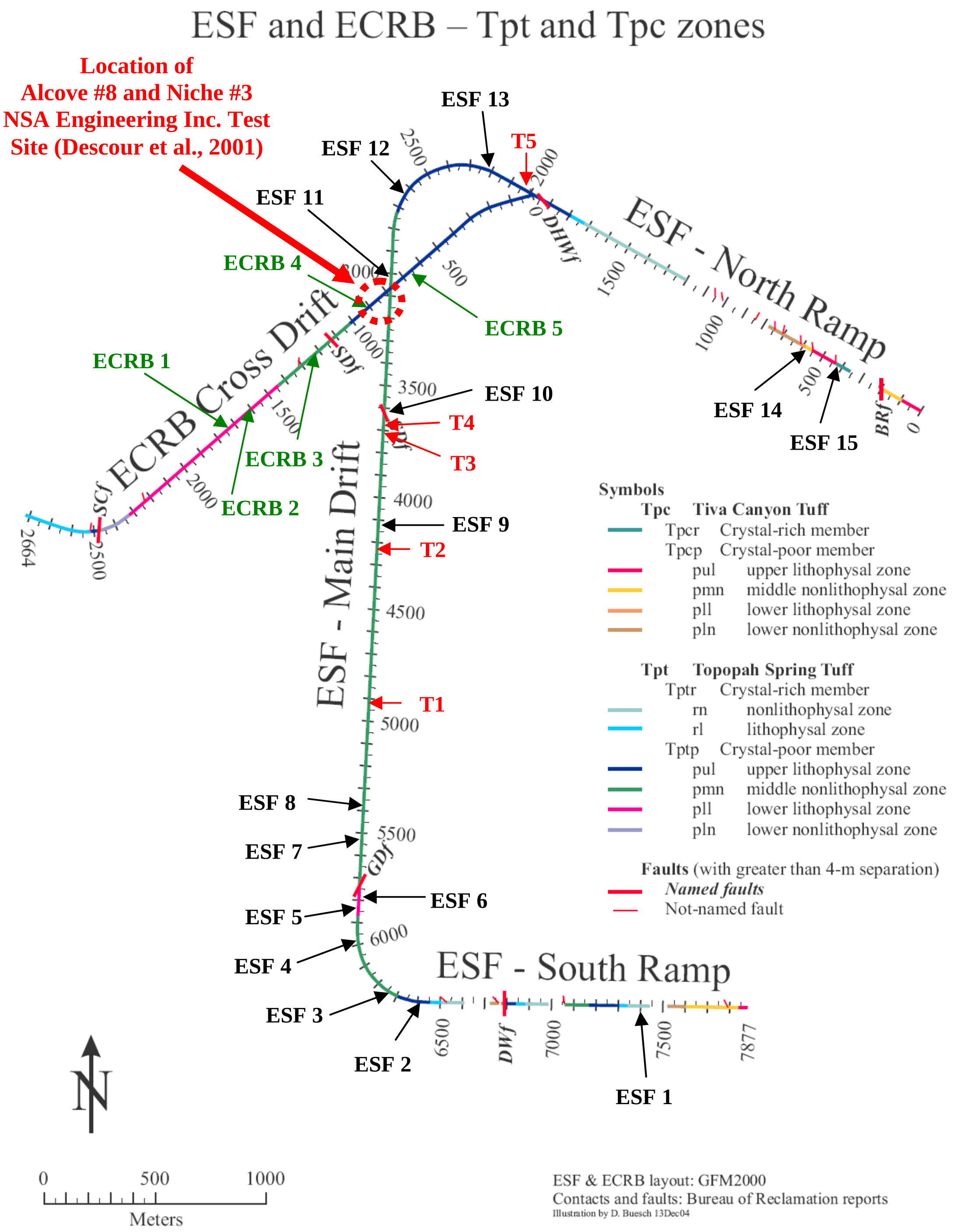

Figure 7.2 General Locations of the SASW Tests Performed in ESF and ECRB Tunnels (from Lin, 2007)

laboratory cores have fewer variations in the amounts, sizes, shapes, and distributions of lithophysal cavities, rimes, spots and fractures than the same material tested in situ. This hypothesis is supported by the larger field σ values in the Tptpmn and Tptpll units. The larger σ in the laboratory data from the Tptpul unit compared with the σ in the field data is taken to indicate that there were larger variations in those features in the laboratory specimens of this unit.

7.2.2 Bandelier Tuff

Similar comparisons of the field and laboratory V_s values over the depth range of 30 to 160 ft (9 to 49 m) from the Los Alamos site are shown in Figure 7.3. At this site, both downhole and crosshole tests were used to evaluate V_S at the site. Three crosshole sites with two or three boreholes and three downhole sites with one borehole were used as described in Stokoe et al., 2006. Contrary to the comparisons in the other Bandelier and the Topopah Spring Tuffs, there is an excellent agreement between the field and laboratory V_S values in the Qbt3L layer (depth range of approximately 75 to 125 ft (23 to 38 m)) of the Bandelier Tuff, with the mean field V_S 93 % above the mean laboratory V_S. Obviously, this material was able to be sampled and represented well. On the other hand, the field V_S values are somewhat smaller than the laboratory values in the layers above and below the Qbt3L layer (the Qbt3U and Qbt2 layers, respectively). This difference likely occurred because the "best" samples were tested in the laboratory. Macroscopic and microscopic fractures and relatively weak components that could not be recovered in the sampling process lead to the higher laboratory measurements. No comparisons in the Qbt3L layer with values from URC tests could be made because no free-free URC tests could be performed in the laboratory with these soft materials since they could not be tested in the

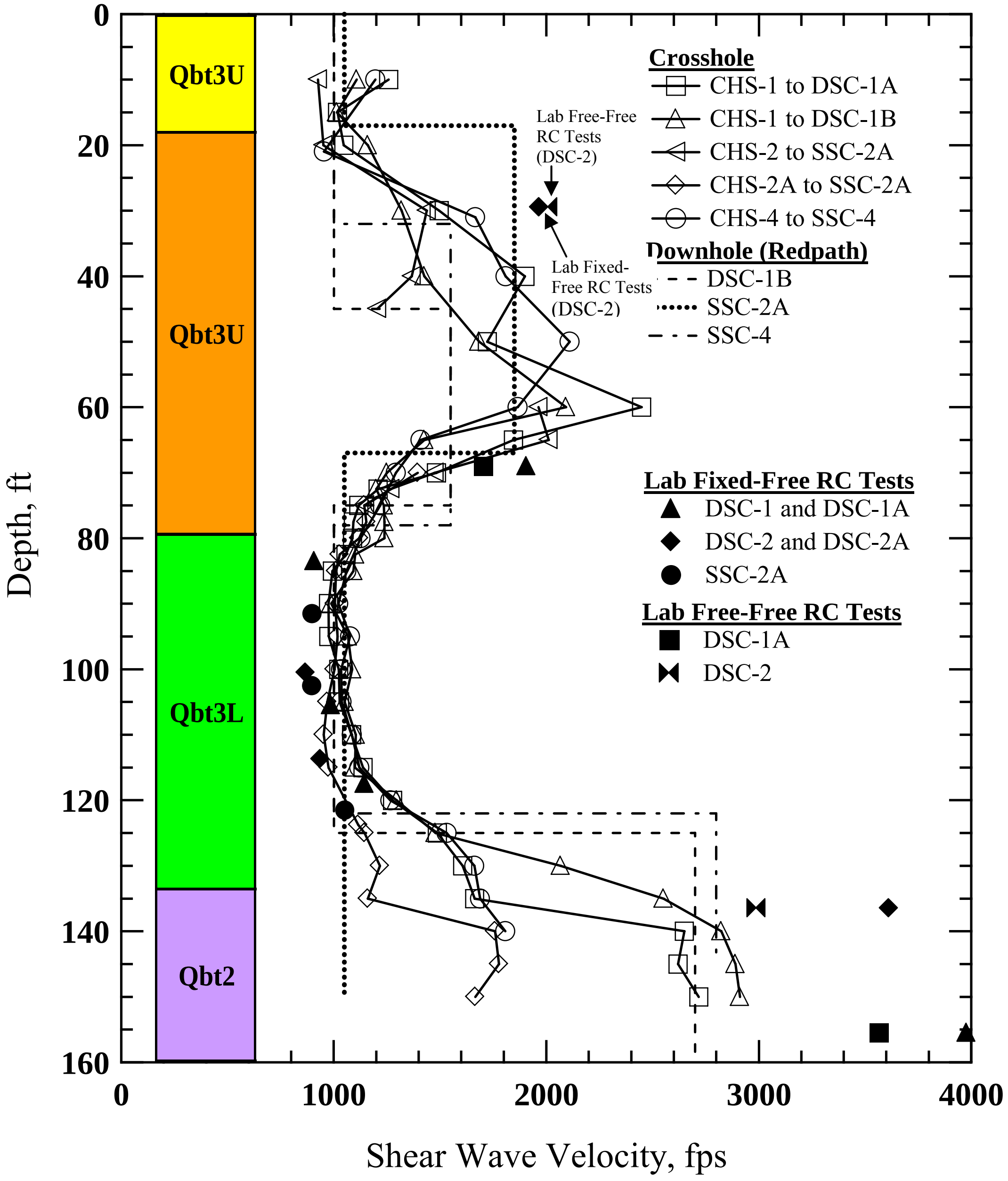

Figure 7.3 Comparison of Vs Values Measured in the Laboratory and In-Situ for Bandelier Tuff (Stokoe et al., 2006)

unconfined state. Comparisons for the units in the deeper depth of the Bandelier Tuff are not included in this study.

The relatively soft layers such as Qbt3L, Qbt1v, Qbt1g, and Qbo exhibited a strong pressure dependency on their small-strain dynamic properties as discussed in Chapter 6. Since the laboratory data do not cover the entire thickness of each unit as shown in Figure 7.3, it is informative to construct a continuous profile of V_S based on the trend lines determined in Section 6.3.2. Borehole DSC-1B was selected for the profile since this borehole is the deepest borehole at the site and includes all lithostratigraphic units at the site. The in-situ mean effective stress (σ_m') along each unit was estimated using the average values of total unit weight and assumed K_o (see Table 2.5). Based on the σ_m', a line for each unit is constructed using Eq. (6.3) with the average A_V and n_V of the specimens from each unit. A complete profile for Borehole DSC-1B is presented with all values determined in the laboratory in Figure 7.4. The range of V_S for soft tuffs within each unit is clearly shown and the relative differences between units are easily seen in the profile. The Qbt2 and Qbt3U are certainly the stiffest layers considering their relatively shallower depth. The V_S values for the Qbt3L are low and increase with depth along the average trend line. The tuffs below the Qbt2 exhibit similar trends of increasing V_S with depth without a significant change in V_S across units. The similarities in the deep units were expected because of the following facts: (1) the assumed K_o values used in the estimations of σ_m' for the units are the same (1.0), (2) the total unit weight (γ_t) does not vary significantly in this depth range, and (3) the A_V and n_V values for the units are very similar.

To investigate the difference between the Qbt3L and the deeper soft layers (Qbt1v through Qbo), the average trend line for the Qbt3L is extended to the bottom of the Qbo

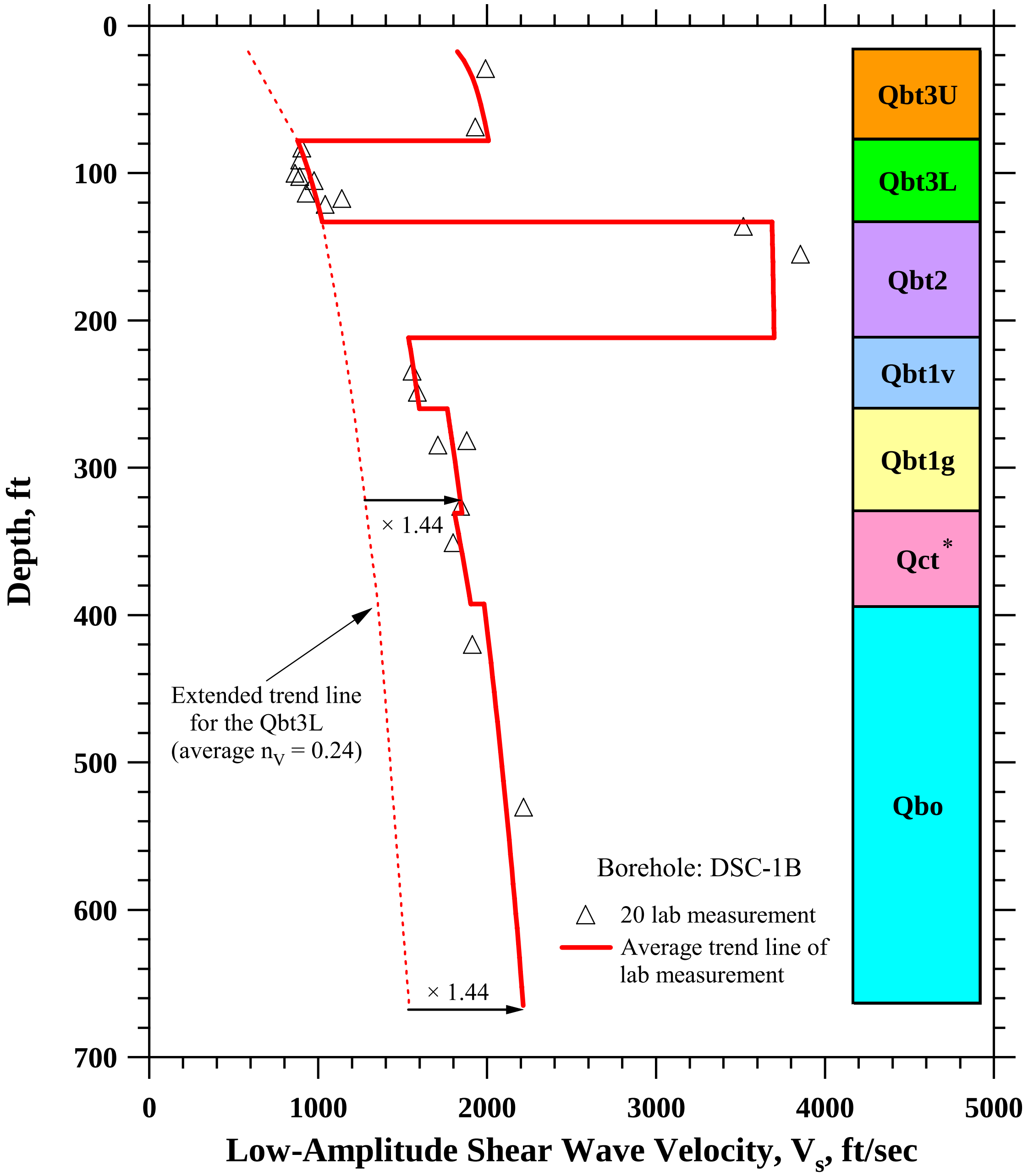

Note: *the Qct is a sand unit. The study on this unit is not included in this research. See Stokoe et al. (2006) for information on this unit.

Figure 7.4 Complete Profile for Borehole DSC-1B Constructed with Average Trend Lines of Shear Wave Velocity with Confining Pressure Determined in the Laboratory as shown in Figure 7.4. At the bottom of the Qbo (615 ft (187 m)), the V_S value expected from the trend line for the Qbo is about 2215 ft/sec (675 m/sec) that is about 44 % higher than the V_S value from the trend line of the Qbt3L (1538 ft/sec (469 m/sec)). Similarly, the V_S expected from the Qbt1g at its bottom depth is about 44 % higher than the V_S expected from the Qbt3L as shown in the figure at the depth of about 331 ft. (101 m). Since the same σ_m' values are used for both trend lines, only differences in A_V and n_V give the 44 % differences. Furthermore, the average n_V for the Qbt3L (0.24) does not differ much (even larger) compared with the n_V for the lower units (0.19 on average). In fact, the average A_V for the lower units is about 1122 ft/sec (341 m/sec) and this is about 57 % higher than the average A_V for the Qbt3L (714 ft/sec (217m/sec)). As seen in Eq. (6.3), A_V is directly related to the estimated V_S while σ_m' (or factors (K_o and γ_t) for σ_m') have the power of n_V that is much less than 1.0. The bottom of the Qbt3L in Borehole DSC-1B is located at 133 ft (40.6 m). The V_S value at this depth is about 960 ft/sec (293 m/sec). The bottom of the Qbo is at about 665 ft (203 m) and the V_S value at this depth is about 1538 ft/sec (469 m/sec) as shown in the trend line of the Qbt3L. This is only an increase of 50 % in V_S over the depth-increase of 532 ft. Therefore, the difference of 57 % in A_V values between the Qbt3L and the lower units is significant, and in turn, it can concluded that the materials in Qbt3L are exceptionally soft compared with the entire profile at the site. This “softness” is directly reflected by A_V of the material skeleton.

7.3 COMPARISON BETWEEN TUFFS AND GRANULAR SOILS

7.3.1 G_{max} Relationships

The small-strain dynamic properties of the poorly welded ignimbrites from the Bandelier Tuff (Groups 3 and 4) are compared with similar properties of granular soils based on the existing literature (e.g. Seed et al. (1986) and Menq (2003)). Seed et al. (1986) proposed that the relationship between G_{max} and the estimated in-situ mean effective stress (σ_m') can be determined as:

$$G_{\max} = 1000(K_2)_{\max}(\sigma'_m)^{1/2} \tag{7.1}$$

where, G_{max} is the small-strain shear modulus in lb/ft^2; $(K_2)_{max}$ is a small-strain shear modulus coefficient; and σ_m' is the estimated in-situ effective stress in lb/ft^2. The authors reported that $(K_2)_{max}$ varies from 30 for very loose sands to 75 for very dense sands. The G_{max} value for very dense sand calculated from Eq. (7.1) using $(K_2)_{max}$ of 75 is about 3450 ksf (165 MPa) at 1.0 atm. This value is very close to the G_{max} values that the materials from the Qbt1v, Qbt1g and Qbo units exhibited at 1.0 atm as shown in Figure 7.5. The average A_G value for the specimens calculated from Eq. (6.6) is about 3209 ksf (153 MPa). Similarly, by using $(K_2)_{max}$ of 30 for the very loose sands, the calculated G_{max} is about 1380 ksf (66 MPa). This value is close to the values the materials from the Qbt3L exhibited at 1.0 atm as shown in Figure 7.5. The average A_G value for the specimens from the Qbt3L is about 1479 ksf (70.8 MPa).

Seed et al. (1986) noted that the $(K_2)_{max}$ values are related to the grain size of the soil particles and relative density. Furthermore, various researchers have found the maximum and minimum void ratios (e_{max} and e_{min}, respectively) are closely related to the uniformity coefficient (C_U). Menq (2003) summarized the e_{max} and e_{min} values for various sands and gravels in the US and Japan (Winterkorn and Fang, 1975; Kokusho et al., 1995; and Rix, 1984) as shown in Figure 7.6. As illustrated in the figure, uniform granular materials can have a large e_{max} and a large difference between e_{max} and e_{min} (on the order of 0.4). The authors suggested relationships between e_{max} and e_{min} for granular soils that can be related to C_U as expressed by:

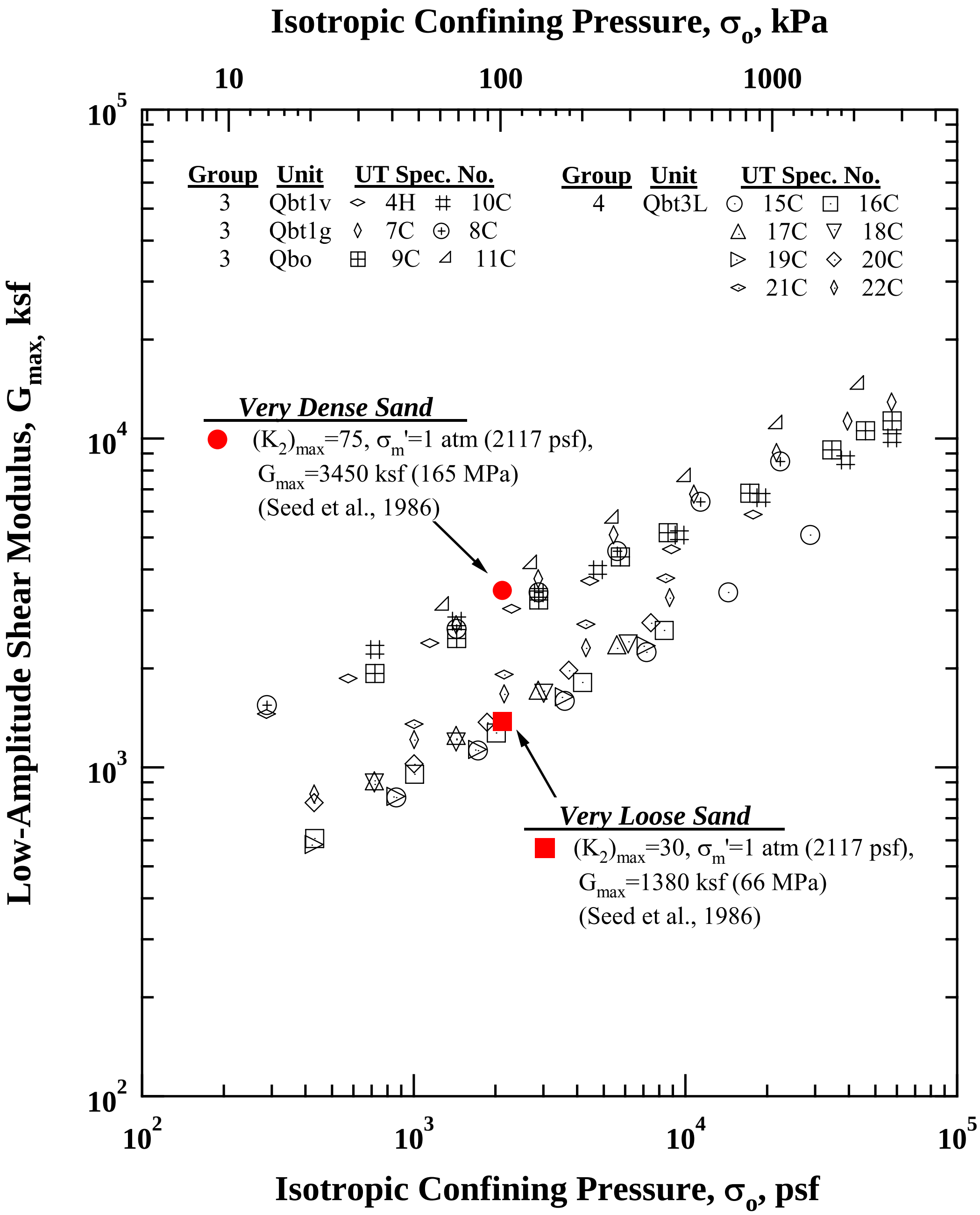

Figure 7.5 Comparison of the Variation in Low-Amplitude Shear Modulus with Isotropic Confining Pressure of Poorly Welded Specimens from the Bandelier Tuff (Groups 3 and 4) and Two Shear Moduli of Very Dense Sand and Very Loose Sand Predicted by Seed et al. (1986)

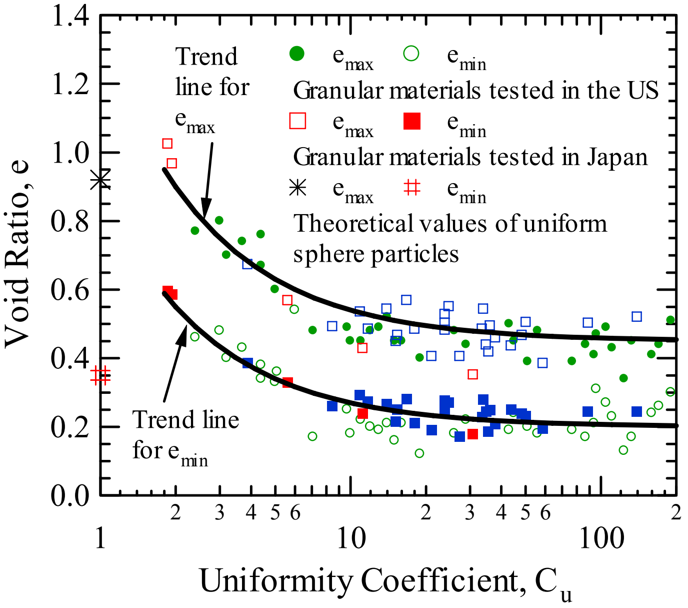

Figure 7.6 Summary of the Variation of e_{max} and e_{min} with Uniformity Coefficient, C_u of Granular Materials Tested in the US and Japan (from Menq, 2003)

$$e_{max} = 0.95 \times (1/C_u) + 0.43 \text{ for } 200 \geq C_u \geq 1.0 \qquad (7.2a)$$

$$e_{min} = 0.60 \times (1/C_u) + 0.22 \text{ for } 200 \geq C_u \geq 1.0 \qquad (7.2b)$$

Menq (2003) discussed the influence of uniformity coefficient (C_U) on the small-strain shear modulus of dry granular materials with given ranges in particle sizes. The empirical relationship for G_{max} proposed by Menq (2003) is:

$$G_{\max} = \frac{67.1 C_U^{-0.2} \left(\frac{\sigma'_o}{Pa} \right)^{0.48 C_U^{0.09}}}{e^{1.0+(D_{50}/20)0.75}} \qquad (7.3)$$

where, G_{max} is in MPa, D_{50} in mm, and Pa is 1 atm (2117 ksf). Most C_U values of dry granular soils tested by Menq ranged from 1.7 to 16, with D_{50} ranging from about 0.47 to 6.7 mm.

Analysis of particle sizes and the distribution of the materials from the Qbt3L were performed by Kleinfelder (2006). An average C_U of 18 and an average D_{50} of 0.7 mm of the Qbt3L material were determined. An average void ratio of 0.91, specific gravity of 2.56 and total unit weight of 88.3 lb/ft (1.4 g/cm^3) were also reported by Kleinfelder (2006). It is very interesting to note that the average C_U for the Qbt3L is a very high number considering the large void ratio (0.91). As clearly seen in Figure 7.6, the maximum void ratios of granular soils with a C_U value of 18 are in the range of about 0.45 to 0.55. In other words, well-graded granular soils cannot be reconstituted with a high void ratio (such as 0.91) without a cementing agent.

Two ranges of G_{max} for dry granular soils are presented in Figure 7.7: (1) poorly graded granular soils with C_U of 1.7 and (2) well-graded granular soils with C_U of 16. Note that the C_U values are based on the general data range of Menq (2003). The G_{max} values for the granular soils having a D_{50} of 0.7 mm were predicted using Eq. (7.3) at the loosest ($e = e_{max}$) and densest ($e = e_{min}$) conditions predicted for C_U values of 1.7 and 16 using Eqs. (7.2a) and (7.2b), respectively. The upper and lower bounds of each range in the figure corresponds the e_{min} and e_{max} values, respectively.

There are several differences between granular soils and these poorly welded tuffs. First, when the C_U is high (16 in this example), all G_{max} measurements of the Qbt3L above about 0.5 atm are lower than the predictions. Second, as Menq (2003) suggested, high C_U values result in a larger change in G_{max} with increasing confining pressure. The n_G values for granular soils with C_U of 1.7 and 16 are about 0.50 and 0.61, respectively. However, the Qbt3L unit (with C_U = 18) has an average n_G of about 0.48. Therefore, the Qbt3L unit is not well predicted by a granular soil with similar grain-size characteristics. On the other hand, if one uses a C_U value of 1.7, granular soils with D_{50}

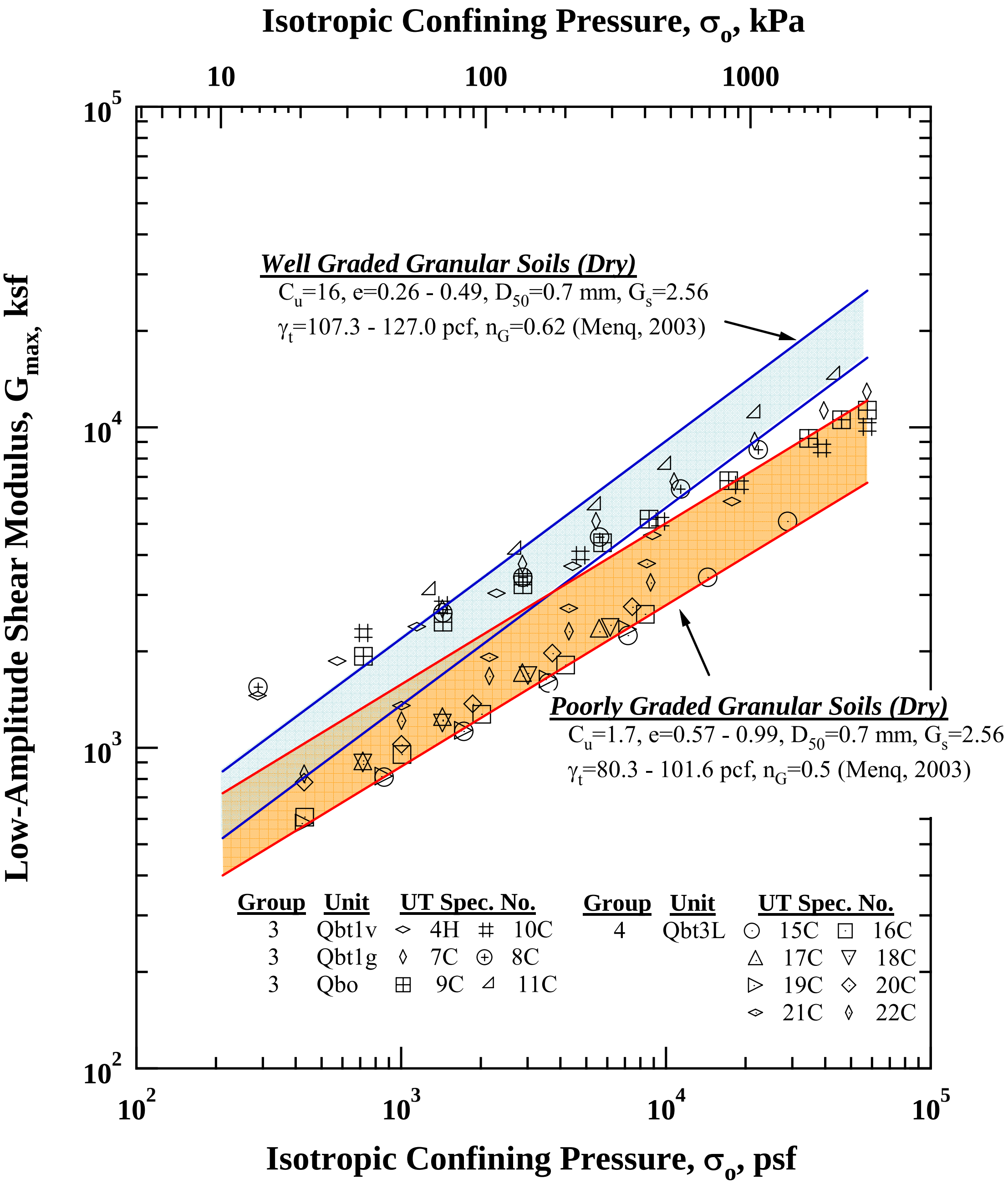

Figure 7.7 Comparison of the Variation in Low-Amplitude Shear Modulus with Isotropic Confining Pressure of Poorly Welded Specimens from the Bandelier Tuff (Groups 3 and 4) and Similar Relationships for Granular Soils

of 0.7 mm normally have G_{max} values smaller at low confining pressure (below about 1 atm) compared with materials in Group 3 (from Qbt1v, Qbt1g, and Qbo).

Seed et al. (1986) also reported that relatively dense gravels have $(K_2)_{max}$ ranging from about 80 to 180 based on their in-situ shear wave velocities. By using the mid-value in the range (130), a G_{max} value of 5981 ksf (286 MPa) is obtained at 1 atm from Eq. (7.1) for dense gravels. This G_{max} value is between Groups 2 and 3 at a lower pressure (like 1 atm) as shown in Figure 7.8. However, the pressure dependency of G_{max} is the same as sand (no difference in the exponent of pressure in Eq. (7.1)). Therefore, the small pressure dependent change in G_{max} of Group 2 (moderately welded tuffs) is somewhat different from the expectations for gravelly soils with C_U values greater than 7 to 10. Similarly, the higher G_{max} is expected for soils containing gravel size particles using larger D_{50} values as shown in Eq. (7.3). However the smallest n_G is 0.48 for the lowest C_U of 1.0, so that the change in G_{max} with confining pressure for gravelly soils predicted by Eq. (7.3) is different from the trend observed in Groups 1 and 2 (average n_G values of 0.015 and 0.12, respectively).

7.3.2 D_{min} Relationships

While Seed et al. (1986) proposed low-amplitude material damping ratio (D_{min}) between about 0.4 to 1.0 % at a confining pressure (σ_o) of about 1 atm for both sands and gravels as a rough range, Menq (2003) proposed an empirical relationship for D_{min} taking particle gradation (C_U and D_{50}) and σ_o into account as:

$$D_{\min} = 0.05 C_U^{0.1} D_{50}^{-0.3} \left(\frac{\sigma_o'}{Pa} \right)^{-0.08} \qquad (7.4)$$

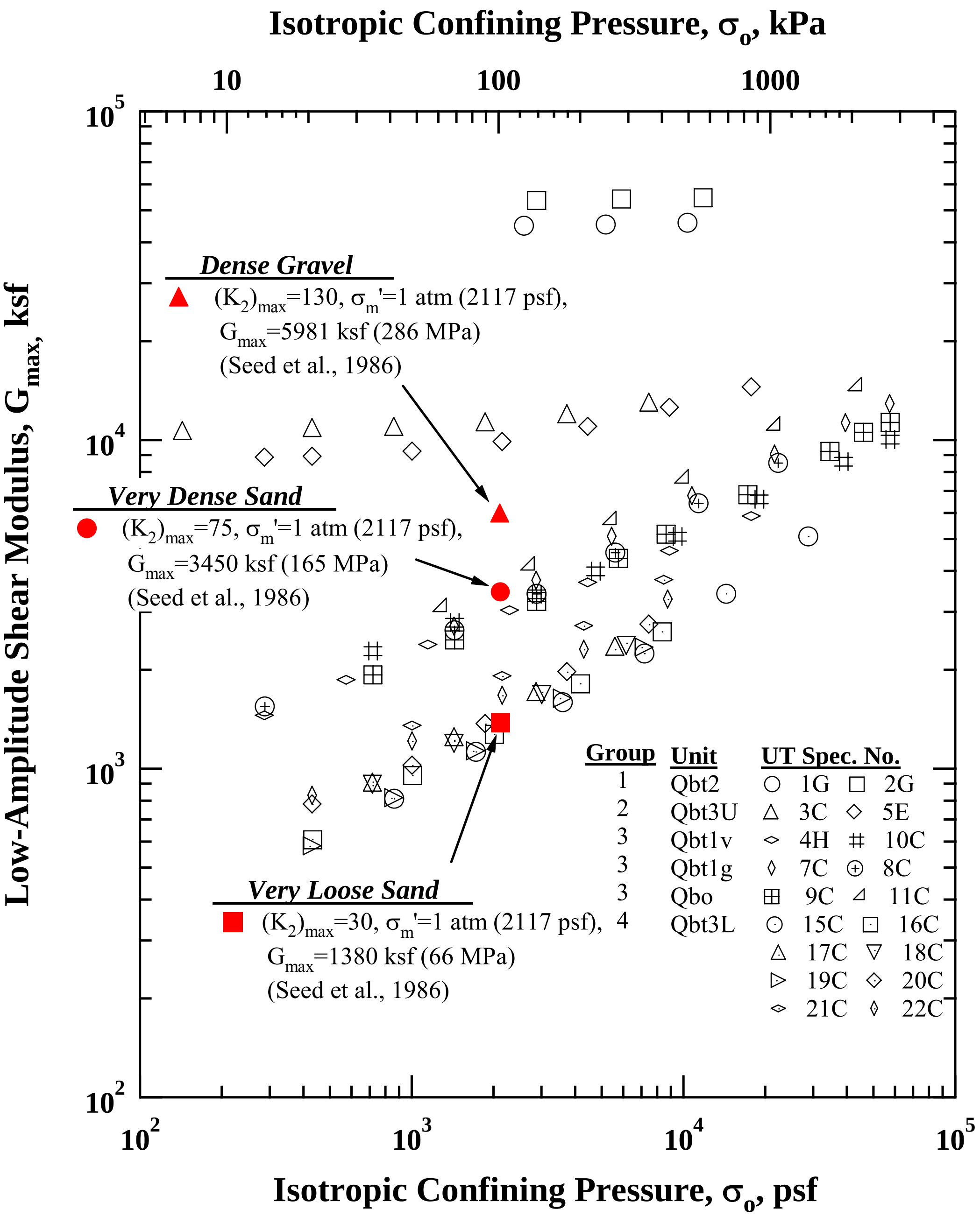

Figure 7.8 Comparison of the Variation in Low-Amplitude Shear Modulus with Isotropic Confining Pressure of Specimens from the Bandelier Tuff (Groups 1 and 4) and Three Shear Moduli of Very Dense Sand, Very Loose Sand, and Dense Gravel Predicted by Seed et al. (1986)

where, D_{min} is in %, D_{50} in mm, and Pa is 1 atm (2117 ksf). As seen in the equation, D_{min} is influenced by $C_{U,}$ D_{50} and pressure. Two lines for granular soils with D_{50} of 0.7 mm are obtained using the minimum and maximum C_U values (C_U = 1.7 and 16) as shown in Figures 7.9 and 7.10 for the materials in Groups 3 and 4, respectively. The difference in the predicted D_{min} values is small (about 0.2 %). to cover all data for Groups 3 and 4 at the given D_{50} and a fixed slope in Eq. (7.4) is somewhat smaller than the trend for poorly welded tuff from the Groups 3 and 4 of the Bandelier Tuff.

Based on the differences observed above, the typical range of n_G for soils and tuffs having various ranges of $V_{S,\ 0.3\ atm}$ are illustrated in the Figure 7.11a. Note that the trend lines of the tuffs determined earlier are presented but $V_{s,\ 0.3atm}$ is in a logarithmic scale to investigate the small velocity range for softer materials. The two ranges for n_G expected for granular soils with the two C_U values are discussed above. The left end of each line represent soils with e_{max} and the right end represent soils with e_{min}. Depending upon D_{50}, the line moves horizontally because $V_{S,\ 0.3\ atm}$ changes. Therefore, the n_G and $V_{S,\ 0.3\ atm}$ values of poorly graded sands are around an SP material and the n_G and $V_{S,\ 0.3\ atm}$ values of well-graded gravels are around a GW material in Figure 7.11a.

Similarly, the typical range of n_D for granular soils and tuffs having various ranges of $V_{S,\ 0.3\ atm}$ are illustrated in the Figure 7.11b. Since n_D of granular soils are independent of C_U, the two lines for granular soils shown in the figure are at the same value of n_D. As with n_G, the left end of each line represent soils with e_{max} and the right end represent soils with e_{min}. Depending upon D_{50}, the lines move horizontally. Therefore, the n_D and $V_{S,\ 0.3\ atm}$ values of poorly graded sands are around SP and the n_G and $V_{S,\ 0.3\ atm}$ values of well-graded gravels are around GW in Figure 7.11b. Clearly, the n_D values of the poorly welded tuffs are slightly higher (more negative) than granular soils.

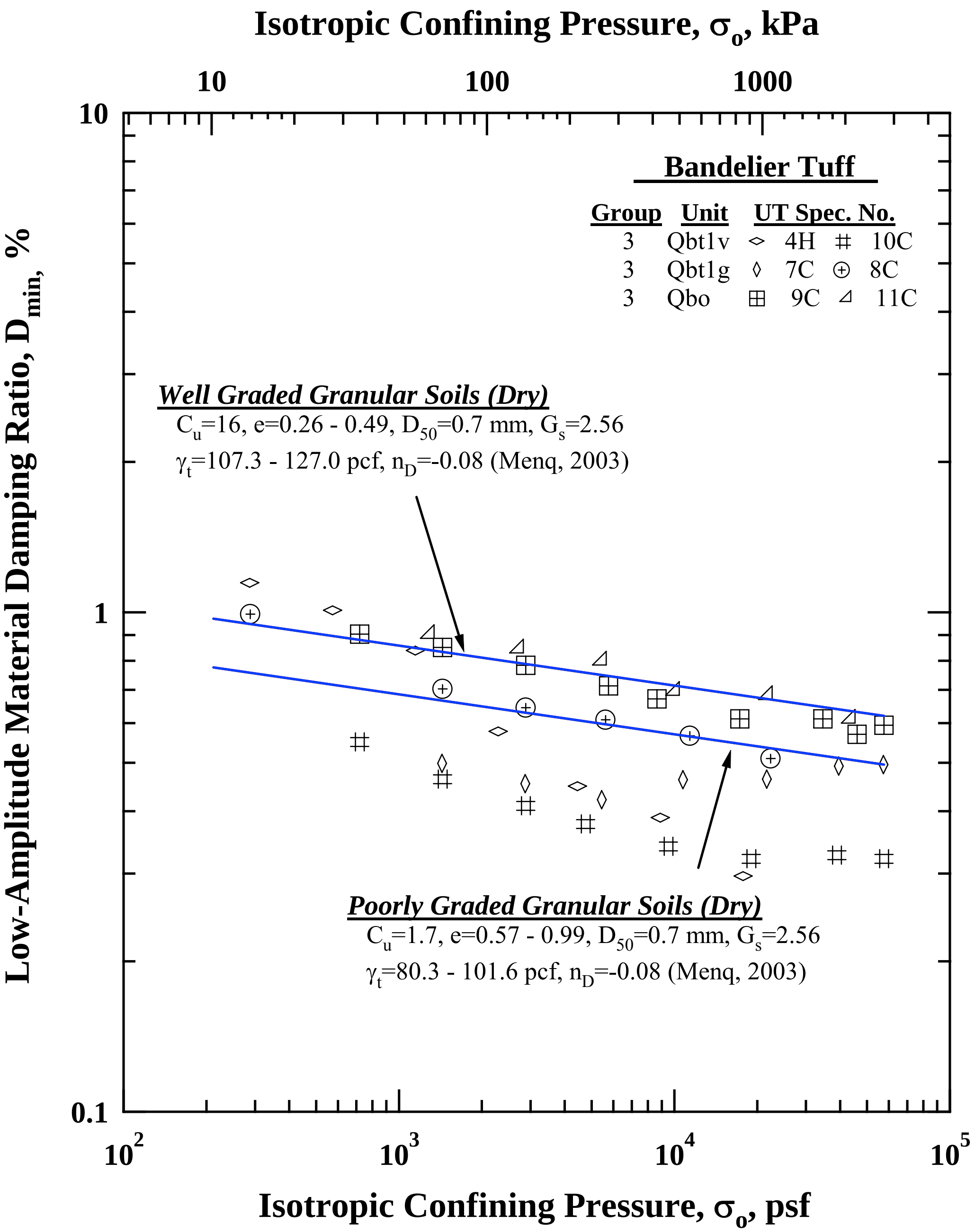

Figure 7.9 Comparison of the Variation in Low-Amplitude Material Damping Ratio with Isotropic Confining Pressure of Poorly Welded Specimens from the Bandelier Tuff (Group 3) and Similar Relationships for Granular Soils

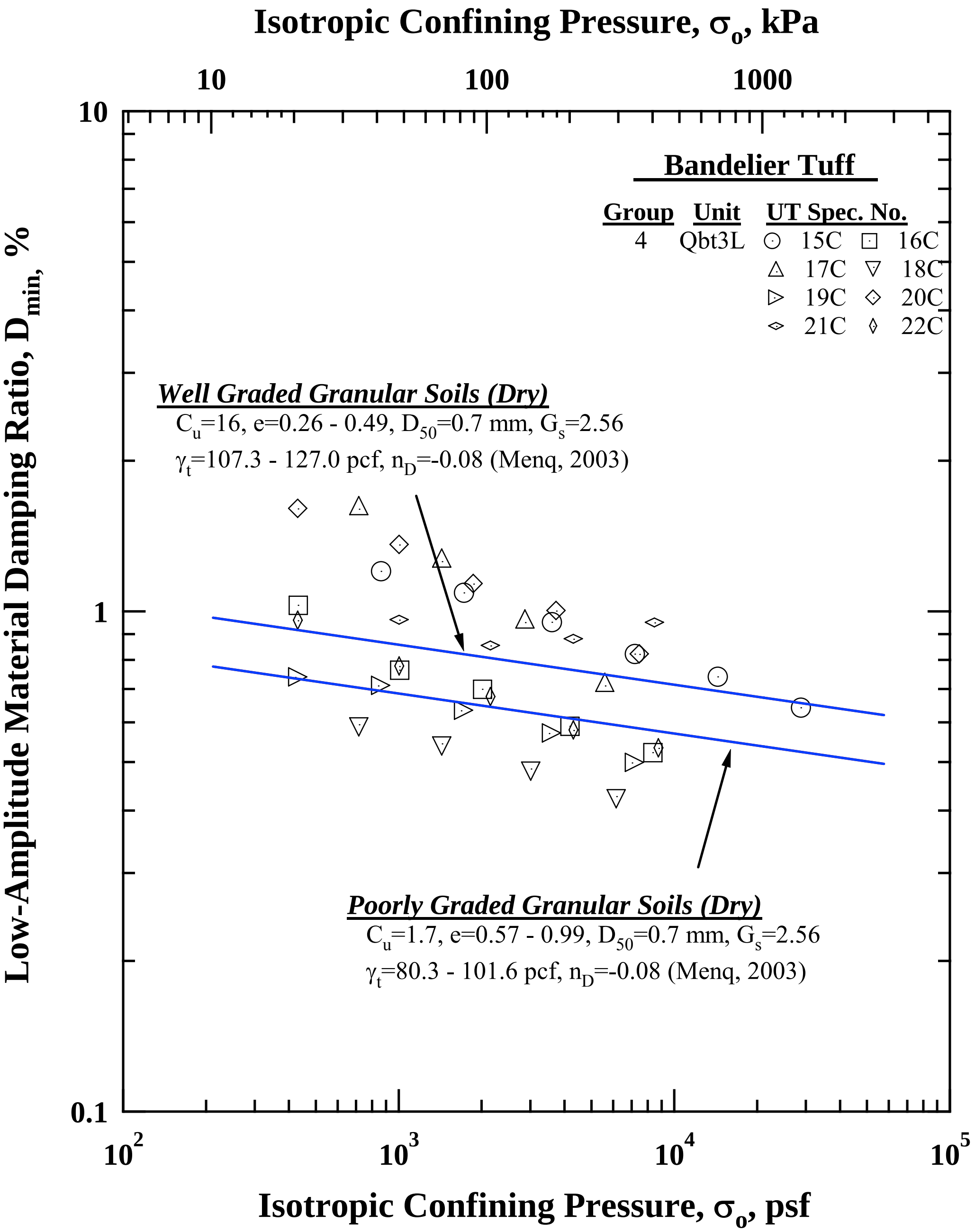

Figure 7.10 Comparison of the Variation in Low-Amplitude Material Damping Ratio with Isotropic Confining Pressure of Poorly Welded Specimens from the Bandelier Tuff (Group 4) and Similar Relationships for Granular Soils

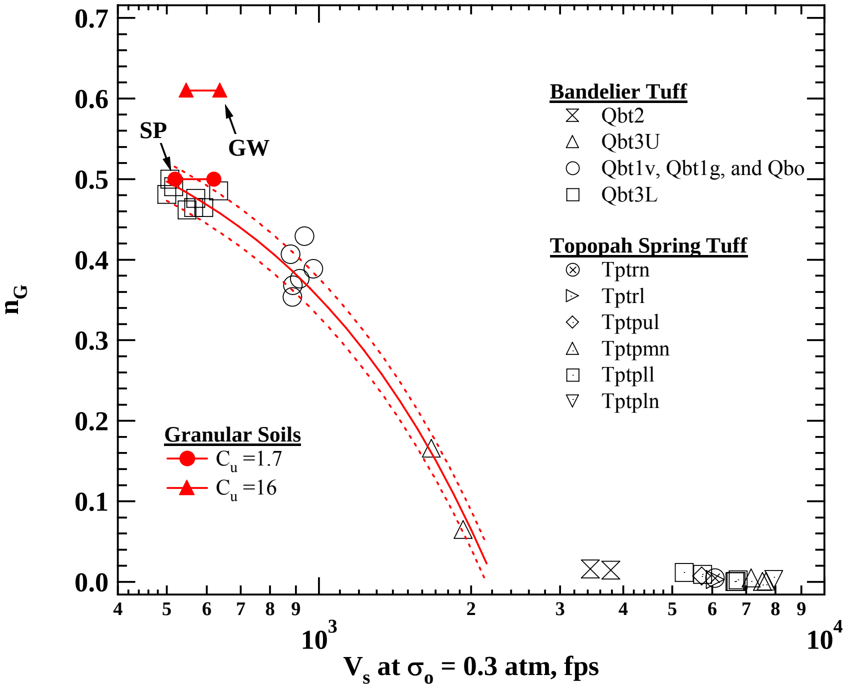

(a) Variation of n_G with V_S at σ_o = 0.3 atm

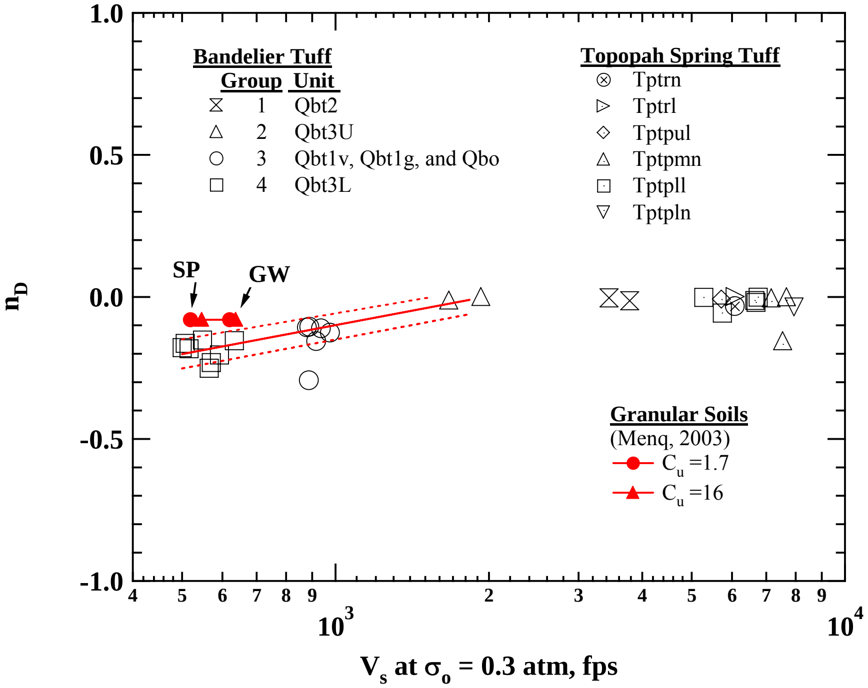

(b) Variation of n_D with V_S at σ_o = 0.3 atm

Figure 7.11 Variations of (a) n_G and (b) n_D with $V_{S,\,0.3\text{ atm}}$ for Granular Soils (D_{50} =0.7 mm) and Ash-Flow Tuffs

7.4 SUMMARY

The small-strain shear wave velocity (V_S) values measured in the laboratory are compared with the V_S values determined in the field from Spectral-Analysis-of-Surface-Wave (SASW), crosshole and downhole tests the in this chapter. The correlation of lithostratigraphic units with V_S values measured in the field is not as strong as the correlation with V_S values measured in the laboratory. Also, the difference between the field and laboratory V_S values is substantial. It was thought that laboratory cores could have somewhat different variations in lithostratigraphic features than the same material tested in situ.

In addition to the comparison between the laboratory and field velocity measurements, the small-strain dynamic properties of the ash-flow tuffs from the Bandelier Tuff are compared with the properties of granular soils that are currently available in the literature. The materials from the Qbt3L unit have similar Vs values of loose sands. However, the average void ratio of the Qbt3L materials is significantly larger than granular soils having the similar uniformity coefficient. The tuffs with higher welding intensity have higher V_S values as denser soils or soils with larger particle size have. However, the small pressure dependent change in G_{max} of the stiffer tuffs is clearly different from the large pressure dependent change in G_{max} of the granular soils.

Most small-strain material damping ratio (D_{min}) values of the tuffs are as small as the values for granular soils that can be found in the literatures. However, the poorly welded tuffs have larger pressure dependency of D_{min} and the tuffs with higher welding conditions have smaller pressure dependency of D_{min} compared with granular soils.

In summary, the typical ranges of n_G, n_D and $V_{S,\ 0.3\ atm}$ of granular soils are presented with those ranges of ash-flow tuffs.

Chapter 8

Nonlinear Dynamic Properties of Ash-Flow Tuffs

8.1 INTRODUCTION

The discussions of the measurements in the strain range where the dynamic properties (G and D) are dependent on strain amplitude are presented in this chapter. This strain range is called the nonlinear range, and measurements and dynamic properties in this strain range are often called large-strain or high-amplitude properties.

A total of 16 specimens from the Topopah Spring Tuff and 18 specimens from the Bandelier Tuff were dynamically tested using the RCTS device. The effects of lithostratigraphic features on the G/G_{max} –log γ and D - log γ relationships are evaluated by comparing the total unit weight (γ_t) and small-strain shear wave velocity at 0.3 atm ($V_{S,\ 0.3\ atm}$) of the specimens, as done in the discussion for the dynamic properties in the linear range in Chapter 6. The effect of confining pressure (σ_o) on the nonlinear relationships is also discussed.

Since the specimens have various lithostratigraphic features and test pressures are different, the ranges of G/G_{max} and D at the largest strain that could be generated vary. In addition, some specimens were not tested at high strains at smaller confining pressures than the target pressures (in-situ pressure and or the highest pressure possible with the equipment). To extrapolate the G/G_{max} – log γ relationship to larger strains, the modified hyperbolic model proposed by Darendeli (2001) was used. For the extension of the D – log γ relationships, a fitting equation is proposed in this chapter. However, care must be exercised in extrapolating the nonlinear data as additional factors such as slippage along cracks or breakage between lithophysae will accentuate the nonlinearity at higher strains.

8.2 G – LOG γ AND G/G_{max} – LOG γ RELATIONSHIPS OF ASH-FLOW TUFFS

8.2.1 Topopah Spring Tuff

The influence of shearing strain, γ, on shear modulus (G) and normalized shear modulus (G/G_{max}) as measured by resonant column testing is shown in Figures 8.1 and 8.2, respectively, for the 16 intact tuff specimens from the Topopah Spring Tuff. A total of ten specimens from the lithophysal zones and six specimens from the lithophysal zones were tested. Only values measured at the highest test pressure of each specimen are shown in the figures. Note that Specimens 11C-1 and 12C-1 were tested only at the unconfined state due to many large voids (lithophysal cavities) on their surfaces as described in Chapter 6. As seen in Figure 8.1, G of each specimen exhibits a linear range where it is constant and equal to G_{max}. This linear range is followed by a nonlinear range where G decreases as γ increases. Since the specimens have various lithostratigraphic features, their G_{max} values range widely from about 6156 MPa to 15600 MPa, although their range in total unit weight (γ_t) is relatively narrow (from 135 pcf to 147 pcf) as seen in the legend in Figure 8.1. It is interesting to note that the two re-cored specimens, Specimens 2C-2 and 3K-2, exhibited the larger linear ranges as well as larger G_{max} values compared with their larger parent specimens, Specimen 2B-3 for 2C-2 and 3C-2 for 3K-2, respectively. Figure 8.2 shows their large linear ranges clearly. It can be seen that the G/G_{max} – log γ relationships for the two, re-cored specimens reach the largest strain ranges with least change in G/G_{max}. The G/G_{max} values of about 0.956 and 0.948 were determined at the largest shearing strains of about 0.040 and 0.058 % for Specimens 2C-2 and 3K-2, respectively. Other specimens could only be tested up to the strain less than about 0.02 % and their lowest G/G_{max} values are about 0.94, in general. Two specimens

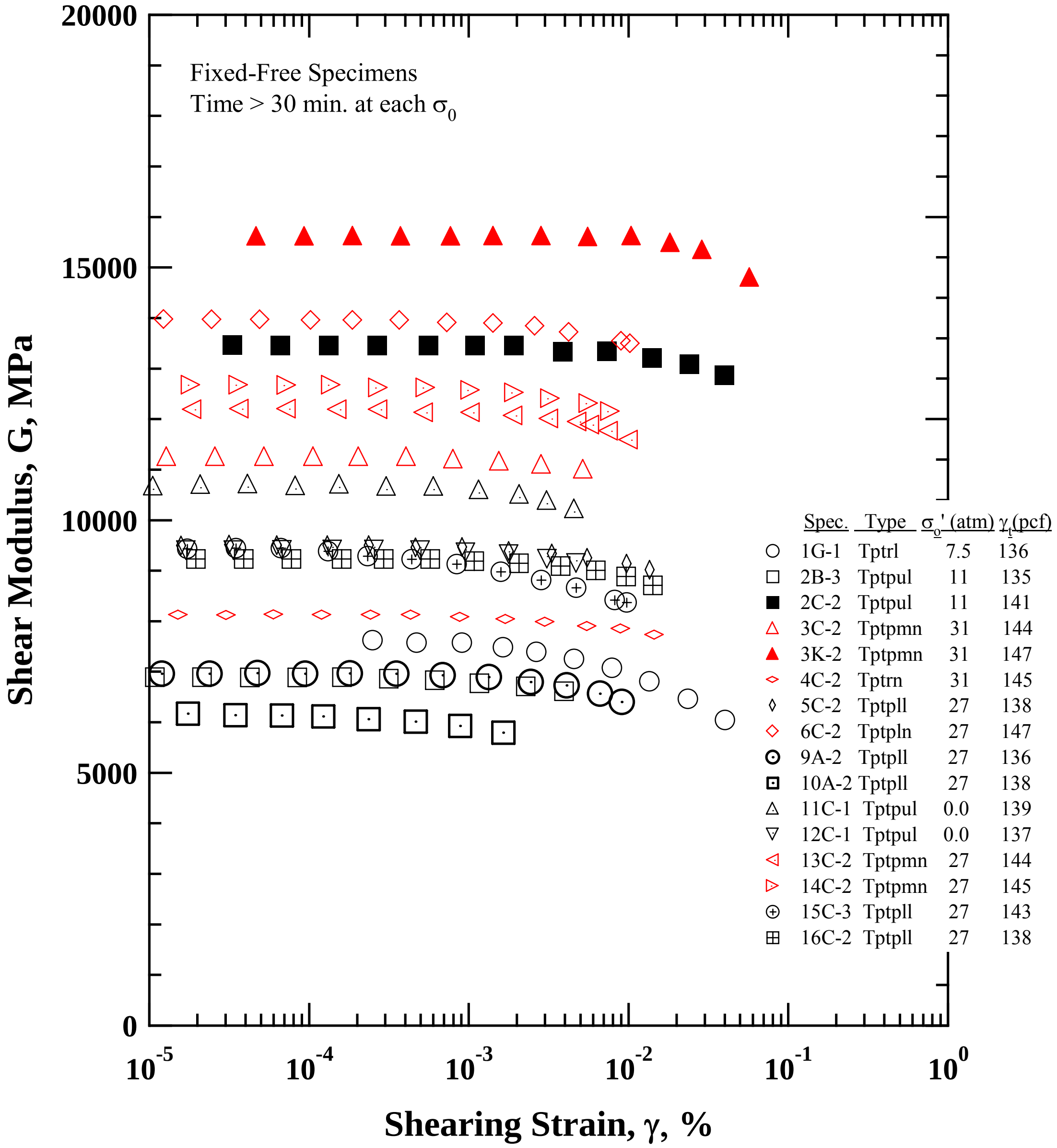

Figure 8.1 Variation of Shear Modulus with Shearing Strain from Fixed-Free Resonant Column Tests of Sixteen Specimens from the Topopah Spring Tuff

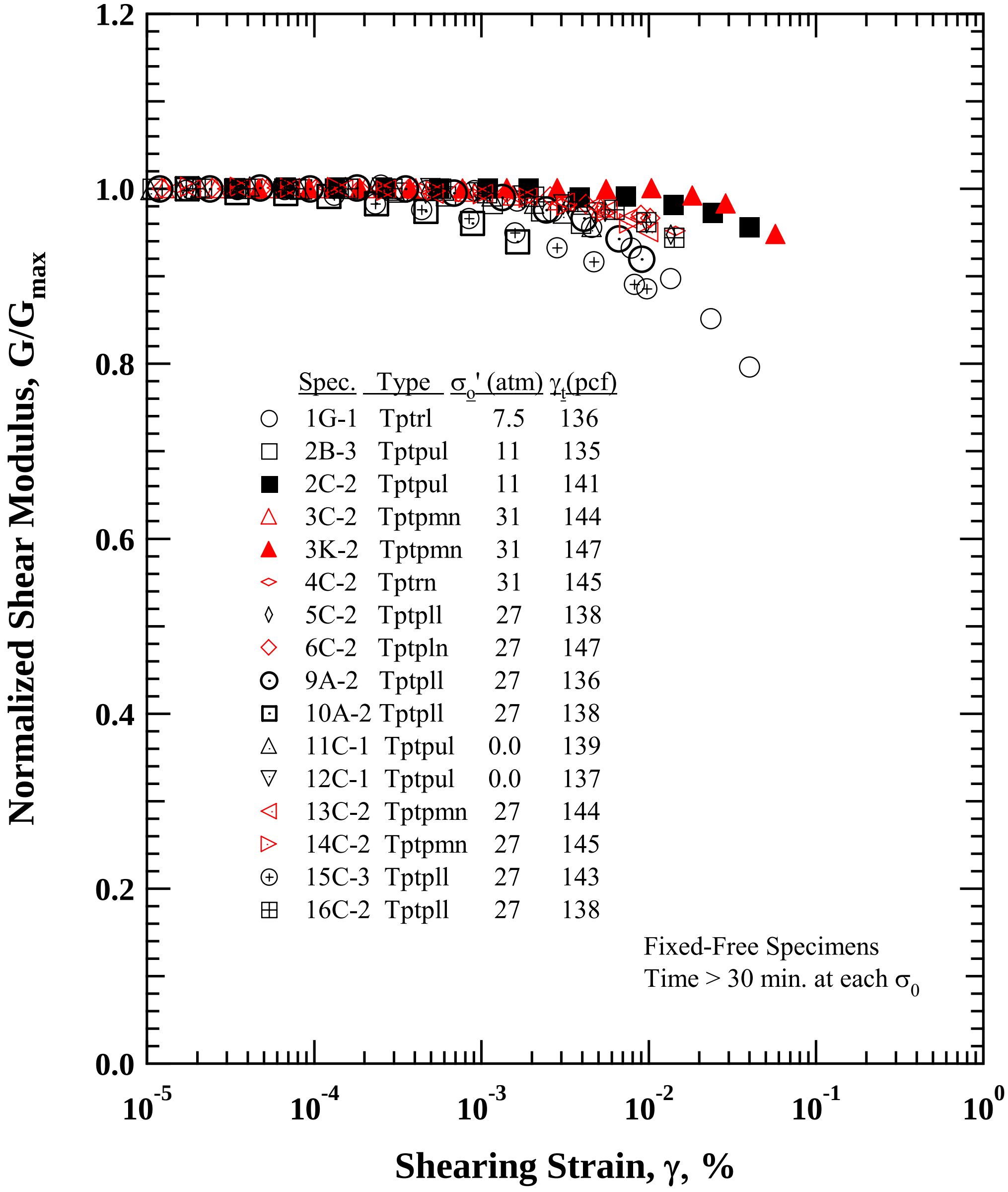

Figure 8.2 Variation of Normalized Shear Modulus with Shearing Strain from Fixed-Free Resonant Column Tests of Sixteen Specimens from the Topopah Spring Tuff

from the Tptpll unit (Specimens 10A-2 and 15C-3) exhibited somewhat more nonlinear; that is, G/G_{max} deceasing more with increasing γ.

Two values of γ were selected to investigate the variation of the G values in detail. The first γ is the γ when G decreases by 2 % from G_{max} ($G/G_{max} = 0.98$). The G_{max} values of the specimens were unaffected by testing these slightly larger strains. All specimens from the Topopah Spring Tuff were tested up to this level of strain in the first series of tests at the lower confining pressure. They did not exhibit any noticeable change in G_{max} and D_{min} values. This level of strain is denoted as $\gamma_{0.98}$ hereafter. The other γ is the γ when G decreases by 6 % from the G_{max} ($G/G_{max} = 0.94$). Most specimens exhibited this decrease in G at the highest strains. This level of strain is denoted as $\gamma_{0.94}$ hereafter.

The variations of $\gamma_{0.98}$ values of the 16 specimens are investigated first in terms of the variations with: (1) their total unit weight (γ_t) and (2) shear wave velocity at 0.3 atm ($V_{S,\,0.3\ atm}$). These relationships are shown in Figures 8.3a and 8.3b, respectively. The specimens with a similar size and recovered from the nonlithophysal units exhibited relatively small variations in both $\gamma_{0.98}$ from about 0.0036 to 0.0055) with γ_t (about from 144 to 147 lb/ft^3). However, the specimens with a similar size and recovered from the lithophysal units exhibited a wider range of $\gamma_{0.98}$ (from about 0.0003 % to 0.005 %) with γ_t (from about 135 lb/ft^3 to 143 lb/ft^3). In other words, the effects of lithophysal cavities on G in the nonlinear range can be significant as observed in the linear range. Moreover, the largest $\gamma_{0.98}$ values of the lithophysal specimens are similar to the values of the nonlithophysal specimens. These larger $\gamma_{0.98}$ values indicate that the dynamic deformability of these specimens was not influenced significantly by their lithophysal

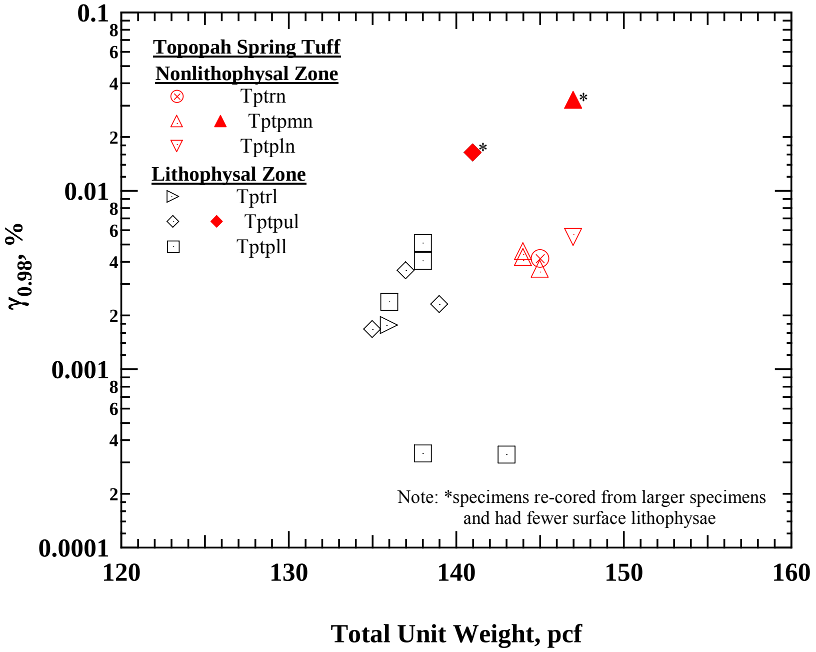

(a) Shearing Strain when G/G_{max} is 0.98 ($\gamma_{0.98}$) versus Total Unit Weight (γ_t)

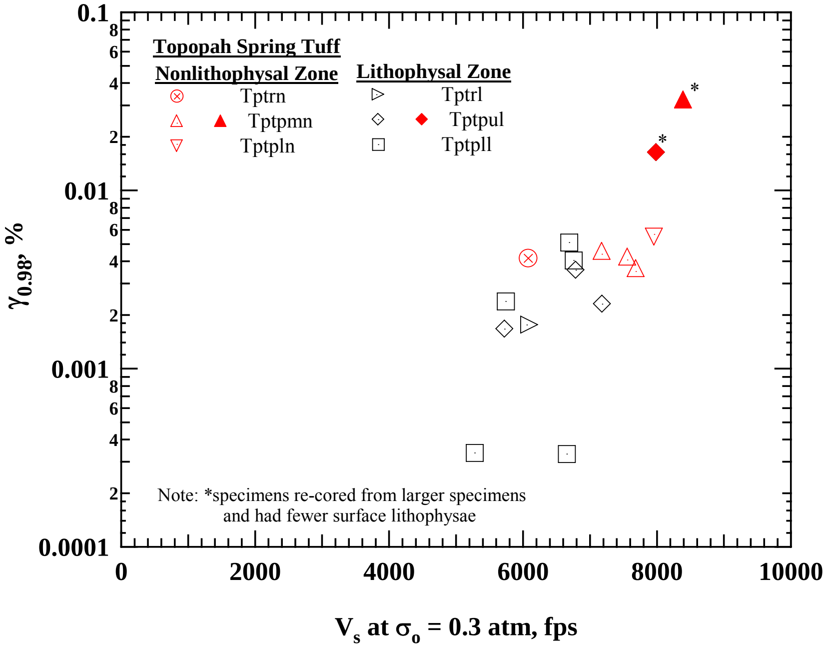

(b) Shearing Strain when G/G_{max} is 0.98 ($\gamma_{0.98}$) versus V_S at 0.3 atm ($V_{S,\ 0.3\ atm}$)

Figure 8.3 Variation of Shearing Strain when G/G_{max} is 0.98 with: (a) Total Unit Weight and (b) V_S at σ_o of 0.3 atm of Sixteen Specimens from the Topopah Spring Tuff features. In fact, the $\gamma_{0.98}$ value of the re-cored specimen from the Tptpul exhibited a larger $\gamma_{0.98}$ value than the larger lithophysal specimens likely due to smaller and fewer lithophysal features in this specimen. The $\gamma_{0.98}$ value was even higher than nonlithophysal specimens and rather close to the $\gamma_{0.98}$ value of the other re-cored specimen from the nonlithophysal units. Therefore, similar high values of $\gamma_{0.98}$ for the large- and small-size lithophysal specimens support the fact that the tuffs from the lithophysal and nonlithophysal zones have very similar matrix-groundmass as discussed in Chapter 6 for the dynamic properties in the linear range. Furthermore, the lithophysal specimen that had the largest density exhibited one of the lowest $\gamma_{0.98}$ values. The γ_t of the specimen was about 143 lb/ft^3 that is close to γ_t of the nonlithophysal specimens. This result seems to indicate not only the amount of lithophysal cavities but also some other factors such as their shape and distribution and microscopic fractures also influence the $\gamma_{0.98}$ values of the specimens. It is also important to point out that the two re-cored specimen had large G values (or V_S values) as discussed previously and that one of the Tptpll specimens (Specimen 10A-2) had the lowest G_{max} value as shown in Figure 8.1.

Figure 8.3b illustrates the overall general trend of increasing $\gamma_{0.98}$ with the $V_{S,\ 0.3\ atm}$. It is also interesting to point out that the nonlithophysal specimen from the crystal-rich unit (Tptrn) have a lower $V_{S,\ 0.3\ atm}$ value (about 6080 ft/sec) compared with mean $V_{S,\ 0.3\ atm}$ value of 7600 ft/sec for the specimens from the crystal-poor materials, but it has a similar $\gamma_{0.98}$ value. This result also possibly indicates that the deformability of the nonlithophysal materials are not influenced by any significant defects like lithophysal features in the lithophysal materials, although the nonlithophysal materials have different stiffness because of softer components such as pumice fragments.

The relationship between G and γ of the specimens are further examined at slightly higher strains in the initial portion of the nonlinear range, $\gamma_{0.94}$. The variation of $\gamma_{0.94}$ of the specimens are examined in terms of variations with γ_t and $V_{S,\,0.3\ \mathrm{atm}}$ values of the specimens, as done for the $\gamma_{0.98}$ values. The variations of $\gamma_{0.94}$ with γ_t and $V_{S,\,0.3\ \mathrm{atm}}$ are shown in Figures 8.4a and 8.4b, respectively. As found for the $\gamma_{0.98}$ values, the specimens from the lithophysal units exhibit a larger variation in $\gamma_{0.94}$, showing the effects of lithophysal features compared with specimens from the nonlithophysal units. The two re-cored specimens have larger $\gamma_{0.94}$ values, and the two specimens that have the smallest $\gamma_{0.98}$ values exhibited the smallest $\gamma_{0.94}$ values. The specimens from the nonlithophysal units have an average $\gamma_{0.94}$ value of about 0.016 % and the specimens from the lithophysal units have an average $\gamma_{0.94}$ value of about 0.0079 %, excluding the two re-cored specimens.

It should be noted that some specimens did not reach G/G_{max} of 0.94 at their highest strains. For these specimens, their $\gamma_{0.94}$ values were extrapolated by using a fitting equation; that is, the modified hyperbolic model for the G/G_{max} – log γ relationship proposed by Darendeli (2001). The model can be expressed as:

$$\frac{G}{G_{max}} = \frac{1}{1+\left(\dfrac{\gamma}{\gamma_r}\right)^{a}} \tag{8.1}$$

where, γ_r = reference shear strain and

a = curvature coefficient (dimensionless exponent).

The reference strain, γ_r, is defined as the value of γ equal to the shear strain at which G/G_{max} equals 0.5. Darendeli (2001) suggested a constant value of 0.92 for the “a” value for soils. Since most of data for the tuff specimens from the Topopah Spring Tuff

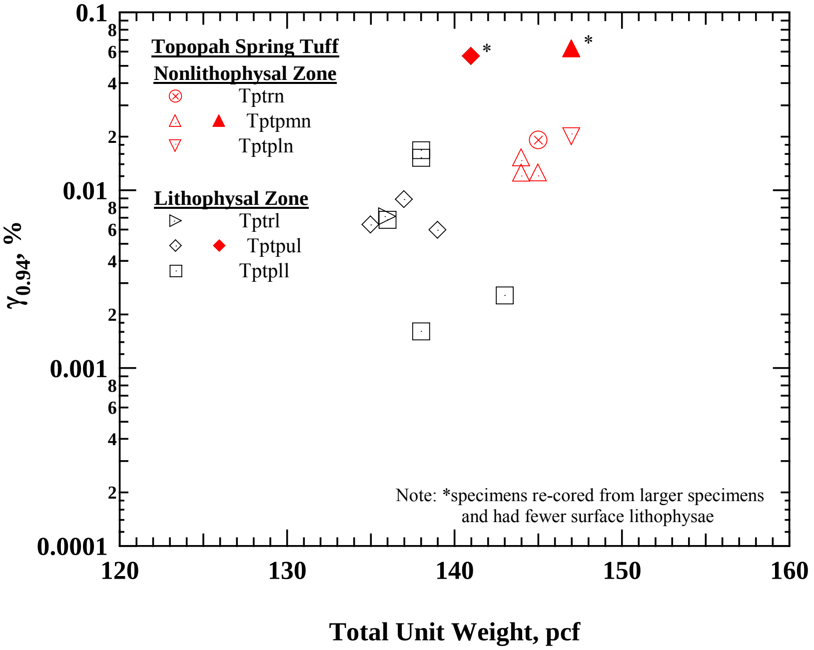

(a) Shearing Strain when G/G_{max} is 0.94 ($\gamma_{0.94}$) versus Total Unit Weight (γ_t)

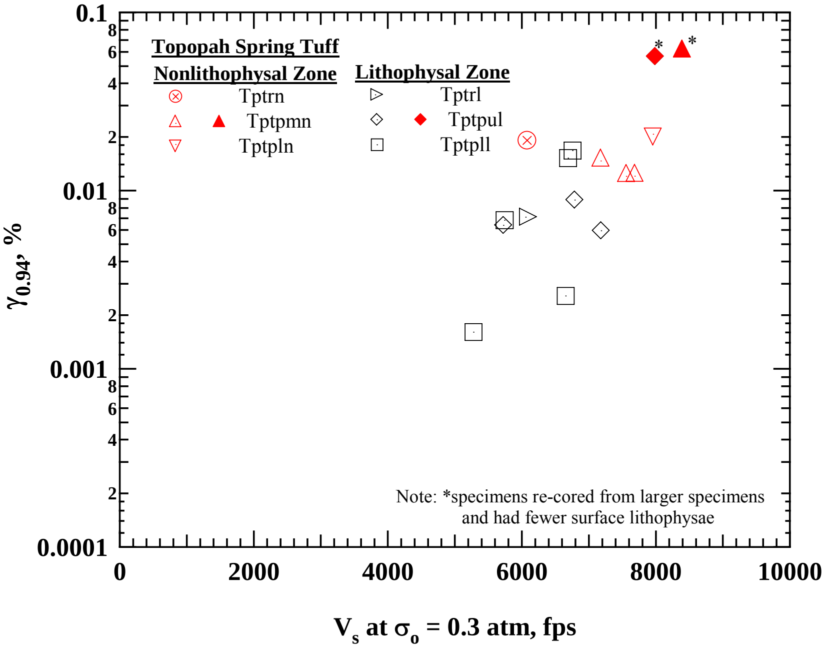

(b) Shearing Strain when G/G_{max} is 0.94 ($\gamma_{0.94}$) versus V_S at 0.3 atm ($V_{S,\ 0.3\ atm}$)

Figure 8.4 Variation of Shearing Strain when G/G_{max} is 0.94 with: (a) Total Unit Weight and (b) V_S at σ_o of 0.3 atm of Sixteen Specimens from the Topopah Spring Tuff exhibited small G/G_{max} ranges and the specimens would fail before their G/G_{max} values reached 0.5, the use of γ_r as predicted values for a high-strain range is not relevant. Furthermore, the "a" value is quite sensitive to small errors in the data if the number of data to describe the curvature of the G/G_{max} – log γ relationship is not sufficient.

Thirteen out of the 16 specimens from the Topopah Spring Tuff were tested at two different confining pressures (σ_o). The ten specimens were tested at a σ_o up to about $\gamma_{0.98}$ and tested again for the largest strain level at 4 times σ_o. Their $\gamma_{0.98}$ and $\gamma_{0.94}$ values determined at each pressure are compared in Figures 8.5a and 8.5b, respectively. Three specimens tested with different pressure increments are also included in the figures. No significant changes in both $\gamma_{0.98}$ and $\gamma_{0.94}$ values were observed with the pressure increments.

8.2.2 Bandelier Tuff

The G/G_{max} –log γ relationships for the 18 tuff specimens from the Bandelier Tuff are presented in Figure 8.6. All relationships were determined at the estimated in-situ effective stresses (σ_m') of the specimens. These specimens have a large range in G_{max} due to various welding conditions and confining pressures used to test these specimens as described in Chapter 6. Therefore, their G – log γ relationships of the specimens are not combined in one figure in this section. Most specimens were tested at shearing strains above 0.01 % and they reached a G/G_{max} value of 0.8. The poorly welded tuffs (the specimens in Groups 3 and 4) could be tested at larger strains than the specimens with larger welding intensity (the specimens in Groups 1 and 2). Six out of eight specimens in Group 4 exhibited 50 % or more decrease in their G values at γ above 0.08 %.

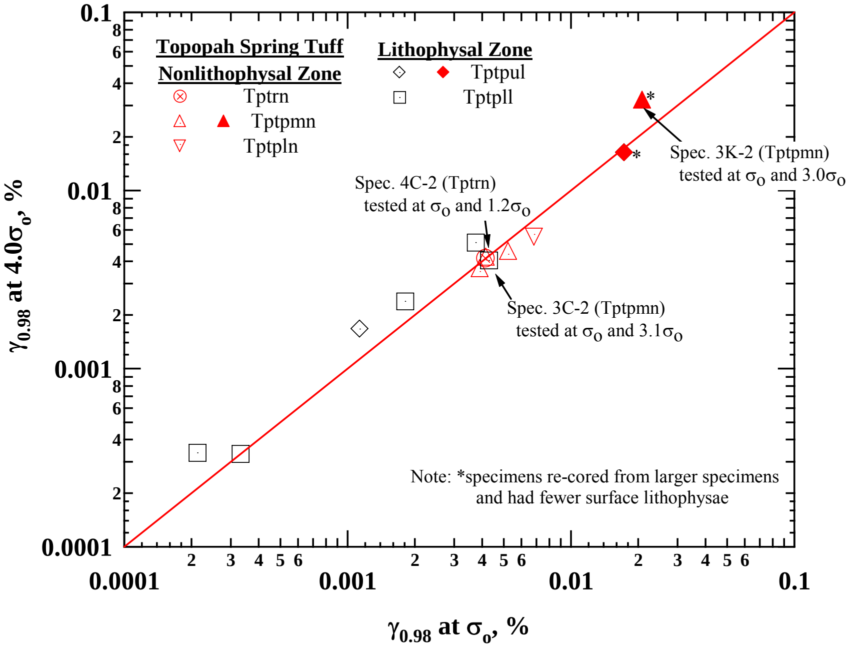

(a) Shearing Strain when G/G_{max} is 0.98 ($\gamma_{0.98}$)

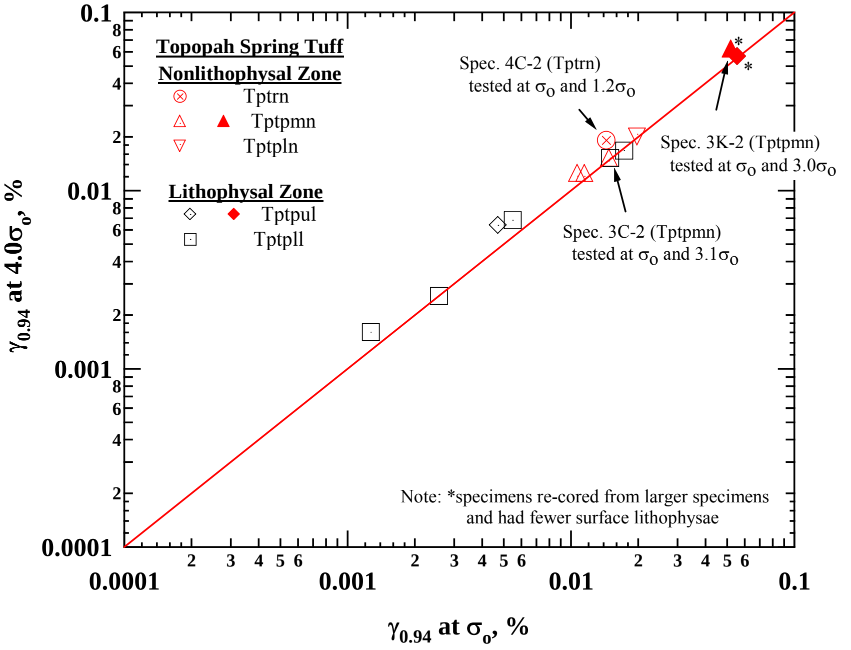

(b) Shearing Strain when G/G_{max} is 0.94 ($\gamma_{0.94}$)

Figure 8.5 Variation of Shearing Strain: (a) when G/G_{max} is 0.98 and (b) when G/G_{max} is 0.94 as Determined at Two Different Pressures of Thirteen Specimens from the Topopah Spring Tuff

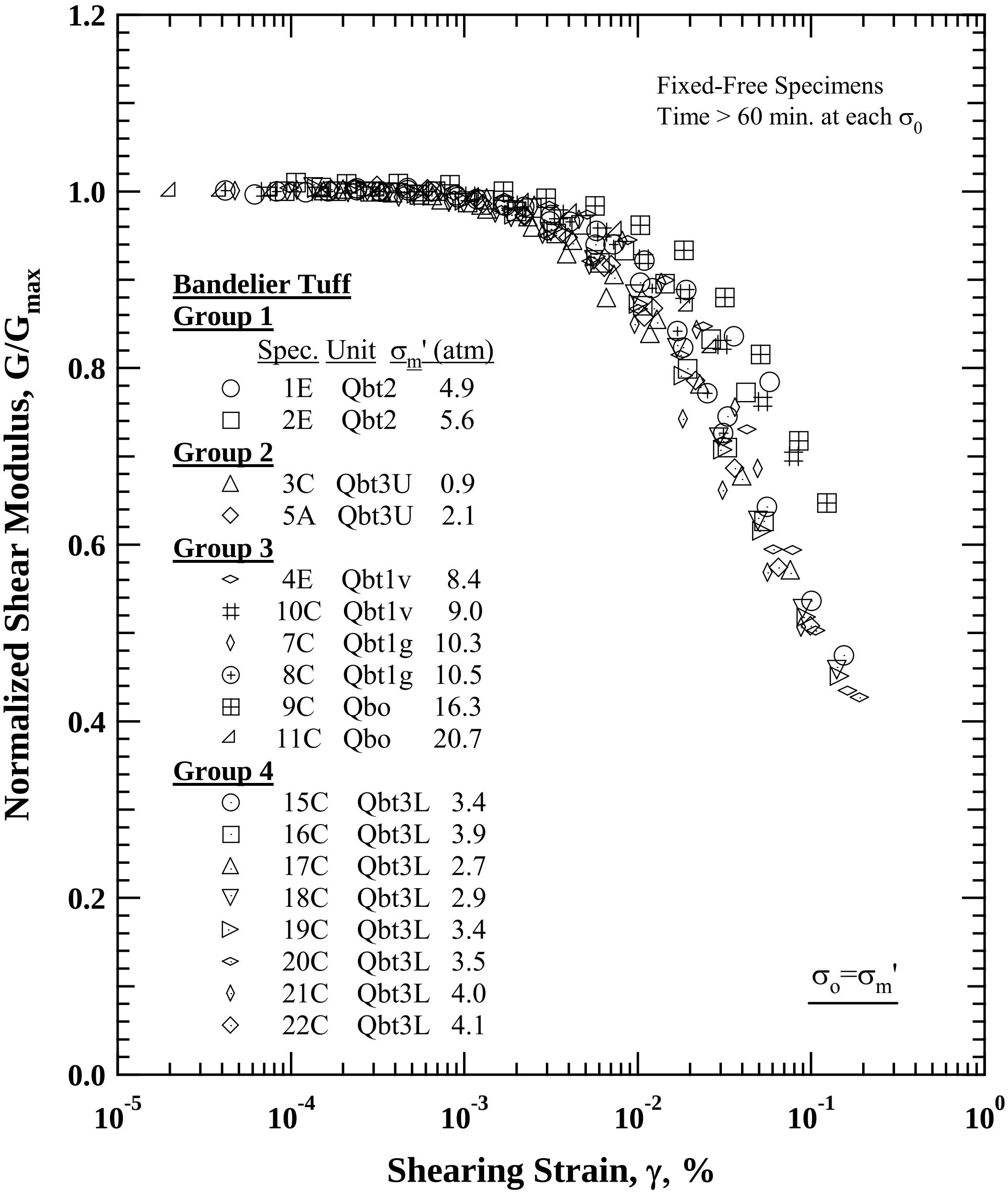

Figure 8.6 Variation of Normalized Shear Modulus with Shearing Strain of Eighteen Specimens from the Topopah Spring Tuff

To investigate the variation of G – log γ in detail, the values of $\gamma_{0.98}$ and $\gamma_{0.94}$ are compared for the specimens from the Bandelier Tuff as done with the Topopah Spring Tuff specimens. Furthermore, the γ values when G decreases by 20 % from the G_{max} (G/G_{max} = 0.80) are also discussed for the specimens from the Bandelier Tuff. Most specimens exhibited this decrease in G at their highest test strains. This level of strain is denoted as $\gamma_{0.80}$ hereafter.

The variations of $\gamma_{0.98}$ values of the 18 tuff specimens from the Bandelier Tuff are investigated first in terms of the variations with: (1) their total unit weight (γ_t) and (2) shear wave velocity at 0.3 atm ($V_{S,\ 0.3\ atm}$) in Figures 8.7a and 8.7b, respectively. The specimens in each group exhibited similar $\gamma_{0.98}$ values and the average $\gamma_{0.98}$ value of each group ranges from about 0.0015 for Group 2 to 0.0036 for Group 3. It is very interesting to note that the most poorly welded tuffs in Group 3 exhibited larger linear ranges than the moderately to densely welded tuffs in Group 1. (Note that this is explained by the effect of confining pressure below.) It is also interesting to note that the $\gamma_{0.98}$ values of the moderately welded specimens in Group 2 are similar to the $\gamma_{0.98}$ values of the poorly welded tuffs in Group 4. No noticeable trend can be observed both with γ_t and $V_{S,\ 0.3\ atm}$.

The $\gamma_{0.98}$ values are plotted against the isotropic confining pressures (σ_o) at which the measurements were performed in Figure 8.8a. A reasonable correlation between the values of $\gamma_{0.98}$ and σ_o is observed. This correlation shows that the linear range of these tuffs is affected by σ_o. All tuffs in Group 3 were recovered from the deeper depth than the other specimens and tested at higher pressures. On the other hand, the two specimens from the Qbt3U unit were from the shallowest depths and tested at the lowest σ_o. The $\gamma_{0.94}$ values also show a strong correlation with σ_o as seen in Figure 8.8b.

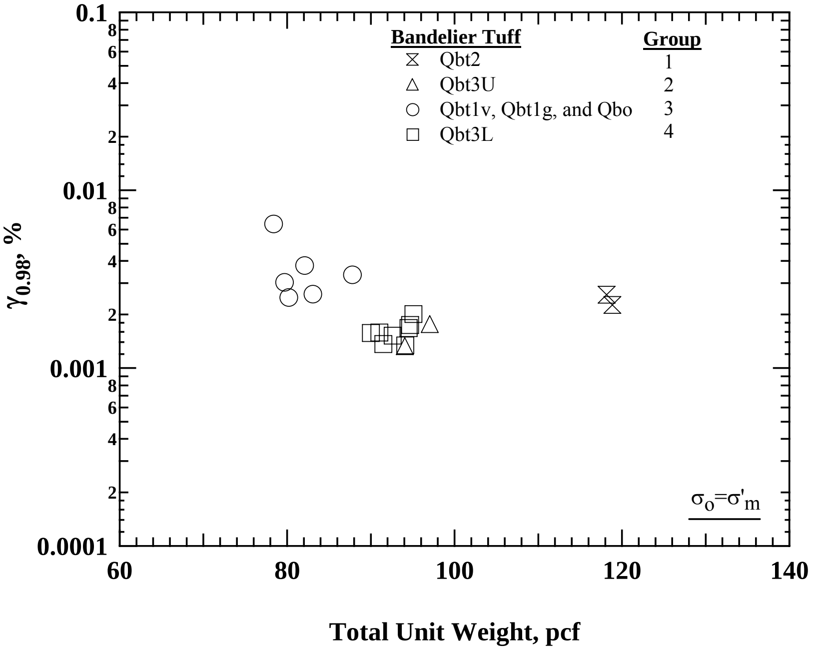

(a) Shearing Strain when G/G_{max} is 0.98 ($\gamma_{0.98}$) versus Total Unit Weight (γ_t)

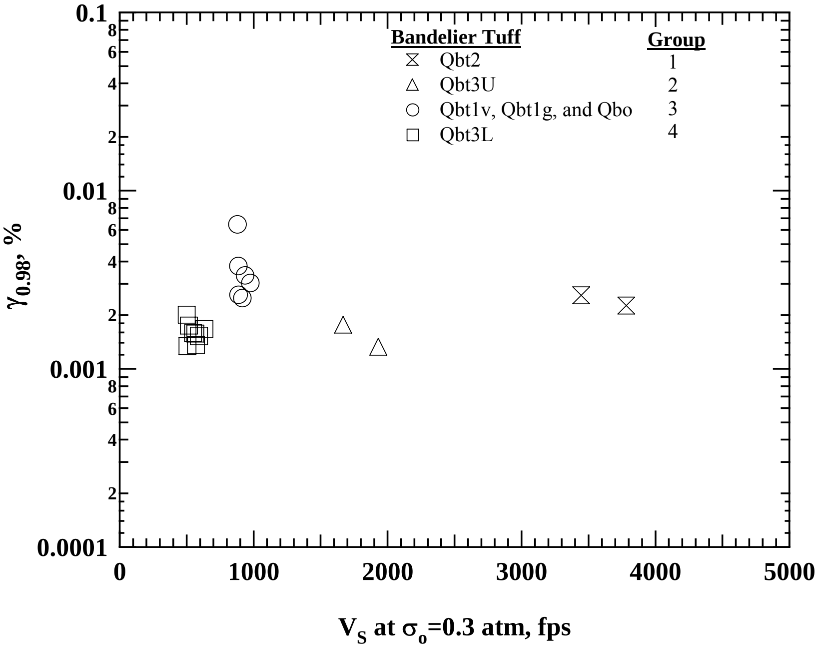

(b) Shearing Strain when G/G_{max} is 0.98 ($\gamma_{0.98}$) versus V_S at 0.3 atm ($V_{S,\ 0.3\ atm}$)

Figure 8.7 Variation of Shearing Strain when G/G_{max} is 0.98 with: (a) Total Unit Weight and (b) V_S at σ_o of 0.3 atm of Eighteen Specimens from the Bandelier Tuff

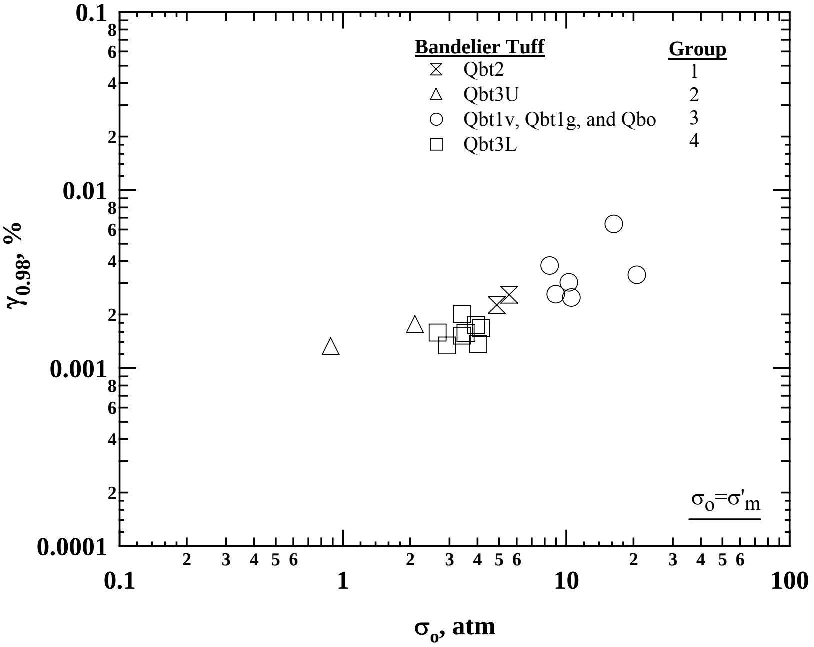

(a) Shearing Strain when G/G_{max} is 0.98 ($\gamma_{0.98}$) versus Confining Pressure (σ_o)

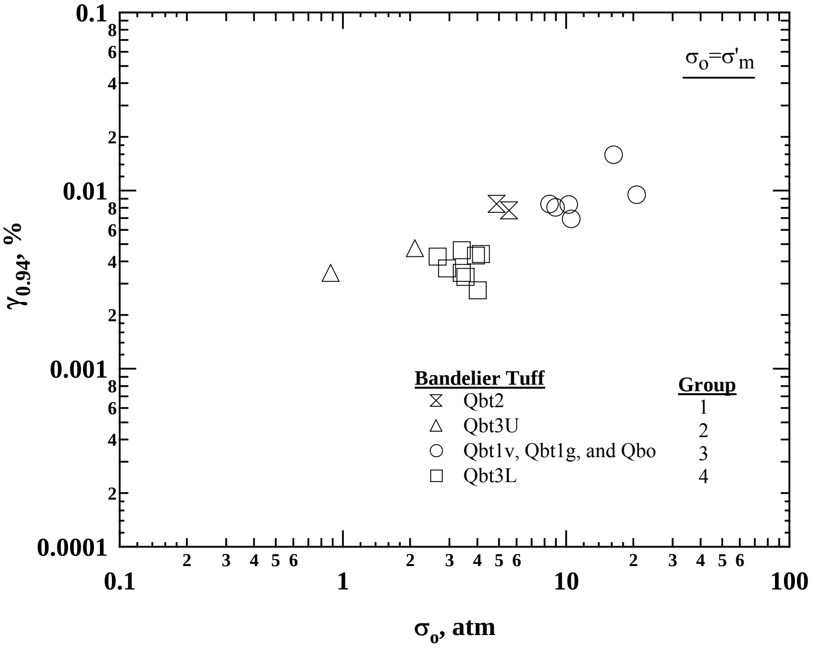

(b) Shearing Strain when G/G_{max} is 0.94 ($\gamma_{0.94}$) versus Confining Pressure (σ_o)

Figure 8.8 Variation of: (a) Shearing Strain when G/G_{max} is 0.98 and (b) Shearing Strain when G/G_{max} is 0.94 with: Isotropic Confining Pressure (σ_o) of Eighteen Specimens from the Bandelier Tuff

The effect of σ_o on the G/G_{max} – log γ relationships at higher strain levels are illustrated in Figures 8.9a and 8.9b for $\gamma_{0.80}$ and γ_r, respectively. It should be noted that γ_r of most specimens in Groups 1 through 3 were extrapolated from the least-squares fitting using Eq. (8.1) and these data must be considered carefully. There are two trends in data shown in Figures 8.8 and 8.9. First, $\gamma_{0.98}$, $\gamma_{0.98}$ and γ_r increases as σ_o increases for all groups. However, the second trend is that Group 1 shows the best nonlinearity because these two specimens have $V_{S,\,0.3\,atm}$ > 3400 ft/sec (1036 m/sec). As a result the various strain levels in the graphs begin to differ from the magnitude in the trends as the strain level increases.

The trends in the various strain levels with σ_o are more easily seen for the specimens in Groups 2 through 4 by adding the results from the two different pressures at which testing was performed. The effect of σ_o observed at each pressure is compared in terms of $\gamma_{0.98}$ and $\gamma_{0.80}$ in Figures 8.10a and 8.10b, respectively. The data at the smaller confining pressures ($\sigma_{o,1}$) are presented in hollow symbols while the data at the larger confining pressures ($\sigma_{o,2}$) are presented in solid symbols in the figure. Both $\gamma_{0.98}$ and $\gamma_{0.80}$ values of most specimens increased as σ_o increased and the increase observed for each specimen is similar to each other. The increments in both σ_o and strain levels are presented in a ratio format in Figures 8.11a and 8.11b, for $\gamma_{0.98}$ and $\gamma_{0.80}$, respectively. It is very interesting to note that the specimens exhibited similar increments in the strains with the same increments. Especially, the 11 specimens for which σ_o increased by a factor of 4 show very similar increments in their $\gamma_{0.8}$ values.

Based on these strong correlations between the strain levels and σ_o, the G/G_{max} – log γ relationships of the poorly welded and moderately welded tuffs of the Bandelier Tuffs can be predicted by the best-fit line through the data collected in this study as shown in Figure 8.12. The relationship between γ_r and σ_o can be expressed as:

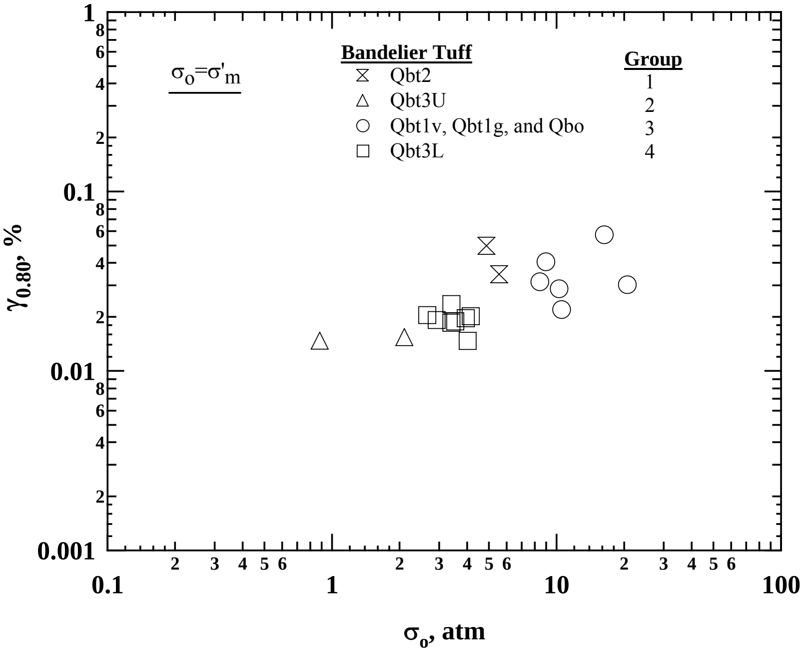

(a) Shearing Strain when G/G_{max} is 0.80 ($\gamma_{0.80}$) versus Confining Pressure (σ_o)

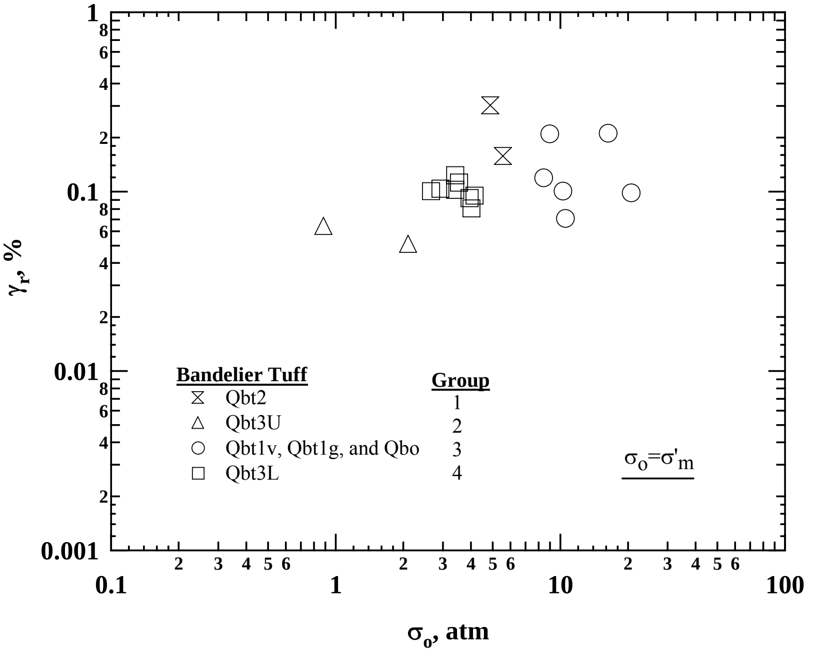

(b) Shearing Strain when G/G_{max} is 0.50 (γ_r) versus Confining Pressure (σ_o)

Figure 8.9 Variation of: (a) Shearing Strain when G/G_{max} is 0.80 and (b) Shearing Strain when G/G_{max} is 0.50 with Isotropic Confining Pressure (σ_o) of Eighteen Specimens from the Bandelier Tuff

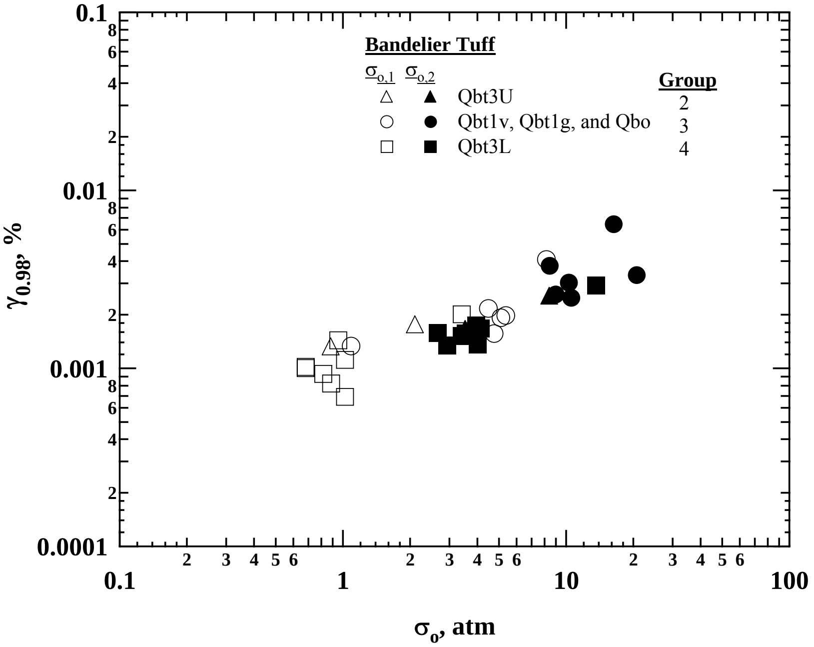

(a) Shearing Strain when G/G_{max} is 0.98 ($\gamma_{0.98}$) versus Confining Pressure (σ_o)

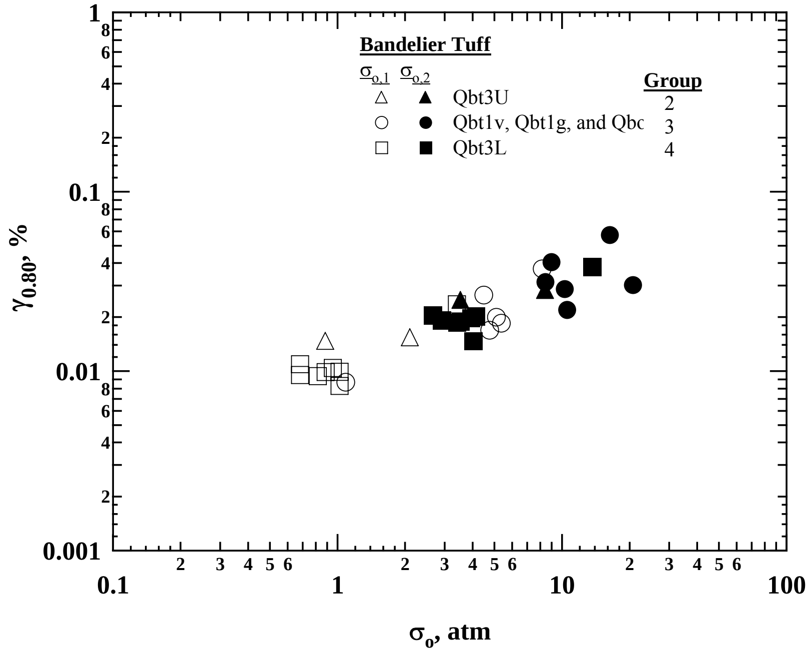

(b) Shearing Strain when G/G_{max} is 0.80 ($\gamma_{0.80}$) versus Confining Pressure (σ_o)

Figure 8.10 Variations of: (a) Shearing Strain when G/G_{max} is 0.98 and (b) Shearing Strain when G/G_{max} is 0.80 with Isotropic Confining Pressure (σ_o) of Sixteen Specimens from the Bandelier Tuff

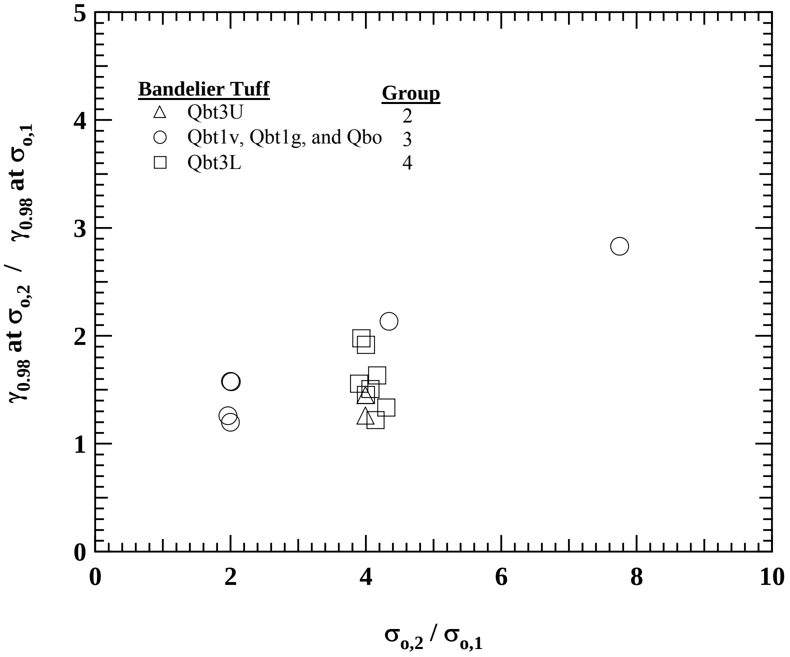

(a) Increment of $\gamma_{0.98}$ versus Increment of σ_o

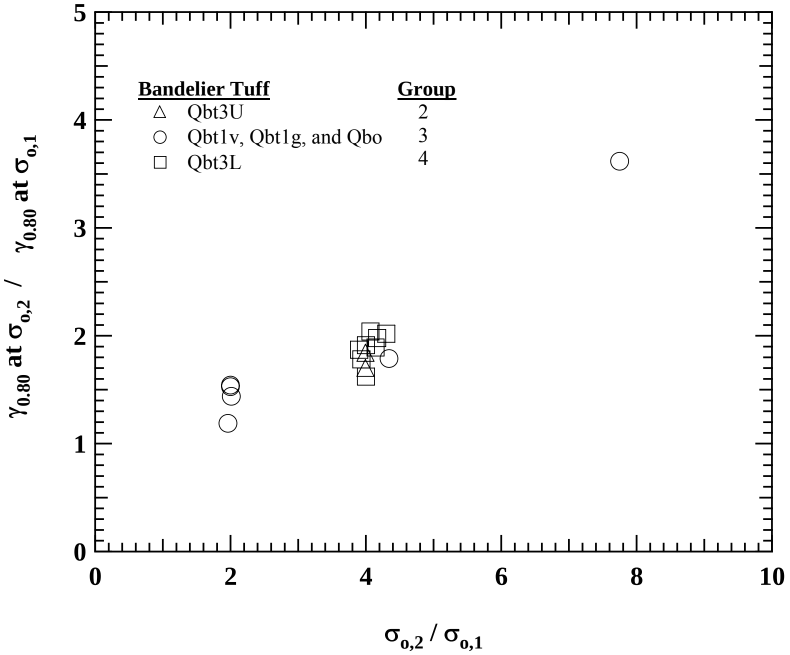

(b) Increment of $\gamma_{0.80}$ versus Increment of σ_o

Figure 8.11 Variations of Increments in: (a) Shearing Strain when G/G_{max} is 0.98 and (b) Shearing Strain when G/G_{max} is 0.80 with Increment in Isotropic Confining Pressure (σ_o) of Sixteen Specimens from the Bandelier Tuff

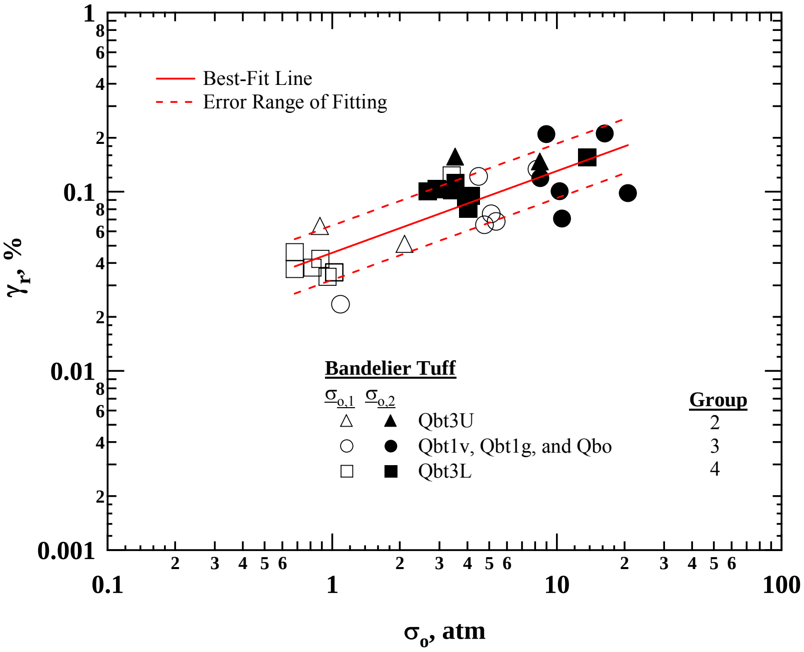

Figure 8.12 Variations of Reference Strain (γ_r) with Isotropic Confining Pressure (σ_o) of Sixteen Specimens from the Bandelier Tuff Determined from the Fixed-Free Resonant Column (RC) Tests at Two Difference Isotropic Confining Pressures (σ_o)

$$\gamma_r = 0.046(\sigma_o / Pa)^{0.46} \tag{8.2}$$

where, γ_r is the reference strain in %,

σ_o is the isotropic confining pressure in the same units as Pa, and

Pa is one atmosphere (2117 psf or 100 kPa).

The standard error of the fitting, $S_{\varepsilon,\ \gamma_r}$, that is the standard deviation of the difference between the measured and predicted values, is about 1.4 in the log-log relationship (Ang and Tang, 1975).

In addition, the "a" value decreases as γ_r increases in general as shown in Figure 8.13. The semi-logarithmic relationship between these values can be expressed as:

$$a = -0.298 \log_{10} \gamma_r + 0.656 \tag{8.3}$$

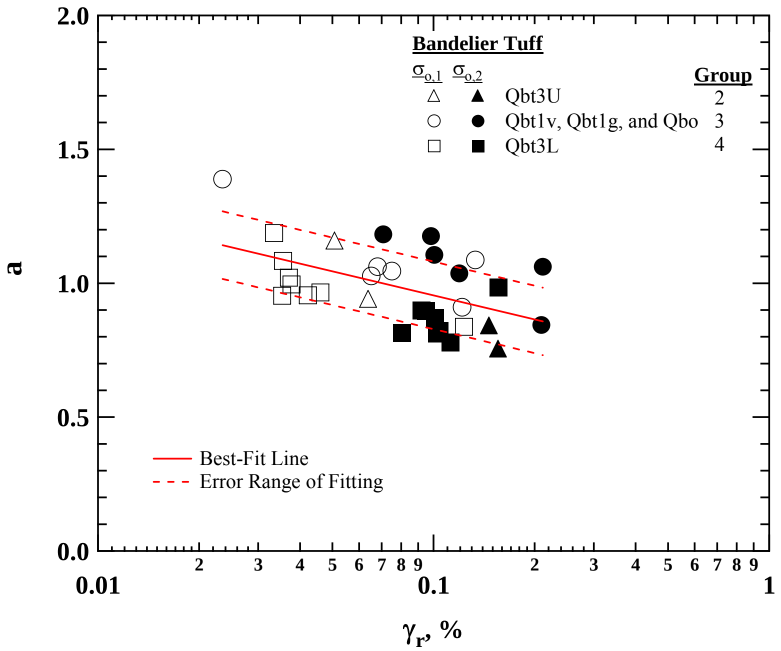

Figure 8.13 Variations of Curvature Coefficient (“a” value) with Reference Strain (γ_r) of Sixteen Specimens from the Bandelier Tuff Determined from the Fixed-Free Resonant Column (RC) Tests at Two Difference Isotropic Confining Pressures (σ_o)

where, a is the curvature coefficient (dimensionless) and

γ_r is the reference strain in %.

The standard error of the fitting, $S_{\varepsilon,\ a}$, that is the standard deviation of the difference between the measured and predicted values, is about 0.126 in the semi-log relationship (Ang and Tang, 1975). One can use the γ_r and “a” values from Eqs. (8.2) and (8.3) to create average trend lines for the G/G_{max} – log γ relationships of the poorly welded tuffs and moderately welded tuffs from the Bandelier Tuff. The error range of the average trend line can be created based on the standard errors of the fittings, $S_{\varepsilon,\ \gamma_r}$ and $S_{\varepsilon,\ a}$.

8.3 D – LOG γ RELATIONSHIPS OF ASH-FLOW TUFFS

8.3.1 Topopah Spring Tuff

The influence of shearing strain, γ, on material damping ratio (D) is shown in Figure 8.14, for the 16 intact tuff specimens from the Topopah Spring Tuff. All D and γ values in the figure were determined by resonant column testing at the highest test pressure of each specimen. As describe in Section 8.2, Specimens 11C-1 and 12C-1 were tested only at the unconfined state due to many large voids (lithophysal cavities) on their surfaces Like the G – log γ and G/G_{max} – log γ relationships, the D – log γ relationships exhibit linear ranges where they are constant and equal to D_{min}. This linear range is followed by a nonlinear range where D increases as γ increases. Moreover, the specimens have various D_{min} values and a wide range in their linear ranges representing various effects of lithostratigraphic features in the specimens. The two re-cored specimens, Specimens 2C-2 and 3K-2 that exhibited large linear ranges in G, also exhibited large linear ranges in D and small D_{min} values when compared with their larger parent specimens, Specimen 2B-3 for 2C-2 and 3C-2 for 3K-2, respectively.

To investigate the linear range of the specimens clearly, the D_{min} values were subtracted from the D values for all 16 specimens as shown in Figure 8.15. It can be seen that the two (D-D_{min}) – log γ relationships for the two, re-cored specimens reach the largest strain ranges with least change in D-D_{min}. Note that D–D_{min} was denoted as "nonlinear damping" by Menq (2003). Menq investigated the variation of the "nonlinear damping" with shearing strain to study the effect of γ on the D values of granular soils.

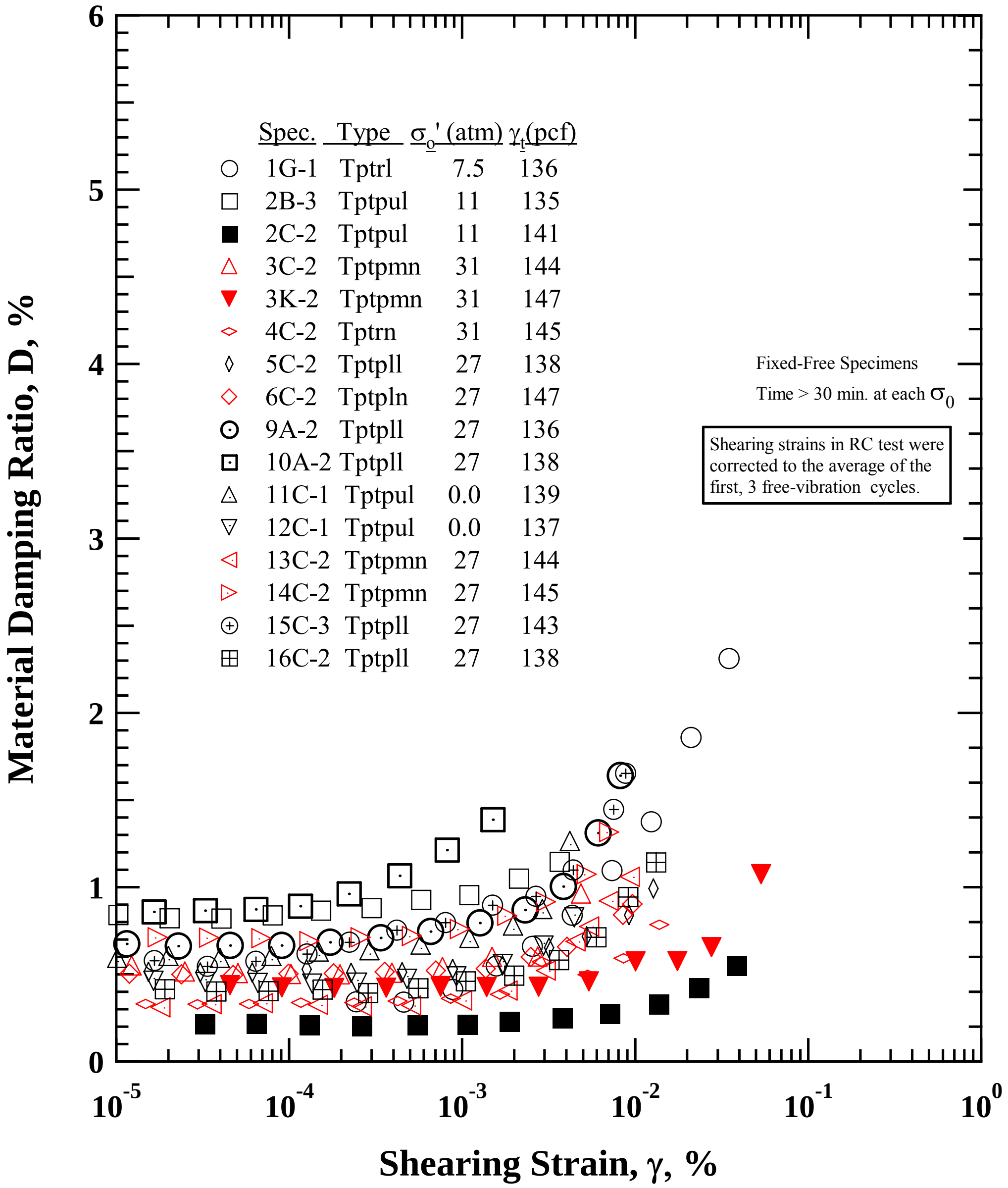

Figure 8.14 Variation of Material Damping Ratio with Shearing Strain from Fixed-Free Resonant Column Tests of Sixteen Specimens from the Topopah Spring Tuff

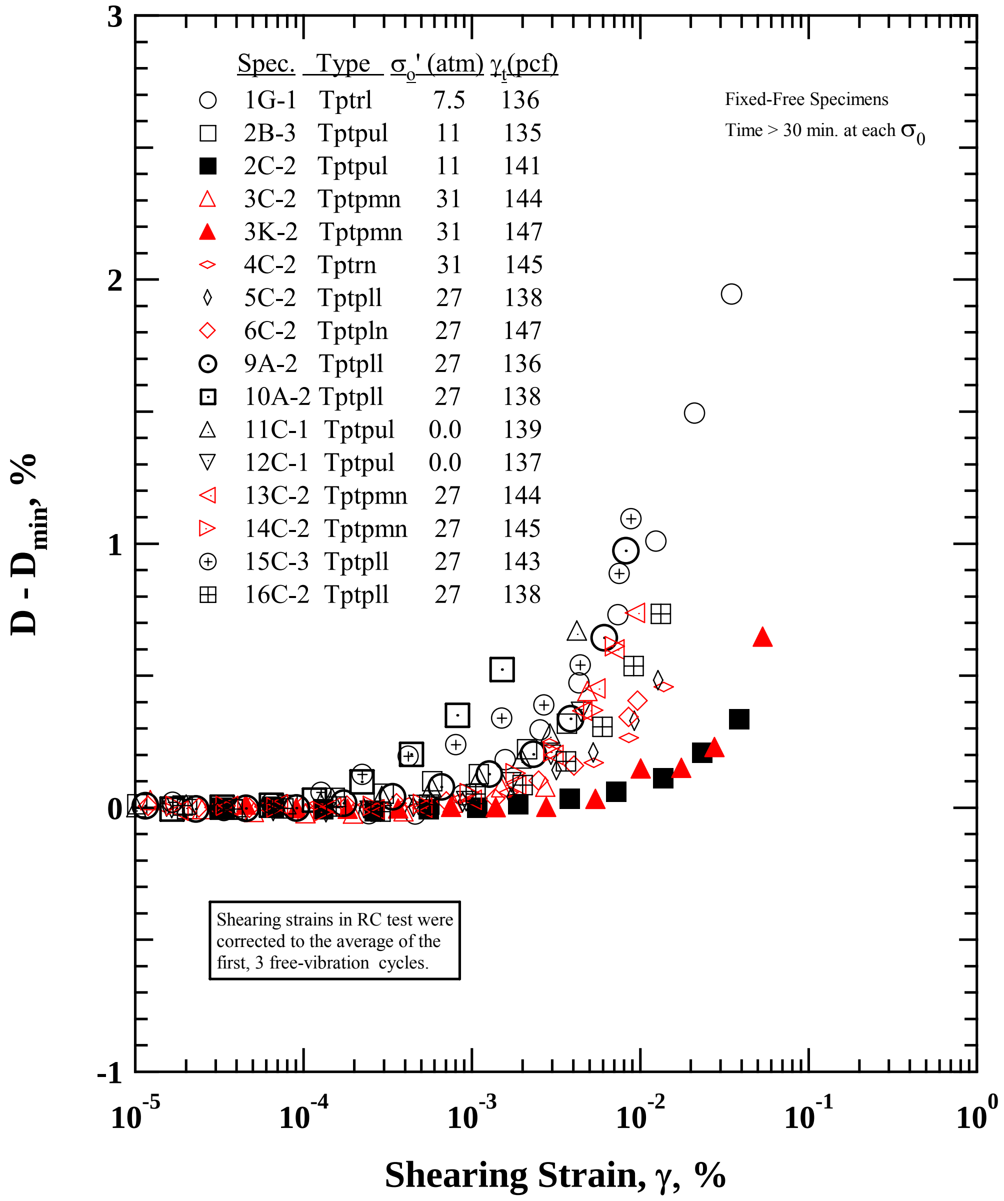

Fixed-Free Specimens
Time > 30 min. at each σ_0

Shearing strains in RC test were corrected to the average of the first, 3 free-vibration cycles.

Figure 8.15 Variation of “Nonlinear Damping” (D-D_{min}) with Shearing Strain from Fixed-Free Resonant Column Tests of Sixteen Specimens from the Topopah Spring Tuff

By removing D_{min} from the nonlinear relationship, the evaluation of $(D–D_{min})$ – log γ relationships can be performed in the similar manner used in the study of the G/G_{max} – log γ relationships; that is, two values of γ were selected to investigate the variation of the D values with γ in detail. The first γ is the γ when D increased by 0.2 % in absolute value from the D_{min}. This γ was selected because $D\text{-}D_{min}$ values of the specimens are about 0.2 % when their G values decreased by 2 % ($\gamma_{0.98}$) as illustrated in Figure 8.16. The $D\text{-}D_{min}$ values at $\gamma_{0.98}$ range from about 0.13 to 0.39. Their average value is about 0.22 %. This level of strain is denoted as $\gamma_{Dmin+0.2\%}$ hereafter. Similarly, the other γ is selected for the γ when D increased by 0.5 % above the D_{min} ($D\text{-}D_{min} = 0.5$ %). The $D\text{-}D_{min}$ values of the specimens are about 0.5 % when their G values decreased by 6 % ($\gamma_{0.94}$). This level of strain is denoted as $\gamma_{Dmin+0.5\%}$ hereafter.

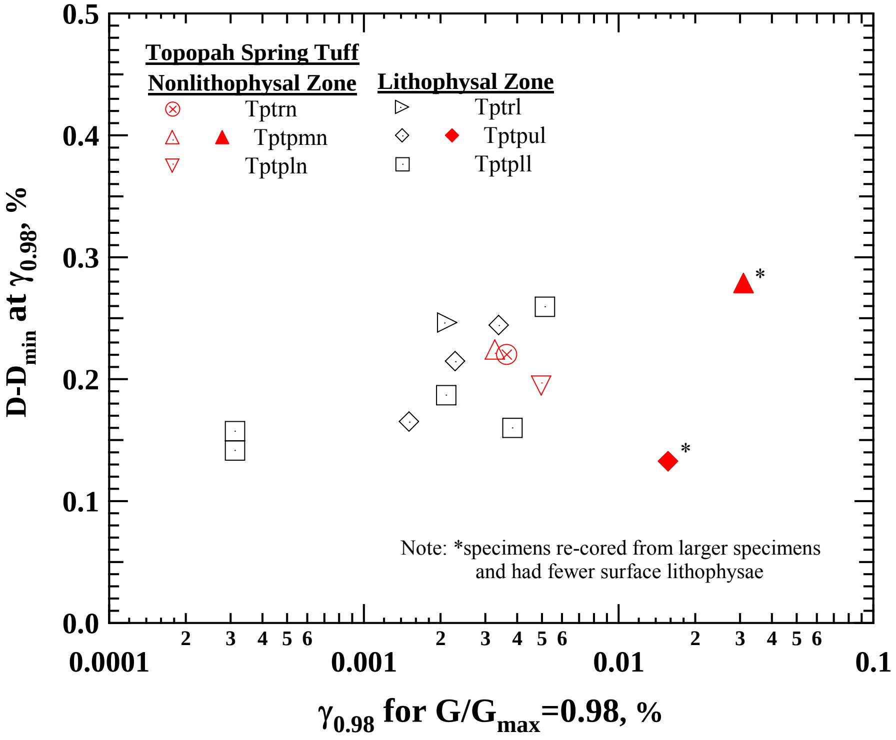

Figure 8.16 Variation of $D\text{-}D_{min}$ at $\gamma_{0.98}$ from Fixed-Free Resonant Column Tests of Sixteen Specimens from the Topopah Spring Tuff

The variations of $\gamma_{Dmin+0.2\%}$ values of the 16 specimens are investigated in terms of the variations with: (1) their total unit weight (γ_t) and (2) shear wave velocity at 0.3 atm ($V_{S,\ 0.3\ atm}$) in Figures 8.17a and 8.17b, respectively. The overall relationships between these parameters are very similar to the relationships observed for $\gamma_{0.98}$ in Section 8.2; that is, there is not a very strong correlation. The specimens with a similar size and recovered from the lithophysal units exhibited relatively large variations in $\gamma_{Dmin+0.5\%}$ as well as γ_t values compared with the nonlithophysal specimens with a similar size. These large variations are indicative of the large variations in the amount and effect of the lithophysal cavities. When specimens were re-cored, their γ_t increased and their linear range for D (larger $\gamma_{Dmin+0.2\%}$) also increased as shown in the figure.

The correlation of $\gamma_{Dmin+0.5\%}$ with the $V_{S,\ 0.3\ atm}$ seems to be larger than with γ_t, because γ_t represents only macroscopic large lithophysal cavities while $V_{S,\ 0.3\ atm}$ is affected by other factors such as the shape and distribution of the features and microscopic-scale fractures for these densely welded tuffs similarly having dense matrix materials.

The relationship between D and γ of the specimens are further examined at higher strain (nonlinear range), $\gamma_{Dmin+0.5\%}$, as illustrated in Figures 8.18a and 8.18b with γ_t and $V_{S,\ 0.3\ atm}$, respectively. Very similar trends were observed in this slightly larger strain range as seen in the figures. Both $\gamma_{Dmin+0.2\%}$ and $\gamma_{Dmin+0.5\%}$ values determined from the D –log γ relationships for these tuffs at two different pressures (σ_o) are presented in Figures 8.19a and 8.19b, respectively. As found in the G – log γ relationship based on the $\gamma_{0.98}$ and $\gamma_{0.94}$ values, the D – log γ relationships of these tuffs were not affected by σ_o based on little change in the $\gamma_{Dmin+0.2\%}$ and $\gamma_{Dmin+0.5\%}$ values with σ_o as shown in the figures.

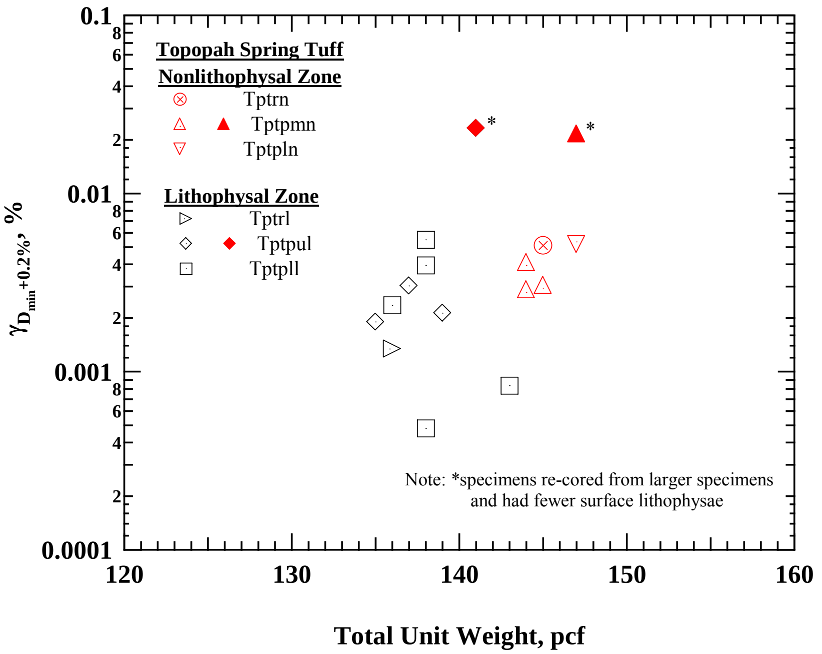

(a) Shearing Strain when D-D$_{min}$ is 0.2 % ($\gamma_{Dmin+0.2\%}$) versus Total Unit Weight (γ_t)

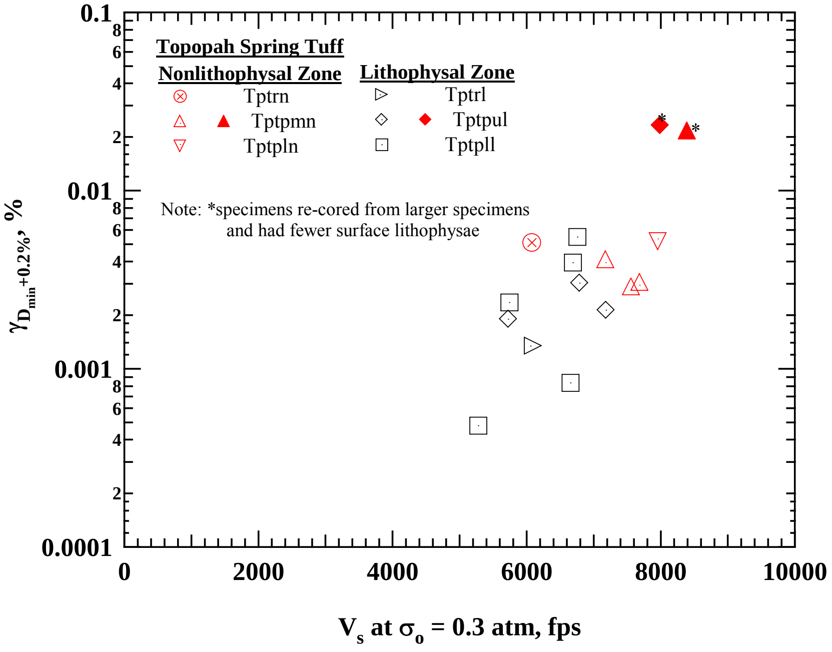

(b) Shearing Strain when D-D$_{min}$ is 0.2 % ($\gamma_{Dmin+0.2\%}$) versus V_S at 0.3 atm ($V_{S,\ 0.3\ atm}$)

Figure 8.17 Variation of Shearing Strain when D-D$_{min}$ is 0.2 with: (a) Total Unit Weight and (b) V_S at σ_o of 0.3 atm of Sixteen Specimens from the Topopah Spring Tuff

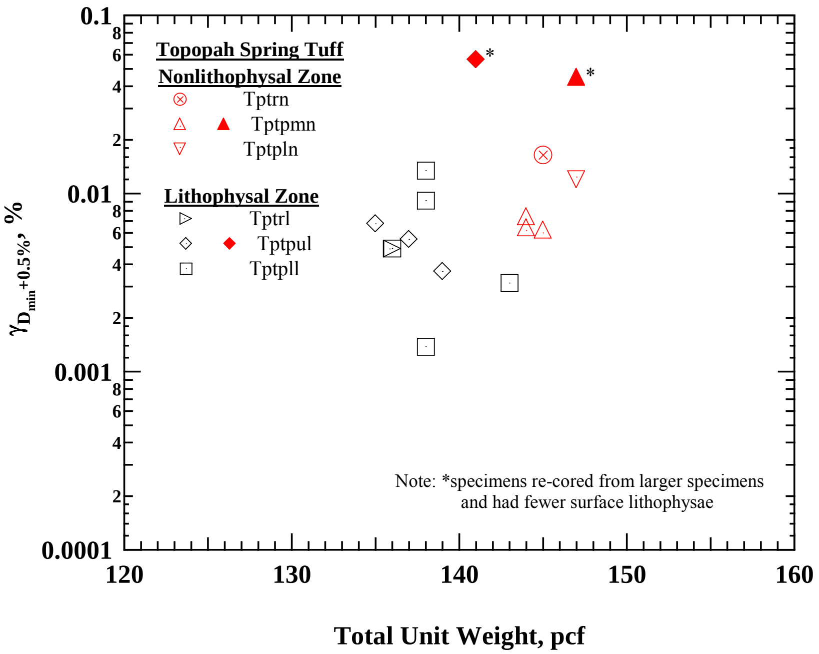

(a) Shearing Strain when D-D$_{min}$ is 0.5 % ($\gamma_{Dmin+0.5\%}$) versus Total Unit Weight (γ_t)

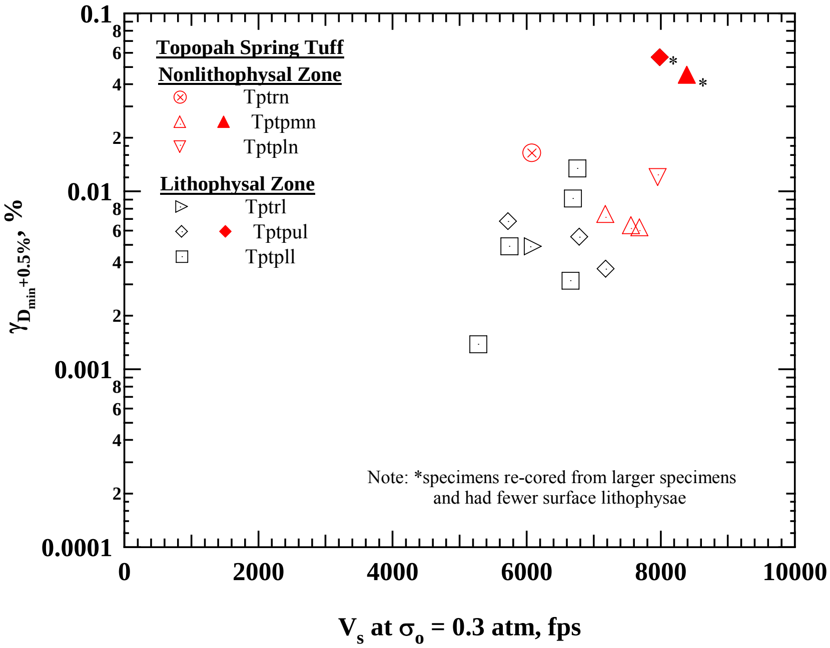

(b) Shearing Strain when D-D$_{min}$ is 0.5 % ($\gamma_{Dmin+0.5\%}$) versus V$_S$ at 0.3 atm ($V_{S,\,0.3\,atm}$)

Figure 8.18 Variation of Shearing Strain when D-D$_{min}$ is 0.5 % with: (a) Total Unit Weight and (b) V$_S$ at σ_o of 0.3 atm of Sixteen Specimens from the Topopah Spring Tuff

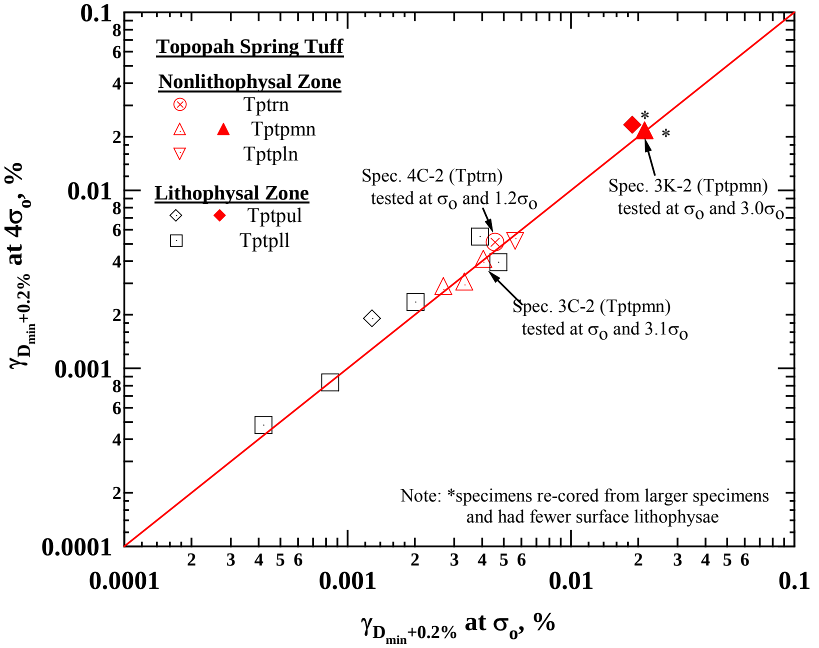

(a) Shearing Strain when D-D_{min} is 0.2 % ($\gamma_{Dmin+0.2\%}$)

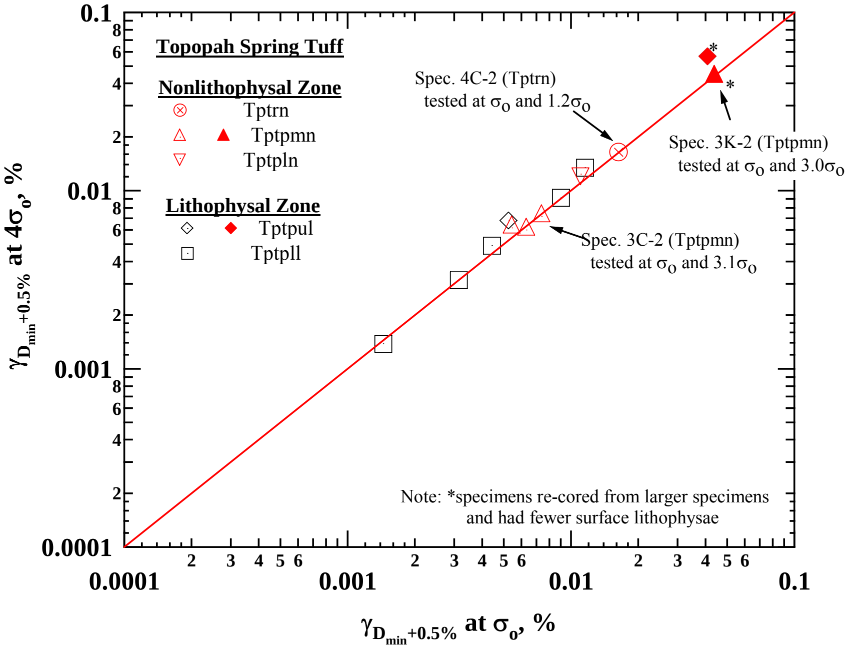

(b) Shearing Strain when D-D_{min} is 0.5 % ($\gamma_{Dmin+0.5\%}$)

Figure 8.19 Variation of Shearing Strain: (a) when D-D_{min} is 0.2 % and (b) when D-D_{min} is 0.5 % as Determined at Two Different Pressures of Thirteen Specimens from the Topopah Spring Tuff

As noted in Section 8.2, the D-D_{min} values of some specimens did not reach 0.5 % as they could not reach the G/G_{max} of 0.94. The following fitting model is proposed to extrapolate the data of these specimens. The model can be expressed as:

$$D - D_{\min} = C\left(\frac{\gamma}{\gamma_D}\right)^{a_D} \tag{8.4}$$

where, γ_D = reference shear strain for D-log γ relationship,

a_D = curvature coefficient (dimensionless exponent) for D - log γ relationship and,

C = reference material damping ratio in percent for the fitting.

The reference strain, γ_D, is defined as the value of γ equal to the shear strain at which D-D_{min} equals the "C" value. In other words, when γ becomes γ_D, D increases by "C" from D_{min} in absolute value. The "C" value can be any single real value in percent for a reference material damping ratio the ones desire to investigate. The "a_D" value is to control the curvature of the D-log γ relationship. An example fitting is shown in Figure 8.20 for the D –log γ relationship determined for Specimen 15C from the Bandelier Tuff (discussed more in the next section). The "C" value of 5 % and D_{min} value of 0.81 % was used in the least-squares fitting with Eq. (8.4). The resulting values of γ_D and a_D are 0.13 % and 0.74, respectively. The effect γ_t and a_D are illustrated in Figures 8.21a and 8.21b, respectively. As seen in Figure 8.21a, the fitting curve moves horizontally with different γ_D values. When a_D increases the curvature of the fitting line increases, but the D value at γ_D is the same as the "C" value as shown in Figure 8.21b.

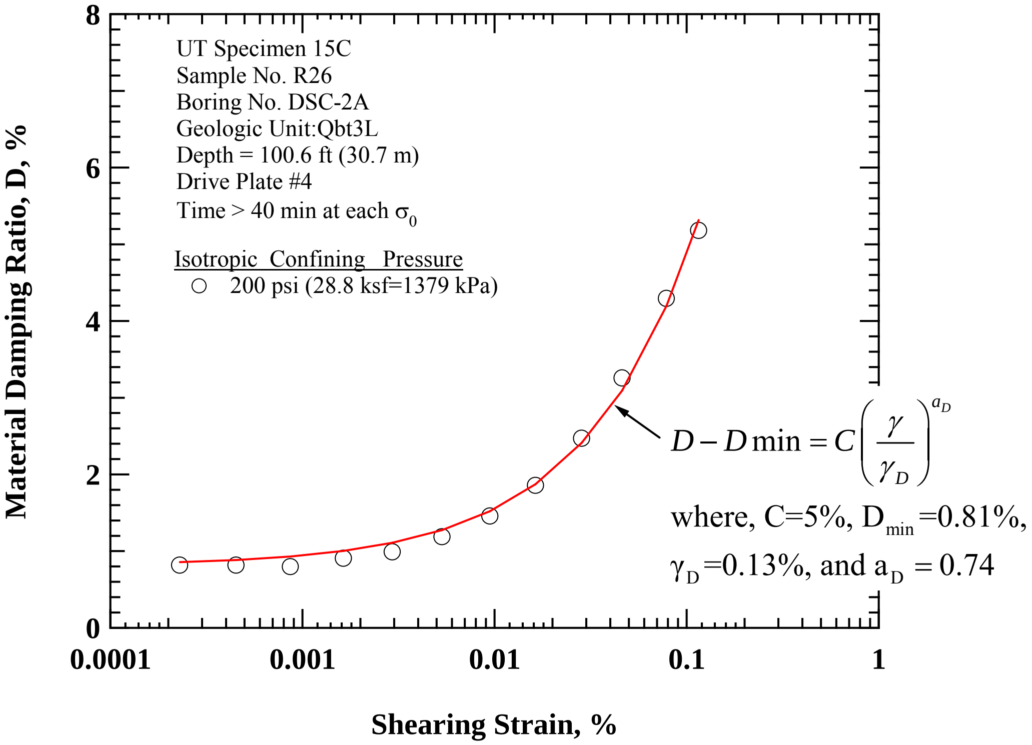

Figure 8.20 Example of Least-Squares Fitting with the Proposed "Nonlinear Damping" Model for D – log γ Relationship at Its Estimated In-Situ Effective Stress Determined from Fixed-Free Resonant Column Tests of Specimen 15C from the Qbt3L Unit of the Bandelier Tuff

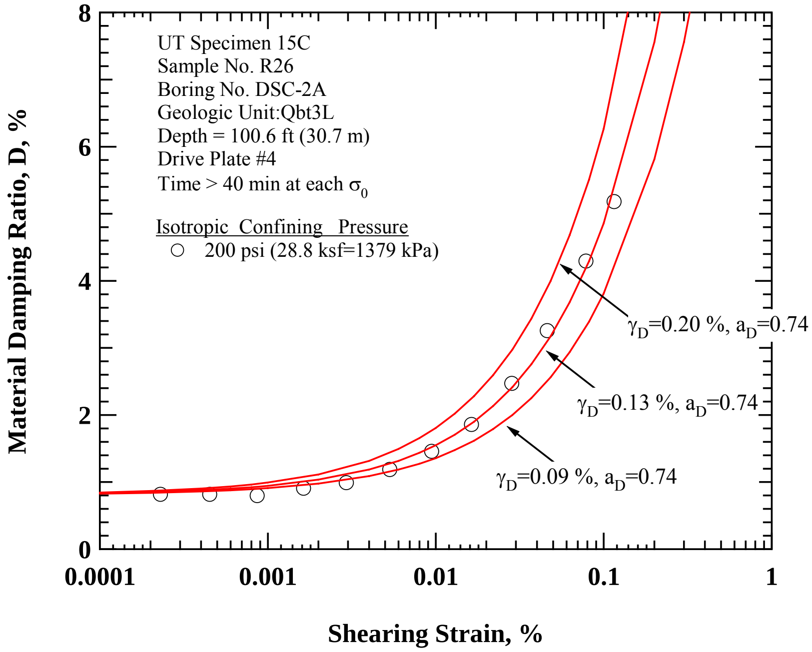

(a) Effect of γ_D

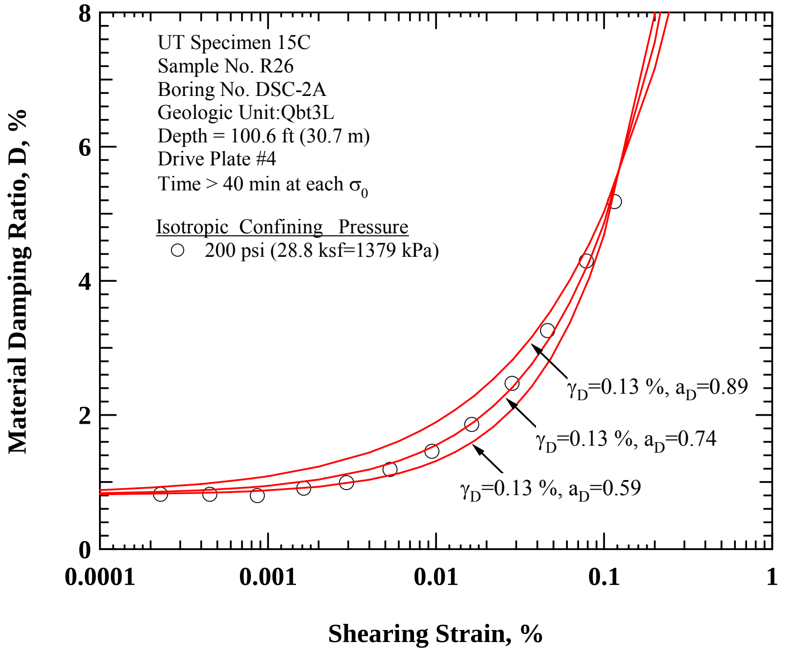

(b) Effect of a_D

Figure 8.21 Example of Fitting the D - log γ Relationship with: (a) Different γ_D Values and (b) Different a_D Values

8.3.1 Bandelier Tuff

The D – log γ relationships for the 18 tuff specimens from the Bandelier Tuff are presented in Figure 8.22. All relationships were determined at the estimated in-situ effective stresses (σ_m') of the specimens. Although these specimens have a large range in G_{max} due to various welding conditions and confining pressures, their D_{min} values are small (about equal or less than 1.0 %) and D – log γ relations seem to form a relatively narrow band. As discussed with G/G_{max} – log γ relationships, most specimens were tested at shearing strains above 0.01 % and the highest D values are equal or above 2.0 %. The poorly welded tuffs (the specimens in Groups 3 and 4) could be tested at larger strains than the specimens with larger welding intensity (the specimens in Groups 1 and 2). Three specimens in Group 4 and two specimens in Group 3 were tested at shearing strain above 0.1 %. The highest D value of about 5.2 % was observed for a specimen in Group 4.

To investigate the nonlinear range of the specimens clearly, the D_{min} value for each specimen was subtracted from the D value at each strain amplitude. Figure 8.23 shows the resulting (D-D_{min}) – log γ relationships for the 16 specimens. Below 0.001 % of shearing strain, most specimens exhibited no increase in their D values. Between 0.001 to 0.003 %, the (D-D_{min}) – log γ relationships of the specimens began to differ from each other. As done for the discussions of the D – log γ relationships of the Topopah Spring tuffs, the values of $\gamma_{Dmin+0.2\%}$ and $\gamma_{Dmin+0.5\%}$ are compared. In addition, the γ when D increased by 2.0 % above D_{min} (D-D_{min} = 2.0 %) are also discussed for the specimens from the Bandelier Tuff. Most specimens exhibited this increase in D from D_{min} at their highest test strains. Moreover, the $\gamma_{0.8}$ of the specimens ranged from about 0.013 to 0.060 % as shown in Figure 8.6 and the similar strain range was observed when their (D–D_{min})

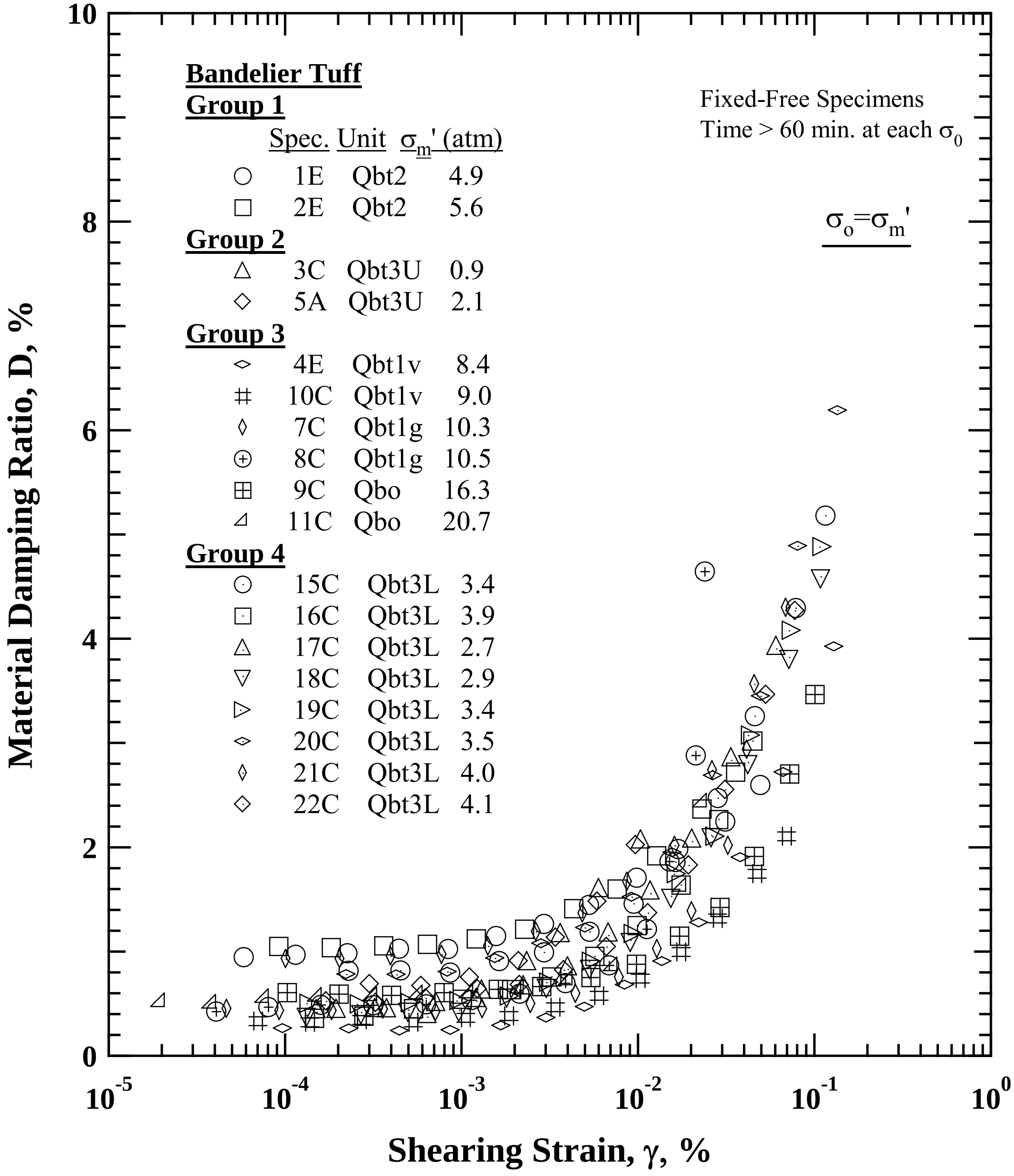

Figure 8.22 Variation of Material Damping Ratio with Shearing Strain of Eighteen Specimens from the Bandelier Tuff at Their Estimated In-Situ Mean Effective Stress (σ_m’) from Resonant Column (RC) Tests

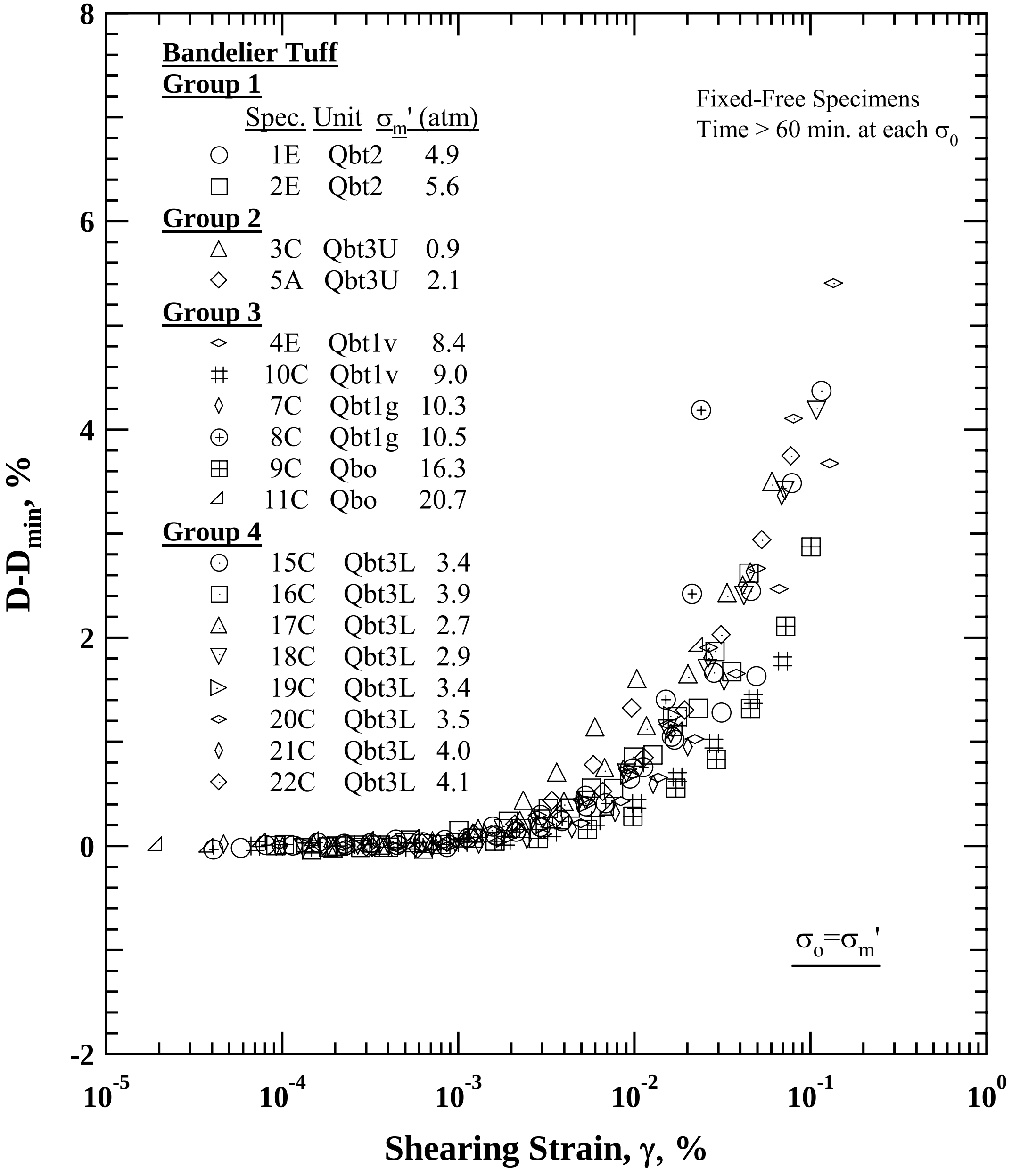

Figure 8.23 Variation of "Nonlinear Damping" with Shearing Strain of Eighteen Specimens from the Bandelier Tuff at Their Estimated In-Situ Mean Effective Stress (σ_m') from Resonant Column (RC) Tests

values are about 2.0 % as seen in Figure 8.23. This level of strain is denoted as $\gamma_{Dmin+2.0\%}$ hereafter.

The variations of $\gamma_{Dmin+0.2\%}$ values of the 18 tuff specimens from the Bandelier Tuff are investigated first in terms of the variations with: (1) their total unit weight (γ_t) and (2) shear wave velocity at 0.3 atm ($V_{S,\ 0.3\ atm}$) in Figures 8.24a and 8.24b, respectively. As with the Topopah Spring tuffs, the variations of $\gamma_{Dmin+0.2\%}$ of the Bandelier tuffs shown in the figures are very similar to the variations of $\gamma_{0.98}$ with γ_t and $V_{S,\ 0.3\ atm}$ in Figure 8.7a and 8.7b, respectively. The specimens in each group exhibited similar $\gamma_{Dmin+0.2\%}$ values and the average $\gamma_{Dmin+0.2\%}$ value of each group ranges from about 0.0017 % for Group 2 to 0.0049 % for Group 3. The poorly welded tuffs in Group 3 interestingly exhibited larger linear ranges (larger $\gamma_{Dmin+0.2\%}$) than the moderately to densely welded tuffs in Group 1. The $\gamma_{Dmin+0.2\%}$ values of the poorly welded tuffs in Group 4 also interestingly exhibited no significant difference on their average value compared with the tuffs with higher welding intensity in Groups 1 and 2. The differences in $V_{S,\ 0.3\ atm}$ values between groups differentiates the differences in degree of welding for the groups, but no noticeable relationship with $\gamma_{Dmin+0.2\%}$ are observed in Figure 8.24b.

The $\gamma_{Dmin+0.2\%}$ values are plotted with the isotropic confining pressures (σ_o) at which the measurements were performed in Figure 8.25a. It seems the $\gamma_{Dmin+0.2\%}$ values are correlated with their σ_o values. The variation of $\gamma_{Dmin+0.5\%}$ with σ_o shows a stronger correlation as shown in Figure 8.25b, confirming the effect of σ_o on the D – log γ relationships of the Bandelier tuffs.

The effect of σ_o at higher strain levels are also investigated with the $\gamma_{Dmin+2.0\%}$ and γ_D values as illustrated in Figures 8.26a and 8.26b, respectively. Note the "C" value of 5

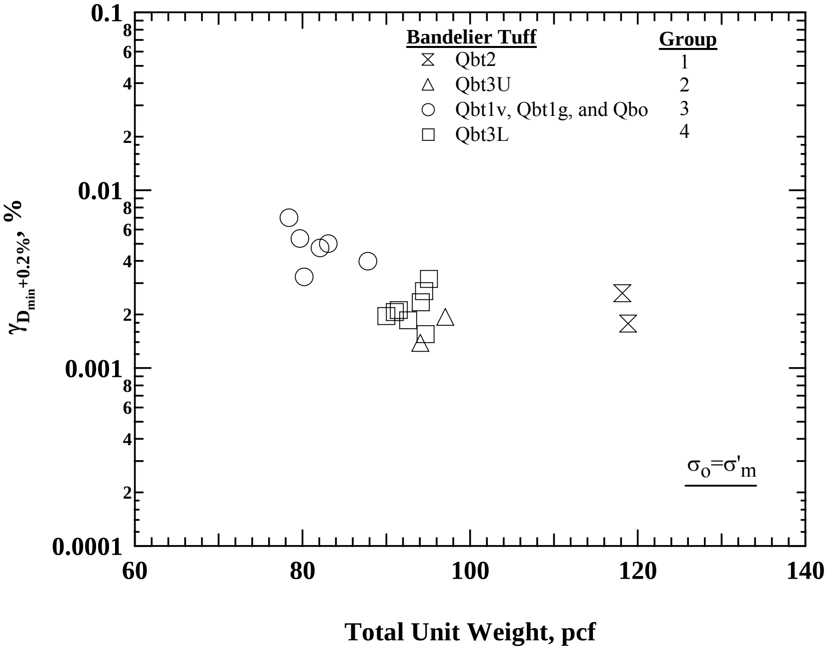

(a) Shearing Strain when D-D_{min} is 0.2 % ($\gamma_{Dmin+0.2\%}$) versus Total Unit Weight (γ_t)

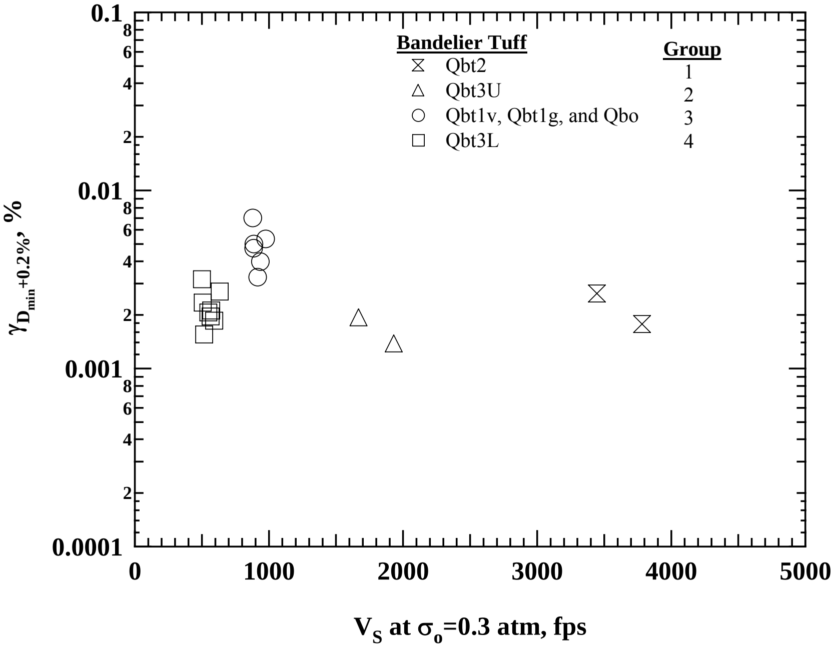

(b) Shearing Strain when D-D_{min} is 0.2 % ($\gamma_{Dmin+0.2\%}$) versus V_S at 0.3 atm ($V_{S,\ 0.3\ atm}$)

Figure 8.24 Variation of Shearing Strain when D-D_{min} is 0.2 % with: (a) Total Unit Weight and (b) V_S at σ_o of 0.3 atm of Eighteen Specimens from the Bandelier Tuff

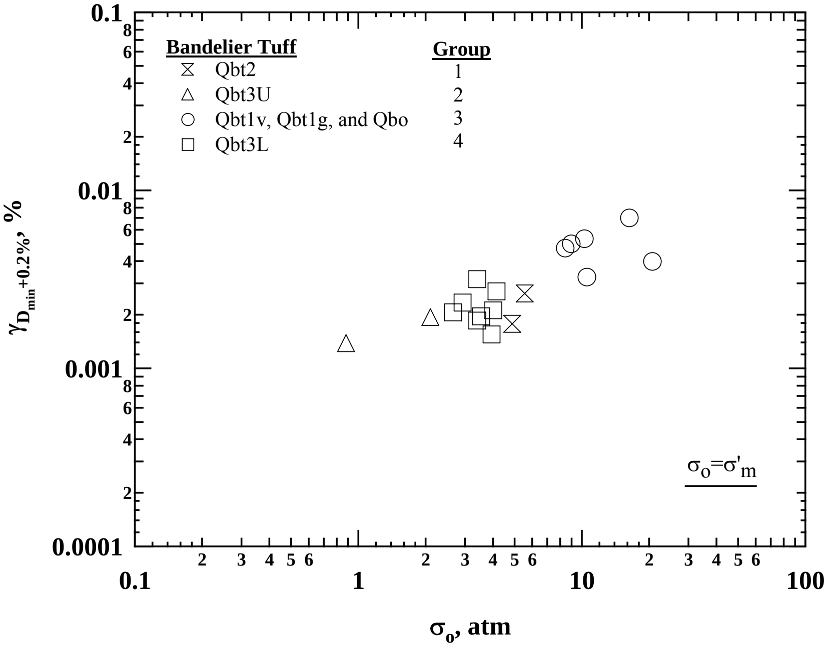

(a) Shearing Strain when D-D$_{min}$ is 0.2 % ($\gamma_{Dmin+0.2\%}$) versus Confining Pressure (σ_o)

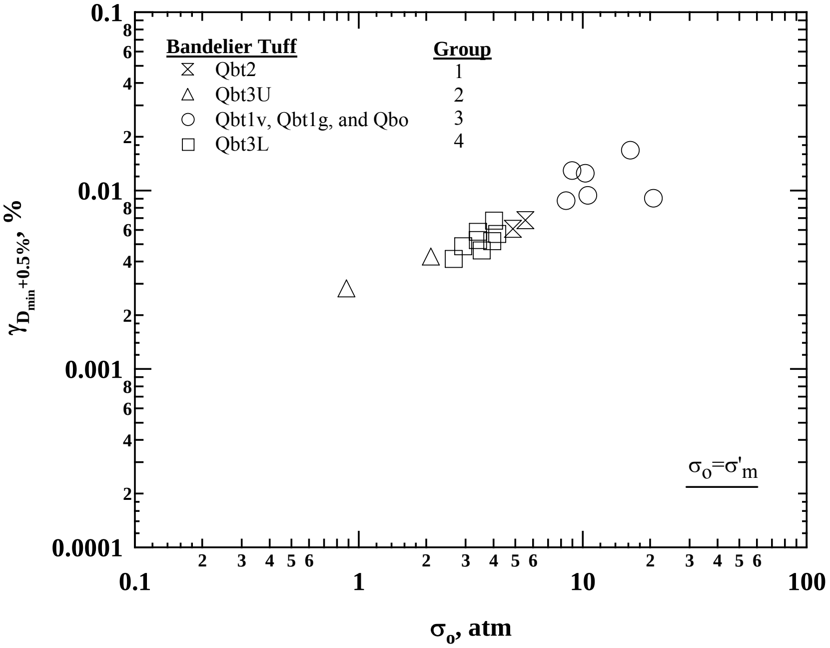

(b) Shearing Strain when D-D$_{min}$ is 0.5 % ($\gamma_{Dmin+0.5\%}$) versus Confining Pressure (σ_o)

Figure 8.25 Variation of: (a) Shearing Strain when D-D$_{min}$ is 0.2 % and (b) Shearing Strain when D-D$_{min}$ is 0.5 % with Isotropic Confining Pressure (σ_o) of Eighteen Specimens from the Bandelier Tuff

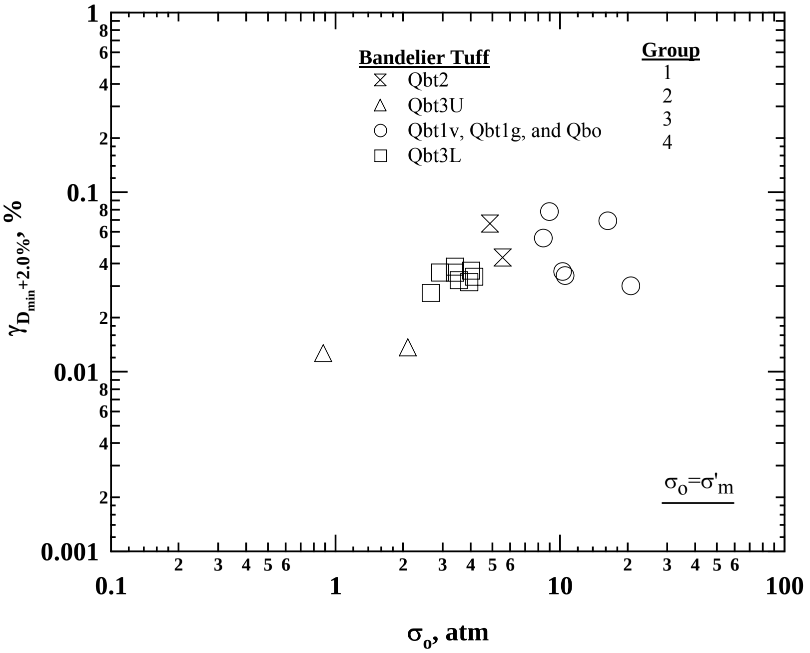

(a) Shearing Strain when D-D$_{min}$ is 2.0 % ($\gamma_{Dmin+2.0\%}$) versus Confining Pressure (σ_o)

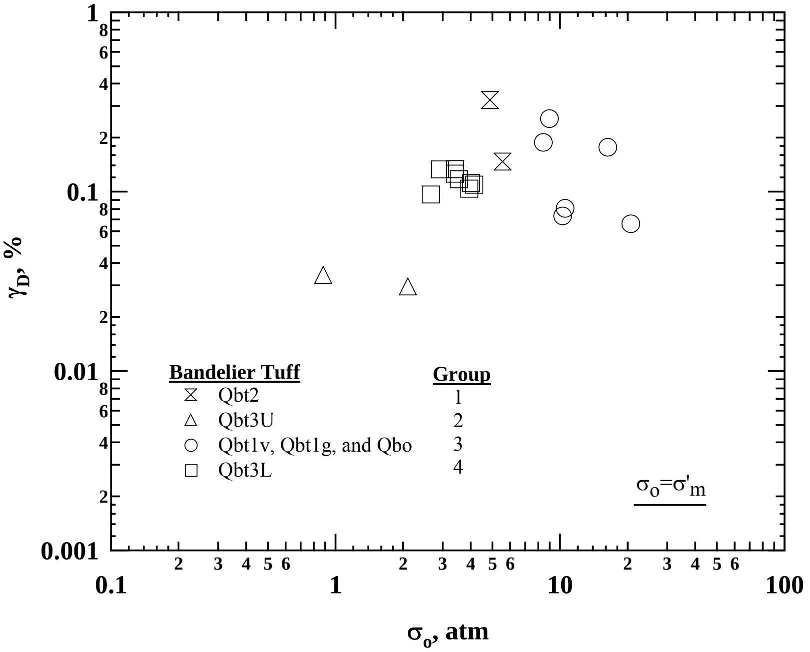

(b) Shearing Strain when D-D$_{min}$ is 5.0 % (γ_D) versus Confining Pressure (σ_o)

Figure 8.26 Variation of: (a) Shearing Strain when D-D$_{min}$ is 2.0 % and (b) Shearing Strain when D-D$_{min}$ is 5.0 % with Isotropic Confining Pressure (σ_o) of Eighteen Specimens from the Bandelier Tuff

% was used; therefore, γ_D is the strain when D-D_{min} is equal to 5 %. Similar trends were observed in both plots, although the scattering in data is somewhat large in Figure 8.26b for γ_D. It should be noted that the γ_D values of most specimens in Groups 1 through 3 were simply obtained from the least-squares fitting using Eq. (8.4). It was thought that the uncertainty in extrapolating the measured D – log γ relationship to γ_D leads to the scattering in Figure 8.26b.

The specimens in Groups 2 through 4 were tested at two different pressures as discussed in Section 8.2.2 for their G/G_{max} – log γ relationships. The effect of σ_o observed at each pressure is compared using $\gamma_{Dmin+0.2\%}$ and $\gamma_{Dmin+2.0\%}$ as presented in Figures 8.27a and 8.27b, respectively. The data at the smaller confining pressures ($\sigma_{o,1}$) are presented in hollow symbols while the data at the larger confining pressures ($\sigma_{o,2}$) are presented in solid symbols in the figure. Both $\gamma_{Dmin+0.2\%}$ and $\gamma_{Dmin+2.0\%}$ values of most specimens increased as σ_o increased and the increase observed for each group is similar to each other. The increments in both σ_o and strain levels are presented in a ratio format in Figures 8.28a and 8.28b, for $\gamma_{Dmin+0.2\%}$ and $\gamma_{Dmin+2.0\%}$, respectively. The specimens in each group exhibited similar increments in strain levels with the similar increments in σ_o. It is interesting to note that the increments observed in $\gamma_{Dmin+0.2\%}$ values are very similar to the increments observed in $\gamma_{0.98}$ observed in Figure 8.11a. It is also very interesting to point out that the increments in $\gamma_{Dmin+2.0\%}$ were slightly larger than the increments in $\gamma_{Dmin+0.2\%}$ with the same pressure increments. Both "a" values for the G - log γ relationship and "a_D" values for the D – log γ relationships decrease in general as σ_o increases as illustrated in Figures 8.29a and 8.29b, respectively. It was thought that the larger decrease in "a_D" value with σ_o resulted in the larger increments in $\gamma_{Dmin+2.0\%}$ values than $\gamma_{Dmin+0.2\%}$ values. The larger scattering in "a_D" values is possibly indicative of the

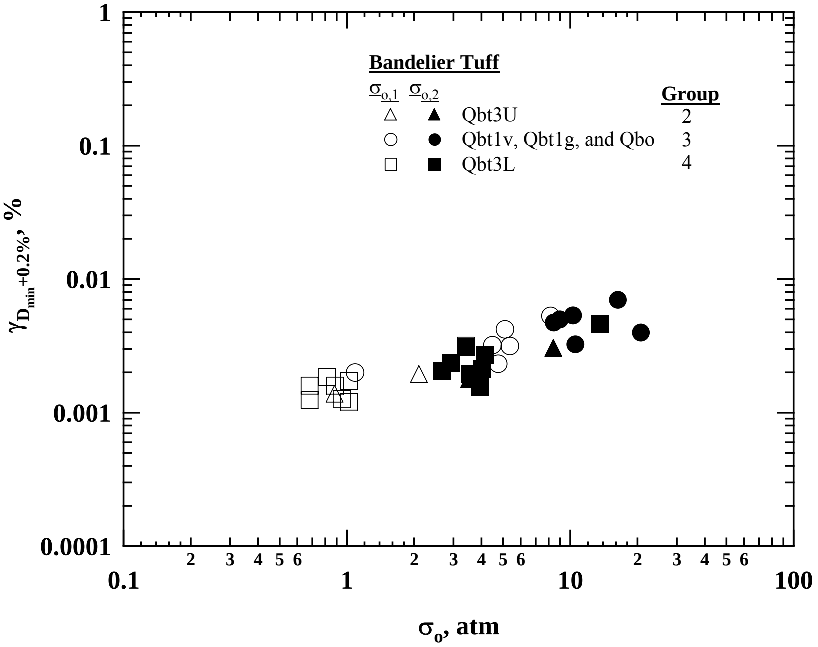

(a) Shearing Strain when D-D_{min} is 0.2 % ($\gamma_{Dmin+0.2\%}$) versus Confining Pressure (σ_o)

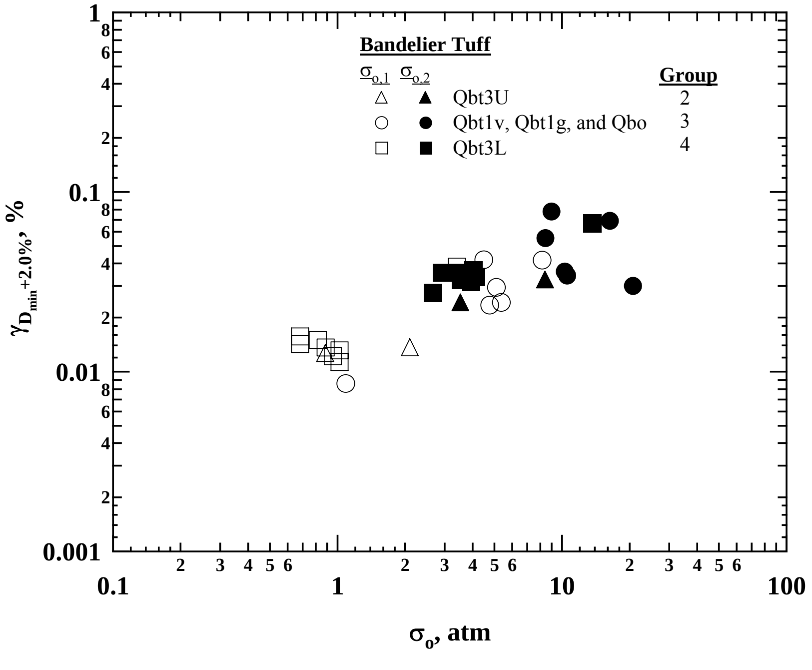

(b) Shearing Strain when D-D_{min} is 2.0 % ($\gamma_{Dmin+2.0\%}$) versus Confining Pressure (σ_o)

Figure 8.27 Variations of: (a) Shearing Strain when D-D_{min} is 0.2 % and (b) Shearing Strain when D-D_{min} is 2.0 % with Isotropic Confining Pressure (σ_o) of Sixteen Specimens from the Bandelier Tuff

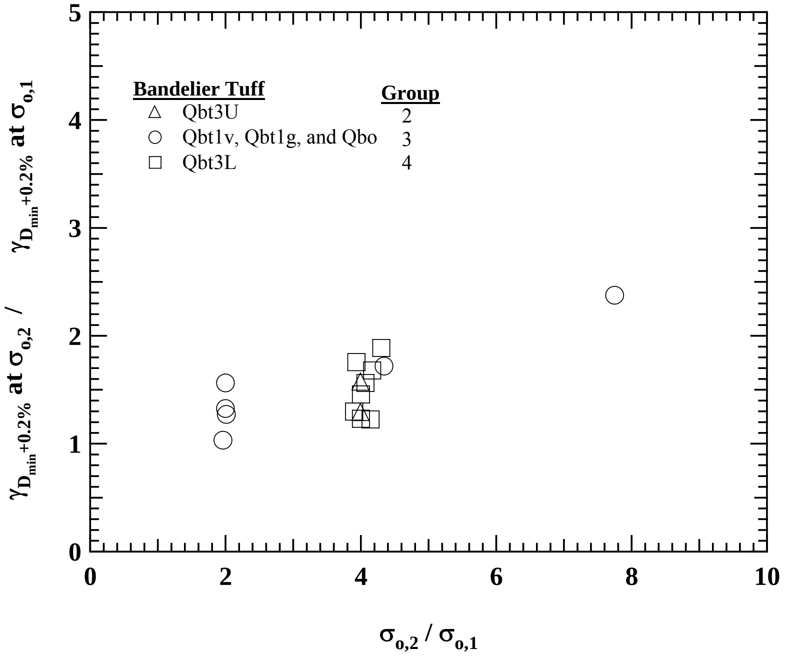

(a) Increment of $\gamma_{Dmin+0.2\%}$ versus Increment of σ_o

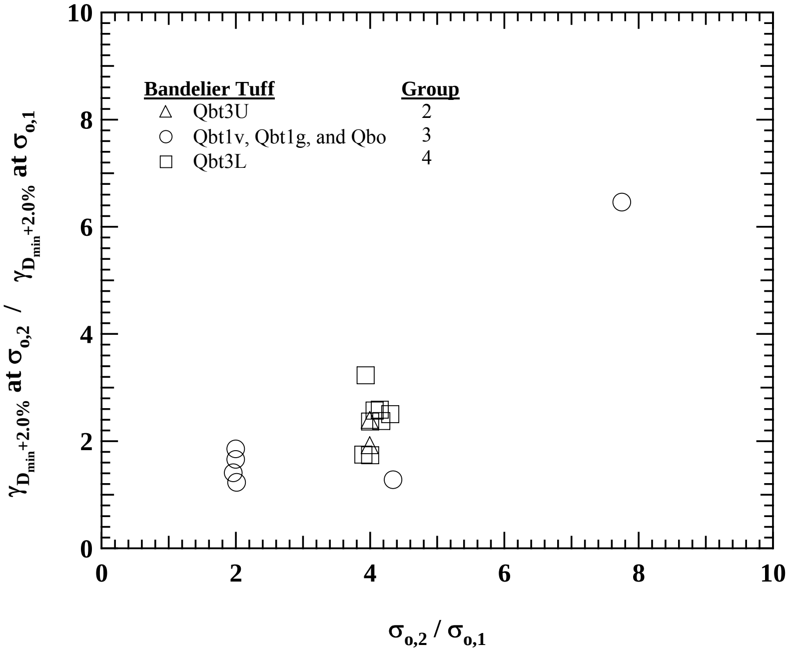

(b) Increment of $\gamma_{Dmin+2.0\%}$ versus Increment of σ_o

Figure 8.28 Variations of Increments in: (a) Shearing Strain when D-D_{min} is 0.2 % and (b) Shearing Strain when D-D_{min} is 2.0 % with Increment in Isotropic Confining Pressure (σ_o) of Sixteen Specimens from the Bandelier Tuff

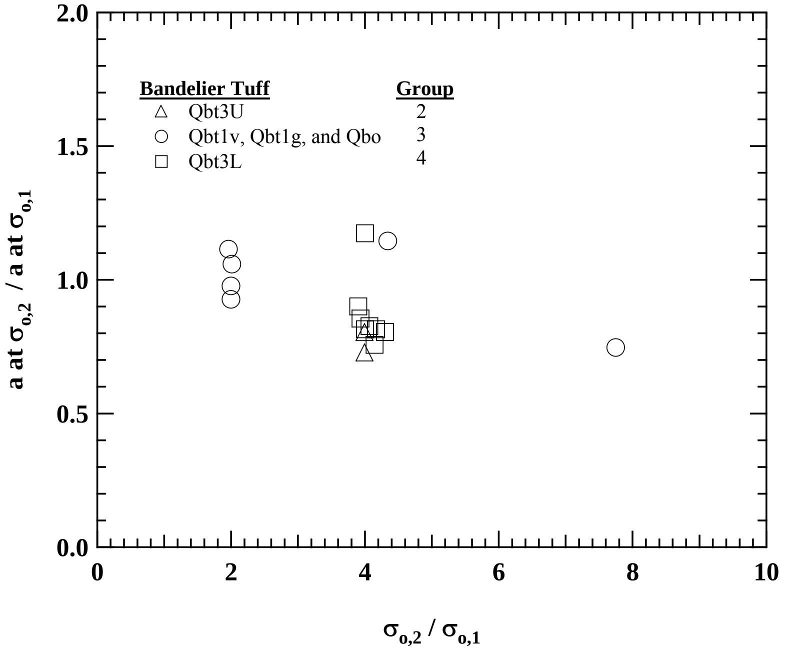

(a) Curvature Coefficient for G/G_{max} – log γ relationship (“a” value) with σ_o

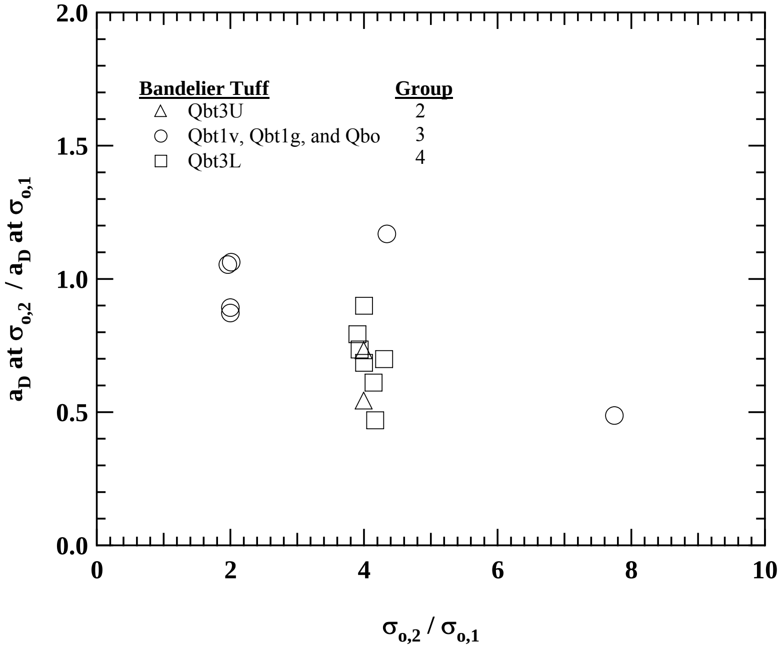

(b) Curvature Coefficient for D – log γ relationship (“a_D” value) with σ_o

Figure 8.29 Variations in: (a) Curvature Coefficient for G/G_{max} – log γ relationship (“a” value) and (b) Curvature Coefficient for D – log γ relationship (“a_D” value) with Isotropic Confining Pressure (σ_o) of Sixteen Specimens from the Bandelier Tuff reason for the larger scattering in $\gamma_{Dmin+2.0\%}$ values in Figure 8.28b, compared with $\gamma_{0.80}$ in Figure 8.11.

Based on these strong correlations between the strain levels and σ_o, the (D - D_{min}) – log γ relationships of the poorly welded and moderately welded tuffs of the Bandelier Tuffs can be predicted by the best-fit line through the data collected in this study as shown in Figure 8.30. The relationship between γ_D and σ_o can be expressed as:

$$\gamma_D = 0.038(\sigma_o / Pa)^{0.54} \qquad (8.5)$$

where, γ_D is the reference strain for D – log γ relationship in %,

σ_o is the isotropic confining pressure in the same units as Pa, and

Pa is one atmosphere (2117 psf or 100 kPa).

The standard error of the fitting, $S_{\varepsilon, \gamma_D}$, that is the standard deviation of the difference between the measured and predicted values, is about 1.6 in the log-log relationship (Ang and Tang, 1975).

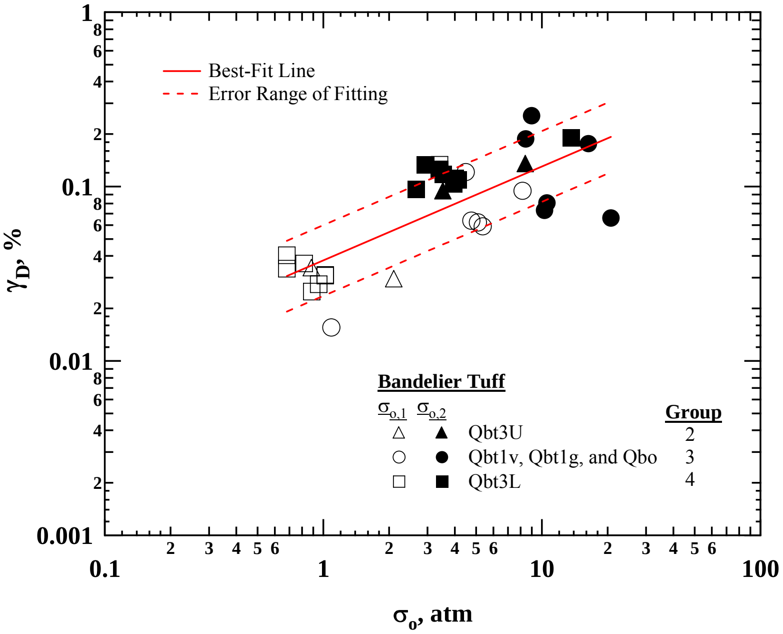

Figure 8.30 Variations of Reference Strain for D – log γ relationship (γ_D) with Isotropic Confining Pressure (σ_o) of Sixteen Specimens from the Bandelier Tuff

In addition, the “a_D” value decreases as γ_D increases in general as shown in Figure 8.31. The semi-logarithmic relationship between these values can be expressed as:

$$a_D = -0.545 \log_{10} \gamma_D + 0.337 \tag{8.6}$$

where, a_D is the curvature coefficient (dimensionless) and

γ_D is the reference strain for D – log γ relationship in %.

The standard error of the fitting, $S_{\varepsilon,\ a_D}$, that is the standard deviation of the difference between the measured and predicted values, is about 0.126 in the semi-log relationship (Ang and Tang, 1975). One can use the γ_D and “a_D” values from Eqs. (8.5) and (8.6) to create average trend lines for the $(D - D_{min})$ - log γ relationships of the poorly welded tuffs and moderately welded tuffs from the Bandelier Tuff. The error range of the average trend line can be created based on the standard errors of the fittings, S_{ε,γ_D} and S_{ε,a_D}.

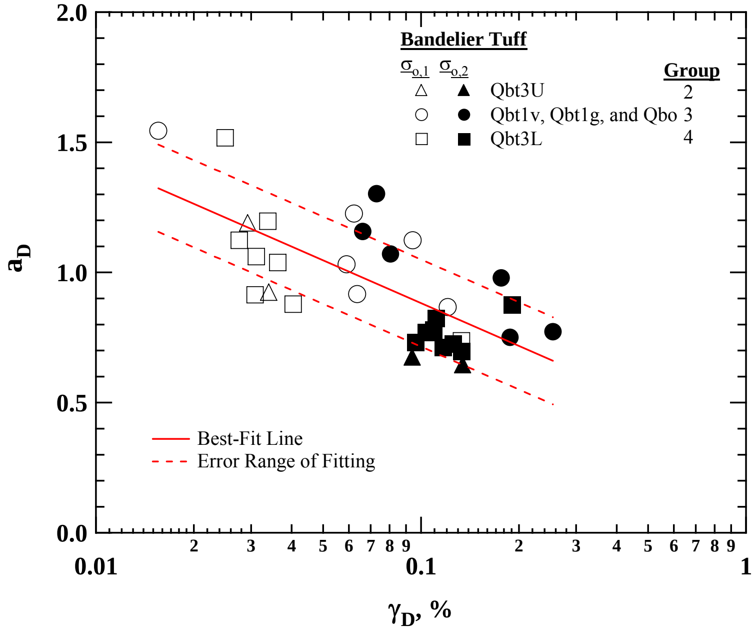

Figure 8.31 Variations of Curvature Coefficient for D – log γ relationship (“a_D” value) with Reference Strain for D – log γ relationship (γ_D) of Sixteen Specimens from the Bandelier Tuff

8.4 G – LOG γ, G/G_{max} – LOG γ AND D– LOG γ RELATIONSHIPS OF ASH-FLOW TUFFS DETERMINED FROM THE LARGE RESONANT COLUMN (LgRC) DEVICE

Four additional samples were tested using both the fixed-free resonant column (RCTS) device and the large resonant column (LgRC) device. These specimens consist of one specimen from the nonlithophysal unit and three specimens from the lithophysal units of the Topopah Spring Tuff. Note that these specimens were tested in the linear range using the URC device prior to the tests discussed in this section. The URC tests were performed to see the effect of the change in water content on the G_{max} and D_{min} as discussed in Section 6.5.2. The information on these specimens is listed in Table 6.1 with the other two nonlithophysal specimens tested with the URC device. All specimens have the same diameter of 1.56 in. (3.96 cm).

The purpose of these additional tests are: (1) to verify the LgRC device with more specimens other than the tuff specimen discussed in Chapter 5 and (2) to extend the nonlinear relationships of the Topopah Spring tuffs with the measurements from the LgRC tests on similar specimens. Figure 8.32 shows the G – log γ relationships determined from both the fixed-free RC and the LgRC tests on the four specimens. The fixed-free RC tests were performed first until G/G_{max} was close to about 0.98. The G_{max} values of the specimens were unaffected by the testing at this strain level. (Testing with the RCTS device could have continued but it was important to not damage the specimen before testing with the LgRC device.) As done with the specimen from the Calico Hills used in the validation tests discussed in Chapter 5, the same top cap and base pedestal of each specimen used in the fixed-free RC tests were directly used in the LgRC device without removing them from the specimen. There was no disturbance from the installation process in the LgRC device. As seen in Figure 8.32, the results from the two

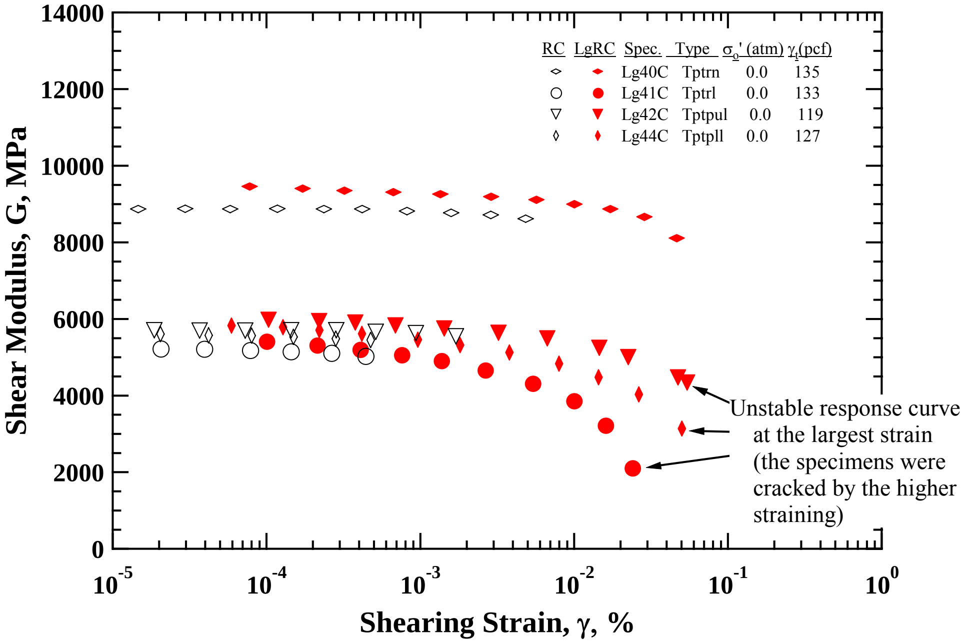

Figure 8.32 G – log γ Relationships from Fixed-Free Resonant Column Tests and Large Resonant Column Tests on Four Specimens from the Topopah Spring Tuff

devices are very similar. The maximum difference in G_{max} is about 5 % for Specimen Lg40C from the Tptrn unit. Although the fixed-free RC tests were tested at smaller strains, the G – log γ relationships determined from the LgRC tests closely follow the relationships from the fixed-free RC tests. Two specimens from the Tptrn and Tptpul units exhibited the system compliance as indicated with unusual scattering and higher values in D at strains below about 0.002 % as illustrated in Figure 8.33. The unusual scattering in D values of the other two specimens is not clearly observed in the small-strain range. However, the D values are higher than the D values from the fixed- free tests indicating the possibility of system compliance adding to D. Therefore, the G values

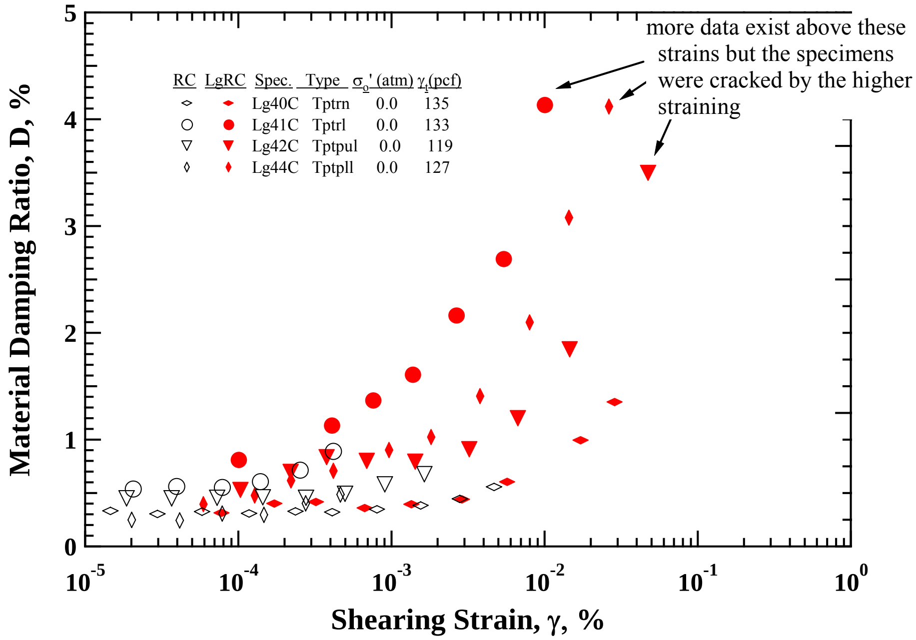

Figure 8.33 D – log γ Relationships from Fixed-Free Resonant Column Tests and Large Resonant Column Tests on Four Specimens from the Topopah Spring Tuff (Only D values Lower than 5 % are Shown for Comparison Purposes.)

of these specimens were normalized by assuming that the G/G_{max} – log γ relationships from the fixed-free RC tests and the LgRC tests are equivalent. The G/G_{max} values from the fixed-free RC tests at γ of about 0.001 % were used to normalize the G values from the LgRC tests. Moreover, the G/G_{max} - log γ relationship from the fixed-free RC tests on Specimens Lg41C and Lg44C were extrapolated using the hyperbolic model shown in Eq. (8.1).

The resulting G/G_{max} – log γ relationships of the four LgRC specimens are shown in Figure 8.34. Specimen Lg40C that was a nonlithophysal tuff and had the highest G_{max} value (about 9299 MPa) was tested up to the γ of about 0.047 %. The specimen did not begin to fail at this strain. The other three specimens that were lithophysal tuffs and had

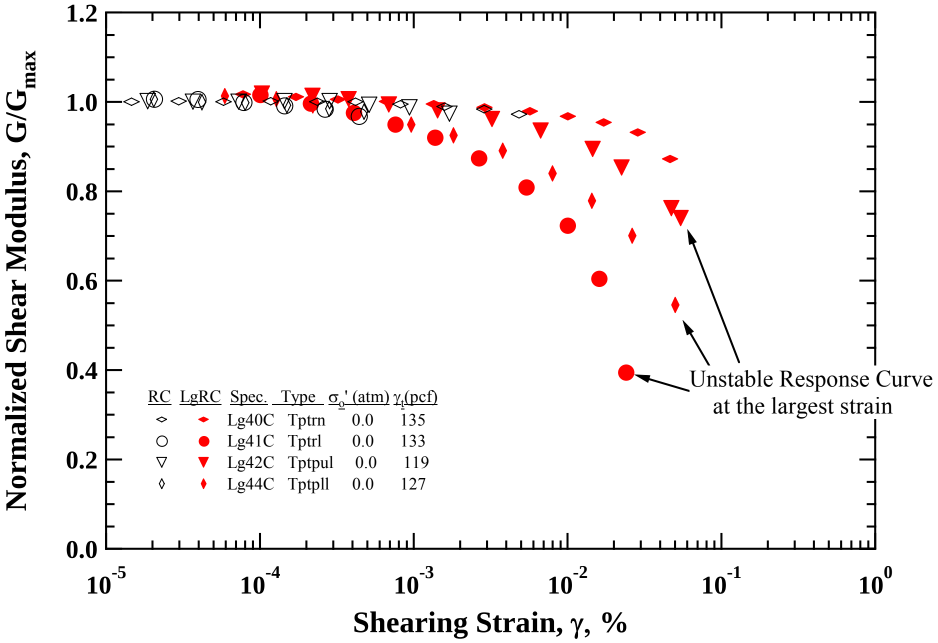

Figure 8.34 G/G$_{max}$ – log γ Relationships from Fixed-Free Resonant Column Tests and Large Resonant Column Tests on Four Specimens from the Topopah Spring Tuff

lower G$_{max}$ values (from about 5400 to 5900 MPa) began to crack and initiate failure at various strain levels as shown in Figure 8.34. Specimen Lg41C began to crack at the lowest strain level (about 0.024 %). Specimen Lg44C began to crack at γ ($\gamma_{failure}$) of about 0.050 % and Specimen Lg42C began to crack at γ of about 0.055 %. It is interesting to note the Specimen Lg41C had the smallest G$_{max}$ and $\gamma_{failure}$ while Specimen Lg44C had the largest G$_{max}$ and $\gamma_{failure}$ among the three lithophysal specimens. The values of the G/G$_{max}$ also varied from about 0.60 for Specimen Lg41C to 0.74 for Specimen Lg44C.

The photographs of the specimens after some cracks developed are presented in Figure 8.35. The failure cracks have been highlighted in Figure 8.35 using a permanent marker. The cracks occurred near lithophysal cavities and the crack only propagated a

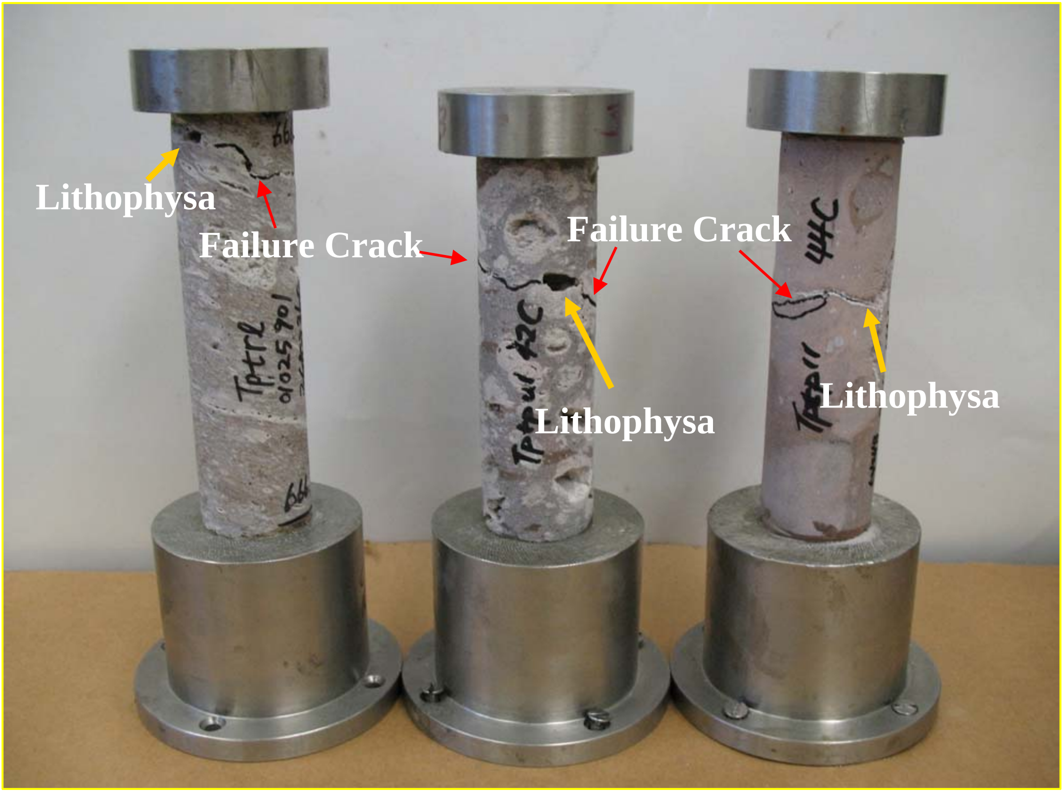

Figure 8.35 Specimens with Cracks that were Created during the Large Resonant Column Tests

short distance. The remaining portions of specimens were still intact. In fact, the cracking in each specimen was recognized based on the shape of the response curve because of the partial failure. The cracks were not easily recognized during the tests. The response curve became unstable and noisy as cracking occurred. This change in the response curve affected the material damping ratio significantly as shown in Figure 8.36. As clearly seen in the figure, the value of D at the largest strain of each specimen was very high (relatively speaking) and deviated from the trend of the other measurements. The response curves at various strains (Strains 1 through 5 as marked in Figure 8.36) for

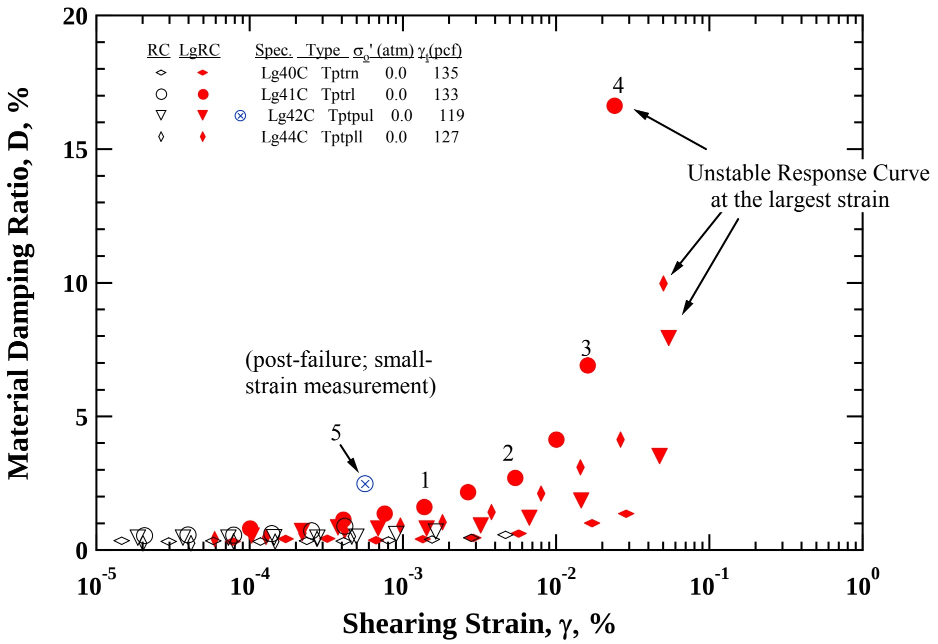

Figure 8.36 D – log γ Relationships from Fixed-Free Resonant Column Tests and Large Resonant Column Tests on Four Specimens from the Topopah Spring Tuff

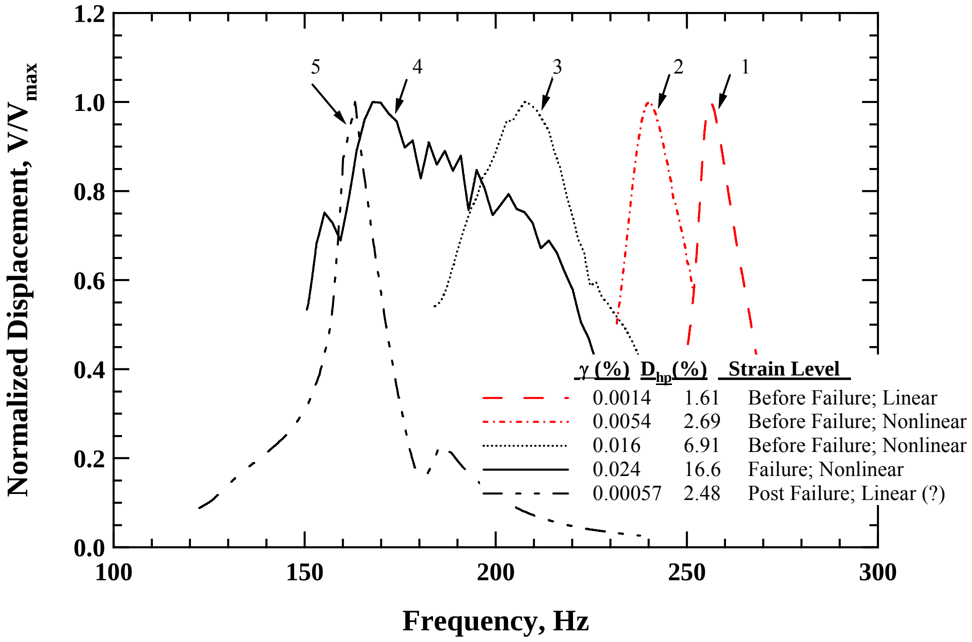

Figure 8.37 Normalized Displacement Response Curves from Large Resonant Column Tests on Specimens Lg41C at Various Strains

Specimen Lg41C are summarized in Figure 8.37. Note that each response curve in Figure 8.37 was normalized by its maximum amplitude so the curves could be easily compared. The curves were smooth and symmetric at Strains 1 and 2 which is in the linear and slightly nonlinear ranges. As the strain increases to the strain right before initial cracking, the shape of the response curve is slightly distorted at Strain 3. The curve became unstable and noisy as cracking occurred (Strain 4). It is felt that this highly distorted response curve should not be used to characterize resonance for the equivalent a linear analyses used to determine G and D from a response curve. After Strain 4, the driving voltage increased but the distortion became more severe and no resonant peak could be recorded. After cracking, a low-amplitude test was performed. The measured D value was about 2.48 %. This value was about 2.2 times higher than the previous D value that was measured before cracking at the similar strain.

The G – log γ relationships determined from the LgRC tests are compared with the eighteen specimens (discussed in the previous sections) in Figure 8.38. The nonlinear relationship of Specimen Lg40C was similar to the relationships for the stiffest lithophysal tuffs (Specimens 5C-2, 12C-1, and 16C-2). Specimen 4C-2 was the only specimen among the 18 fixed-free RC specimens from the Tptrn. This specimen exhibited slightly a lower G_{max} value than Specimen Lg40C from the same crystal-rich, nonlithophysal unit. However, the overall relationships are very similar to each other. The three lithophysal specimens tested using the LgRC exhibited the lowest values of G_{max}. The LgRC tests at small strains below about 0.002 % had system compliance problems as discussed earlier. However, they all could be tested up to cracking while none of the fixed-free with a similar size could be tested to this level. In these comparisons, the LgRC device increased the peak strain level by a factor of 4 or more.

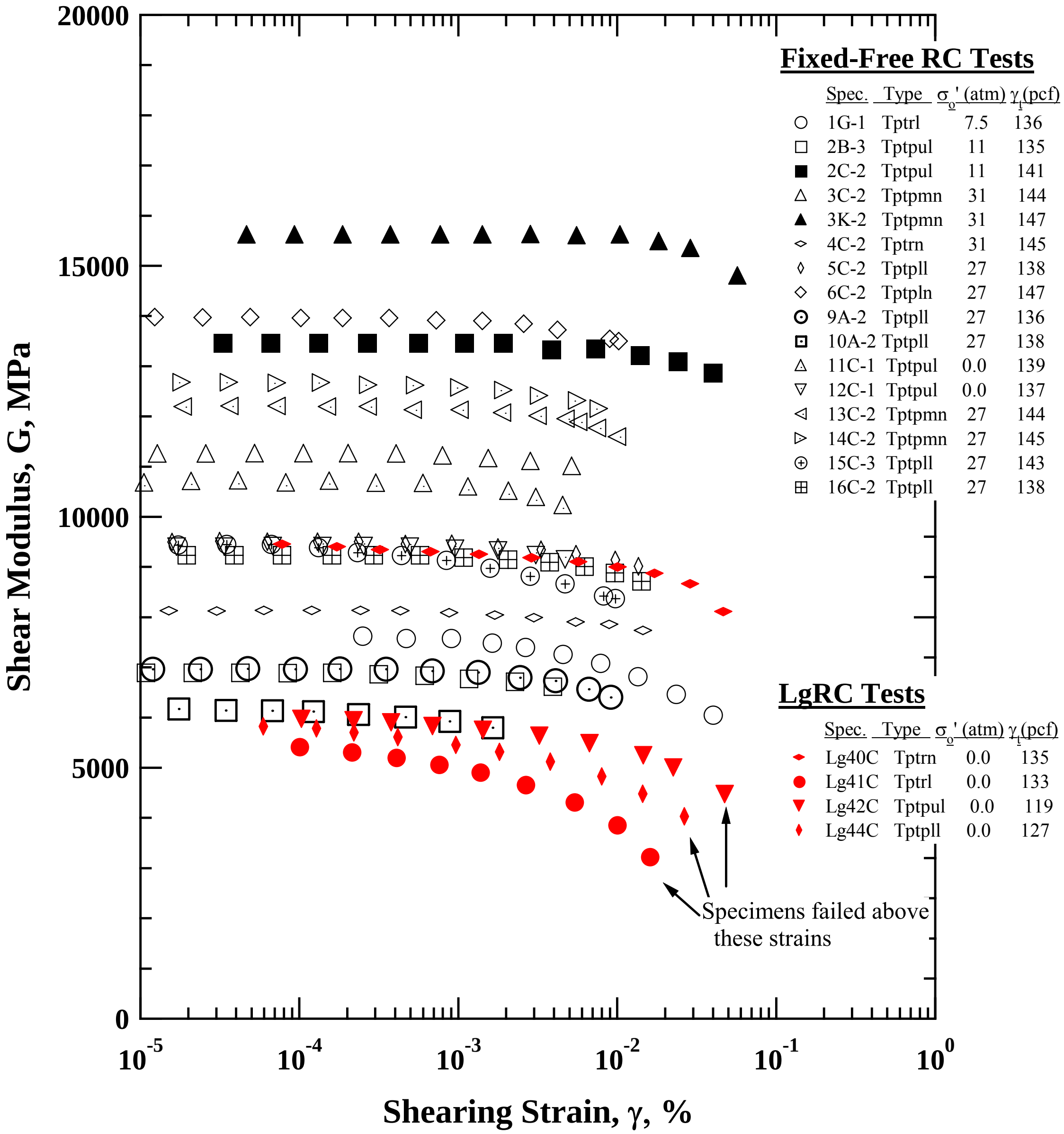

Figure 8.38 Comparison of G – log γ Relationships from Fixed-Free Resonant Column Tests on Eighteen Specimens and from Large Resonant Column Tests on Four Specimens from the Topopah Spring Tuff

To investigate the nonlinearity in G and D values of the tuffs from the nonlithophysal units, their G/G_{max} – log γ and D – log γ relationships are plotted in Figures 8.39a and 8.39b, respectively. All the nonlithophysal specimens with a similar size exhibited very similar nonlinear relationships and Specimen Lg40C follow the relationships well and extended them to about four times larger strain level (about 0.047 %). This strain level is close to the maximum strain that smaller re-cored specimens exhibited. Both re-cored fixed-free RC specimen (Specimen 3K-2) and the LgRC specimen (Specimen Lg40C) did not fail at their maximum strains.

Similarly, the G/G_{max} – log γ and D – log γ relationships of the Tptrl, Tptpul and Tptpll specimens are plotted together in Figures 8.40a and 8.40b, respectively. Because of various amount, size, and distribution of the lithophysal features, the lithophysal tuffs exhibited wide variation in their linear ranges based on the values of $\gamma_{0.98}$ and $\gamma_{Dmin+.0.2\%}$ as discussed in the previous sections. Analysis can be performed at slightly higher ranges but not to strains significantly above the strains achieved in the RCTS tests because the specimens begin to crack.

The three specimens provide good guide lines. The stiff lithophysal tuffs follow the trend of Specimen Lg42C, which began to crack at the strain level above 0.048 %. The softest specimens follow the trend of Specimen Lg41C, which began to crack at the strain level above 0.016 %. The nonlinear relationships of Specimen 44C seem to provide a median trend in this data.

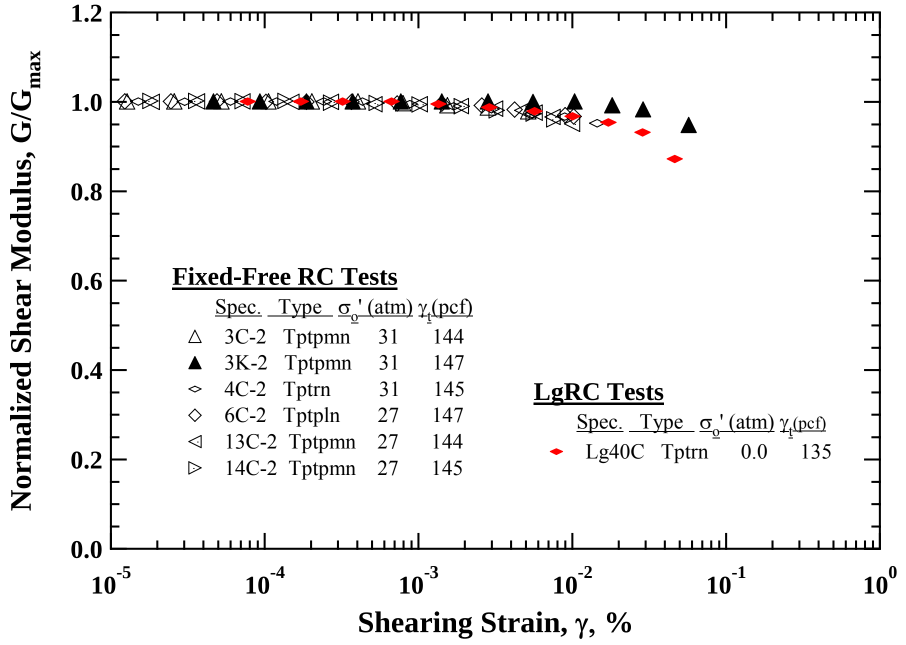

(a) Normalized Shear Modulus (G/G_{max}) versus Shearing Strain (γ)

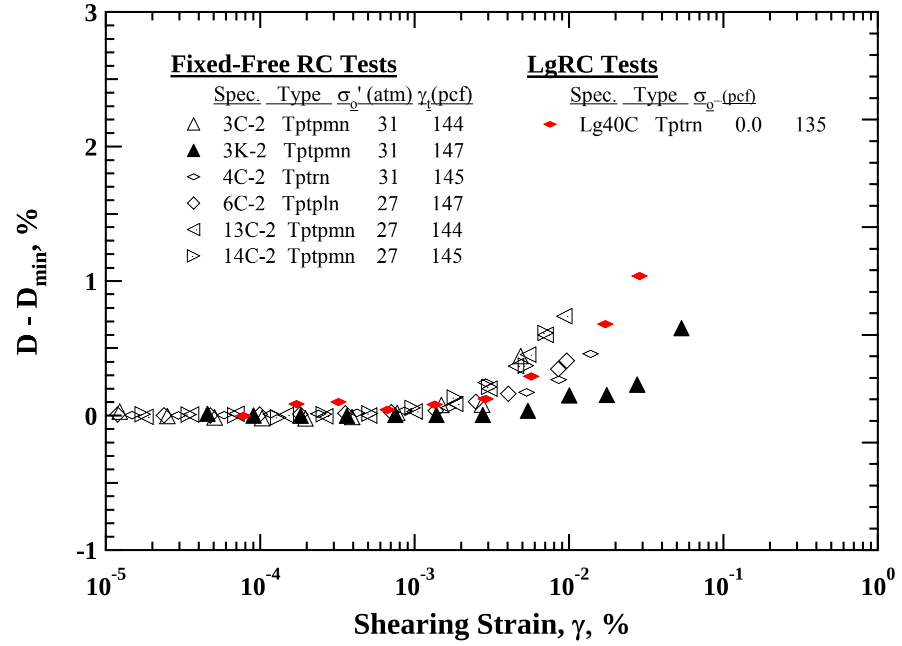

(b) “Nonlinear Damping” ($D - D_{min}$) versus Shearing Strain (γ)

Figure 8.39 Comparisons in: (a) $G/G_{max} - \log \gamma$ relationships and (b) $(D - D_{min}) - \log \gamma$ relationships from Fixed-Free Resonant Column Tests and Large Resonant Column Tests on Specimens from the Nonlithophysal Units

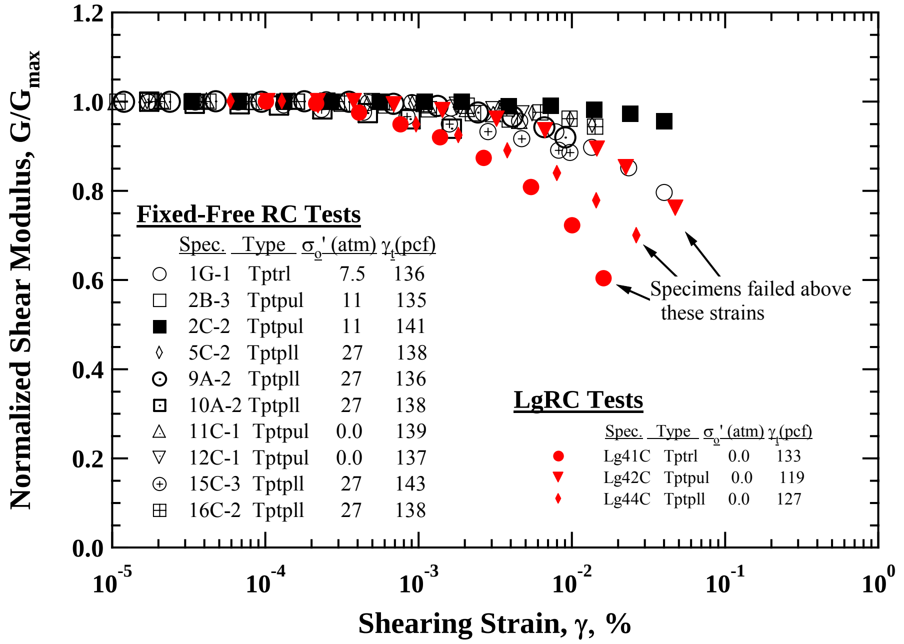

(a) Normalized Shear Modulus (G/G_{max}) versus Shearing Strain (γ)

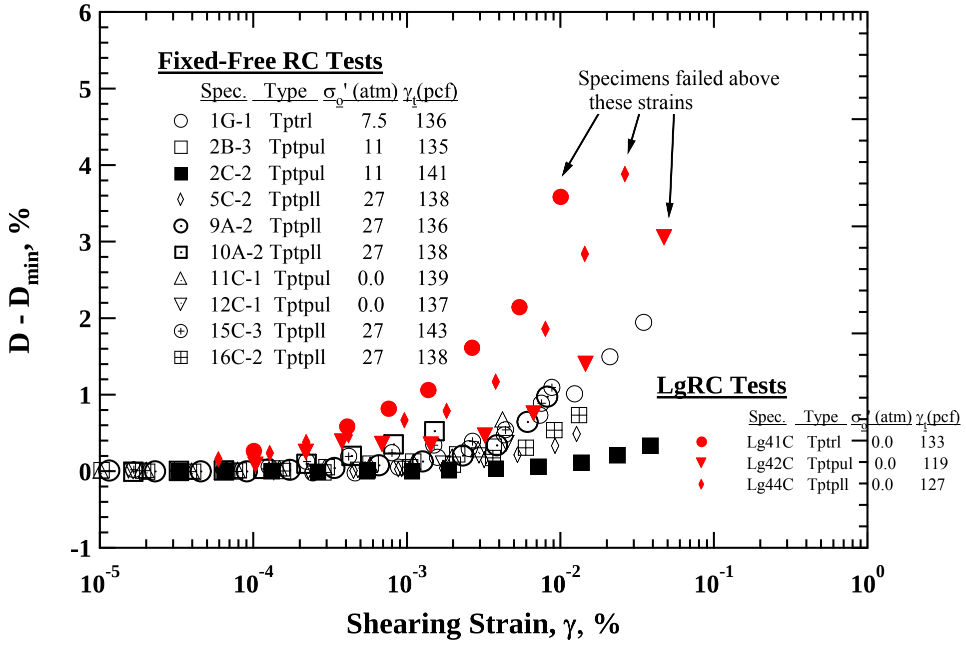

(b) "Nonlinear Damping" ($D - D_{min}$) versus Shearing Strain (γ)

Figure 8.40 Comparisons in: (a) G/G_{max} – log γ relationships and (b) ($D - D_{min}$) – log γ relationships from Fixed-Free Resonant Column Tests and Large Resonant Column Tests on Specimens from the Lithophysal Units

8.5 EFFECT OF LITHOPHYSAL CAVITIES IN NONLINEAR RANGE

Two specimens were dynamically tested using the RCTS device to investigate the effect of the lithophysal cavities on their dynamic properties in nonlinear ranges. These specimens are the same specimens discussed in Chapter 6. The initial dimensions and dynamic properties (G_{max} and D_{min}) in the linear range measured in the unconfined state are presented in Table 6.2. To simulate the lithophysal cavities, seven Artificial Void Segments (AVS) were drilled on Specimen 8C-2 from the Calico Hills (Tac) formation at Yucca Mountain and Specimen 13C-2 from the Topopah Spring Tuff formation at Yucca Mountain. All seven AVS were drilled before the tests were performed for each AVS size as described in Chapter 6.

The $G/G_{max} – \log \gamma$ and $(D – D_{min}) – \log \gamma$ relationships of Specimen 8C-2 are presented in Figures 8.41a and 8.41b, respectively. The total unit weight (γ_t) of Specimen 8C-2 decreased by about 24 % and G_{max} decreased by about 50 % until the larges size of AVS were drilled. However, the AVS do not significantly affect the nonlinear relationships for G and D as clearly shown in the figures. Very similar trends are observed for Specimen 13C-2 as shown in Figures 8.42a and 8.42b for the $G/G_{max} –\log \gamma$ and $(D – D_{min}) – \log \gamma$ relationships, respectively. Both nonlinear relationships were not significantly affected by the AVS. Note the total unit weight (γ_t) of Specimen 13C-2 decreased by about 28 % and G_{max} decreased by about 47 % until the larges size of AVS were drilled. The shearing strains when G/G_{max} is 0.98 ($\gamma_{0.98}$) and (D-D_{min}) is 0.2 % ($\gamma_{Dmin+0.2\%}$) of these two specimens are compared with those for the natural specimens with real variation of γ_t in Figures 8.43a and 8.43b for the $G/G_{max} – \log \gamma$ and $(D – D_{min}) – \log \gamma$ relationships, respectively. The small change in $\gamma_{0.98}$ and $\gamma_{Dmin+0.2\%}$ of Specimen

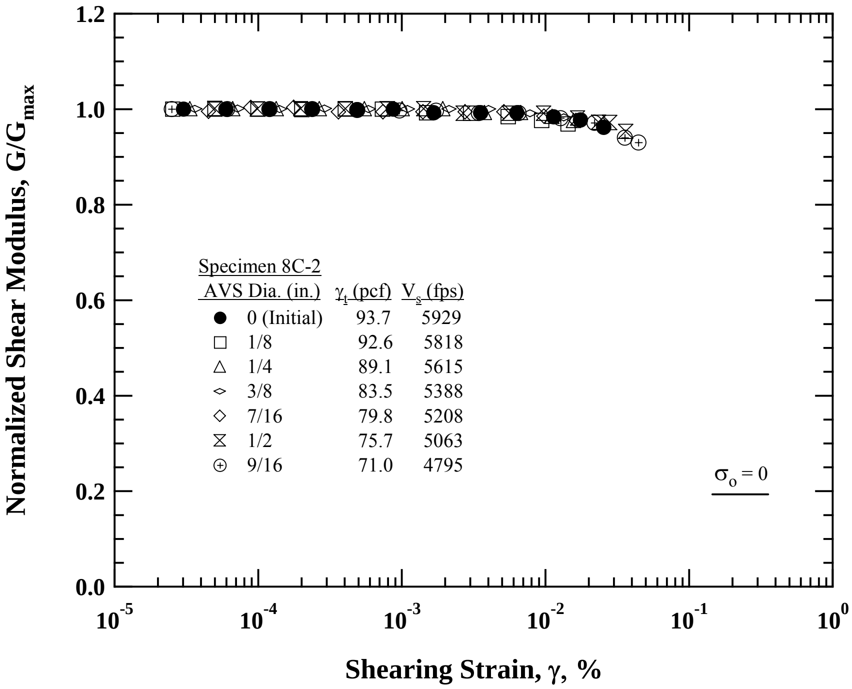

(a) Normalized Shear Modulus (G/G$_{max}$) versus Shearing Strain (γ)

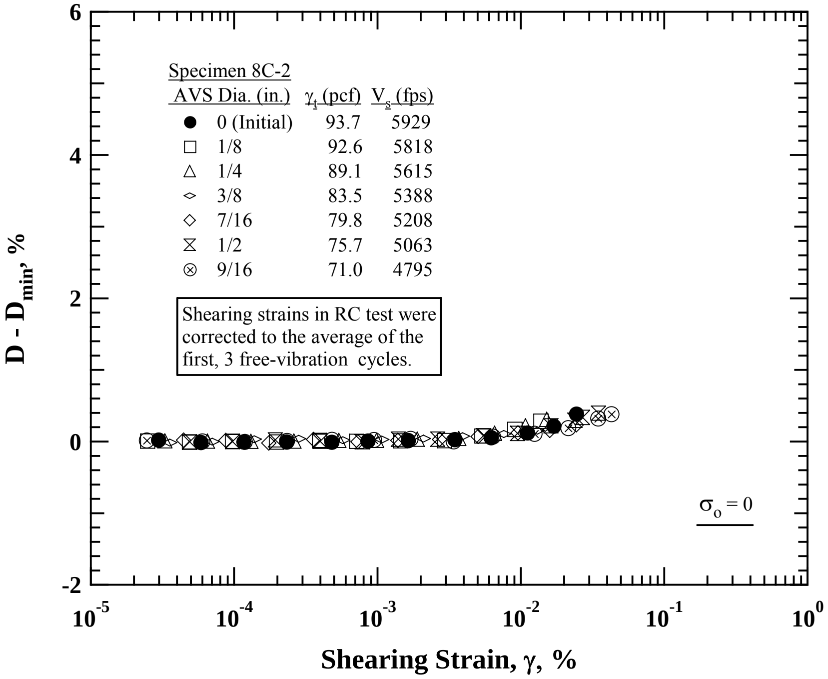

(b) "Nonlinear Damping" (D – D$_{min}$) versus Shearing Strain (γ)

Figure 8.41 Comparisons in: (a) G/G$_{max}$ – log γ relationships and (b) (D – D$_{min}$) – log γ relationships from Fixed-Free Resonant Column Tests on Specimen 8C-2 with Seven Artificial Void Segments (AVS) with Different Sizes

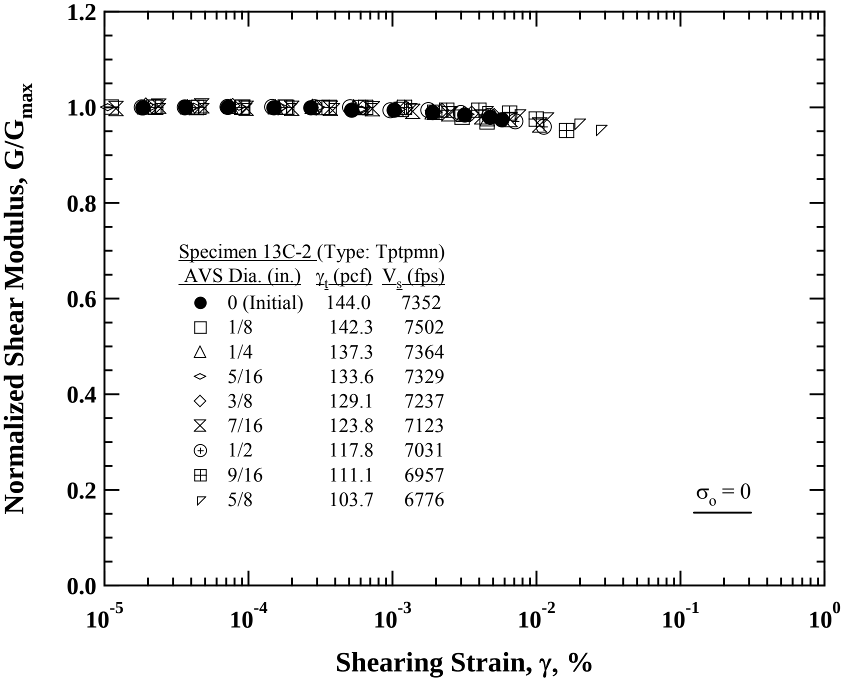

(a) Normalized Shear Modulus (G/G_{max}) versus Shearing Strain (γ)

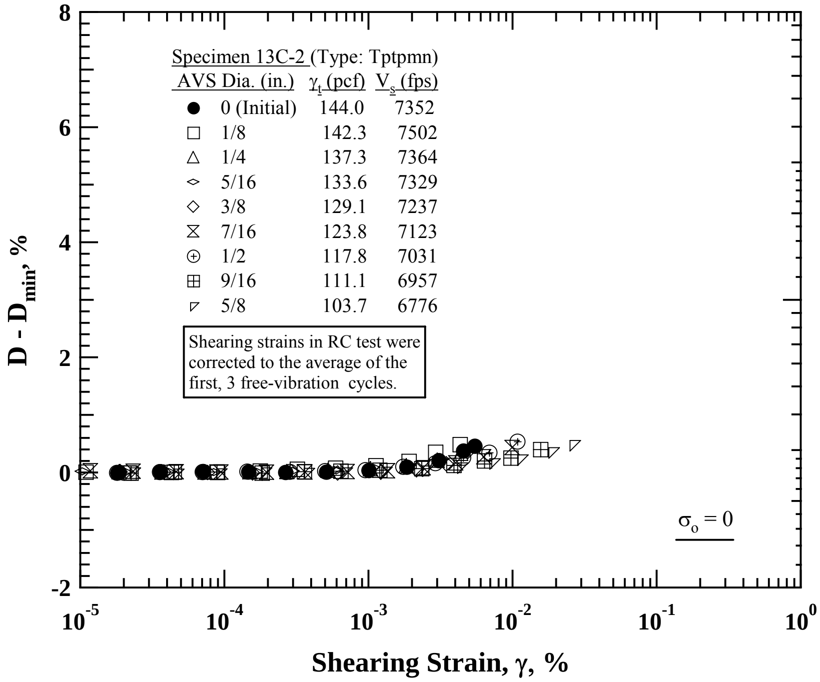

(b) “Nonlinear Damping” ($D - D_{min}$) versus Shearing Strain (γ)

Figure 8.42 Comparisons in: (a) $G/G_{max} - \log\gamma$ relationships and (b) $(D - D_{min}) - \log\gamma$ relationships from Fixed-Free Resonant Column Tests on Specimen 13C-2 with Seven Artificial Void Segments (AVS) with Different Sizes

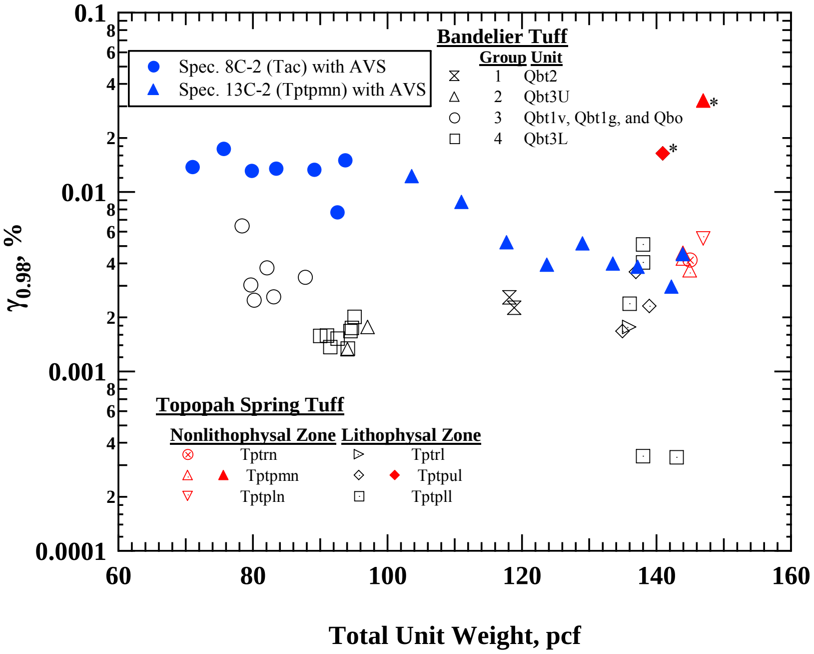

(a) Normalized Shear Modulus (G/G_{max}) versus Shearing Strain (γ)

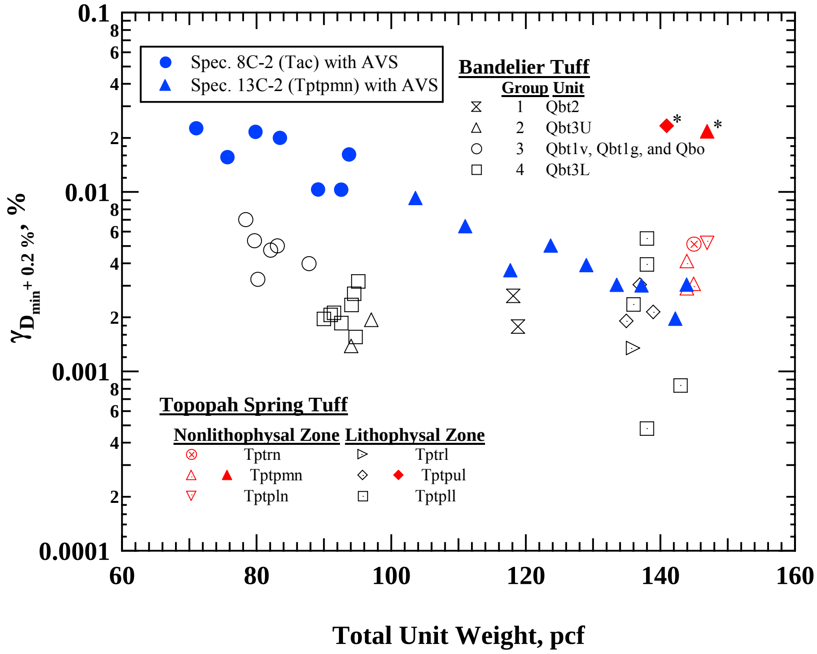

(b) “Nonlinear Damping” ($D - D_{min}$) versus Shearing Strain (γ)

Note: the data for the Bandelier Tuff were determined at their estimated in-situ pressure and the data for the Topopah Spring Tuff were determined at unconfined state.

Figure 8.43 Comparisons of (a) G/G_{max} – log γ and (b) ($D - D_{min}$) – log γ relationships from Fixed-Free Resonant Column Tests on Natural Specimens and Specimens with AVS with Different Sizes

13C-2 can indicate that the effect of the size of lithophysal cavities in the crystal-poor Topopah Spring tuffs is not significant and other factors such as the shape and distribution of the cavities and cracks can dominate the nonlinear relationships. On the other hand, the differences in the values between Specimen 8C-2 and the Bandelier tuffs can indicate that differences in the density of the matrix and any potential microscopic features in two different tuff formations can be significant.

8.6 SUMMARY

The nonlinear dynamic properties of ash-flow tuffs were studied by investigating the G/G_{max} –log γ and D – log γ relationships. The values of G/G_{max} and D at different strain levels provided a quantitative and systematic evaluation of the effects of lithostratigraphic features and test conditions on the nonlinear relationships. The modified hyperbolic model suggested by Darendeli (2001) was used when the strain levels needed to be extrapolated from the measured G/G_{max} – log γ relationship. However, care must be exercised in extrapolating the nonlinear data as additional factors such as slippage along cracks or breakage between lithophysae will accentuate the nonlinearity at higher strains. A fitting model for the measured D – log γ relationships was proposed for systematic comparisons at various strain levels and for extrapolating the measured relationships to slightly higher strain levels.

Chapter 9

Summary, Conclusions, and Recommendations

9.1 SUMMARY

A total of 38 tuff specimens from the Topopah Spring Tuff, Yucca Mountain, Nevada, were dynamically tested in this research. The lithostratigraphic features in the Topopah Spring Tuff at Yucca Mountain represent the processes of deposition, welding, crystallization, and cooling. Zones of the Topopah Spring Tuff are mainly defined by crystallization and development of lithophysae and spots. The samples tested in this research were recovered from 27 surface boreholes and 11 tunnel boreholes and represent six crystallized lithophysal and nonlithophysal zones that are classified and denoted as: (1) Tptrn which is a crystal-rich, nonlithophysal unit, (2) Tptrl which is a crystal-rich, lithophysal unit, (3) Tptpul which is a crystal-poor, upper lithophysal unit, (4) Tptpmn which is a crystal-poor, middle nonlithophysal unit, (5) Tptpll which is a crystal-poor, lower lithophysal unit and (6) Tptpln which is a crystal-poor, lower nonlithophysal unit.

Tests on 18 tuff specimens from the Bandelier Tuff, Pajarito Plateau, New Mexico, were also included in this research. The Bandelier Tuff consists of two sequential ignimbrite deposits that were created from two major eruptions. The deposits are denoted as: (1) Otowi member and (2) Tshirege member. The younger deposit (Tshirege member) is further subdivided by four distinct cooling units (Cooling Units 1 through 4 as denoted as Qbt1 through Qbt4). The Qbt1 is divided into two layers: (1) a lower glassy tuff layer (Qbt1g) and an upper devitrified and vapor-phase crystallized tuff layer (Qbt1v). The Qbt3 is also divided into two layers: (1) an upper cliff-forming tuff (Qbt3U) and a lower slope-forming tuff (Qbt3L). Various welding and crystallization conditions of the deposit represent complex variations in the depositional process at the site. Samples recovered from six surface boreholes were transported and handled as critical-care samples until dynamic testing was performed.

Published literature discussing the geologic characteristics of pyroclastic deposits and mechanical properties of the major components (ash-flow tuffs) are summarized. The classification schemes for the deposit in terms of welding intensity and the related geologic and/or physical properties proposed by various researchers are presented. The variation of Young's modulus (E or shear modulus, G), Poisson's ratio (ν), and their correlations with porosity are then discussed. In addition, the factors that affect the mechanical properties of specimens with various degrees of welding and lithostratigraphic features are discussed. The factors include confining pressure, strain rate, saturation, and strain amplitude.

Various test parameters were controlled to evaluate the dynamic properties of the tuffs in this research by using: (1) the combined resonant column and torsional shear (RCTS) device, and (2) the unconfined, free-free, resonant column (URC) device. The effects of confining pressure, strain amplitude, and excitation frequency were studied with the RCTS device. With the URC device, both compression and shear modes were studied.

The Large Resonant Column (LgRC) device was developed as part of this study. A theoretical approach to estimate the mass polar moment of inertia of the system is proposed for the LgRC device. The equations for the shearing strain estimation in the free-free boundary condition are presented and the equations for the equipment-generated damping estimation are also proposed and discussed. Verification of the system using a metal and five rock specimen is presented.

Small-strain shear modulus (G_{max}) and small-strain material damping ratio (D_{min}) of the ash-flow tuffs are discussed in terms of the effects of lithophysal cavities, flaws (fractures and missing pieces of the core) and the degree of welding at different confinement pressures (σ_o). Correlations between G_{max} and γ_t and D_{min} and γ_t are studied. Empirical relationships are proposed to describe the small-strain dynamic properties of ash-flow tuffs at various conditions. Discussions of the effects of excitation frequency (f), change in water content (w) due to specimen preparation (coring process using water as lubricant), and large lithophysal cavities on G_{max} and D_{min} are presented.

The small-strain shear wave velocity (V_S) values measured in the laboratory are compared with the V_S values determined in the field from Spectral-Analysis-of-Surface-Wave (SASW), crosshole and downhole tests. In addition to the comparison between the laboratory and field velocity measurements, the small-strain dynamic properties of the poorly welded ash-flow tuffs from the Bandelier Tuff are compared with the properties of granular soils that are currently available in the literature.

Nonlinear dynamic properties of ash-flow tuffs are discussed in terms of the effect of shearing strain on the dynamic properties. The effect of the lithostratigraphic characteristics of the specimens is discussed. A fitting model for the nonlinear material damping curve is proposed.

9.2 CONCLUSIONS

9.2.1 Small-Strain Dynamic Properties of Ash-Flow Tuffs

While all materials from the Topopah Spring Tuff are densely welded, the materials from the Bandelier Tuff have a range in welding intensities. The difference in welding intensity is significantly related to the mechanical properties of the tuffs, since the matrix of the tuffs change throughout the welding process. As welding intensifies, the density of the tuff increases and porosity decreases. The welding intensity is also related to the small-strain dynamic properties and their pressure dependent characteristics. Poorly welded tuffs exhibit small low-amplitude shear wave velocity (V_S) values at low confining pressures and a strong pressure dependency, similar to that exhibited by poorly graded sands. The tuffs with higher degrees of welding exhibit higher V_S values with small pressure dependency. The change in V_S with confining pressure (σ_o) of each specimen was evaluated by performing a least-squares fitting using the following equation:

$$V_S = A_V(\sigma_o / Pa)^{n_V} \tag{9.1}$$

where, A_V = small-strain shear wave velocity at σ_o = 1 atm,

σ_o = isotropic confining pressure in the same units as Pa,

Pa = one atmosphere (2117 psf or 100 kPa), and

n_V = a dimensionless exponent of the log V_S – log σ_o relationship.

Figure 9.1 illustrates the variation of n_V with respect to V_S at σ_o of 0.3 atm ($V_{S,\ 0.3\ atm}$). The strong correlation between n_V and $V_{S,\ 0.3\ atm}$ for poorly and moderately welded tuffs can be expressed as:

$$n_V = \frac{-0.142}{1000} V_{S,0.3atm} + 0.316 \tag{9.2}$$

where, $V_{S,\ 0.3\ atm}$ is in ft/sec. The standard error of this fitting, S_{ε,n_V}, is about 0.0117. The tuffs with higher welding intensity from both the Topopah Spring Tuff and the Bandelier Tuff exhibit higher $V_{S,\ 0.3\ atm}$ values and small (or zero) n_V values, behaving like competent rock. These prominent trends provide the ranges of n_V and $V_{S,\ 0.3\ atm}$ as good quantitative characteristics of the ash-flow tuffs with various welding intensities which are normally defined qualitatively. In addition, the trend line from Eq. (9.2) meats the trend

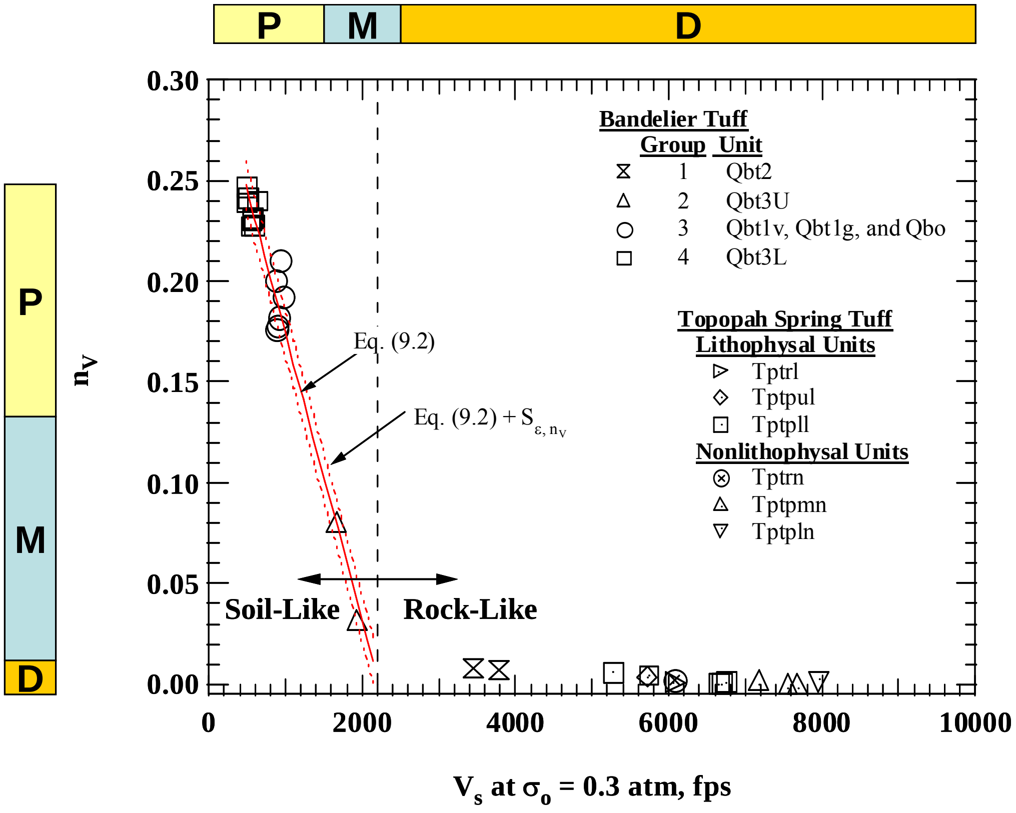

Notes: P=Poorly Welded Tuff; M=Moderately Welded Tuff;D=Densely Welded Tuff

Figure 9.1 Variation of n_V with V_S at σ_o of 0.3 atm for the Specimens from the Topopah Spring and Bandelier Tuffs

line for the densely welded tuffs at about $V_{S,\ 0.3\ atm}$ of 2200 ft/sec. This velocity of 2200 ft/sec can be a good quantitative guideline for classifying soft and stiff rocks at shallow depths (or possibly at the unconfined state), thereby, replacing the loosely defined and vague terms (e.g., rock-like or soil-like) sometimes used in the literature.

The strong relationship between n_V and $V_{S,\ 0.3\ atm}$ also provides the possibility of estimating the V_S at the in-situ pressure for similar tuffs with the V_S at a low pressure. The

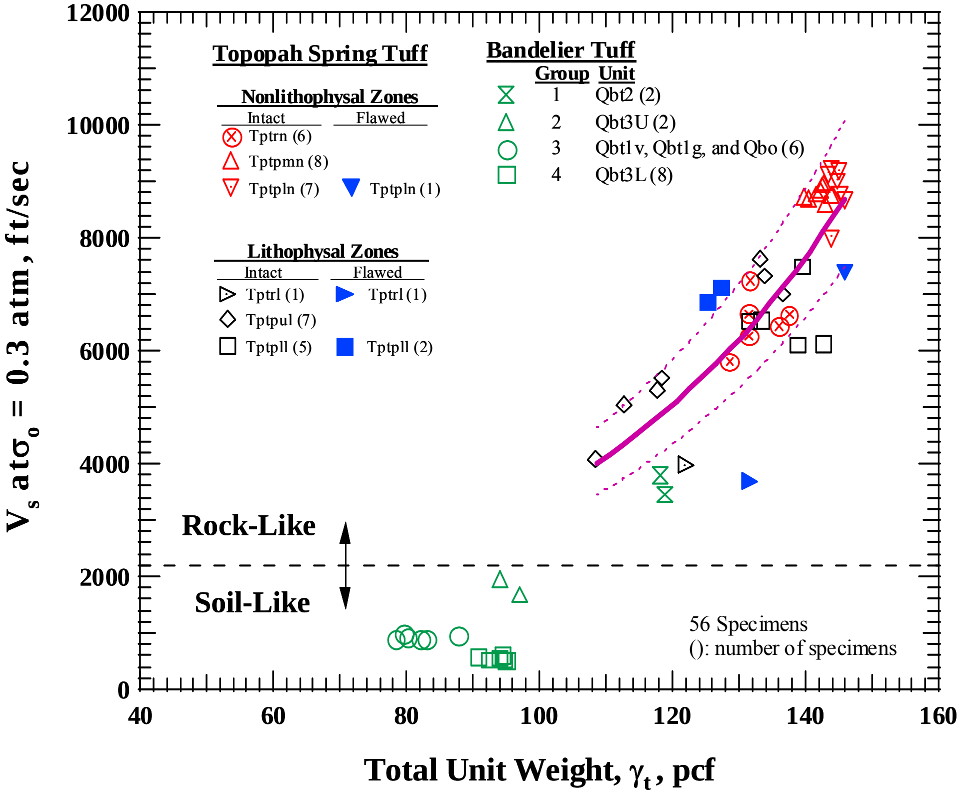

Figure 9.2 Variation of V_S at σ_o of 0.3 atm with Total Unit Weight for Specimens from the Topopah Spring and Bandelier Tuffs

value of $V_{S,\,0.3\text{ atm}}$ can be estimated from the total unit weight (γ_t) of the sample as shown in Figure 9.2. The specimens from each formation exhibited a generally good correlation between γ_t and $V_{S,\,0.3\text{ atm}}$. The lithostratigraphic features in the Topopah Spring tuffs are reflected and various welding intensities of the Bandelier tuffs are also well presented in the figure. The best-fit line through the Topopah Spring tuffs can be expressed as:

$$V_{S,0.3atm} = 100\sqrt{\frac{883e^{0.0491\gamma_t}}{\gamma_t}} \qquad (9.3)$$

where V_S is in ft/sec and γ_t is in pcf. The standard error of the fitting, $S_{\varepsilon,V_{S,0.3atm}}$, which is the standard deviation of the difference between the measured and predicted values, is about 0.111 in the semi-logarithmic relationship (Ang and Tang, 1975). Extension of this trend line to cover the Bandelier tuffs with low γ_t values is not recommended. The differences in the density of the matrix and any potential microscopic features in the two tuff formations can mislead the estimation of the $V_{S,\,0.3\,atm}$ from the extended line for the Bandelier tuffs.

As with $V_{S,\,0.3\,atm}$, the small-strain shear modulus (G_{max}) and small-strain material damping ratio (D_{min}) for the densely welded Topopah Spring Tuff specimens can be estimated as shown in Figures 9.3a and 9.3b, respectively. The best-fit line for G_{max} of the Topopah Spring Tuff specimens can be expressed as:

$$G_{\max} = 274e^{0.049\gamma_t} \tag{9.4}$$

where G_{max} are in ksf and γ_t is in pcf. Equation (9.4) can be expressed in SI units as:

$$G_{\max} = 13.1e^{0.0031\gamma_t} \tag{9.5}$$

where G_{max} are in MPa and γ_t is in kg/m^3. The standard error of fitting, $S_{\varepsilon,G_{max}}$, which is the standard deviation of the difference between the measured and predicted values, is about 0.222 in the semi-logarithmic relationship (Ang and Tang, 1975). Similarly, the best-fit line for D_{min} of the Topopah Spring Tuff specimens can be expressed as:

$$D_{\min} = 119e^{-0.042\gamma_t} \tag{9.6}$$

where D_{min} is in percent and γ_t is in lb/ft^3. Equation (9.6) can be expressed in SI units as:

$$D_{\min} = 119e^{-0.0026\gamma_t} \tag{9.7}$$

where D_{min} is in percent and γ_t is in kg/m^3. The standard error of the fitting, $S_{\varepsilon,D_{min}}$, is about 0.237 in the semi-logarithmic relationship. For the specimens from the Bandelier Tuff, a single line cannot be used for each estimation because their G_{max} and D_{min} values

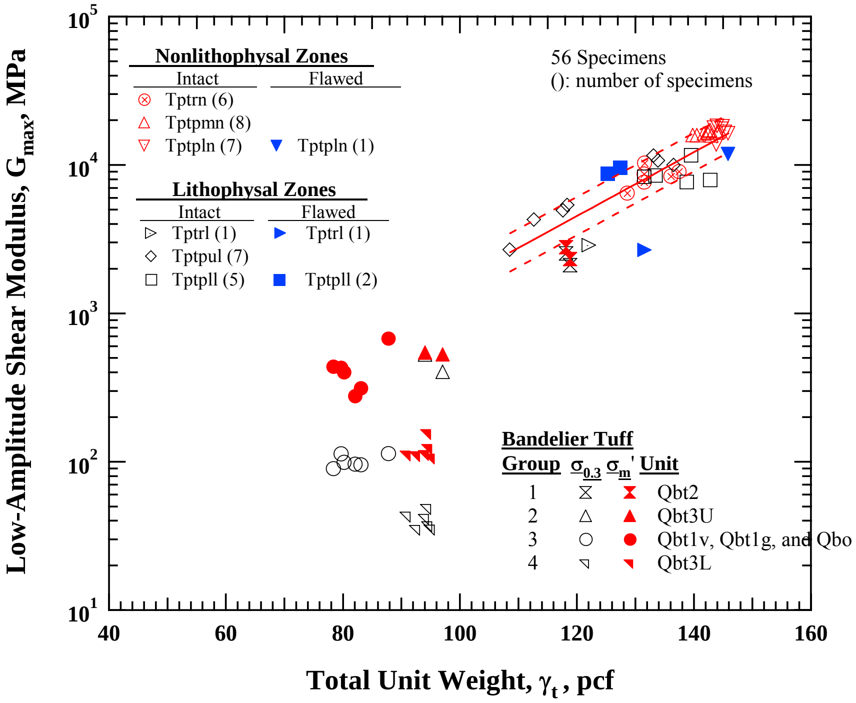

(a) Low-Amplitude Shear Modulus versus Total Unit Weight

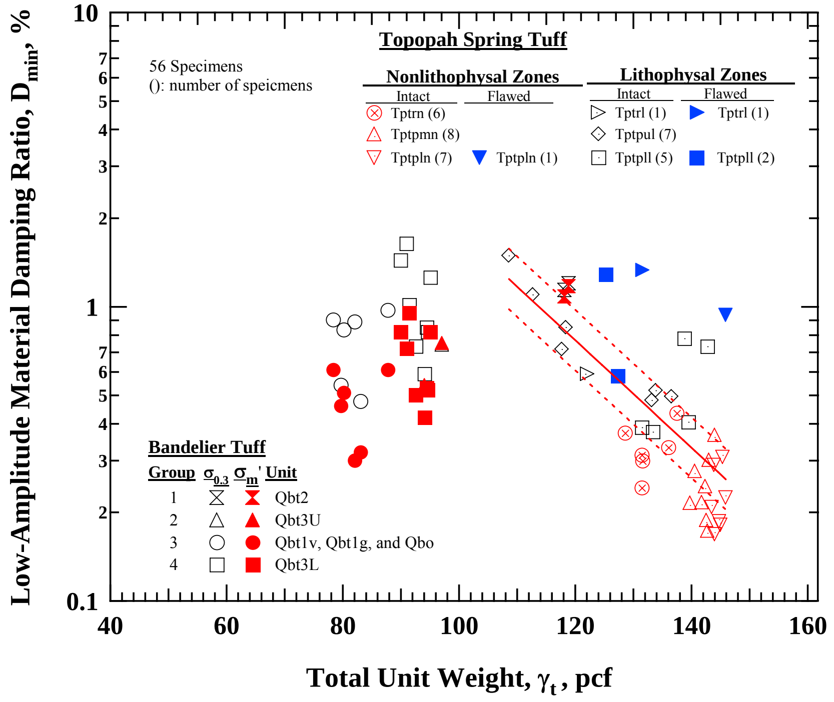

(b) Low-Amplitude Material Damping Ratio versus Total Unit Weight

Figure 9.3 Variation of: (a) Low-Amplitude Shear Modulus and (b) Low-Amplitude Material Damping Ratio with Total Unit Weight are dependent upon confining pressure (σ_o) as shown in Figures 9.3a and 9.3b, respectively. The changes in these values from 0.3 atm ($\sigma_{0.3}$) to the estimated in-situ mean effective stress (σ_m') seem to be equally large or even bigger than the errors in the trend lines for the Topopah Spring Tuff specimens.

9.2.2 Nonlinear Dynamic Properties of Ash-Flow Tuffs

The nonlinear dynamic properties of ash-flow tuffs were studied by investigating the G/G_{max} –log γ and D – log γ relationships. The values of G/G_{max} and D at different strain levels provide a quantitative and systematic evaluation of the effects of lithostratigraphic features and test conditions on the nonlinear relationships. The variations of strain amplitude (γ) when $G/G_{max} = 0.98$ ($\gamma_{0.98}$) and the strain amplitude when $D = D_{min}+0.2$ % ($\gamma_{Dmin+0.2\ \%}$) with γ_t are illustrated in Figures 9.4a and 9.4b, respectively. Both $\gamma_{0.98}$ and $\gamma_{Dmin+0.2\ \%}$ well represent the large variation of the linear range of G and D for the lithophysal specimens from the Topopah Spring Tuff caused by various lithophysal features. The specimens with a similar size and recovered from the nonlithophysal units exhibited relatively small variations in both $\gamma_{0.98}$ and $\gamma_{Dmin+0.2\ \%}$. On the other hand, the two small re-cored specimens equally exhibit the largest linear ranges. This difference is likely indicative of the smaller amount of defects in the smaller specimens. For the specimens from the Bandelier Tuff, these values need to be considered in terms of confining pressure because of their large pressure dependent characteristics.

It is interesting to note that the values of $\gamma_{0.98}$ and $\gamma_{Dmin+0.2\ \%}$ are very similar as shown in Figures 9.4a and 9.4b, respectively. In other words, when G decreases by about 2 %, D increases by about 0.2 %. This relationship can be clearly seen when $\gamma_{0.98}$ and

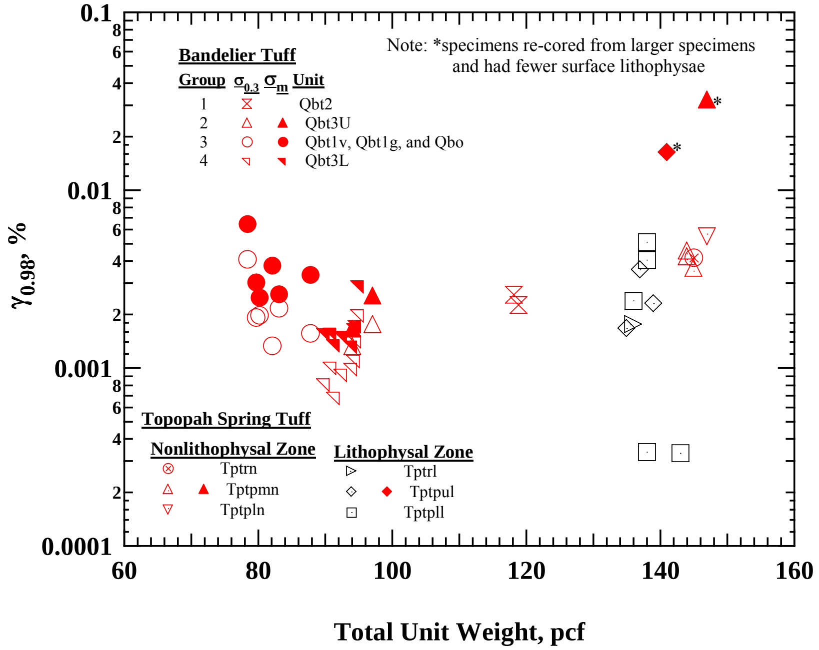

(a) Strain when $G/G_{max} = 0.98$ versus Total Unit Weight

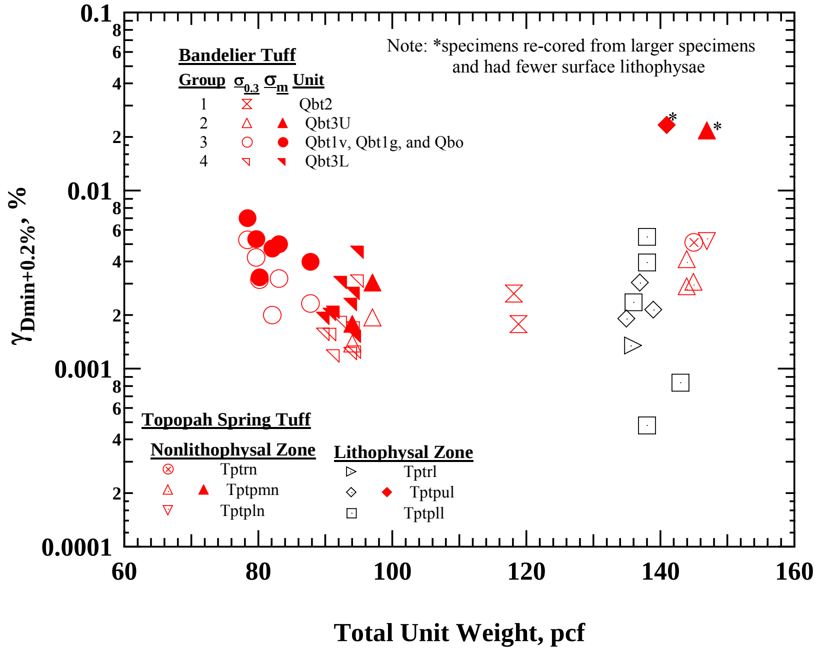

(b) Strain when $D = D_{min}+0.2$ % versus Total Unit Weight

Figure 9.4 Variation of: (a) $\gamma_{0.98}$ and (b) $\gamma_{Dmin+0.2\%}$ with Total Unit Weight of Specimens from the Topopah Spring and Bandelier Tuffs

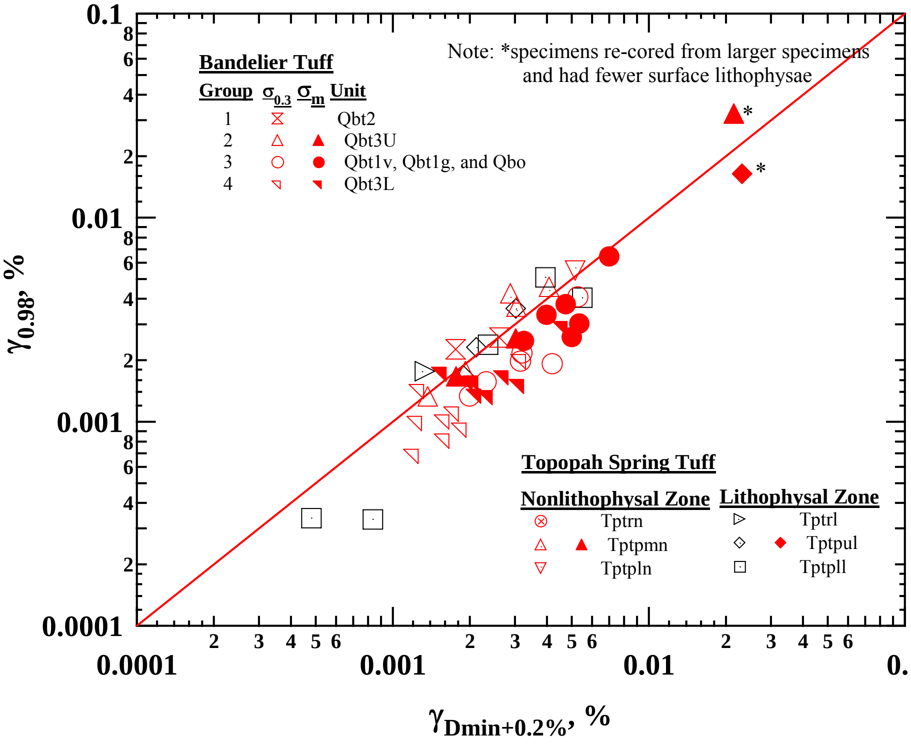

Figure 9.5 Comparison between $\gamma_{0.98}$ with $\gamma_{\mathrm{Dmin+0.2\%}}$ of Specimens from the Topopah Spring and Bandelier Tuffs

$\gamma_{\mathrm{Dmin+0.2\,\%}}$ are plotted against each other as shown in Figure 9.5. These strain levels can be used as a pair for a systematic comparison of the nonlinear relationships.

It is also interesting to note that the values of $\gamma_{0.98}$ have linear relationships with $\gamma_{0.94}$ (γ when $G/G_{max} = 0.94$) and $\gamma_{0.80}$ (γ when $G/G_{max} = 0.80$) as illustrated in Figures 9.6a and 9.6b respectively. These linear relationships indicate that the specimens that had higher linear ranges exhibited less decrease in G at higher strains. In other words, the measurement at the smaller strain level can be used to expect the relative difference in the nonlinearity of the specimens at higher strains. Similar trends were observed for D – log γ relationships based on the values of $\gamma_{\mathrm{Dmin+0.5\,\%}}$ (γ when $D = D_{min}+0.5$ %) and $\gamma_{\mathrm{Dmin+2.0\,\%}}$ (γ when $D = D_{min}+2.0$ %) with respect to $\gamma_{\mathrm{Dmin+0.2\%}}$. Figures 9.7a and 9.7b show the

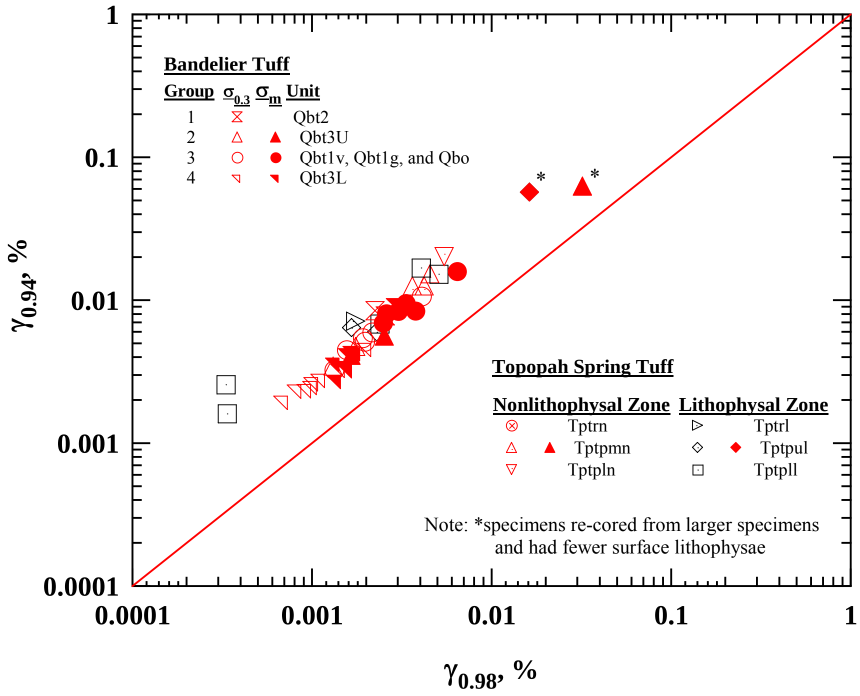

(a) Strain when G/G_{max} = 0.94 versus Strain when G/G_{max} = 0.98

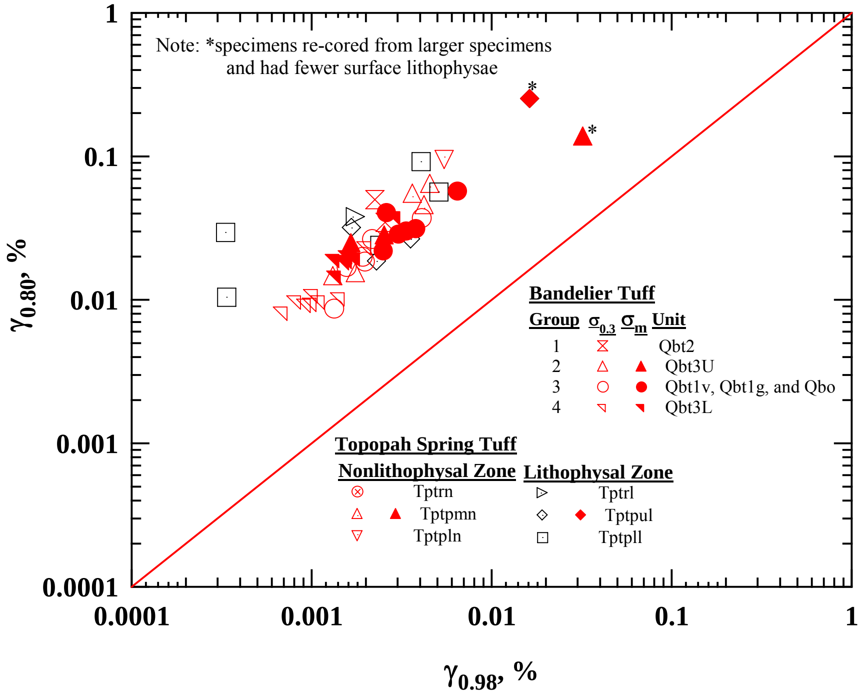

(b) Strain when G/G_{max} = 0.80 versus Strain when G/G_{max} = 0.98

Figure 9.6 Comparisons of: (a) $\gamma_{0.94}$ and (b) $\gamma_{0.80}$ with $\gamma_{0.98}$ of Specimens from the Topopah Spring and Bandelier Tuffs

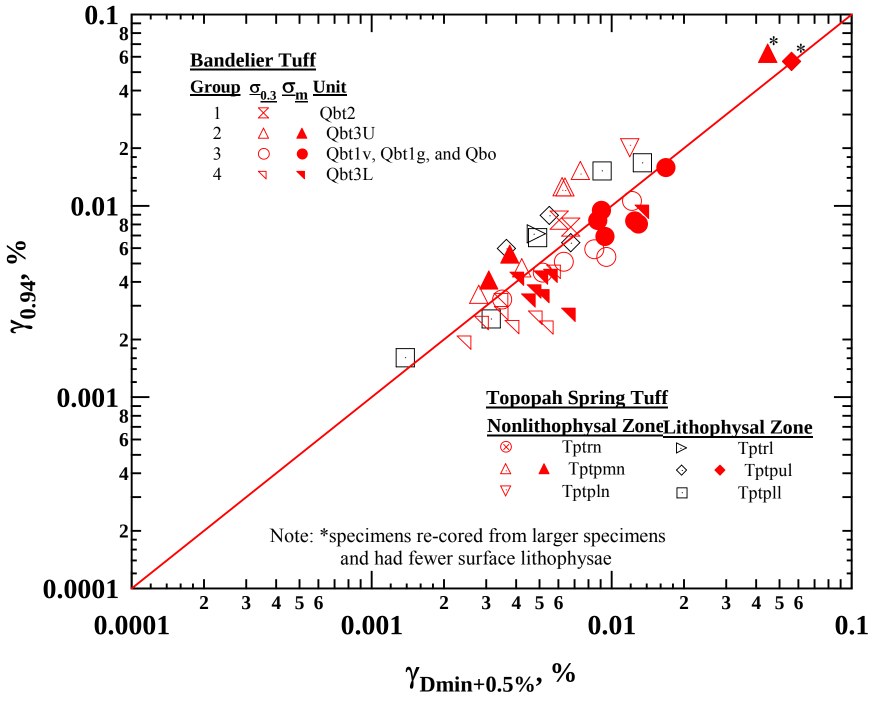

(a) Strain when G/G_{max} = 0.94 versus Strain when D = D_{min}+0.5 %

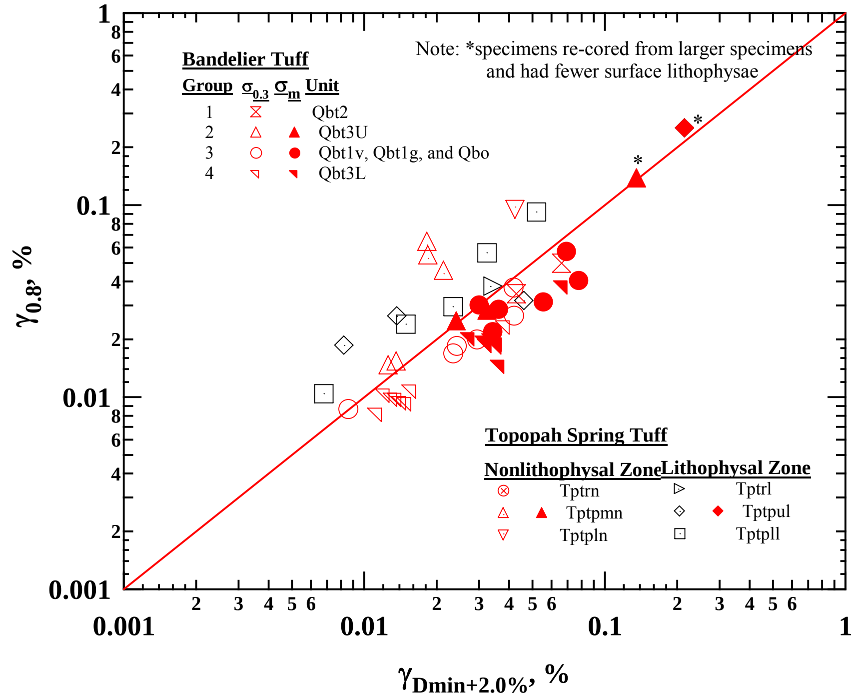

(b) Strain when G/G_{max} = 0.80 versus Strain when D = D_{min}+2.0 %

Figure 9.7 Comparison between: (a) $\gamma_{0.94}$ and $\gamma_{Dmin+0.5\%}$ and (b) $\gamma_{0.80}$ and $\gamma_{Dmin+2.0\%}$ of Specimens from the Topopah Spring and Bandelier Tuffs comparisons between $\gamma_{0.94}$ and $\gamma_{Dmin+0.5\,\%}$ and between $\gamma_{0.80}$ and $\gamma_{Dmin+2.0\,\%}$, respectively. Note that the $\gamma_{0.80}$ and $\gamma_{Dmin+2.0\,\%}$ values of most specimens from the Topopah Spring Tuff were extrapolated from the least-squares fitting using Eq. (9.9) (discussed later). The similarity observed in each comparison indicates that the nonlinear relationships can be similarly examined as done at the smaller strain level of $\gamma_{0.98}$ and $\gamma_{Dmin+0.2\,\%}$.

The modified hyperbolic model suggested by Darendeli (2001) was used when the strain levels need to be extrapolated from the measured data. The model can be expressed as:

$$\frac{G}{G_{\max}} = \frac{1}{1+\left(\dfrac{\gamma}{\gamma_r}\right)^{a}} \tag{9.8}$$

where, γ_r = reference shear strain and

a = curvature coefficient (dimensionless exponent).

The reference strain, γ_r, is defined as the value of γ equal to the shear strain at which G/G_{max} equals 0.5. For the D – log γ relationships, the following fitting model is proposed. The model can be expressed as:

$$D - D_{\min} = C\left(\frac{\gamma}{\gamma_D}\right)^{a_D} \tag{9.9}$$

where, γ_D = reference shear strain for D-log γ relationship,

a_D = curvature coefficient (dimensionless exponent) for D - log γ relationship and,

C = reference material damping ratio in percent for the fitting.

The reference strain, γ_D, is defined as the value of γ equal to the shear strain at which $D-D_{min}$ equals the “C” value. Figure 9.8a and 9.8b illustrate the variations of $\gamma_{0.94}$ and

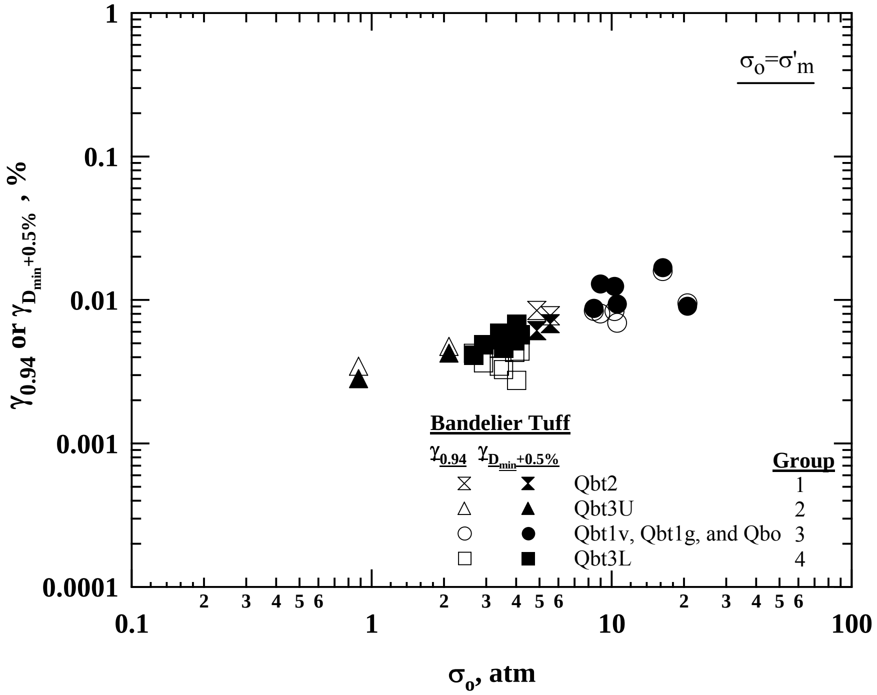

(a) $\gamma_{0.94}$ or $\gamma_{Dmin+0.5\%}$ versus σ_o

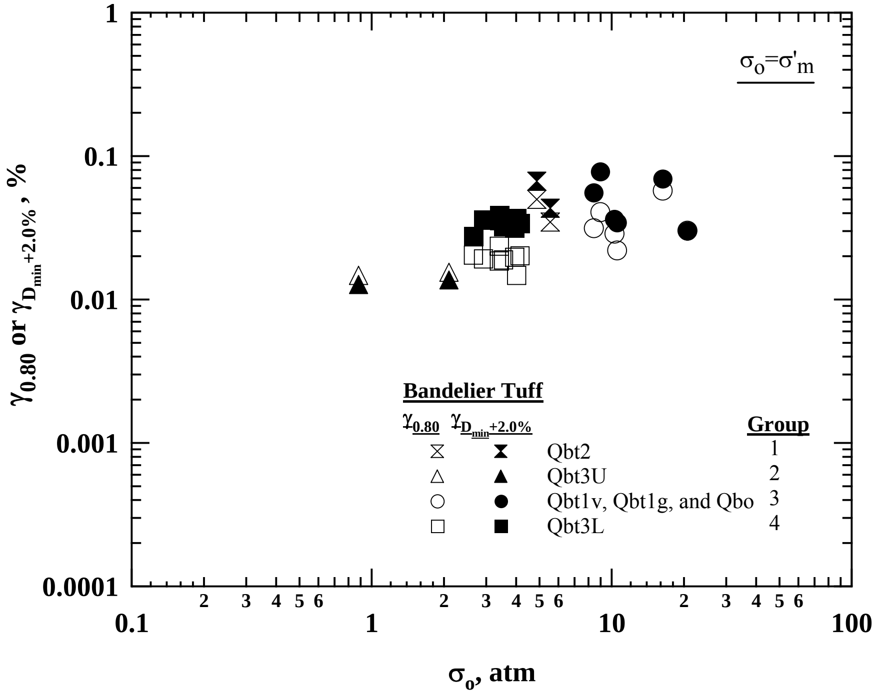

(b) $\gamma_{0.80}$ or $\gamma_{Dmin+2.0\%}$ versus σ_o

Figure 9.8 Variations of: (a) $\gamma_{0.94}$ and $\gamma_{Dmin+0.5\%}$ (b) $\gamma_{0.80}$ and $\gamma_{Dmin+2.0\%}$ with Isotropic Confining Pressure of Specimens from the Bandelier Tuffs

$\gamma_{Dmin+0.5\ \%}$ and the variations of $\gamma_{0.80}$ and $\gamma_{Dmin+2.0\ \%}$ with confining pressure, respectively. The very similar values and trends observed from these strain levels indicates that: (1) the pressure effects on the G/G$_{max}$ –log γ and D – log γ relationships at the two different strain levels are similar, (2) these strain levels can be used as the other good pairs for a systematic comparison of the nonlinear relationships, and (3) the proposed fitting model for D – log γ relationships works well.

The average trend of the G/G$_{max}$ –log γ relationships of the poorly welded and moderately welded tuffs from the Bandelier Tuff can be predicted from the best-fit lines of γ_r and “a” values through the data obtained in this research that can be expressed as:

$$\gamma_r = 0.046(\sigma_o / Pa)^{0.46} \tag{9.10}$$

$$a = -0.298 \log_{10} \gamma_r + 0.656 \tag{9.11}$$

where, γ_r is the reference strain for G/G$_{max}$ – log γ relationship in %,

σ_o is the isotropic confining pressure in the same units as Pa,

Pa is one atmosphere (2117 psf or 100 kPa), and

a is the curvature coefficient (dimensionless exponent).

Similarly, the average trend of the (D – D$_{min}$) - log γ relationships of the poorly welded and moderately welded tuffs from the Bandelier Tuff can be predicted from the best-fit lines of γ_D and “a_D” values through the data obtained in this research that can be expressed as:

$$\gamma_D = 0.038(\sigma_o / Pa)^{0.54} \tag{9.12}$$

$$a_D = -0.545 \log_{10} \gamma_D + 0.337 \tag{9.13}$$

where, γ_D is the reference strain for D – log γ relationship in %,

σ_o is the isotropic confining pressure in the same units as Pa,

Pa is one atmosphere (2117 psf or 100 kPa), and

a_D is the curvature coefficient for D – log γ relationship (dimensionless).

9.3 RECOMMENDATIONS

1. It has been observed that the lithophysal features in the specimens from the lithophysal units of the Topopah Spring Tuff exist with various amounts, shapes and distributions. The linear and nonlinear dynamic properties of these materials vary significantly due to these features. By increasing the number of specimens in each unit, the uncertainty associated with the lithophysal features was examined to some extent. However, more tests could be performed to reduce some of the uncertainty.

2. The large resonant column (LgRC) device can be used to test specimens with larger sizes. Tests on larger specimens could be performed to evaluate the effect of sample size on some of the lithophysal features.

3. Total unit weight was mainly used to describe the physical condition of the specimens in this study. Measurements of other parameters such as porosity would provide more information on macroscopic or microscopic (if possible) features in the specimens.

4. Comparisons with strength parameters of the tuffs would be also informative. The numerous research findings available in the literature can be compared and correlate with the findings in this research.

5. The fitting model for the D – log γ relationship proposed in this research works well capturing the differences in the linear range and the curvature of the relationships for the tuff specimens in the nonlinear range. This model can be used for other types of geomaterials. Systematic comparisons between specimens and between G – log γ and D – log γ relationships of each specimen are possible with the model.

Appendix A

Small-Strain Moduli and Small-Strain Material Damping Ratios and Poisson's Ratios of Ash-Flow Tuffs

A.1 INTRODUCTION

As discussed in Chapter 4, the dynamic tests in the URC set-up consist of two general types of small-strain seismic tests: (1) free-free resonance tests and (2) direct-travel-time tests. The free-free resonance tests involve the measurements in both shear mode in torsional motion and compression in longitudinal motion. In torsional motion, shear wave velocity, V_S, shear modulus, G_{max}, and material damping ratio in shear, D_{min} or $D_{S\ min}$ are measured. In longitudinal motion, unconstrained compression wave velocity, V_C, Young's modulus, E_{max}, and material damping ratio in unconstrained compression, $D_{C\ min}$ are measured. Direct-travel-time measurements of compression waves are performed to estimate the constrained compression wave velocity, V_P, and constrained modulus, M_{max}. In addition, Poisson's ratio (ν) can be calculated from the small-strain velocities or moduli using the following relationships:

$$\nu_{MG} = \frac{M_{max}-2G_{max}}{2(M_{max}-G_{max})} \qquad (A.1)$$

$$\nu_{ME} = \frac{1}{4M_{max}}\left(-M_{max}+E_{max}+\sqrt{9M_{max}{}^2-10M_{max}E_{max}+E_{max}^2}\right) \qquad (A.2)$$

$$\nu_{EG} = \frac{E_{max}-2G_{max}}{2G_{max}} \qquad (A.3)$$

where each subscript of ν indicates the combination of small-strain moduli for each relationship. Note that V_P, V_C and V_S can be substitute for M_{max}, E_{max} and G_{max} in the equations, respectively.

A.1 SMALL-STRAIN DYNAMIC PROPERTIES FROM UNCONFINED, FREE-FREE RC TESTS

The small-strain dynamic properties determined from the unconfined, free-free resonant column (URC) tests on the 38 specimens from the Topopah Spring Tuff are presented in Figures A.1 through A.5. The values of small-strain Young's modulus (E_{max}) and small-strain constrained compression modulus (M_{max}) of the specimens are presented with their total unit weights (γ_t) in Figures A.1 and A.2, respectively. The values of Poisson's ratio (ν) calculated from the relationships of: (1) M_{max} and G_{max}, (2) M_{max} and E_{max}, and (3) E_{max} and G_{max} are presented in Figures A.3 through A.5, respectively.

The small-strain velocities (V_S, V_C and V_P) of the 4 specimens from the Bandelier Tuff are presented in Tables A.1. The values of small-strain moduli (M_{max}, E_{max} and G_{max}) are presented in Table A.2 with small-strain material damping ratio values (D_{min} and $D_{C\ min}$) and Poisson's ratio from the relationship of V_P and V_S.

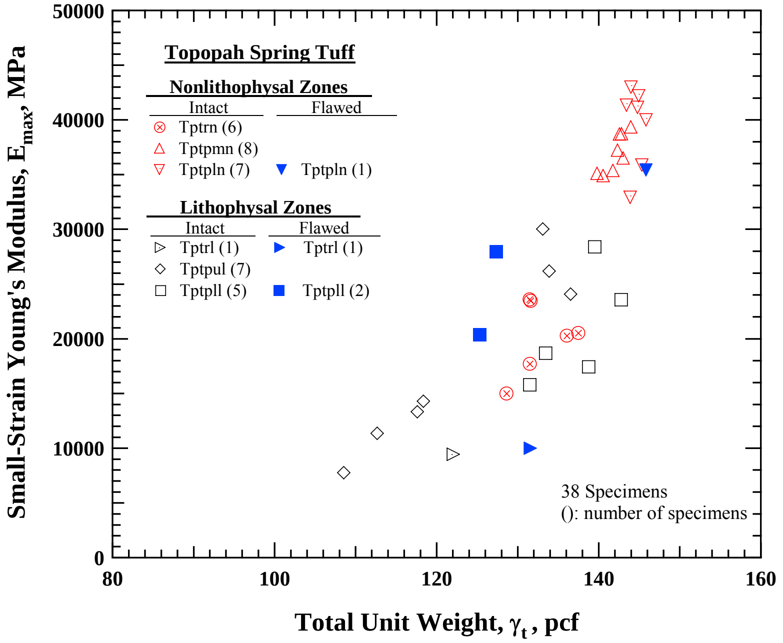

Figure A.1 Variation of Small-Strain Young's Modulus (E_{max}) with Total Unit Weight of Thirty Eight Specimens from the Topopah Spring Tuff

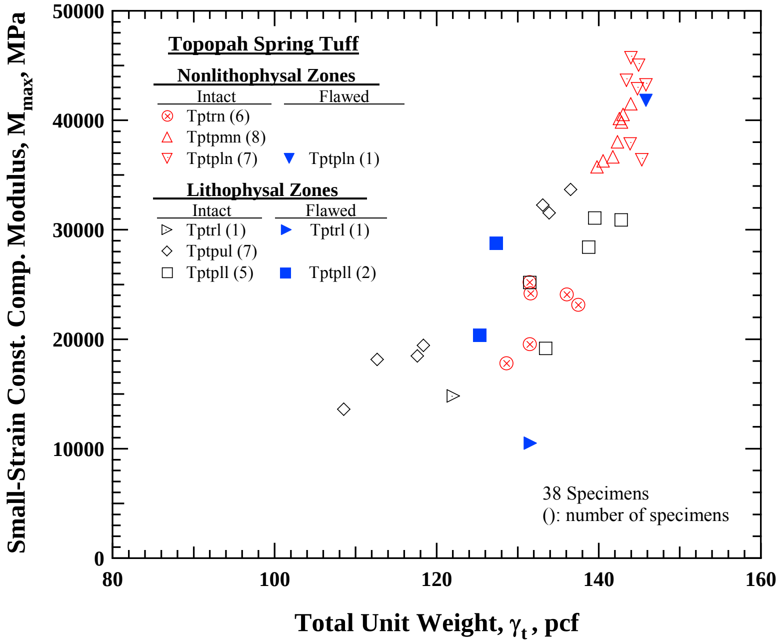

Figure A.2 Variation of Small-Strain Constrained Compression Modulus (M_{max}) with Total Unit Weight of Thirty Eight Specimens from the Topopah Spring Tuff

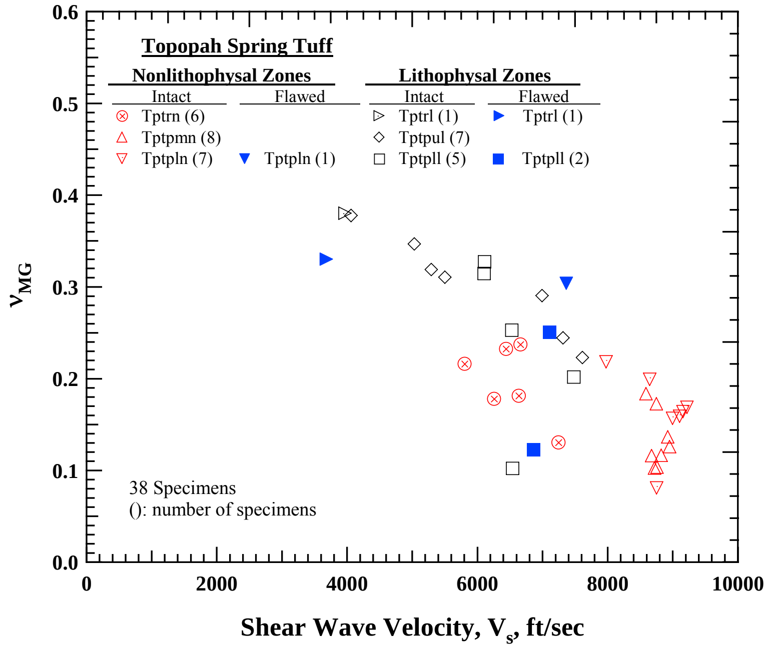

Figure A.3 Variation of Poisson's Ratio (ν_{MG}) from the Relationship between M_{max} and G_{max} with Small-Strain Shear Wave Velocity of Thirty Eight Specimens from the Topopah Spring Tuff

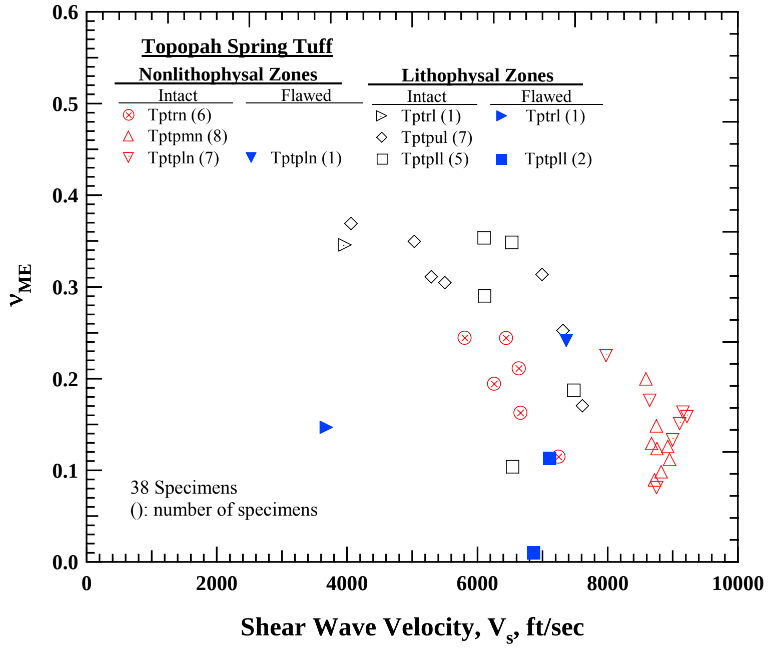

Figure A.4 Variation of Poisson's Ratio (ν_{ME}) from the Relationship between M_{max} and E_{max} with Small-Strain Shear Wave Velocity of Thirty Eight Specimens from the Topopah Spring Tuff

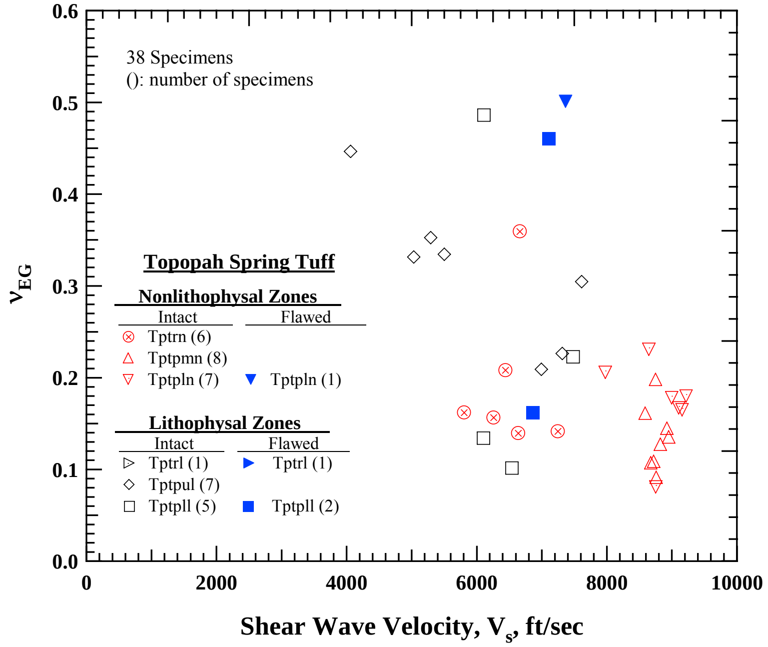

Figure A.5 Variation of Poisson's Ratio (ν_{EG}) from the Relationship between E_{max} and G_{max} with Small-Strain Shear Wave Velocity of Thirty Eight Specimens from the Topopah Spring Tuff

Table A.1 Small-Strain Wave Velocities of Four Specimens from the Bandelier Tuff

UT Spec. ID	Boring No.	Sample No.	Geologic Unit	Depth (ft)		Total Unit Weight, γ_t, lb/ft^3	V_P from Direct Arrival Test, fps	V_C from Free-Free RC Test, fps	V_S from Free-Free RC Test, fps
				Top	Bottom				
1G	DSC-2	R29	Qbt2	136.2	136.7	118.9	4554	4242	2989
2G	DSC-1A	R40	Qbt2	155.2	155.6	118.2	5677	5287	3566
3A	DSC-2	R6	Qbt3U	28.9	29.8	95.8	3262	3006	2010
5C	DSC-1A	R14	Qbt3U	68.5	69.2	99.0	2952	2058	1704

Table A.2 Small-Strain Moduli and Material Damping Ratios and Poisson's Ratios of Four Specimens from the Bandelier Tuff

UT Spec. ID	Boring No.	Depth (ft)		Constrained Modulus, M, from V_P, psf	Unconstrained Modulus, E, from V_C, psf	Shear Modulus, G, from V_S, psf	Material Damping in Unconstrained Compression, D_C, %	Material Damping in Shear, D_S, %	Poisson's Ratio, ν_{MG}, from Relationship of V_P and V_S
		Top	Bottom						
1G	DSC-2	136.2	136.7	7.66E+07	6.64E+07	3.30E+07	0.99	1.97	0.12
2G	DSC-1A	155.2	155.6	1.18E+08	1.03E+08	4.67E+07	0.82	0.76	0.17
3A	DSC-2	28.9	29.8	3.17E+07	2.69E+07	1.20E+07	0.86	0.86	0.19
5C	DSC-1A	68.5	69.2	2.68E+07	1.30E+07	8.92E+06	3.13	2.57	0.25

References

ASTM D4220-95 (2000). "Standard Practices for Preserving and Transporting Soil Samples," pp. 1-10.

Avar, B.B., Hudyma, N. and Karakouzian, M. (2003). "Porosity Dependence of the Elastic Modulus of Lithophysae-Rich Tuff: Numerical and Experimental Investigations," *International Journal of Rock Mechanics & Mining Science*, Vol. 40, pp. 919-928.

Bailey, R.A., Smith, R.L., and Ross, C.S. (1969). "Stratigraphic Nomenclature of Volcanic Rocks in the Jemez Mountains, New Mexico," *USGS Bulletin*, Washington, DC, p. 1274.

Broxton, D.E. and Reneau, S.L. (1995). "Stratigraphic Nomenclature of the Bandelier Tuff for the Environmental Restoration Project at Los Alamos National Laboratory," *Los Alamos National Laboratory Report*, LA-13010-MS, August 1995.

Broxton, D.E. and Vaniman, D.T. (2005). "Geologic Framework of a Groundwater System on the Margin of a Rift Basin, Pajarito Plateau, North-Central New Mexico," *Vadose Zone Journal*, Vol. 4, pp. 522-550.

Buesch, D.C., Dickerson, R.P., Drake, R.M., and Spengler, R.W. (1994). "Integrated Geology and Preliminary Cross Section along the North Ramp of the Exploratory Studies Facility, Yucca Mountain," *Proceedings of the Fifth Annual International High-Level Radioactive Waste Management Conference*, American Nuclear Society, Vol. 2, pp. 1055-1065.

Buesch, D.C., Spengler, R.W., Moyer, T.C. and Geslin, J.K. (1996). "Proposed Stratigraphic Nomenclature and Macroscopic Identification of Lithostratigraphic Units of the Paintbrush Group Exposed at Yucca Mountain, Nevada," *USGS Open-File Report 94-469*, Denver, Colorado.

Buesch, D.C. and Spengler, R.W. (1998). "Character of the middle nonlithophysal zone of the Topopah Spring Tuff at Yucca Mountain," *International High-Level Radioactive Waste Management Conference*, American Nuclear Society, Le Grange Park, Illinois, pp. 16-23.

Buesch, D.C., Stokoe K.H., Choi W.K., Jeon S.Y., Lee J.J., and Schuhen M.D. (2006). "Lithostartigraphy and Shear-Wave Velocity in the Crystallized Topopah Spring Tuff, Yucca Mountain, Nevada," *International High-Level Radioactive Waste Management Conference*, April 30 – May 4, 2006, Las Vegas, Nevada.

Byers, F.M., Jr., Carr, M.J., Christiansen, R.L., Lipman, P.W., Orkild, P.P., and Quinlivan, W.D. (1976a). "Geologic map of the Timber Mountain caldera area, Nye County, Nevada," U.S. Geological Survey Miscellaneous Investigations Map I-891, Scale 1:48,000.

Byers, F.M., Jr., Carr, M.J., Orkild, P.P., Quinlivan, W.D., and Sargent, K.A., (1976b). "Volcanic Suites and Related Cauldrons of the Timber Mountain-Oasis Valley Caldera Complex, Southern Nevada," U.S. Geological Survey Professional Paper 919, 70 p.

Chen, A. T. F., and Stokoe, K. H., II (1979). "Interpretation of Strain Dependent Modulus and Damping from Torsional Soil Tests," *Report No. USGS-GD-79-002*, NTIS No. PB-298479, U. S, Geological Survey, 46 p.

Chipera, S.J., Vaniman, D.T., Carlos, B.A., and Bish, D.L. (1995). "Mineralogy Variation in Drill Core UE-25 UZ#16, Yucca Mountain, Nevada," *Los Alamos National Laboratory Report LA-12810-MS*, 39 p.

Christiansen, R.L., Lipman, P.W., Carr, M.J., Byers, F.M., Jr., Orkild, P.P., and Sargent, K.A. (1977). "The Timber Mountain-Oasis Valley Caldera Complex of Southern Nevada," *Geological Society of America Bulletin*, v. 88, pp. 943-959.

Darendeli, B.M. (2001). "Development of a New Family of Normalized Modulus Reduction and Material Damping Curves," Ph.D. Dissertation, University of Texas at Austin, Austin, Texas.

Descour, J. M., Hanna K., Conover D. and Hoekstra B., (2001). "Seismic Tomography Technology for the Water Infiltration Experiment," TDR-EBS-MD-000017 REV 00, Las Vegas, Nevada: Bechtel SAIC Company.

Flint, L.E., Buesch, D.C., AND Flint, A.L.(2006). "Characterization of Unsaturated Zone Hydrogeologic Units using Matrix Properties and Depositional History in a Complex Volcanic Environment," *Vadose Zone Journal* Vol. 5, pp. 480–492.

Gardner, J.N., and F. Goff. (1984). "Potassium-Argon Dates from the Jemez Volcanic Field: Implications for Tectonic Activity in the North-Central Rio Grande rift," *New Mexico Geol. Soc. Guide- book, 35th Field Conference, Rio Grande Rift*, Northern New Mexico, University of New Mexico, Albuquerque, pp. 75–81.

Gardner, J.N., Kolbe, T., and Chang, S. (1993). "Geology, Drilling, and Some Hydrologic Aspects of Seismic Hazards Program Core Holes," *Los Alamos National Laboratory*, New Mexico, Los Alamos National Laboratory Report LA-12460-MS, 19 p.

Haupt, R.W., Martin, R.J. III, Tang, X., Dupree, W.J., Price, R.H. (1991). "Modulus Dispersion and Attenuation in Tuff and Granite," *U.S. Symposium on Rock Mechanics, Rock Mechanics Proceedings of the 33rd U.S. Symposium*, pp. 899-908.

Hoek, E. and Brown, E.T. (1980). Underground excavations in rock, Inst. Min. & Metall., London, United Kingdom, 527 pp.

Houston, Tom E., and Carl J. Costantino, 2003. "Site Response Sensitivity Study for the CMRR Facility," December 17, 2003.

Hwang, S. K. (1997). "Investigation of the Dynamic Properties of Natural Soils," Ph.D. Dissertation, University of Texas at Austin, 394 pp.

International Code Council, Building Officials and Code Administrators International, International Conference of Building Officials and Southern Building Code Congress International, (2006). International Building Code, Falls Church, Va.

Izett, G.A. and Obradovich, J.D. (1994). "40Ar/39Ar Age Constraints for the Jaramillo Normal Subchron and the Matuyama-Brunhes Geomagnetic Boundary," *Journal of Geophysical Research*, Vol. 99, pp. 2925–2934.

Kleinfelder, Inc. (2005). "Laboratory Test Plan for Resonant Column/Torsional Shear Tests," May 13, 2005.

Kleinfelder, Inc. (2007). "Geotechnical Data Report Chemistry and Metallurgy Research Facility Replacement (CMRR) Project," *Los Alamos National Laboratory Kleinfelder Project No. 19435*, Rev. 0," May 24, 2007.

Kokusho, T., Yoshida Y. and Tanaka, Y. (1995). "Shear Wave Velocity in Gravelly Soils with Different Particle Grading," Static and Dynamic Properties of Gravelly Soils, *Geotech. Spec. Pub. No. 56*, ASCE, pp. 92-105.

Lewis, M.D. (1990). "A Laboratory Study of the Effect of Stress State on the Elastic Moduli of Sand," Ph.D. Dissertation, University of Texas at Austin, Austin, Texas.

Limpman, P.W., Christiansen, R.L., and O'Connor, J.T. (1966). "A Compositionally Zoned Ash-Flow Sheet in Southern Nevada," *U.S. Geological Survey Professional Paper 524-F*, 47 p.

Lin, Y.C. (2007). "Characterizing VS Profiles by the SASW Method and Comparison with Other Seismic Methods," Ph.D. Dissertation, University of Texas at Austin, 277 pp.

Martin, R.J., III, Price, R.H., Boyd, P.J. and Haupt, R.W. (1992). "Anisotropy of the Topopah Spring Member Tuff," *Sandia Report SAND91-0894*, Albuquerque, New Mexico: Sandia.

Martin, R.J., III., Price, R.H., Boyd, P.J. and Noel, J.S. (1993). "The Influence of Strain Rate and Sample Inhomogeneity on the Moduli and Strength of Welded Tuff," *International Journal of Rock Mechanics and Mining Science & Geomechanics Abstracts*, 30, (7), 1507–1510.

Menq, F.-Y. (2003). "Dynamic Properties of Sandy and Gravelly Soils," Ph.D. Dissertation, University of Texas at Austin, 364 pp.

Olsson, W.A. and Jones, A.K. (1980). “Rock Mechanics Properties of Volcanic Tuffs from the Nevada Test Site,” *Sandia Report SAND80-1453*, Albuquerque, New Mexico: Sandia National Laboratories.

Olson, R.E. (1974). “Shearing Strength of Kaolinite, Illite, and Montmorillonite,” *J. Geotech. Div. A.S.C.E. 100/GT11*, p.1215-1229.

Peterson, D.W. (1979). “Significance of the flattening of pumice fragments in ash-flow tuffs. In: Ash-flow tuffs. Special Paper -Geological Society of America,” *Geological Society of America (GSA)*, Boulder, CO, United States, pp. 195-204.

Price, R.H. (1983). “Analysis of the Rock Mechanics Properties of Volcanic Tuff Units from Yucca Mountain, Nevada Test Site,” *Sandia Report SAND82-1315*, Albuquerque, New Mexico: Sandia National Laboratories.

Price, R.H. and Bauer, S.J. (1985). “Analysis of the Elastic and Strength Properties of Yucca Mountain Tuff, Nevada,” *Research & Engineering Applications in Rock Masse, Proceedings of the 26th U.S. Symposium on Rock Mechanics*, Rapid City, South Dakota, June 26-28, 1985. pp. 89-96.

Price, R.H., Boyd, P.J., Martin, R.J., Haupt, R.W. and Noel, J.S. (1991). “Mechanical Anisotropy of the Yucca Mountain Tuffs," *High Level Radioactive Waste Management, Proceedings of the Second Annual International Conference*, Las Vegas, Nevada, April 28-May 3, 1991. 1, 268-271.

Price, R.H., Martin, R.J., III, Boyd, P.J., and Noel, J.S. (1994). “Mechanical and Bulk Properties in Support of ESF Design Issues,” *High Level Radioactive Waste Management, Proceedings of the Fifth Annual International Conference,* Las Vegas, Nevada, May 22-26, 1994. 4, 1987-1992.

Price, R.H. (1986). “Effects of Sample Size on the Mechanical Behavior of Topopah Spring Tuff,” *Sandia Report SAND85-0709*, Albuquerque, New Mexico: Sandia National Laboratories.

Price, R.H. (2004). “The Mechanical Properties of Lithophysal Tuff: Laboratory Experiments,” TDR-EBS-MD-000027 REV 00. Las Vegas, Nevada: Bechtel SAIC Company.

Quane, S.L. and Russell, J.K. (2003). “Rock Strength as a Metric of Welding Intensity in Pyroclastic Deposits,” *European Journal of Mineralogy*, Vol. 15, p. 855–864.

Quane, S.L. and Russell, J.K. (2005). “Ranking Welding Intensity in Pyroclastic Deposits,” *Bulletin of Volcanology*, Vol. 67, pp. 129-143.

Ragan, D.M. and Sheridan, M.F. (1972). “Compaction of the Bishop Tuff, California,” *Geological Society of America (GSA)*, 83(1):95–106.

Rigby, D.B. (2004). “Lithophysal Rock Mass Mechanical Properties of the Repository Host Horizon,” 800-K0C-SS00-00200-000-00A. Las Vegas, Nevada: Bechtel SAIC Company.

Rix, G. J (1984). "Correlation of Elastic Moduli and Cone Penetration Resistance," M.S. Thesis, University of Texas at Austin, 291 p.

Ross, C.S., Smith, R.L. (1961). "Ash-flow tuffs; their origin, geologic relations, and identification," *USGS Professional Paper 366 Reston*, VA, 81 pp.

Russell, J.K. and Quane, S.L. (2005). "Rheology of welding: inversion of field constraints," *Journal of Volcanology and Geothermal Research*, Vol. 142, pp. 173–191.

Sawyer, D.A., Fleck, R.J., Lanphere, M.A., Warren, R.G. and Broxton, D.E. (1994). "Episodic Volcanism in the Miocene Southwest Nevada Volcanic Field - Stratigraphic revisions of the ^{40}Ar/^{39}Ar Geochronologic Framework, and Implications for Magmatic evolution," *Geological Society of America Bulletin*, Vol. 106, pp.1304–1318.

Seed, H.B., R.T. Wong, I.M. Idriss, and K. Tokimatsu (1986). "Moduli and Damping Factors For Dynamic Analyses of Cohesionless Soils," *Journal of the Soil Mechanics and Foundations Division*, Vol. 112, No. SM11, pp. 1016-1032.

Smith, R.L. (1960a). "Ash Flows," *Geological Society of America Bulletin*, Vol. 71, pp. 795-842.

Smith, R.L. (1960b). "Zones and Zonal Variations in Welded Ash Flows," *Geological Survey Professional Paper 354-F*, Washington, DC.

Smith, R.L. and Bailey, R.A. (1966) "The Bandelier Tuff; a study of ashflow eruption cycles from zoned magma chambers," *Bulletin of Volcanology*, Vol. 29, pp. 83–103.

Smith, R.L., Bailey, R.A. and Ross, C.S. (1970). "Geologic map of the Jemez Mountains, New Mexico," *USGS Misc. Geol. Inv. Map I-571*. Map scale 1:125,000

Stimac, J.A., Broxton, D.E., Kluk, E.C., and Chipera, S.J. (1995). "Preliminary Stratigraphy of Tuffs from Borehole 49-2-700-1 at Technical Area 49," *Los Alamos National Laboratory Report*, New Mexico, Los Alamos National Laboratory.

Stokoe, K.H., II, Hwang, S.K., Laird, J.P. (1993). "Dynamic Properties of Undisturbed Soil Samples from Los Alamos, New Mexico," Geotechnical Engineering Report GR93-7, Civil Engineering Department, The University of Texas at Austin, Austin, TX, March.

Stokoe, K.H., II, Hwang, S.K., Lee J.N.K, and Andrus, R.D. (1994a). "Effects of Various Parameters on the Stiffness and Damping of Soils at Small to Medium Strains," *International Symposium on Pre-failure Deformation Characteristics of Geomaterials*, Shibuya, Mitachi and Miura, eds., Sapporo, Japan, September, pp. 785-816.

Stokoe, K.H., Hwang, S.K., Roesset, J.M., and Sun, W.S. (1994b). “Laboratory Measurements of Small-Strain Material Damping of Soil Using The Free-Free Resonant Column,” *Proceedings Earthquake Resistant Construction and Design, ERCAD*, Berlin, pp 195-202.

Stokoe, K.H., II, Darendeli, M.B., Andrus, R.D. and Brown, L.T. (1999). “Dynamic Soil Properties: Laboratory, Field and Correlation Studies,” Proceedings, Second *International Conference on Earthquake Geotechnical Engineering*, Sêco e Pinto, Editor, A.A. Balkema Publishers/Rotterdam & Brookfield, Netherlands, Vol. 3, pp. 811-845.

Stokoe, K.H, Choi, W.K., Jeon, S.Y., and Lee, J.J. (2006). “Intact Dacite, Tuff and Soil Specimens, Chemistry and Metallurgical Research Replacement (CMRR) Project, Los Alamos National Laboratory, Los Alamos, New Mexico,” Geotechnical Engineering Report GR06-1, Civil, Architectural and Environmental Engineering Department, the University of Texas at Austin, Austin, TX, November.

Streck, M.J. and Grunder, A.L. (1995). “Crystallization and Welding Variations in a Widespread Ignimbrite Sheet; the Rattlesnake Tuff, Eastern Oregon, USA,” *Bulletin of Volcanology*, Vol. 57(3), pp. 151–169.

Sun, C.W. (1983). “Stiffness and Damping from the Frequency Response of a Free-Free Specimen,” M.S. Thesis, University of Texas at Austin, Austin, Texas.

Veghela, J. G. (1995). “Small-Strain Dynamic Properties of Dry Sand from the Free-Free Resonant Column,” M.S. Thesis, University of Texas at Austin, 291 p.

Weston, T. R. (1995). “Effect of Grain Size and Particle Distribution on the Stiffness and Damping of Granular Soils at Small-Strain,” M.S. Thesis, University of Texas at Austin, 229 p.

Wilson, C.J.N., Hildreth W. (2003) “Assembling an Ignimbrite: Mechanical and Thermal Building Blocks in the Bishop Tuff, California,” *Journal of Geology*, Vol. 111, pp.653–670.

Winterkorn. F.H. and Fang H.-Y. (1975). “Foundation Engineering Handbook,” Van Nostrand Reinhold Company, New York, New York, pp.257.

Vita

Won Kyoung Choi was born in Seoul, Korea, on January 3, 1975 (the year of tiger), the son of Kyu Seong Choi and Yung Hee Kang. After graduated from Sung Sil High School, Seoul, Korea, he entered the Sung Kyun Kwan University, Seoul, Korea in March, 1993. He served military service from May, 1995 to July, 1997. He received the B.S. Degree in Civil Engineering in February, 2000. In August 2000, he entered the Graduate School of the University of Texas at Austin. He received his Master of Science (M.S.) degree in August, 2003. He continued his studies in geotechnical earthquake engineering at UT. He married Kyung Ah Rhee in Jun 24, 2000. They have a son, Ryan K Choi.

Permanent address: 816 HyunDae Apt. 1803 Ho.
DuckYang Gu, GoYang Si,
Kyunggi Do, Korea

This dissertation was typed by the author.